BEILSTEIN JOURNAL OF NANOTECHNOLOGY

Nanoscale patterning and characterization

Edited by Shelley Claridge and Wei-Ssu Liao

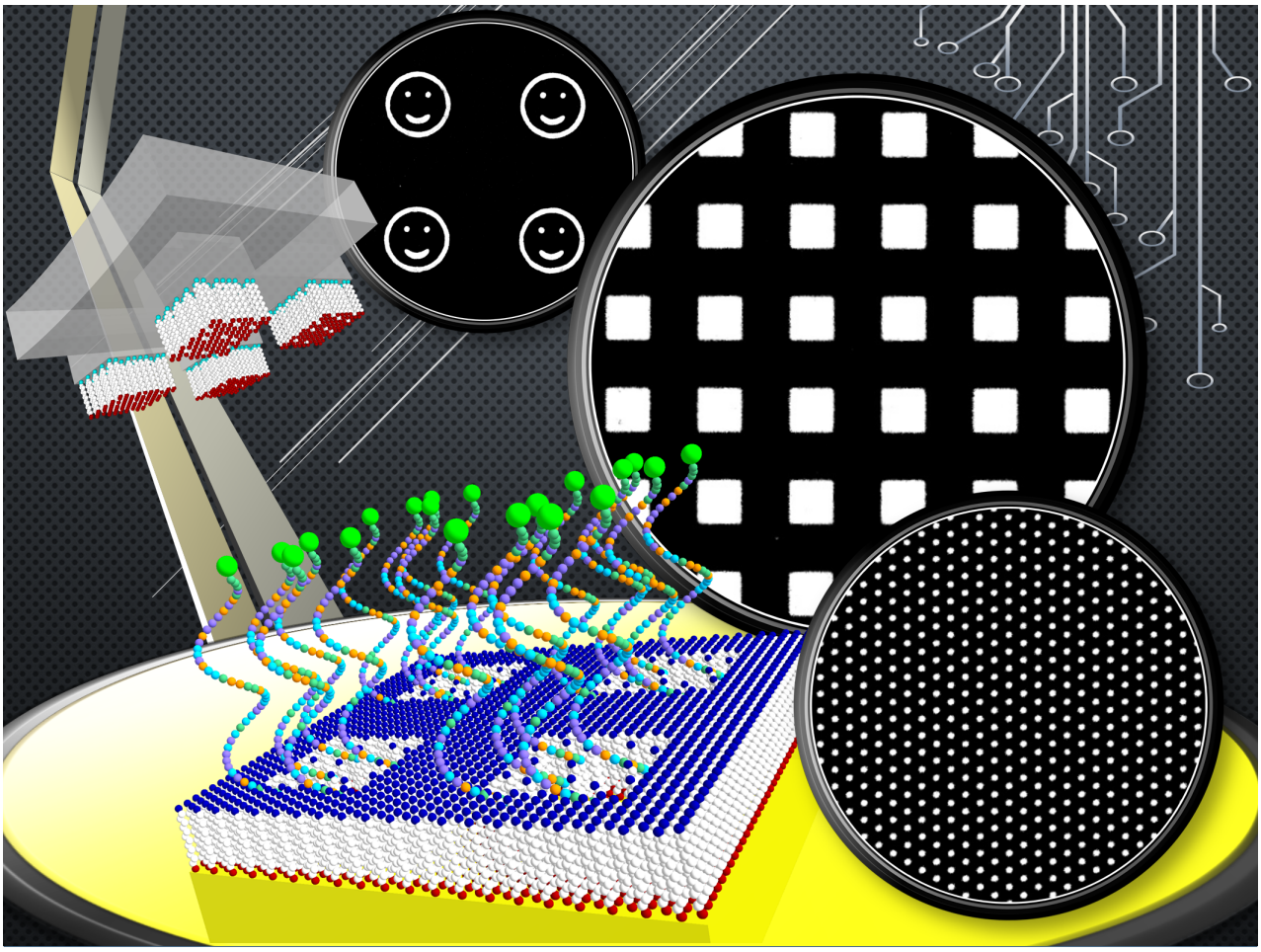

Generated on 07 February 2026, 15:03

Imprint

Beilstein Journal of Nanotechnology
www.bjnano.org
ISSN 2190-4286
Email: journals-support@beilstein-institut.de

The *Beilstein Journal of Nanotechnology* is published by the Beilstein-Institut zur Förderung der Chemischen Wissenschaften.

Beilstein-Institut zur Förderung der Chemischen Wissenschaften
Trakehner Straße 7–9
60487 Frankfurt am Main
Germany
www.beilstein-institut.de

BEILSTEIN JOURNAL OF NANOTECHNOLOGY

Non-intuitive clustering of 9,10-phenanthrenequinone on Au(111)

Ryan D. Brown[1], Rebecca C. Quardokus[2], Natalie A. Wasio[3], Jacob P. Petersen[1], Angela M. Silski[1], Steven A. Corcelli[1] and S. Alex Kandel[*1]

Full Research Paper

Open Access

Address:
[1]Department of Chemistry and Biochemistry, University of Notre Dame, Notre Dame, IN 46556 USA, [2]Department of Chemistry, University of Connecticut, Storrs, CT 06269 USA and [3]Department of Chemistry, Tufts University, Medford, MA 02155 USA

Email:
S. Alex Kandel[*] - skandel@nd.edu

* Corresponding author

Keywords:
metastable clusters; 9,10-phenanthrenequinone; scanning tunneling microscopy; self-assembly

Beilstein J. Nanotechnol. **2017,** *8,* 1801–1807.
doi:10.3762/bjnano.8.181

Received: 16 May 2017
Accepted: 11 August 2017
Published: 30 August 2017

This article is part of the Thematic Series "Nanoscale patterning and characterization".

Guest Editor: S. A. Claridge

Abstract

The direct injection of a 9,10-phenanthrenequinone in tetrahydrofuran solution on a Au(111) substrate in high vacuum results in the formation of metastable clusters with a non-intuitive structure. Metastable, rectangular tetramers of this molecule form in which the net molecular dipoles all orient toward the center of the cluster. This structure does not allow for additional hydrogen bonding and thus the origin of its metastability is not clear. We compare this feature to other structures observed on this surface, as well as those formed during the deposition of 9-fluorenone, which does not exhibit this anomalous clustering behavior.

Introduction

The goal of crystal engineering is to utilize a combination of intermolecular interactions, molecule–substrate interactions and growth conditions to produce a desired mesoscale or nanoscale structure through self-assembly [1,2]. Generally, this involves a careful selection of these interactions to produce an equilibrium supramolecular assembly that has the desired two- or three-dimensional structure [3-9]. While this technique has been shown to be quite effective at achieving this goal, it is limited to geometries allowed by crystalline structures. Self-assembly under conditions far from equilibrium, under kinetic control, can produce a variety of supramolecular structures not available through equilibrium growth techniques [10,11]. Recently, non-equilibrium growth conditions combined with competing hydrogen bonding elements have been shown to produce supramolecular conformations not formed under thermodynamically controlled growth conditions, including clusters with pentagonal symmetry [12-15] and quasicrystalline assemblies of these pentagonal subunits [16]. In order to exploit non-equilibrium growth methods to produce nanoscale structures, the origin of these metastable species needs to be investigated. An improved understanding of these processes not only allows for the creation of nanoscale structures with non-equilibrium geome-

tries, but also might improve our understanding of polymorphism in organic crystals [17,18].

Some hydrogen-bonding organic molecules have a common feature in that C–H···O bonding plays a critical role in stabilizing metastable clusters [13,14,19,20]. This makes 9,10-phenanthrenequinone (Figure 1) an attractive target for study, since it has two carbonyl hydrogen-bonding acceptors and multiple aromatic hydrogen donors on the fused ring structure. Possibly as a result, there are six reported polymorphs of the bulk crystal structure [21]. Additionally, the asymmetry of the phenanthrene ring should allow for the determination of the molecular orientation during scanning tunneling microscopy experiments. This molecule has been studied in the past for its role in surface passivation of semiconductor interfaces [22] and its assembly behavior at the liquid–solid interface on graphite [23] but not as extensively on metal surfaces.

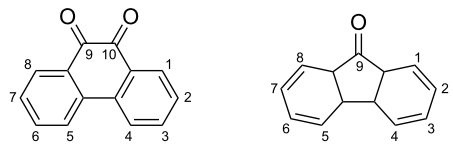

Figure 1: 9,10-phenanthrenequinone (left) and 9-fluorenone (right).

Scanning tunneling microscopy is well suited for interrogating large supramolecular structures, as well as determining the structure and orientation of individual molecules at a solid interface [24-26]. This study utilizes scanning tunneling microscopy to demonstrate that the pulse deposition of 9,10-phenanthrenequinone produces metastable clusters, which do not form due to hydrogen bonding considerations alone. They rather have a non-intuitive internal structure, which likely arises after adsorption of a cluster formed in solution. This behavior is not observed after the pulse deposition of 9-fluorenone (Figure 1), which indicates that the origin of this feature must be related to the molecular structure of 9,10-phenanthrenequinone.

Results and Discussion

Pulse deposition usually results in a heterogeneous surface, most likely due to the fact that any cluster formation that occurs in the rapidly evaporating droplet will proceed under non-equilibrium conditions and thus can produce kinetic intermediates [13,14,19,27-30]. For 9,10-phenanthrenequinone we observe three broad categories of assembly: disordered molecules, rectangular tetramers, and ordered linear rows, as seen in Figure 2. The crescent- (or banana-)shaped appearance of molecular features suggests that molecules adsorb with the conjugated π-system parallel to the surface.

In the bulk crystal structures of 9,10-phenanthrenequinone, the carbonyls of one molecule form C–H···O bonds with the hydrogens on the rear of the fused ring of another molecule, resulting in row-like bonding motifs. Of the two ordered structures observed on the surface, the linear rows are the feature that most strongly resemble the reported bulk crystalline structures. For some polymorphs, these rows line up exactly such that the molecule is oriented in the direction of the row propagation, while the other reported polymorphs have the molecular orientation offset such that there is a tilt of the molecule relative to the direction of the row [21]. The resulting difference in spacing of neighboring molecules (approximately 0.3 Å) is below the accuracy of our imaging, but the orientation of molecules relative to the direction of the row is easily observable. Our calculations indicate that the pairwise binding energy of these two motifs are essentially isoenergetic (−15.75 kJ/mol for the tilted motif and −15.55 kJ/mol for the tilted and end-to-end orientations, respectively), which could be the reason why both are present in the reported crystal structures.

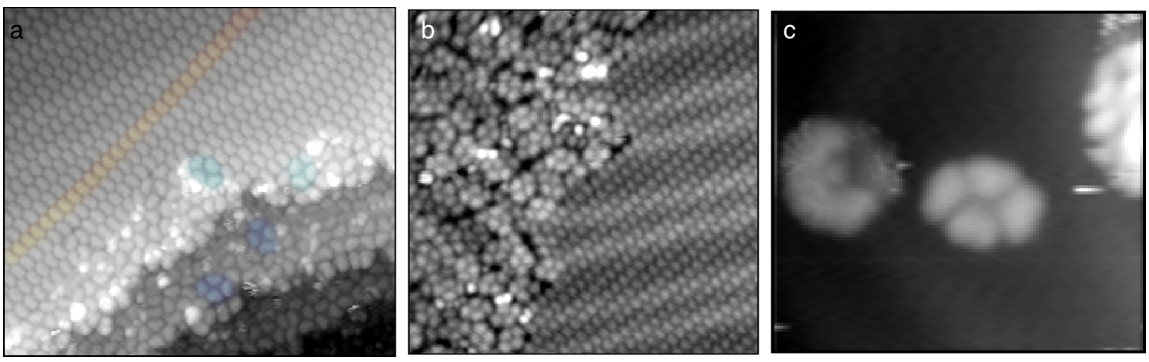

Figure 2: a) STM topography image, 250 Å × 250 Å, of 9,10-phenanthrenequinone on Au(111), with a representative row (red) and some representative tetramers (blue) highlighted. b) STM topography image, 250 Å × 245 Å, of a boundary of tetramers and ordered rows on a single terrace. c) A 79 Å × 72 Å topography image (20 pA, +1.00 V) of an isolated tetramer in a low-coverage region of the surface.

Figure 3 shows an area of the surface completely covered by rows of 9,10-phenanthrenequinone. Positional order is evident in both the regular appearance of the lattice and the sharpness of the Fourier transform, and the pseudo-unit cell obtained from this FT gives a rhombohedral unit cell with axes of 7.0 Å along a row, and 9.8 Å between rows, with an angle of 75° between the two axes. This spacing is approximately 1 Å shorter than predicted from bulk crystal structures, but this is likely due to uncertainty in the lateral calibration and possible drift or warping in the image.

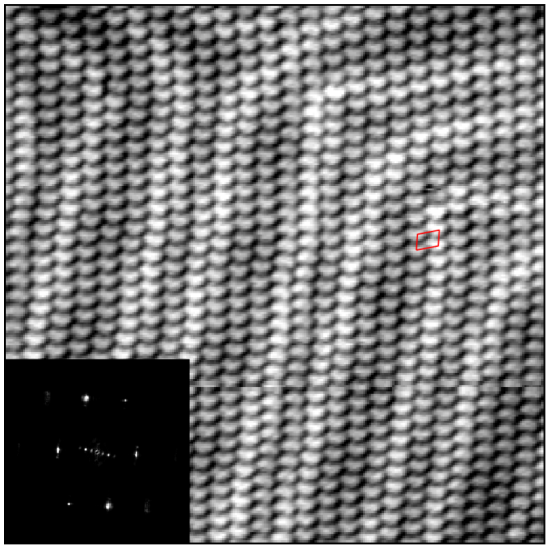

Figure 3: A 237 Å × 237 Å STM topography image acquired at a tip–sample bias of −0.5 V, and a 5 pA setpoint. This image is a large array of 9,10-phenanthrenequinone rows, with the Au(111) herringbone visible underneath. The inset is the 2D Fourier transform of the image, and the red overlay shows the periodicity obtained from the 2D FFT.

A careful inspection of the orientation of molecules within the rows in Figure 3 reveals that neighboring rows can have two orientations. There appears to be a preference for adjacent rows to align in the same direction, but there are also several flips across the area imaged, with no apparent periodicity for this reversal of orientation. The monolayer structure is therefore not actually crystalline, but rather a domain of very stable rows that are positionally ordered. The bulk crystal structures do have alternating directions in adjacent rows, and for a given row-bonding motif the polymorphs are simply different packing of these rows. However, there is no obvious facet of any of these structures that would result in this apparently random pattern, although faceting of a high-index crystal plane has not been ruled out at this time.

The tetramer, in contrast, does not appear to have any intermolecular bonding motif observed in the crystal. Figure 4 shows an area of high tetramer density, along with some disordered

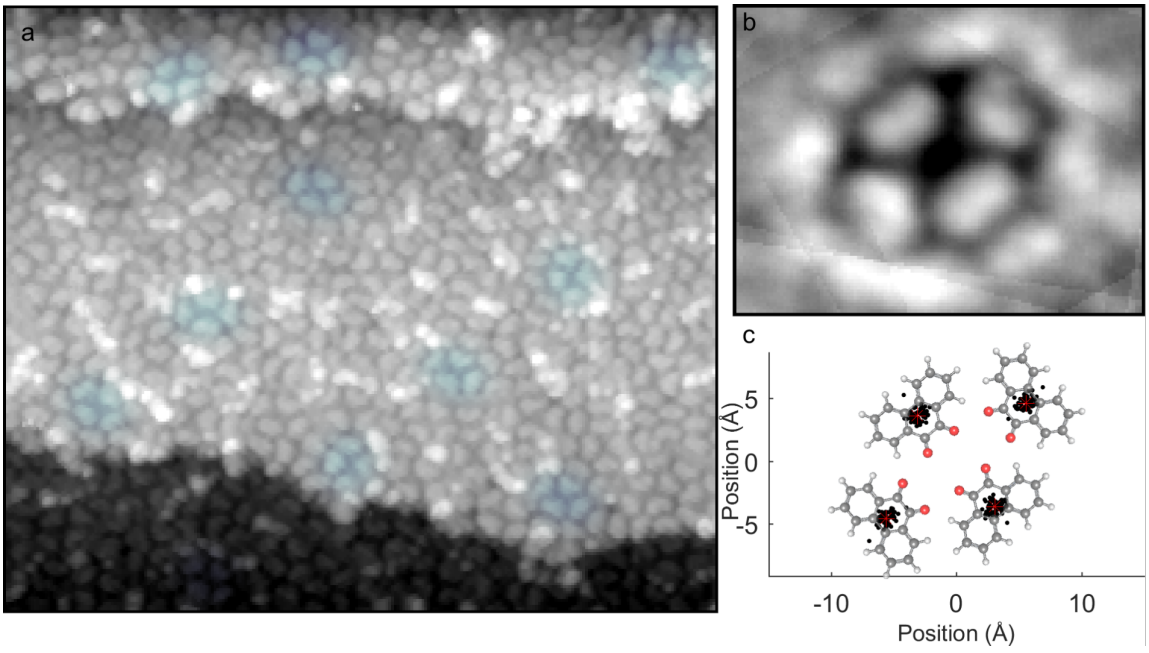

Figure 4: a) A 250 Å × 212 Å STM topography image containing a region of disordered molecules and rectangular tetramers, with some representative tetramers highlighted in blue. A composite image of the 59 fully-resolved tetramers present in this image is shown in panel b), with the proposed molecular conformation as an overlay. The average position of each molecular centroid (red asterisk) is plotted with the actual measured position of each centroid (black) for these 59 clusters in c).

species. Adjacent molecules have centroids approximately 8.6 to 8.7 Å apart and are oriented 90° apart from each other. Opposite molecules are 14.5 Å and 9.5 Å apart from each other for the long and short diagonals, respectively, and are oriented 180° with respect to each other. It is apparent from the original image and the tetramer composite image that within this cluster the molecules orient with the carbonyl groups projecting into the center of this cluster.

If considered as a gas-phase species, the observed tetramer conformation positions the net dipole of each molecule so that it is oriented toward the center. This is not an energetically favorable configuration from an electrostatic standpoint. While in some cases weak dipoles on coinage metals can direct self-assembly [31], a combination of charge transfer and screening of in-plane adsorbate dipoles can result in dipole–dipole interactions being overwhelmed by stronger intermolecular interactions (i.e., van der Waals forces and hydrogen bonding) during growth processes [32-35].

However, the arrangement of molecules in the tetramer does not allow for half of the carbonyl groups present to form C–H···O bonds. Hence, it is difficult to see how this would be a favorable conformation for a cluster formed on the surface. The tetramers are found both on terraces and step edges, and in regions of high and low coverage, as seen in Figure 2; while it is possible that step edges and defect sites play some role in nucleating aggregations of these structures, the role of defects does not seem to be a controlling one. Instead, we propose the explanation that tetramers initially form in solution, either in the rapidly evaporating droplet in transit or a rapidly evaporating film at the Au(111) surface. Given past studies that have observed both direct [30] and indirect [13,14,19] evidence of the formation of metastable clusters in solution during pulse deposition, we think that this mechanism is a plausible one for the formation of these tetramers.

In solution, clusters of four molecules could adopt a metastable 3D configuration with more favorable dipole–dipole and hydrogen-bonding interactions. Then, precipitation onto the Au(111) surface could force it into the observed two-dimensional configuration, where it could be kinetically trapped. If this mechanism is indeed responsible for the presence of these tetramers, then it might be an exploitable method for producing nanoscale structures via kinetically controlled self-assembly.

These experiments were repeated using 9-fluorenone in order to test the role of molecular geometry in determining the metastable species produced during pulse deposition. This molecule did not exhibit any tetramer clusters, and this absence suggests that those anomalous features might be particular to 9,10-phenanthrenequinone. The three main molecular features of this surface are disordered molecules, linear rows, and close-packed domains, as seen in Figure 5.

When comparing the two ordered features of this surface, it is useful to consider the only reported crystal structure of 9-fluorenone. The bulk crystal structure is comprised of 9-fluorenone dimers, slightly offset and oriented 180° apart so that the carbonyls face the hydrogen atoms at the 1- or 8-positions of

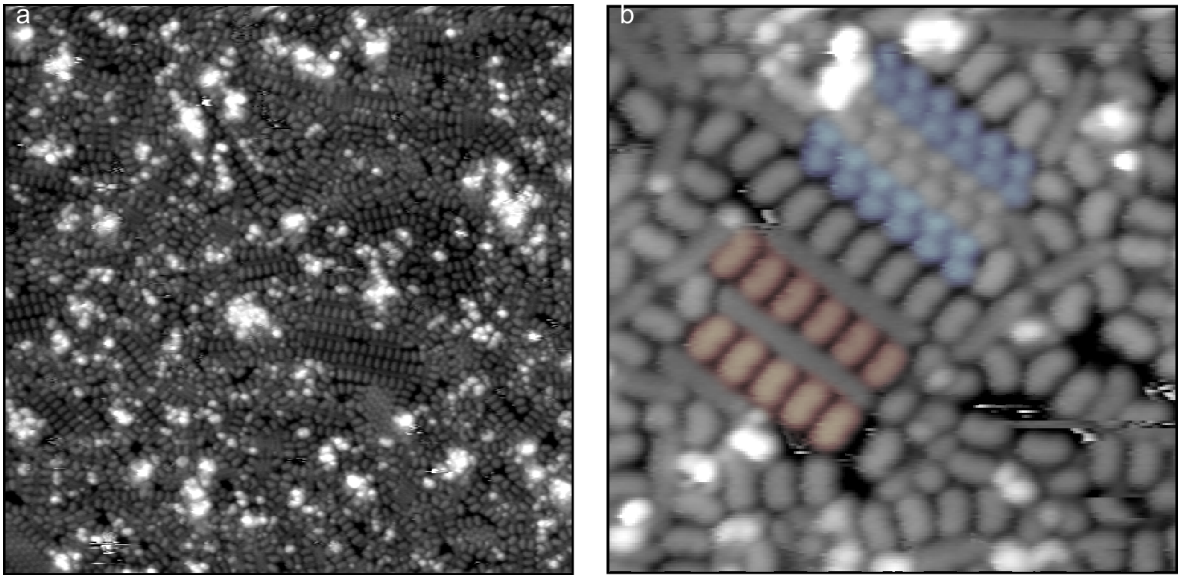

Figure 5: a) A 500 Å × 500 Å STM topography image of 9-fluorenone on Au(111). b) A 110 Å × 109.5 Å STM topography image containing examples of the linear row structures (red), and regions of a close-packed domain (blue).

the aromatic rings for each molecule [36]. This is very different from the binding motifs present in the polymorphs of 9,10-phenanthrenequinone, and the fact that this molecule can form dimers with this orientation might be the reason that tetramers do not form. There might be little to no kinetic barrier to dimer formation for two molecules adopting the orientation needed to form a tetramer. Within the linear rows, the molecules have a spatial periodicity of approximately 7.4 Å apart, and are oriented in the same direction of the row propagation. This implies that the C–H···O bonding occurs between the carbonyl and hydrogen atoms of the 4 and 5 positions for each molecule in the row, save the end molecules. This model is in agreement with the density functional theory calculations, which predict a 7.7 Å periodicity for this binding motif, and find it to be more stable than hydrogen-bonding motifs involving the hydrogens at the 3,4- and 2,3-positions by at least 2.3 kJ/mol.

The identity of the close-packed regions (blue in Figure 5a) is less clear. Assuming that each bright circular region represents one of the benzene rings of the fused heterocycle, the width of these molecules are consistent with the 9-fluorenone molecules in the linear rows and disordered regions, and the close-packed regions have a similar orientation to those in the crystal structure. However, the spatial periodicity between these bi-lobed features is approximately 6.6 Å, which is roughly 90% of the spacing between the molecules of the linear dimer row. The spacing in the bulk dimer is 8.5 Å, and thus this feature is packed too closely to represent a planar dimer structure with the binding motif of the bulk crystal. Even accounting for inaccuracy in the STM imaging, the close-packed periodicity should be larger than the linear rows by about 0.5 Å if this feature actually was comprised of 9-fluorenone dimers. Another bonding motif of 9-fluorenone is a catemer, in which each molecule binds to two other molecules in the structure, in a co-crystal with perfluoro-*ortho*-phenylmercury [37]. The orientation of the molecules in this catemer does not match those in the close-packed domains on this surface, and thus this is also not a plausible assignment for this feature. Another possibility is that this feature consists of molecules that do not adsorb with the π-rings parallel with the surface plane, i.e., there is some tilt associated with their adsorption geometry, but the imaging data is insufficient to strongly support this assignment, or any conclusive assignment, at this time.

The linear rows have less positional order than the 9,10-phenanthrenequinone rows, quite possibly due to the weaker total intermolecular interactions directing the assembly of the rows. It is possible to observe kinks within the rows, which were not present to a noticeable degree in the 9,10-phenanthrenequinone rows. Density functional theory calculations find that the pairwise binding energies are −15.75 kJ/mol and −7.53 kJ/mol for the observed 9,10-phenanthrenequinone rows and 9-fluorenone rows, respectively. Figure 6 displays the calculated structure of pairwise interactions in the linear rows for both molecules. It is evident that the 9,10-phenanthrenequinone dimer has more hydrogen-bonding contacts and is, thus, more stable than that of 9-fluorenone. This disparity might be the reason for a higher fidelity of orientation in linear 9,10-phenanthrenequinone rows relative to 9-fluorenone.

Conclusion

Pulse deposition of 9,10-phenanthrenequinone on Au(111) results in two types of ordered structures: Ordered linear rows of molecules the bonding motif of which strongly resembles that of some bulk crystal polymorphs, and rectangular tetramers, which have a non-intuitive intermolecular conformation. These tetramers do not appear to be stabilized by competing hydrogen-bonding elements, but do exist as metastable species at this interface. A comparison with the assembly behavior of 9-fluorenone further complicates this

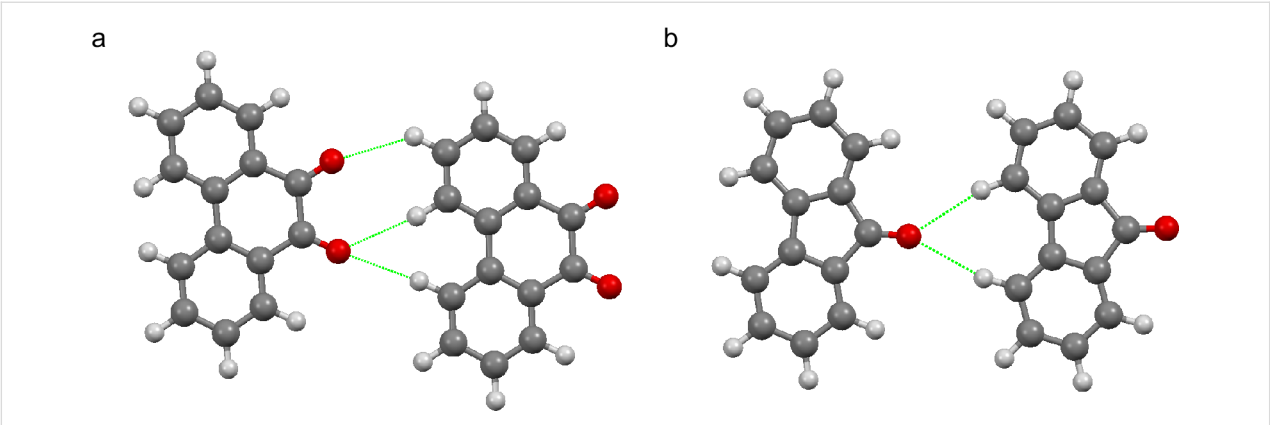

Figure 6: The calculated structure of pairwise interactions in linear rows for (a) 9,10-phenanthrenequinone and (b) 9-fluorenone with the C-H···O hydrogen-bond contacts indicated in green.

picture, in that no tetramers were observed after pulse deposition. 9-fluorenone has two types of ordered feature after pulse deposition: linear rows and close-packed arrays. The linear rows all contain molecules oriented end-to-end in the direction of the row propagation, while the close-packed arrays resemble the orientation of dimers observed in the crystal structure, but have a periodicity inconsistent with any known hydrogen-bonding motif for this molecule. This study demonstrates the importance of developing an improved understanding of self-assembly proceeding under kinetically controlled growth conditions. The ultimate goal of studying non-equilibrium self-assembly is to use both intermolecular interactions and deposition technique to "engineer" metastable states of a given supramolecular conformation. Non-intuitive results such as the 9,10-phenanthrenequinone tetramer suggest that these considerations need to account for the environment in which metastable species evolve.

Experimental

The Au(111)-on-mica substrates were heated to approximately 350 to 400 °C, then cleaned via three 15 min cycles of argon sputtering followed by a 15 min annealing. The substrates were allowed to cool to room temperature prior to deposition. The samples were produced by preparing a 2 mg/mL solution of either 9,10-phenanthrenequinone or 9-fluorenone in tetrahydrofuran and injecting microliter droplets of this solution at a clean Au(111)-on-mica substrate in a high-vacuum preparation chamber using a solenoid pulse valve (Parker Instruments 9-series, 0.5 mm nozzle diameter, with an IOTA ONE controller). These conditions were sufficient for producing a high-quality substrate and near-monolayer coverages of molecules after deposition.

The samples were then transferred to a cryogenically cooled STM (Omicron LT-STM) in an ultrahigh-vacuum chamber, and imaged once the temperature had equilibrated at 77 K. Typical imaging conditions used were a 10 pA tunneling setpoint with a tip–sample bias of +1.00 V, unless otherwise noted, and used a mechanically-cut Pt/Ir tip.

All calculations were performed using the Q-Chem software package. Structures were optimized with density functional theory (DFT) utilizing the B3LYP functional [38,39]. The 6-311++G(3df,3pd) basis set was employed with a Lebedev quadrature containing 100 radial shells with 302 angular points. Dimers of both species were originally generated to replicate experimental results, but multiple orientations were also created to determine the relative energies of binding motifs that deviate from the experimentally observed supramolecular structure. To address basis-set superposition error, the Boys and Bernardi counterpoise correction was applied to all systems.

Acknowledgements

This research was supported by funding from the National Science Foundation (NSF Grant No. CHE-1507213).

References

1. Blake, A. J.; Champness, N. R.; Hubberstey, P.; Li, W.-S.; Withersby, M. A.; Schroder, M. *Coord. Chem. Rev.* **1999,** *183,* 117–138. doi:10.1016/S0010-8545(98)00173-8
2. Desiraju, G. R. *Angew. Chem., Int. Ed.* **1995,** *34,* 2311–2327. doi:10.1002/anie.199523111
3. Chen, Q.; Bae, S. C.; Granick, S. *Nature* **2011,** *469,* 381–384. doi:10.1038/nature09713
4. Ivasenko, O.; Perepichka, D. F. *Chem. Soc. Rev.* **2011,** *40,* 191–206. doi:10.1039/c0cs00022a
5. Gutzler, R.; Cardenas, L.; Rosei, F. *Chem. Sci.* **2011,** *2,* 2290–2300. doi:10.1039/c1sc00531f
6. Gatti, R.; MacLeod, J. M.; Lipton-Duffin, J. A.; Moiseev, A. G.; Perepichka, D. F.; Rosei, F. *J. Phys. Chem. C* **2014,** *118,* 25505–25516. doi:10.1021/jp507729w
7. Liu, P.; Miao, X.; Li, Z.; Zha, B.; Deng, W. *CrystEngComm* **2014,** *16,* 9690–9696. doi:10.1039/c4ce01183j
8. Hirsch, B. E.; McDonald, K. P.; Flood, A. H.; Tait, S. L. *J. Chem. Phys.* **2015,** *142,* 101914. doi:10.1063/1.4906895
9. Li, N.; Gu, G.; Zhang, X.; Song, D.; Zhang, Y.; Teo, B. K.; Peng, L.-m.; Hou, S.; Wang, Y. *Chem. Commun.* **2017,** *53,* 3469–3472. doi:10.1039/c7cc00566k
10. Barth, J. V.; Costantini, G.; Kern, K. *Nature* **2005,** *437,* 671–679. doi:10.1038/nature04166
11. Weigelt, S.; Bombis, C.; Busse, C.; Knudsen, M. M.; Gothelf, K. V.; Laegsgaard, E.; Besenbacher, F.; Linderoth, T. R. *ACS Nano* **2008,** *2,* 651–660. doi:10.1021/nn7004365
12. Karan, S.; Wang, Y.; Robles, R.; Lorente, N.; Berndt, R. *J. Am. Chem. Soc.* **2013,** *135,* 14004–14007. doi:10.1021/ja405456k
13. Quardokus, R. C.; Wasio, N. A.; Christie, J. A.; Henderson, K. W.; Forrest, R. P.; Lent, C. S.; Corcelli, S. A.; Kandel, S. A. *Chem. Commun.* **2014,** *50,* 10229–10232. doi:10.1039/c4cc03664f
14. Wasio, N. A.; Quardokus, R. C.; Brown, R. D.; Forrest, R. P.; Lent, C. S.; Corcelli, S. A.; Christie, J. A.; Henderson, K. W.; Kandel, S. A. *J. Phys. Chem. C* **2015,** *119,* 21011–21017. doi:10.1021/acs.jpcc.5b06634
15. Li, C.; Li, N.; Liu, L.; Zhang, Y.; Yuan, C.; Peng, L.; Hou, S.; Wang, Y. *Chem. Commun.* **2017,** *53,* 2252–2255. doi:10.1039/c6cc08148g
16. Wasio, N. A.; Quardokus, R. C.; Forrest, R. P.; Lent, C. S.; Corcelli, S. A.; Christie, J. A.; Henderson, K. W.; Kandel, S. A. *Nature* **2014,** *507,* 86. doi:10.1038/nature12993
17. Desiraju, G. R. *Angew. Chem., Int. Ed.* **2007,** *46,* 8342–8356. doi:10.1002/anie.200700534
18. Cruz-Cabeza, A. J.; Reutzel-Edens, S. M.; Bernstein, J. *Chem. Soc. Rev.* **2015,** *44,* 8619–8635. doi:10.1039/c5cs00227c
19. Quardokus, R. C.; Wasio, N. A.; Brown, R. D.; Christie, J. A.; Henderson, K. W.; Forrest, R. P.; Lent, C. S.; Corcelli, S. A.; Kandel, S. A. *J. Chem. Phys.* **2015,** *142,* 101927. doi:10.1063/1.4909517
20. Miao, K.; Hu, Y.; Zha, B.; Xu, L.; Dong, M.; Miao, X.; Deng, W. *J. Phys. Chem. C* **2017,** *121,* 3947–3957. doi:10.1021/acs.jpcc.7b00040
21. Rae, A.; Willis, A. *Z. Kristallogr.* **2009,** *218,* 221–230. doi:10.1524/zkri.218.3.221.20753

22. Avasthi, S.; Qi, Y.; Vertelov, G. K.; Schwartz, J.; Kahn, A.; Sturm, J. C. *Appl. Phys. Lett.* **2010,** *96,* 222109. doi:10.1063/1.3429585
23. Zhao, H.; Zhang, S.; Li, S.; Song, X.; Liu, W.; Liu, B.; Dong, M. *RSC Adv.* **2015,** *5,* 103316–103320. doi:10.1039/c5ra20316c
24. Rosei, F.; Schunack, M.; Naitoh, Y.; Jiang, P.; Gourdon, A.; Laegsgaard, E.; Stensgaard, I.; Joachim, C.; Besenbacher, F. *Prog. Surf. Sci.* **2003,** *71,* 95–146. doi:10.1016/S0079-6816(03)00004-2
25. Sykes, E. C. H.; Han, P.; Kandel, S. A.; Kelly, K. F.; McCarty, G. S.; Weiss, P. S. *Acc. Chem. Res.* **2003,** *36,* 945–953. doi:10.1021/ar970286l
26. De Feyter, S.; De Schryver, F. C. *Chem. Soc. Rev.* **2003,** *32,* 139–150. doi:10.1039/B206566P
27. Rabani, E.; Reichman, D. R.; Geissler, P. L.; Brus, L. E. *Nature* **2003,** *426,* 271–274. doi:10.1038/nature02087
28. Drisdell, W. S.; Saykally, R. J.; Cohen, R. C. *Proc. Natl. Acad. Sci. U. S. A.* **2009,** *106,* 18897–18901. doi:10.1073/pnas.0907988106
29. Smith, J. D.; Cappa, C. D.; Drisdell, W. S.; Cohen, R. C.; Saykally, R. J. *J. Am. Chem. Soc.* **2006,** *128,* 12892–12898. doi:10.1021/ja063579v
30. Brown, R. D.; Coman, J. M.; Christie, J. A.; Forrest, R. P.; Lent, C. S.; Corcelli, S. A.; Henderson, K. W.; Kandel, S. A. *J. Phys. Chem. C* **2017,** *121,* 6191–6198. doi:10.1021/acs.jpcc.7b00996
31. Baber, A. E.; Jensen, S. C.; Sykes, E. C. H. *J. Am. Chem. Soc.* **2007,** *129,* 6368. doi:10.1021/ja0709526
32. Talapin, D. V.; Shevchenko, E. V.; Murray, C. B.; Titov, A. V.; Král, P. *Nano Lett.* **2007,** *7,* 1213–1219. doi:10.1021/nl070058c
33. Kunkel, D. A.; Simpson, S.; Nitz, J.; Rojas, G. A.; Zurek, E.; Routaboul, L.; Doudin, B.; Braunstein, P.; Dowben, P. A.; Enders, A. *Chem. Commun.* **2012,** *48,* 7143–7145. doi:10.1039/c2cc32462h
34. Kunkel, D. A.; Hooper, J.; Simpson, S.; Miller, D. P.; Routaboul, L.; Braunstein, P.; Doudin, B.; Beniwal, S.; Dowben, P.; Skomski, R.; Zurek, E.; Enders, A. *J. Chem. Phys.* **2015,** *142,* 101921. doi:10.1063/1.4907943
35. Murphy, C. J.; Miller, D. P.; Simpson, S.; Baggett, A.; Pronschinske, A.; Liriano, M. L.; Therrien, A. J.; Enders, A.; Liu, S.-Y.; Zurek, E.; Sykes, E. C. H. *J. Phys. Chem. C* **2016,** *120,* 6020–6030. doi:10.1021/acs.jpcc.5b11970
36. Luss, H. R.; Smith, D. L. *Acta Crystallogr., Sect. B* **1972,** *28,* 884. doi:10.1107/S056774087200336X
37. Fisher, S. P.; Reinheimer, E. W.; Groeneman, R. H. *Polyhedron* **2016,** *114,* 213–217. doi:10.1016/j.poly.2015.12.007
38. Lee, C.; Yang, W.; Parr, R. G. *Phys. Rev. B* **1988,** *37,* 785–789. doi:10.1103/PhysRevB.37.785
39. Becke, A. D. *J. Chem. Phys.* **1993,** *98,* 5648–5652. doi:10.1063/1.464913

License and Terms

BEILSTEIN JOURNAL OF NANOTECHNOLOGY

Photobleaching of YOYO-1 in super-resolution single DNA fluorescence imaging

Joseph R. Pyle and Jixin Chen*

Full Research Paper

Open Access

Address:
Department of Chemistry and Biochemistry, Nanoscale and Quantum Phenomena Institute, Ohio University, Athens, Ohio 45701, USA

Email:
Jixin Chen* - chenj@ohio.edu

* Corresponding author

Keywords:
diffusion; PAINT; single-molecule photophysics; super-resolution imaging

Beilstein J. Nanotechnol. **2017,** *8,* 2296–2306.
doi:10.3762/bjnano.8.229

Received: 30 June 2017
Accepted: 05 October 2017
Published: 02 November 2017

This article is part of the Thematic Series "Nanoscale patterning and characterization".

Guest Editor: W.-S. Liao

Abstract

Super-resolution imaging of single DNA molecules via point accumulation for imaging in nanoscale topography (PAINT) has great potential to visualize fine DNA structures with nanometer resolution. In a typical PAINT video acquisition, dye molecules (YOYO-1) in solution sparsely bind to the target surfaces (DNA) whose locations can be mathematically determined by fitting their fluorescent point spread function. Many YOYO-1 molecules intercalate into DNA and remain there during imaging, and most of them have to be temporarily or permanently fluorescently bleached, often stochastically, to allow for the visualization of a few fluorescent events per DNA per frame of the video. Thus, controlling the fluorescence on–off rate is important in PAINT. In this paper, we study the photobleaching of YOYO-1 and its correlation with the quality of the PAINT images. At a low excitation laser power density, the photobleaching of YOYO-1 is too slow and a minimum required power density was identified, which can be theoretically predicted with the proposed method in this report.

Introduction

Fluorescence imaging of DNA with intercalating dyes is important for DNA sensing [1,2], nucleic acid imaging inside cells and viruses [3-5], DNA protein studies [6,7], and optical mapping [8-10]. YOYO-1 is a common dye chosen for these studies due to its favorable optical properties. YOYO-1 has a high extinction coefficient of 10^5 M^{-1} cm^{-1} [11] and strongly binds to DNA (binding constant 10^8–10^9 M^{-1}) [12] with little sequence preference. Its fluorescent brightness at visible wavelengths is enhanced over 1,000-fold upon intercalation into DNA as compared to free YOYO-1 in water [13-15], which has triggered a revolution in DNA labeling since the 1990s [16].

YOYO-1 has been one of the major dyes used for super-resolution DNA imaging [17-20]. A recent trend in fluorescent

imaging is the use of super-resolution imaging to resolve fine structures below the typical diffraction limit of visible light microscopy at ≈250 nm [21]. This is important in visualizing the conformation of DNA molecules, such as DNA looping by proteins, a necessary process for gene regulation and expression [22], characterizing DNA origami [23,24], and imaging the unpacking of DNA [25]. Two main categories of super-resolution techniques were developed in the past two decades: (1) using hardware to beat the diffraction limit, using methods such as stimulated emission depletion (STED) microscopy [26,27]; (2) using software to super-localize single molecules [28-31], such as stochastic optical reconstruction microscopy (STORM) [32], photo-activated localization microscopy (PALM) [33], single-molecule high-resolution imaging with photobleaching (SHRIMP) [34], and point accumulation for imaging in nanoscale topography (PAINT) [35,36]. The main principle behind the latter techniques is to take a fluorescent video of single molecules over time. Each frame of the video is then processed to determine the center of each fluorescent point spread function (PSF) by fitting it to, for example, a Gaussian function (Figure 1). Then all the frames are overlaid to construct the super-resolved image. The difference between each technique is how the single molecules are visualized, typically through blinking, photobleaching, binding activation, photoswitching, or a combination thereof [34,37,38]. Dye photobleaching is one of the most utilized methods in PAINT fluorescently turn-off the dye molecules and is commonly used in most all types of fluorescent imaging [17,19,20,39,40]. Thus, carefully tuning the photobleaching rate is an important step for super-resolution imaging. However, finding suitable photobleaching lifetimes for YOYO-1 in PAINT imaging has not been reported in the literature.

In this paper, we study the effect of laser power on both conventional fluorescent imaging and PAINT imaging of single DNA molecules using the intercalating dye YOYO-1. YOYO-1 is very dim in aqueous solutions and is bright when intercalated into the DNA molecule. Thus, stochastic binding and photobleaching of YOYO-1 molecules enable PAINT imaging (Figure 1). While high laser power is desired for higher resolution and fast photobleaching of the bound YOYO-1, low laser power is also desired to reduce photodamage to the immobilized DNA and to the YOYO-1 molecules in the bulk solution [39,41]. Thus, the effect of laser power is an important parameter to control during imaging to maintain single-molecule fluorescence while also preserving the DNA from photocleavage (photodamage).

Experimental

Sample preparation

All λ-DNA (Thermo Fisher) and YOYO-1 (Invitrogen) solutions were prepared in the buffer of 10 mM HEPES (pH 7.4, Acros Organics) with 10 mM NaCl (Sigma-Aldrich). All water used was from a Barnstead E-Pure ultrapure water purification system with a resistivity of 18 MΩ cm^{-1}.

Glass coverslips were first cleaned by sonication in 1% detergent (Liquinox) followed by rinsing with 18 MΩ water. Then the coverslips were immersed in 1:1:5 (v/v/v) of ammonium hydroxide/hydrogen peroxide/water for 15 min at 60 °C. Afterwards they were rinsed with water and dried with nitrogen. The coverslips were immersed in a solution of 1 vol % 3-aminopropyltriethoxysilane (APTES, TCI America) in HPLC grade acetone (Fisher) at 50 °C for 20 min. Afterwards, they were washed with ethanol and water and dried under nitrogen.

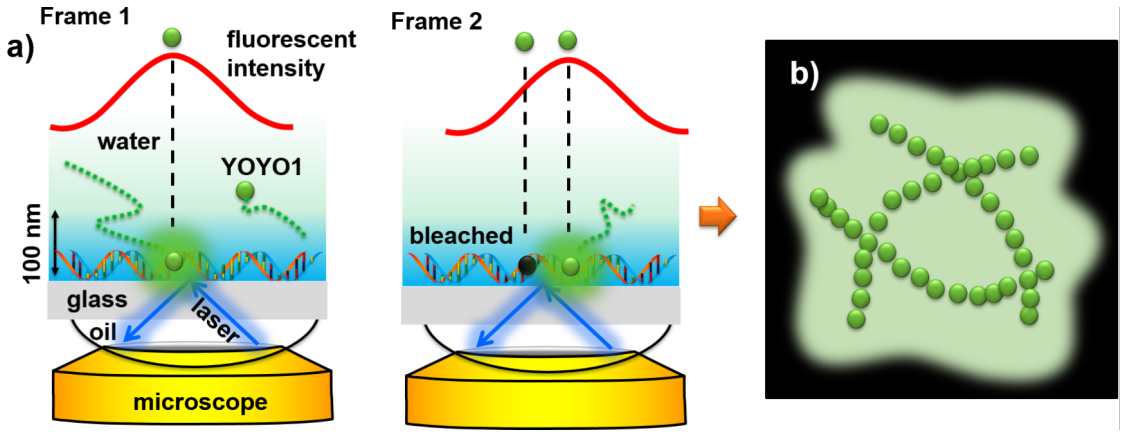

Figure 1: Scheme of super-resolution imaging of DNA with PAINT. (a) A scheme depicting the localization of single molecules in each frame. (b) Scheme of the reconstruction of a super-resolution image on top of a regular fluorescence image from the super-localized molecules in each frame.

PDMS blocks were made by thoroughly mixing Sylgard 184 silicone elastomer base (Dow Corning) with the provided curing agent (10:1 by mass), which was poured into a Petri dish, vacuum desiccated to remove bubbles, and cured overnight. After curing, the PDMS blocks were cut into similar sizes as the coverslips. Syringe tips were inserted through the PDMS block. These tips were cut and connected to tubes. Microfluidic channels were constructed by adhering double-sided tape to the coverslip and the PDMS. A rectangle was cut out of the tape before adhering to the coverslip to form a channel with dimensions of approximately 2 cm × 2 mm × 30 µm (length, width, height). The height is defined by the thickness of the tape.

Fluorescence imaging

All fluorescence measurements were carried out with a home-built microscope under total internal reflection fluorescence (TIRF) mode (Figure 2) equipped with four solid state lasers (Dragon Lasers, China), two beam expanders and a flat-top beam shaper (piShaper, AdlOptica GmbH, Germany), in addition to a Nikon Ti-U inverted microscope with a Nikon 100× oil-immersed TIRF objective (CFI Apo 100×, NA 1.49, WD 0.12 mm), and an EMCCD camera (Andor iXon Ultra 897). TIRF fluorescent filter cubes were equipped with a microscope for each laser source. The blue fluorescent filter cube used in this study was a model TRF49904 (Chroma) for the 473 nm laser.

All diffraction-limited experiments were accomplished using 1:10 dye/base pair YOYO-1-stained λ-DNA. The YOYO–DNA was incubated at 50 °C for two hours to achieve homogeneous staining as described by Carlsson et al. [42]. Approximately 200 µL of the YOYO–DNA solution was injected into the microfluidic channel using a syringe pump (New Era Pump Systems Inc., model NE-1000) at 0.40 mL/min. YOYO–DNA adhered to the surface of the amine-modified glass through electrostatic attraction between the negatively charged phosphate groups in the DNA backbone and the positively charged amine groups on the surface. The DNA molecules were stretched by flow through the channel. The channel was then washed with buffer solution to remove the non-immobilized YOYO–DNA.

Single DNA intensity measurements

Short videos of single YOYO–DNA molecules (≈200 frames) using 50 ms integration time and an electron-multiplying (EM) gain of 200 were obtained. To limit the effect of bleaching on the measurements, the sample was focused under illumination of a low-power 532 nm laser. Then the 532 nm laser was blocked and the video started recording in the dark. Then the 473 nm laser with a measured power was switched on. A MATLAB code was used to select the area of single YOYO–DNA molecules. The frame when the DNA first appeared was designated as time zero.

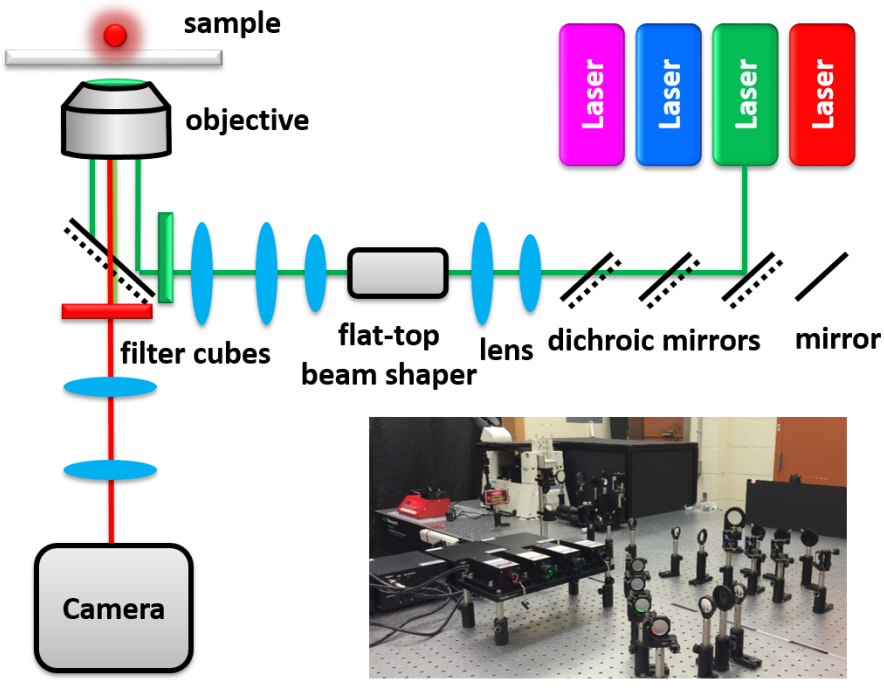

Figure 2: Scheme and image of the optical microscope.

Bleaching lifetime measurements

Identical experimental conditions were used as described above except much longer videos were taken (1000–2500 frames) in order to monitor longer YOYO-1 bleaching. The intensity of each YOYO–DNA molecule was found in each frame. A double exponential function was used to fit the decay data using a home-written MATLAB code.

Super-resolution imaging

The microfluidic channels (described earlier) were washed with water and then ≈0.1 mL of 300 pg/μL λ-DNA in the buffer was flowed through at a rate of 0.4 mL/min followed by 1 mL of buffer solution to wash away any excess DNA that did not bind to the surface. YOYO-1 (5 nM) was flowed through the channel at 0.05 mL/min while recording 5100 frame videos of binding to DNA under TIRF illumination from the 473 nm laser with an exposure time of 50 ms and an EM gain of 200. The super-resolution images were constructed using a MATLAB code that has been previously described [43-45].

Results and Discussion

Conventional DNA immobilization and imaging

All fluorescence measurements were carried out on a home-built optical microscope (Figure 2). The power density of the illumination from the 473 nm laser is calculated from the total illumination power over the illumination spot area. This calculation is reasonable because our flat-top beam shaper tunes the power density within the illumination spot uniformly. Without the beam shaper, the illumination intensities in the spot are usually Gaussian distributed. The total power is measured using a light detector (Op-2-Vis, Coherent) after the laser passes through a control sample that has no absorbers on it under epifluorescence mode. The spot size of the 100× (1.49 NA) objective was determined by bleaching polymer dots (PF-TC6FQ-Pc) [46] and then viewing the bleached area in the 20× objective (0.50 NA). The bleaching profile (Supporting Information File 1, Figure S1) is uniform in the beam spot indicating a relatively uniform light distribution of the laser after the flat-top beam shaper, consistent with a relatively even photocount distribution in a typical fluorescent image. Note that the actual photons emitted from a molecule is a function of the measured photocounts, the EM gain (fixed at 200× during all measurements), and the photon collection efficiency of the optical pathway [47,48]. The number of photocounts is at the linear response region of the EMCCD under our imaging conditions [48].

We can stretch, immobilize, and image a single DNA using the established protocol and our fluorescence microscope. Glass cover slip substrates modified with amino silane are used to immobilize single DNA molecules (Figure 3). After surface modification, the water contact angle for the cover slips is 48 ± 4° which is consistent with the literature for such surfaces [49-51]. These modified cover slips are then used to fabricate flow channels for DNA imaging. YOYO-1 is mixed and incubated for 2 h at 50 °C with a λ-DNA solution before immobilization. The DNA solution is then flowed into the channel with a flow speed (0.4 mL/min) that is capable of stretching the DNA molecules. The DNA is negatively charged and the surface is positively charged in the buffer solution. Thus, the electrostatic interaction between them provides the immobilization force for the DNA molecules. The stretched DNA molecules are visualized under the microscope showing that sample preparation and our microscope work performed as expected (Figure 3b).

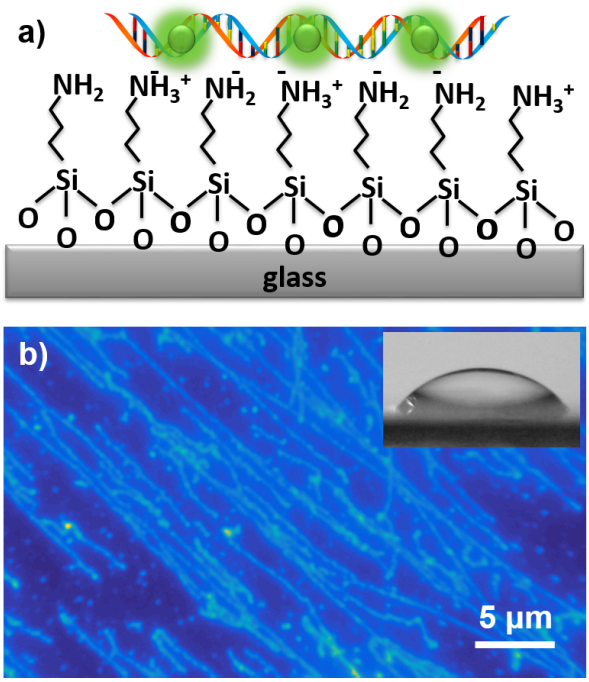

Figure 3: (a) Scheme of glass surface modification and DNA immobilization. (b) Fluorescent image of stretched DNA molecules on the substrate that have been labeled with YOYO-1. The inset shows a droplet of water on the substrate before DNA immobilization, giving a water contact angle of 48 ± 4°.

In order to measure the heterogeneity among DNA molecules, DNA molecules were immobilized on the substrate at a lower density than in Figure 3. This lower density allows the DNA molecules to be separated from each other. They are manually removed from the fluorescent image using in-house developed MATLAB code to avoid errors from other events (Figure 4a). Then the single DNA fluorescence intensity is calculated as the total photocounts per micrometer (μm) length of the λ-DNA molecules (Figure 4b). Only well-separated single DNA mole-

cules are chosen for the purpose of easy quantification. The DNA strands are prelabeled with YOYO-1 at a dye–DNA base pair ratio of 1:10. The average dye concentration in each DNA is calculated to be ≈300 dye molecules/μm for a given length of a DNA molecule, assuming 0.34 nm per base pair and that the DNA is fully stretched.

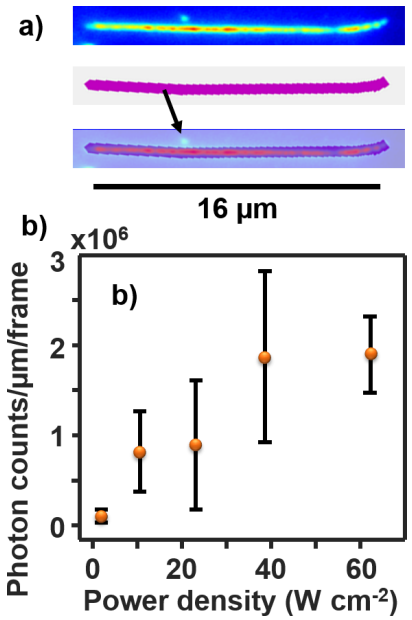

Figure 4: (a) A single DNA molecule (top), the mask used (middle), and overlay (bottom) to select the DNA and filter the other events (the arrow). (b) The intensity (total photocounts) per micrometer of single DNA molecules as a function of laser power density. The images are obtained under TIRF mode but the power densities are measured under epifluorescence mode. YOYO-1 molecules are premixed with λ-DNA at a dye/base pair ratio of 1:10. The error bars represent the standard deviation between at least 25 DNA for two samples.

A linear trend is observed which is expected at laser powers low enough for single photon absorption. The two-photon absorption probability can be estimated by comparing the number of photons absorbed by the dye per unit time to the fluorescence lifetime of the dye. The number of photons absorbed can be estimated using the following equation [47]: Photon absorption = $\sigma P/E_{ph}$, where σ is the absorption cross section, P is the laser power density and E_{ph} is the energy of a photon. The photons absorbed by each YOYO-1 molecule at the highest laser power studied (62 W cm^{-2}) is calculated to be 24 photons/ms using the energy of a photon at 473 nm (4.2×10^{-19} J/photon) and calculating the absorption cross section, 1.64×10^{-16} cm^2 that is calculated from the extinction coefficient, 9.89×10^7 cm^2 mol^{-1} (≈10^5 M^{-1} cm^{-1}) [11]. Since the fluorescence lifetime of YOYO-1 in DNA is 2–5 ns [52], that is, much shorter than the photon flux interval, all laser powers studied in this work should not be high enough for two-photon absorption to occur. Thus, the error in the experiment is due to both inhomogeneous dye staining and DNA stretching quality (Supporting Information File 1, Figure S2).

YOYO-1 photobleaching in a single DNA

Photobleaching lifetimes of the YOYO–DNA were measured from the video of YOYO-1 labeled and immobilized DNA. PAINT imaging of DNA requires bleaching of YOYO-1 to maintain single-molecule fluorescence (the sparsity principle). YOYO-1 binds very strongly to DNA ($K_a = 10^8$–10^9 M^{-1}) [12], and stays in the DNA for a long time. If not bleached, the whole DNA strand will eventually light up instead of a few isolated dye molecules per frame. Thus, the bleaching lifetime of YOYO-1 should be tuned for PAINT. The bleaching lifetime can be obtained from the fluorescent intensity decay of the molecules in the video (Figure 5). From the bulk experiments, YOYO-1 photobleaching kinetics can be fitted with a double-exponential decay function to represent the photobleaching of two differently bound YOYO-1 molecules: intercalated and non-intercalated [40]:

$$I = A_1 e^{-t/\tau_1} + A_2 e^{-t/\tau_2} + B. \quad (1)$$

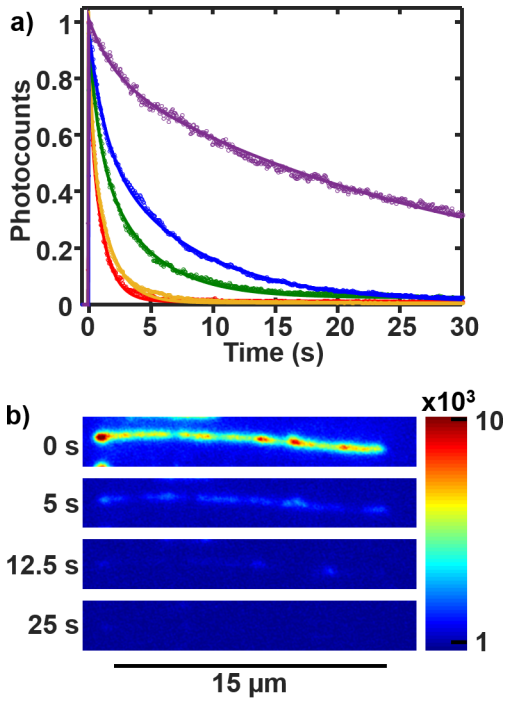

Figure 5: (a) The time trace of the photocounts per micrometer of a single DNA strand for power densities of 62 W cm^{-2} (red), 38 W cm^{-2} (orange), 23 W cm^{-2} (green), 10 W cm^{-2} (blue), and 1.9 W cm^{-2} (violet). (b) Image of a DNA molecule at different times of the video. All images have the same color scale. A laser power density of 38 W cm^{-2} was used.

The average bleaching lifetime shows an exponential-like decay with increasing laser power (Table 1, Figure 6). For the two highest powers, 38 and 62 W cm^{-2}, the fast lifetime is ≈1 s. Thus, ≈3% of molecules are bleached within the first imaging frame, 50 ms, and ≈2/3 are bleached within the first second of laser exposure.

Table 1: Average fitting constants for the double-exponential bleaching curves (error bars are shown in Figure 6).

Power density (W cm^{-2})	A_1	τ_1 (s)	A_2	τ_2 (s)	R^2
62	2 × 10^6	0.68	1.1 × 10^6	1.2	0.97
38	3 × 10^6	0.69	1.7 × 10^6	1.7	0.98
23	9 × 10^5	1.4	5 × 10^5	6.3	0.98
10	7 × 10^5	3.7	2 × 10^5	17	0.99
1.9	4 × 10^4	8.6	5 × 10^4	51	0.99

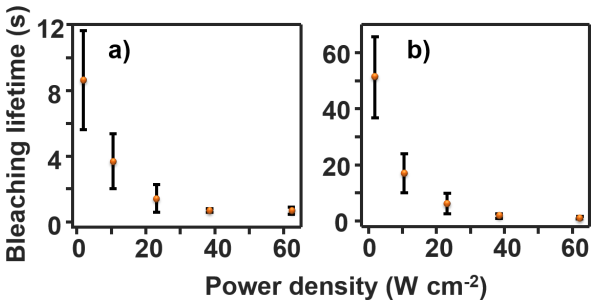

Figure 6: (a) The fast component of the bleaching lifetime for YOYO–DNA as a function of power density. (b) The slow component of the bleaching lifetime for YOYO–DNA as a function of power density. The error bars represent the standard deviation between at least 20 DNA for two samples.

Super-resolution imaging

A super-resolution image of DNA molecules is obtained from analyzing each video when non-labeled DNA is immobilized and YOYO-1 (5 nM) is flowed in for in situ labeling. The theoretical resolution of a PAINT image is dependent on the photocounts per molecule during the imaging period. The theoretical square uncertainty of a super-resolved dye location using Gaussian fitting of the point spread function of a dye can be calculated with the Thompson equation [28,53]:

$$\left\langle (\Delta x)^2 \right\rangle = \frac{s^2 + a^2/12}{N} + \frac{8\pi s^4 b^2}{a^2 N^2}, \qquad (2)$$

where s is the standard deviation of the point spread function, a is the size of a pixel, N is the number of photons collected, and b is the background noise.

The resolution of the experimental measurements (PAINT) is consistent with the theoretical prediction. Figure 7 shows the regular fluorescent image (Figure 7a) and the super-resolved image (Figure 7b) of YOYO–DNA at a power density of 23 W cm^{-2}. In Figure 7, on average, s = 112 nm, a = 72 nm, and b = 120 counts. The total photocounts of a dye can be calculated by integrating the fitted volume under each point spread function (PSF) $N = 2\pi A_{PSF} \sigma_x \sigma_y$, where A_{PSF} is the PSF peak intensity in photocounts, and σ_x and σ_y are the fitted Gaussian standard deviation in pixel units (Supporting Information File 1, Figure S3). In Figure 7, A_{PSF} = 420 counts, and $\sigma_x = \sigma_y$ = 1.5 pixels, so $N \approx 6000$ counts. This value is consistent with the sum of the photocounts of all pixels in a measured PSF, which is proportional to the actual photon emission at the linear detector response region [47,48]. Thus, the theoretical uncertainty is ≈17 nm. The full width at half maximum (FWHM) will be ≈40 nm if multiple events of each dye are represented in a Gaussian distribution. This value is consistent with our experimental measurement of ≈50 nm shown in Figure 7b. The resolution of a regular fluorescent image is ≈300 nm corresponding to the FWHM of the PSF of a single dye. Thus, when two DNA are close, conventional fluorescent imaging cannot resolve them. The super-resolved image has ≈50 nm resolution and can resolve DNA molecules greater than this separation. The contrast of the super-resolution image is also better than the regular fluorescent image because some background has been filtered out and the weight of the very bright dye molecules has been reduced. Figure 7c shows a single frame from the 5000-frame video involved in generating Figure 7b. The frames contain two signals, background and single-molecule fluorescent emission. The background is represented by a Gaussian distribution whose center is set to zero photocounts. The fluorescent molecules are identified when its maximum has intensity larger than three times the standard deviation of the background distribution. Because the background varies over frames and regions on the images, a local background method is used instead of the global background [45]. The distributions of the background and the PSF maximum are shown in Figure 7d, where the average PSF maximum is ≈3.5 times the standard deviation of the overall background distribution. Several bright spots of fluorescent dye molecules (events) are identified on the frame in Figure 7c. They are separated into two groups, a group that is consistent with the single-molecule PSF (circles) and the other group (arrows) that is not because of irregular shapes and/or too large sizes. The former locations are stored and the latter locations are filtered out. The PSF peak intensities of single YOYO-1 dyes are shown in Figure 7d. They are calculated from the center of the peak intensity histograms of single YOYO-1 molecules (Supporting Information File 1, Figure S3). The graph is roughly linear which is expected at this range of power densities.

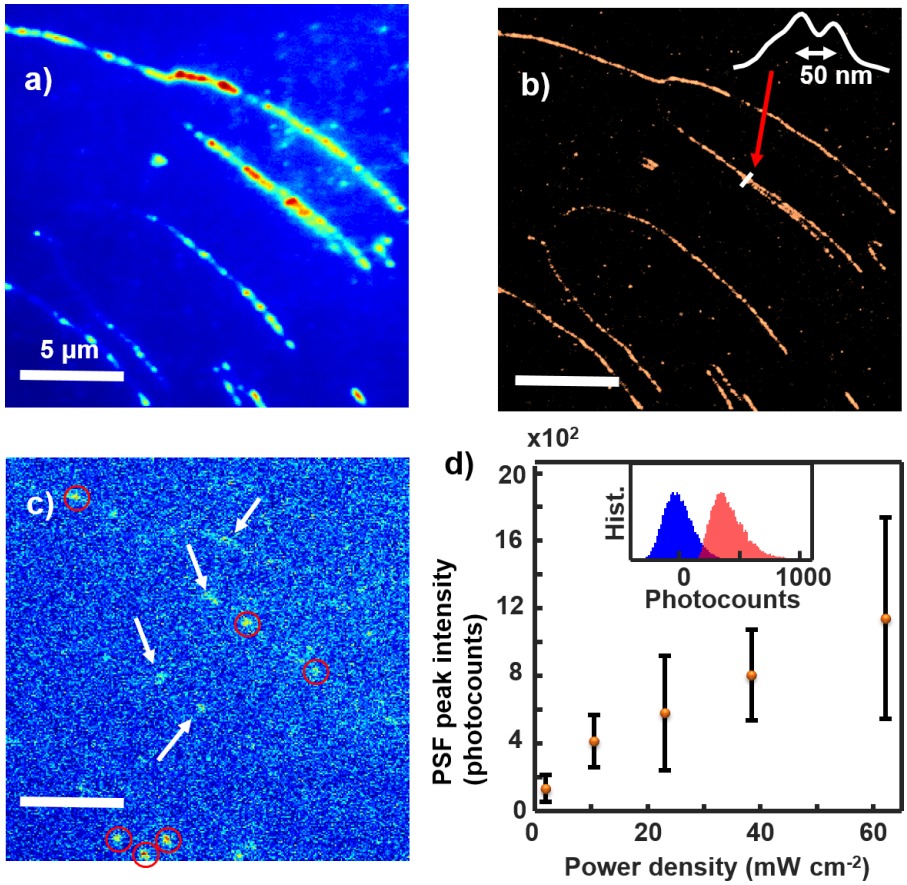

Figure 7: (a) Fluorescence images of regular and (b) super-resolved YOYO–DNA (inset shows a line profile across two nearby DNA molecules). Laser power density 23 W cm^{-2}. (c) A single frame of the video of fluorescent images. The circles are events chosen and the arrows are events discarded in generating the image in (b). (d) PSF peak intensity as a function of laser power density (inset shows histograms of the background and PSF peak intensities, see Supporting Information File 1, Figure S4 for larger images). The error bars represent the standard deviation of the photocounts of YOYO-1 molecules for three samples.

Resolving DNA strands with PAINT requires an optimal power density to view single dye molecules throughout the video (Figure 7c, Figure 8). During a PAINT image acquisition, YOYO-1 molecules continuously bind to the DNA and eventually fill the whole DNA strand. At a certain laser power photobleaching prevents the YOYO-1 from being observed and establishes an equilibrium for single-molecule imaging. Figure 8a,b shows selected frames from two example videos of YOYO-1 binding to non-labeled DNA molecules. At a low power density, 1.9 W cm^{-2}, almost the entire strand is visible at ≈35 s (Figure 8a). This limits PAINT from identifying single dyes (against the sparsity principle). Thus, the useful time range for PAINT is the first 15 s of data acquisition even though the equilibrium between the binding and the bleaching is reached at a time after 100 s (Figure 8d). This short time is not enough to generate a complete super-resolution image of the DNA stands (Figure 8c). At a higher laser power density, 38 W cm^{-2}, YOYO-1 molecules continuously bind at the same rate but are bleached at a higher rate (Figure 6). Thus, the equilibrium is reached faster at ≈20 s (Figure 8e). Because single-molecule separation is still clearly seen at equilibrium (Figure 8b), the whole video can be used to generate the PAINT image (Figure 8c) and the video can run even longer until the DNA is saturated with YOYO-1.

The theoretical YOYO-1 binding rate can be estimated with Einstein's Brownian motion and Fick's second law: the YOYO-1 molecules diffuse in the solution where the location probability is a Gaussian distribution after an evolution time Δt (Figure 9),

$$p(z,\Delta t)=\frac{1}{(4\pi D\Delta t)^{1/2}}e^{-z^2/4D\Delta t}, \quad (3)$$

where $p(z, \Delta t)$ is the probability distribution of a diffuser in the solution at time Δt over one dimension z, and D is the diffusion constant. The integration of the error function of this distribu-

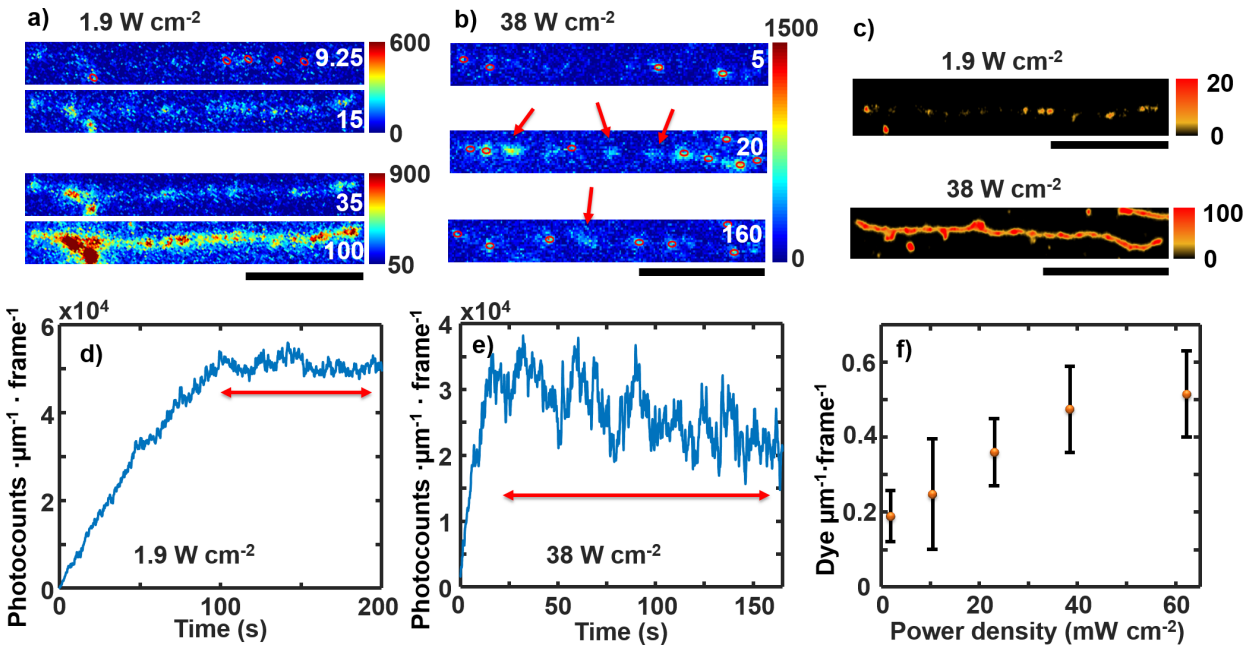

Figure 8: Single-frame images of a single DNA molecule at (a) 1.9 W cm^{-2} and (b) 38 W cm^{-2} power densities (time shown is in unit of seconds) and (c) corresponding PAINT images. Red circles show events selected and arrows show the events discarded by the code and bleached later. All scale bars are 5 µm. (d, e) Normalized total photocounts of 1 µm of DNA in each frame at 1.9 W cm^{-2} and 38 W cm^{-2} power densities, respectively. The red double arrows indicate where equilibrium is maintained. (f) The average number of dye molecules selected in the frames during the PAINT analysis. The error bars represent the standard deviation between ≈20 DNA for two samples.

tion over all molecules in the solution represents the hitting rate (HR) of the molecules to a substrate (Figure 9):

$$\mathrm{HR} = \int_0^\infty dz \times a \times C \int_z^\infty \frac{1}{\sqrt{4\pi D\Delta t}} e^{\frac{-x^2}{4D\Delta t}} dx = \frac{aC\sqrt{\pi D\Delta t}}{2}, \quad (4)$$

where a is the surface area, C is the concentration, and Δt is the evolution time (frame time here). The diffusion constant can be estimated using the Stokes–Einstein equation assuming no frequency dependence at our measuring window:

$$D = \frac{kT}{6\pi\eta\left(\frac{3M_w}{4\pi N\rho}\right)^{1/3}}, \quad (5)$$

where k is the Boltzmann constant, T is the temperature, η is the solution viscosity, M_w is the solute's molecular weight, N is Avogadro's number, and ρ is the solute solid density. The molecular weight of YOYO-1 is 1271 g mol^{-1}, its density can be estimated to be 0.8 g cm^{-3}, and the viscosity of water is 8.9 × 10^{-4} Pa s. At room temperature, the diffusion constant of YOYO-1 in water is ≈2.9 × 10^{-10} m^2 s^{-1}. The area of 1 µm of double-stranded DNA is ≈2 × 10^{-15} m^2. The YOYO-1 concentration is 5 nM, and the frame time is 50 ms. Thus, every frame has 0.02 YOYO-1 molecules that hit every 1 µm length of a DNA molecule (0.4 s^{-1}). This value is consistent with our measurement (Figure 8c). The slope of the 1.9 W cm^{-2} curve at the first 10 s is ≈600 counts/s when photobleaching is insignificant. The PSF peak intensity at this laser power is ≈100 counts, representing a total photocount per molecule of ≈1400. Thus, an

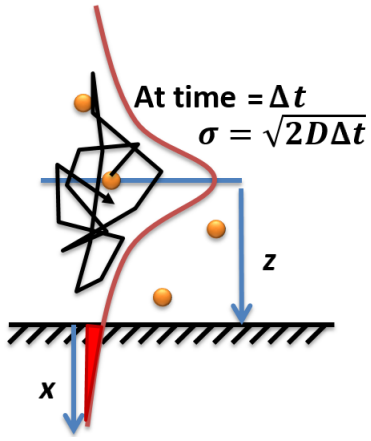

Figure 9: Scheme of molecular diffusion in the solution.

increase of ≈0.4 molecules per second is observed in this increasing part of the 1.9 W cm^{-2} slope which is consistent with the theoretical calculation. Note that this is only tested at the fixed flow rate and frame rate. This agreement suggests that under this condition, the electrostatic interaction between YOYO-1 and DNA does not provide an effective area for the YOYO-1 to bind that is larger than its physical size. This is reasonable because the Debye length of our buffer solution is ≈2 nm, while YOYO-1 molecules are separated from each other by ≈700 nm (5 nM), where the long range interaction is negligible. It also indicates an efficient binding of YOYO-1 onto DNA that is consistent with the large binding constant measured in ensemble (i.e., every YOYO-1 molecule interacting with DNA gets caught).

The competition between binding and bleaching regulates the number of useful video frames for PAINT imaging. Figure 8f shows the average dyes selected by PAINT in the frames at different power densities. The average useful dye molecules increase with increasing power density. A preliminary analysis shows that the balance between binding and bleaching is reached around a power density of 23 W cm^{-2}. Below this power density, the bleaching is too slow to remove adjacent dyes, and above this power density, bleaching is fast enough to satisfy single-molecule imaging. At 23 W cm^{-2}, ≈0.35 dye molecules are observed per 1 μm length of DNA per frame (one dye molecule every ≈3 μm of DNA). Less than 10 dye molecules (≈3/0.3) can be filled in this length on average to maintain the single-molecule separation (PSF overlap avoided), where 0.3 μm is the FWHM of the PSF. Assuming a new dye molecule arrives randomly to an area with one existing dye molecule, there is a 3/10 probability that a new one will hit the area on top or nearby this existing dye molecule. Roughly three dye molecule hitting cycles are left, which takes ≈3/0.02 = 150 frames to reach without photobleaching, where 0.02 dye molecules per frame per 1 μm length of DNA is the average binding rate we have measured. Thus, the existing dye molecule must be bleached within ≈150 × 0.05 s = 4.5 s. This value is consistent with the average photobleaching lifetime measured at this power density, that is ≈3 s (Table 1). The same calculations for lower power density yield a required photobleaching lifetime that is shorter than that measured, thus only the beginning of the videos are useful. However, for higher power densities, the measured bleaching lifetimes meet the requirement. This is confirmed by the visual analysis of single frames at the equilibrium stage (Figure 8a,b).

Thus, the required power density is predictable. In order to obtain the whole DNA image at a resolution of 50 nm, ≈20 total dye molecules per micrometer of DNA are required, which requires 20/0.02 = 1000 frames or 50 s for the YOYO-1 molecules to diffuse to the DNA under the current YOYO-1 concentration (5 nM). If 10 s is desired to image the whole DNA, a 25 nM YOYO-1 concentration should be used instead. Under this concentration, YOYO-1 binds to DNA at an average of 0.1 per frame per 1 μm length of DNA, which requires a photobleaching lifetime of each YOYO-1 molecule to be ≈30 × 0.05 s = 1.5 s in order to resolve single YOYO-1 molecules at the frame time of 50 ms per frame. This YOYO-1 photobleaching lifetime requires ≈50 W/cm^2 laser power density under our experimental conditions (Figure 6). Lower laser power densities can be used with the help of data analysis methods that tolerate a higher active-dye density and slight overlap of the PSFs, such as SHRIMP [34,54], Bayesian analysis of the blinking and bleaching (3B) [37,55], compressed sensing [56], and super-resolution optical fluctuation imaging (SOFI) [57,58], or methods that provide higher time resolution such as supertemporal-resolved microscopy (STReM) [59].

Conclusion

We have measured the single-molecule photobleaching lifetimes of YOYO-1 dye in DNA at different excitation laser power densities. We have also established a correlation between the photobleaching lifetimes with the quality of the super-resolution PAINT images. Under PAINT conditions, the dye molecules in the solution continuously bind to the target surfaces and are photobleached by the excitation laser. In order to maintain single-molecule resolution (the sparsity principle), they have to be photobleached fast enough, using a power density as low as possible to avoid photodamage to the samples. In this work, we are able to screen a set of power densities to find this optimal value of the power density and a generalized method is provided to estimate it theoretically.

Supporting Information

Additional experimental information.

Supporting Information File 1

Laser spot size, DNA length, PSF, and photocount histograms.
[http://www.beilstein-journals.org/bjnano/content/supplementary/2190-4286-8-229-S1.pdf]

Acknowledgements

The authors thank Dr. Hugh Richardson, Dr. Katherine Cimatu, Kurt Sy Piecco, and Juvinch Vicente for beneficial discussions. The authors thank Ohio University startup fund, Nanoscale and Quantum Phenomena Institute (NQPI), and the Condensed Matter and Surface Sciences (CMSS) program for financial support.

References

1. Lopez, S. G.; Ruedas-Rama, M. J.; Casares, S.; Alvarez-Pez, J. M.; Orte, A. *J. Phys. Chem. B* **2012,** *116,* 11561–11569. doi:10.1021/jp303438d
2. Talavera, E. M.; Bermejo, R.; Crovetto, L.; Orte, A.; Alvarez-Pez, J. M. *Appl. Spectrosc.* **2003,** *57,* 208–215. doi:10.1366/000370203321535132
3. Idziorek, T.; Estaquier, J.; De Bels, F.; Ameisen, J.-C. *J. Immunol. Methods* **1995,** *185,* 249–258. doi:10.1016/0022-1759(95)00172-7
4. Michel, A. D.; Kaur, R.; Chessell, I. P.; Humphrey, P. P. A. *Br. J. Pharmacol.* **2000,** *130,* 513–520. doi:10.1038/sj.bjp.0703368
5. Eriksson, M.; Härdelin, M.; Larsson, A.; Bergenholtz, J.; Åkerman, B. *J. Phys. Chem. B* **2007,** *111,* 1139–1148. doi:10.1021/jp064322m
6. Matsuura, S.; Komatsu, J.; Hirano, K.; Yasuda, H.; Takashima, K.; Katsura, S.; Mizuno, A. *Nucleic Acids Res.* **2001,** *29,* e79. doi:10.1093/nar/29.16.e79
7. Xu, C.; Losytskyy, M. Y.; Kovalska, V. B.; Kryvorotenko, D. V.; Yarmoluk, S. M.; McClelland, S.; Bianco, P. R. *J. Fluoresc.* **2007,** *17,* 671–685. doi:10.1007/s10895-007-0215-z
8. Reisner, W.; Larsen, N. B.; Silahtaroglu, A.; Kristensen, A.; Tommerup, N.; Tegenfeldt, J. O.; Flyvbjerg, H. *Proc. Natl. Acad. Sci. U. S. A.* **2010,** *107,* 13294–13299. doi:10.1073/pnas.1007081107
9. Nilsson, A. N.; Emilsson, G.; Nyberg, L. K.; Noble, C.; Stadler, L. S.; Fritzsche, J.; Moore, E. R. B.; Tegenfeldt, J. O.; Ambjörnsson, T.; Westerlund, F. *Nucleic Acids Res.* **2014,** *42,* e118. doi:10.1093/nar/gku556
10. Baday, M.; Cravens, A.; Hastie, A.; Kim, H.; Kudeki, D. E.; Kwok, P.-Y.; Xiao, M.; Selvin, P. R. *Nano Lett.* **2012,** *12,* 3861–3866. doi:10.1021/nl302069q
11. Tian, N.; Xu, Q.-H. *Adv. Mater.* **2007,** *19,* 1988–1991. doi:10.1002/adma.200700654
12. Flors, C. *Photochem. Photobiol. Sci.* **2010,** *9,* 643–648. doi:10.1039/b9pp00119k
13. Rye, H. S.; Yue, S.; Wemmer, D. E.; Quesada, M. A.; Haugland, R. P.; Mathies, R. A.; Glazer, A. N. *Nucleic Acids Res.* **1992,** *20,* 2803–2812. doi:10.1093/nar/20.11.2803
14. Netzel, T. L.; Nafisi, K.; Zhao, M.; Lenhard, J. R.; Johnson, I. *J. Phys. Chem.* **1995,** *99,* 17936–17947. doi:10.1021/j100051a019
15. Fürstenberg, A.; Julliard, M. D.; Deligeorgiev, T. G.; Gadjev, N. I.; Vasilev, A. A.; Vauthey, E. *J. Am. Chem. Soc.* **2006,** *128,* 7661–7669. doi:10.1021/ja0609001
16. Selvin, P. *Science* **1992,** *257,* 885–886. doi:10.1126/science.1502555
17. Flors, C.; Ravarani, C. N. J.; Dryden, D. T. F. *ChemPhysChem* **2009,** *10,* 2201–2204. doi:10.1002/cphc.200900384
18. Persson, F.; Bingen, P.; Staudt, T.; Engelhardt, J.; Tegenfeldt, J. O.; Hell, S. W. *Angew. Chem., Int. Ed.* **2011,** *50,* 5581–5583. doi:10.1002/anie.201100371
19. Miller, H.; Zhou, Z.; Wollman, A. J. M.; Leake, M. C. *Methods* **2015,** *88,* 81–88. doi:10.1016/j.ymeth.2015.01.010
20. Schoen, I.; Ries, J.; Klotzsch, E.; Ewers, H.; Vogel, V. *Nano Lett.* **2011,** *11,* 4008–4011. doi:10.1021/nl2025954
21. Biteen, J.; Willets, K. A. *Chem. Rev.* **2017,** *117,* 7241–7243. doi:10.1021/acs.chemrev.7b00242
22. Vilar, J. M. G.; Saiz, L. *Curr. Opin. Genet. Dev.* **2005,** *15,* 136–144. doi:10.1016/j.gde.2005.02.005
23. Jungmann, R.; Steinhauer, C.; Scheible, M.; Kuzyk, A.; Tinnefeld, P.; Simmel, F. C. *Nano Lett.* **2010,** *10,* 4756–4761. doi:10.1021/nl103427w
24. Rajendran, A.; Endo, M.; Hidaka, K.; Sugiyama, H. *Angew. Chem., Int. Ed.* **2014,** *53,* 4107–4112. doi:10.1002/anie.201308903
25. Ortega-Esteban, A.; Bodensiek, K.; San Martín, C.; Suomalainen, M.; Greber, U. F.; de Pablo, P. J.; Schaap, I. A. T. *ACS Nano* **2015,** *9,* 10571–10579. doi:10.1021/acsnano.5b03020
26. Hell, S. W.; Wichmann, J. *Opt. Lett.* **1994,** *19,* 780–782. doi:10.1364/OL.19.000780
27. Blom, H.; Widengren, J. *Chem. Rev.* **2017,** *117,* 7377–7427. doi:10.1021/acs.chemrev.6b00653
28. von Diezmann, A.; Shechtman, Y.; Moerner, W. E. *Chem. Rev.* **2017,** *117,* 7244–7275. doi:10.1021/acs.chemrev.6b00629
29. Liu, S.; Cao, K.; Li, H.; Song, J.; Han, J.; Shen, Y.; Wang, M. *Sol. Energy* **2017,** *144,* 158–165. doi:10.1016/j.solener.2017.01.019
30. Lee, A.; Tsekouras, K.; Calderon, C.; Bustamante, C.; Pressé, S. *Chem. Rev.* **2017,** *117,* 7276–7330. doi:10.1021/acs.chemrev.6b00729
31. Sydor, A. M.; Czymmek, K. J.; Puchner, E. M.; Mennella, V. *Trends Cell Biol.* **2015,** *25,* 730–748. doi:10.1016/j.tcb.2015.10.004
32. Rust, M. J.; Bates, M.; Zhuang, X. *Nat. Methods* **2006,** *3,* 793–796. doi:10.1038/nmeth929
33. Betzig, E.; Patterson, G. H.; Sougrat, R.; Lindwasser, O. W.; Olenych, S.; Bonifacino, J. S.; Davidson, M. W.; Lippincott-Schwartz, J.; Hess, H. F. *Science* **2006,** *313,* 1642–1645. doi:10.1126/science.1127344
34. Gordon, M. P.; Ha, T.; Selvin, P. R. *Proc. Natl. Acad. Sci. U. S. A.* **2004,** *101,* 6462–6465. doi:10.1073/pnas.0401638101
35. Sharonov, A.; Hochstrasser, R. M. *Proc. Natl. Acad. Sci. U. S. A.* **2006,** *103,* 18911–18916. doi:10.1073/pnas.0609643104
36. Molle, J.; Raab, M.; Holzmeister, S.; Schmitt-Monreal, D.; Grohmann, D.; He, Z.; Tinnefeld, P. *Curr. Opin. Biotechnol.* **2016,** *39,* 8–16. doi:10.1016/j.copbio.2015.12.009
37. Cox, S.; Rosten, E.; Monypenny, J.; Jovanovic-Talisman, T.; Burnette, D. T.; Lippincott-Schwartz, J.; Jones, G. E.; Heintzmann, R. *Nat. Methods* **2012,** *9,* 195–200. doi:10.1038/Nmeth.1812
38. van de Linde, S.; Sauer, M. *Chem. Soc. Rev.* **2014,** *43,* 1076–1087. doi:10.1039/C3CS60195A
39. Åkerman, B.; Tuite, E. *Nucleic Acids Res.* **1996,** *24,* 1080–1090. doi:10.1093/nar/24.6.1080
40. Kanony, C.; Åkerman, B.; Tuite, E. *J. Am. Chem. Soc.* **2001,** *123,* 7985–7995. doi:10.1021/ja001047n
41. Tycon, M. A.; Dial, C. F.; Faison, K.; Melvin, W.; Fecko, C. J. *Anal. Biochem.* **2012,** *426,* 13–21. doi:10.1016/j.ab.2012.03.021
42. Carlsson, C.; Johnson, M.; Åkerman, B. *Nucleic Acids Res.* **1995,** *23,* 2413–2420. doi:10.1093/nar/23.13.2413
43. Chen, J.; Bremauntz, A.; Kisley, L.; Shuang, B.; Landes, C. F. *ACS Appl. Mater. Interfaces* **2013,** *5,* 9338–9343. doi:10.1021/am403984k
44. Kisley, L.; Chen, J.; Mansur, A. P.; Shuang, B.; Kourentzi, K.; Poongavanam, M.-V.; Chen, W.-H.; Dhamane, S.; Willson, R. C.; Landes, C. F. *Proc. Natl. Acad. Sci. U. S. A.* **2014,** *111,* 2075–2080. doi:10.1073/pnas.1318405111
45. Shuang, B.; Chen, J.; Kisley, L.; Landes, C. F. *Phys. Chem. Chem. Phys.* **2014,** *16,* 624–634. doi:10.1039/c3cp53968g
46. Ke, C.-S.; Fang, C.-C.; Yan, J.-Y.; Tseng, P.-J.; Pyle, J. R.; Chen, C.-P.; Lin, S.-Y.; Chen, J.; Zhang, X.; Chan, Y.-H. *ACS Nano* **2017,** *11,* 3166–3177. doi:10.1021/acsnano.7b00215
47. Hou, L.; Adhikari, S.; Tian, Y.; Scheblykin, I. G.; Orrit, M. *Nano Lett.* **2017,** *17,* 1575–1581. doi:10.1021/acs.nanolett.6b04726

48. Chen, T.-Y.; Santiago, A. G.; Jung, W.; Krzemiński, Ł.; Yang, F.; Martell, D. J.; Helmann, J. D.; Chen, P. *Nat. Commun.* **2015,** *6,* 7445. doi:10.1038/ncomms8445
49. Janssen, D.; De Palma, R.; Verlaak, S.; Heremans, P.; Dehaen, W. *Thin Solid Films* **2006,** *515,* 1433–1438. doi:10.1016/j.tsf.2006.04.006
50. Han, Y.; Mayer, D.; Offenhäusser, A.; Ingebrandt, S. *Thin Solid Films* **2006,** *510,* 175–180. doi:10.1016/j.tsf.2005.11.048
51. Fiorilli, S.; Rivolo, P.; Descrovi, E.; Ricciardi, C.; Pasquardini, L.; Lunelli, L.; Vanzetti, L.; Pederzolli, C.; Onida, B.; Garrone, E. *J. Colloid Interface Sci.* **2008,** *321,* 235–241. doi:10.1016/j.jcis.2007.12.041
52. Krishnamoorthy, G.; Duportail, G.; Mély, Y. *Biochemistry* **2002,** *41,* 15277–15287. doi:10.1021/bi020440y
53. Thompson, R. E.; Larson, D. R.; Webb, W. W. *Biophys. J.* **2002,** *82,* 2775–2783. doi:10.1016/S0006-3495(02)75618-X
54. Simonson, P. D.; Rothenberg, E.; Selvin, P. R. *Nano Lett.* **2011,** *11,* 5090–5096. doi:10.1021/nl203560r
55. Rosten, E.; Jones, G. E.; Cox, S. *Nat. Methods* **2013,** *10,* 97–98. doi:10.1038/nmeth.2342
56. Zhu, L.; Zhang, W.; Elnatan, D.; Huang, B. *Nat. Methods* **2012,** *9,* 721–723. doi:10.1038/nmeth.1978
57. Dertinger, T.; Colyer, R.; Iyer, G.; Weiss, S.; Enderlein, J. *Proc. Natl. Acad. Sci. U. S. A.* **2009,** *106,* 22287–22292. doi:10.1073/pnas.0907866106
58. Kisley, L.; Brunetti, R.; Tauzin, L. J.; Shuang, B.; Yi, X.; Kirkeminde, A. W.; Higgins, D. A.; Weiss, S.; Landes, C. F. *ACS Nano* **2015,** *9,* 9158–9166. doi:10.1021/acsnano.5b03430
59. Wang, W.; Shen, H.; Shuang, B.; Hoener, B. S.; Tauzin, L. J.; Moringo, N. A.; Kelly, K. F.; Landes, C. F. *J. Phys. Chem. Lett.* **2016,** *7,* 4524–4529. doi:10.1021/acs.jpclett.6b02098

License and Terms

BEILSTEIN JOURNAL OF NANOTECHNOLOGY

Tailoring the nanoscale morphology of HKUST-1 thin films via codeposition and seeded growth

Landon J. Brower, Lauren K. Gentry, Amanda L. Napier and Mary E. Anderson*

Full Research Paper

Open Access

Address:
Hope College, Department of Chemistry, Holland, MI 49422, United States

Email:
Mary E. Anderson* - meanderson@hope.edu

* Corresponding author

Keywords:
atomic force microscopy; copper(II) 1,3,5-benzenetricarboxylate; ellipsometry; surface-anchored metal-organic frameworks

Beilstein J. Nanotechnol. **2017,** *8,* 2307–2314.
doi:10.3762/bjnano.8.230

Received: 27 June 2017
Accepted: 29 September 2017
Published: 03 November 2017

This article is part of the Thematic Series "Nanoscale patterning and characterization".

Guest Editor: S. A. Claridge

Abstract

Integration of surface-anchored metal-organic frameworks (surMOFs) within hierarchical architectures is necessary for potential sensing, electronic, optical, or separation applications. It is important to understand the fundamentals of film formation for these surMOFs in order to develop strategies for their incorporation with nanoscale control over lateral and vertical dimensions. This research identified processing parameters to control the film morphology for surMOFs of HKUST-1 fabricated by codeposition and seeded deposition. Time and temperature were investigated to observe film formation, to control film thickness, and to tune morphology. Film thickness was investigated by ellipsometry, while film structure and film roughness were characterized by atomic force microscopy. Films formed via codeposition resulted in nanocrystallites anchored to the gold substrate. A dynamic process at the interface was observed with a low density of large particulates (above 100 nm) initially forming on the substrate; and over time these particulates were slowly replaced by the prevalence of smaller crystallites (ca. 10 nm) covering the substrate at a high density. Elevated temperature was found to expedite the growth process to obtain the full range of surface morphologies with reasonable processing times. Seed crystals formed by the codeposition method were stable and nucleated growth throughout a subsequent layer-by-layer deposition process. These seed crystals templated the final film structure and tailor the features in lateral and vertical directions. Using codeposition and seeded growth, different surface morphologies with controllable nanoscale dimensions can be designed and fabricated for integration of MOF systems directly into device architectures and sensor platforms.

Introduction

Metal-organic frameworks (MOFs), composed of both metal ions and organic ligands, represent a class of extremely porous, crystalline materials with high surface area. Research has investigated their integration as thin films, namely surface-anchored metal-organic frameworks (surMOFs), into a wide variety of technologies from sensing to low-κ dielectric applications [1-9]. Different morphologies and a range of film thicknesses (10 nm to 100 μm) are required depending on the desired application.

For example, rough surfaces present a higher surface area for analytes to access the internal porous networks; and conformal, continuous surfaces are necessary for the incorporation of the MOF within the multilayer stacks commonly implemented for device architectures. Additionally, thin nanoscale films are necessary for the incorporation of surMOFs as dielectric layers and thick microscale films are advantageous for applications in which the MOF pores are utilized for analyte storage.

Layer-by-layer (LBL) solution-phase deposition has been studied for the HKUST-1 system, which consists of Cu(II) ions and trimesic acid (TMA) [10], deposited onto a self-assembled monolayer (SAM) on Au substrates [11-14]. The growth mechanism for HKUST-1 surMOF films fabricated by LBL deposition was found to be Volmer–Weber, with small crystallites nucleating and ripening on the substrate upon continued deposition cycles, as opposed to a van der Merwe growth mechanism that produces a conformal film [11,12]. For surMOF film growth via LBL deposition, it was found that temperature and surface chemistry (terminal functional group of SAM) control the crystal face growth of the crystallites on the substrate [11,12,15-17]. This provides some degree of control over roughness, particle size, surface coverage, and film thickness. In juxtaposition to the LBL method that generated films and crystallites in the sub-100 nm regime, MOF film deposition from mother liquor solutions, which are used to solvothermally produce powders, yield films that have thickness, roughness, and grain sizes on the microscale [2,18,19].

To fabricate the MOF for integration, methods such as microcontact printing and nanografting have been utilized to create chemical patterns onto which the surMOF is selectively grown [20,21]. Confined geometries have been utilized in conjunction with conventional and nonconventional lithography techniques to trap the precursor solution for subsequent solvent evaporation to produce isolated MOF crystallites in predetermined positions [22-24]. Microfluidics and ink-jet printing work in similar manners, delivering the solution according to a predefined design for subsequent MOF crystal formation [25,26]. Processing conditions have been optimized for some specific MOF systems to utilize conventional lithography for patterning of the film [8,27,28]. While these methods offer means to control the spatial location of the MOF for integration, they typically do not present processing parameters to control the morphology of the MOF with regards to nanoscale features such as thickness, roughness, and grain size.

Herein, means for fabricating surMOFs of HKUST-1 via codeposition and seeded growth have been investigated to gain further control over the morphology of these thin films. By varying temperature, time, and deposition method, the goal was to develop and expand design rules to tailor surMOFs with desired thickness, roughness, and grain size. In order to understand the growth mechanism and identify key variables, atomic force microscopy (AFM) and ellipsometry were used to characterize samples, investigating surface morphology, surface roughness, and film thickness.

Results and Discussion

For this study of codeposition and seeded surMOF film growth, the MOF was anchored to the substrate by a SAM of 16-mercaptohexadecanoic acid (MHDA), which was formed on a thermally deposited gold film on a silicon wafer. To form the HKUST-1 surMOF, this substrate was then immersed in a codeposition solution containing both the inorganic (Cu(II) ions) and organic (trimesic acid) components in dimethyl sulfoxide (DMSO). Deposition time and temperature were studied to understand the surMOF formation. Means for seeding surMOF growth were investigated by combining codeposition and LBL deposition.

Time study at room temperature (25 °C)

The effect of codeposition time on film thickness was investigated by ellipsometry. Initially, it was hypothesized that this would be a means to control film thickness with potentially thicker films forming after prolonged exposure. The ellipsometric data (Table 1) shows that while the film thickness increased from 0.5 to 1.5 h by almost a factor of two, the film thickness decreased after 5 h and 24 h of deposition and increased after 48 h of deposition. A linear increase in film thickness as a function of time was not observed in contrast to LBL deposition in which film thickness increased as a function of deposition cycles [11]. The film thickness decreases measured for the samples after 5 and 24 h of deposition suggested that the crystallites were not stable after initial formation when the sample was maintained in the DMSO codeposition solution. However, the film thickness increase observed for the 48 h sample may suggest that film growth reoccurred after dissolution of the initial crystallites. This revealed a dynamic process at the interface that affected the amount of MOF anchored to the substrate. Ellipsometry, with its laser beam spot size of ca. 1 mm, allowed for fast and efficient sampling across the entire substrate. In contrast to AFM with sampled region sizes on the micro- and nanoscale, ellipsometry provided a more global overview of the film than the local sampling of the AFM. AFM has been integral to mapping out the nanoscale morphology of surMOF thin films as well as identifying features formed on the surface of MOF crystals [11,12,29-32].

AFM was employed to investigate how the morphology of the film changed as a function of the deposition time. Representative images for the different time points at room temperature are

Table 1: Average film thickness and roughness values along with standard deviations observed for specified codeposition conditions.

temperature (°C)	time (h)	thickness (nm)	roughness (nm)
25	0.5	4.08 ± 0.45	11.8 ± 2.2
	1.5	7.6 ± 1.3	19.3 ± 5.6
	5	4.8 ± 1.5	14.9 ± 2.0
	24	3.08 ± 0.79	15.6 ± 2.6
	48	6.22 ± 0.88	4.5 ± 2.3
35	1.5	5.9 ± 1.4	10.7 ± 3.0
	5	12.3 ± 1.2	21.3 ± 6.5
50	1.5	5.9 ± 1.4	11.8 ± 4.7
	5	5.5 ± 1.0	6.3 ± 1.3
75	1.5	11.4 ± 2.4	10.0 ± 4.0
	5	4.6 ± 2.4	5.7 ± 2.0

shown in Figure 1 with the average film roughness (*R*q) given in Table 1. Between the time points of 0.5 and 1.5 h (Figure 1a,b), the feature size of the crystallites and the average film roughness increased (from 11.8 ± 2.2 nm to 19.3 ± 5.6 nm) corresponding with increased surface coverage that reflected the ellipsometrically observed film thickness increase. When the deposition time was increased to 5 and 24 h (Figure 1c,d), fewer large particles were observed and the average observed film roughness decreased slightly (from 19.3 ± 5.6 nm after 1.5 h to 14.9 ± 2.0 nm and 15.6 ± 2.6 nm after 5 and 24 h, respectively). This corresponded to the decreased average film thickness observed by ellipsometry (from 7.6 ± 1.3 nm after 1.5 h to 4.8 ± 1.5 nm and 3.08 ± 0.79 nm after 5 and 24 h, respectively). In addition at these time points (5 and 24 h), the presence of smaller particles between the larger particles became prevalent, as is shown in the higher magnification images (Figure 1h,i). After 48 h of deposition (Figure 1e,j), the film had a very high coverage of small (predominantly sub-10 nm height) crystallites (most clearly seen in Figure 1j) consistent with the decrease in film roughness to a third (from 15.6 ± 2.6 nm after 24 h to 4.5 ± 2.3 nm after 48 h). The film thickness after 48 h (6.22 ± 0.88 nm) increased above the 24 h sample (3.08 ± 0.79 nm) and was within error the same as the 1.5 h (7.6 ± 1.3 nm) and 5 h (4.8 ± 1.5 nm) samples. The similarity of the ellipsometric film thicknesses with significantly different feature sizes (quantitatively shown as a three- and four-fold difference in film roughness) suggested that while deposition time could not control film thickness, it could tune film morphology.

Time and temperature study

In addition to codeposition at 25 °C, three addition temperatures were investigated (35 °C, 50 °C, 75 °C) at time points of 1.5 and 5 h. These two time points were selected for this investigation because they were distinctly different from one another in the 25 °C samples. The 1.5 h sample at 25 °C had the highest thickness and roughness values. The 25 °C sample submerged for 5 h had a marked decrease in thickness and was the initial time point at which the proliferation of small particles was observed. In addition, durations of 1.5 and 5 h were reasonable time lengths for chemical processing. It was postulated that an increase in temperature could increase film thickness or accelerate the dynamic process observed at room temperature.

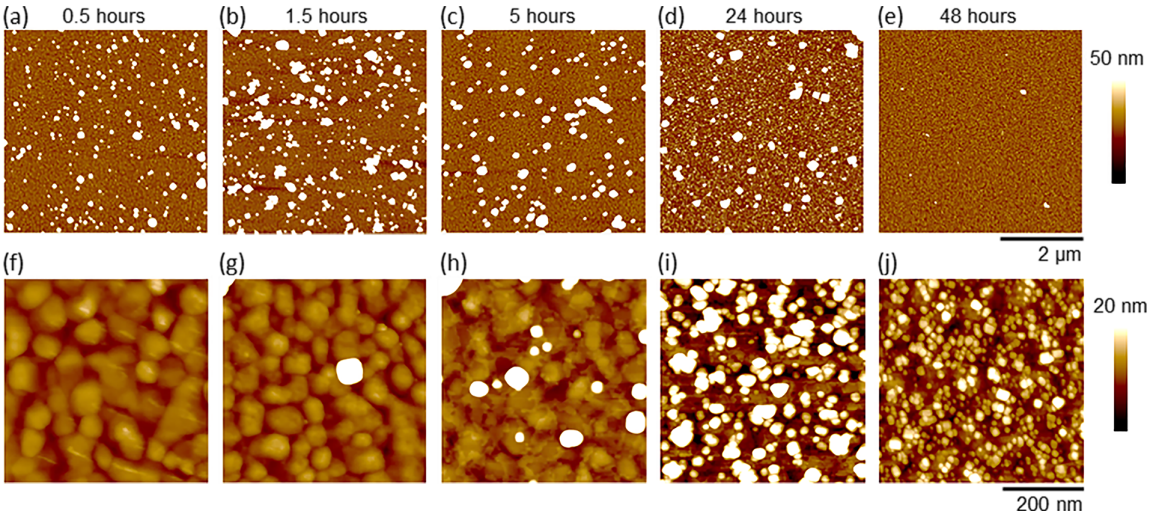

Figure 1: Representative AFM images of HKUST-1 surMOFs fabricated via codeposition at 25 °C on SAM-coated Au surfaces. Samples were synthesized over varied lengths of time (as indicated above each column of images). Shown in (a–e) are 5 µm × 5 µm images set to the same *z*-scale (50 nm) and shown in (f–j) are 500 nm × 500 nm images set to the same lower *z*-scale (20 nm) to visually render the smallest particles on the substrate. The higher magnification images were taken in regions between the largest MOF crystallites and selected specifically to characterize the smallest crystallites nucleated on the surface. Note the gold grain structure in the background of these higher resolution images.

Deposition at higher temperatures did indeed produce thicker films than were observed for the different time conditions investigated at room temperature. For the 1.5 h time point, ellipsometry showed that the thickest film (11.4 ± 2.4 nm) occurred at the highest temperature (75 °C). At the lower temperatures for the 1.5 h duration, lower film thicknesses consistent within error were found (7.6 ± 1.3 nm, 5.9 ± 1.4 nm, and 5.9 ± 1.4 nm). In contrast for the 5 h time point, the thickest film (12.3 ± 1.2 nm) was found for the film fabricated at 35 °C. The other films were found to have thicknesses again consistent within error (4.8 ± 1.5 nm, 5.5 ± 1.0 nm, and 4.6 ± 2.4 nm).

To explore how the morphology of these films was affected by deposition at higher temperatures, AFM images were collected (Figure 2). The 35 °C and 50 °C samples after 1.5 h were indistinguishable regarding film thickness and roughness. The AFM images (Figure 2b,c) show similar morphologies composed of large particles with small particles being observable. Note that these small particles were absent at 25 °C (Figure 2a). After 5 h at 35 and 50 °C, these samples that were quite similar became distinctly different. This is especially apparent in the AFM images (Figure 2f,g), as well as in the average film thickness that doubled for the 35 °C sample (from 5.9 ± 1.4 nm to 12.3 ± 1.2 nm) and remained unchanged for the 50 °C sample (at 5.9 ± 1.4 nm and 5.5 ± 1.0 nm). These 35 °C and 50 °C samples after 5 h of deposition had distinct morphologies and roughnesses that mirrored samples deposited at 25 °C for 24 and 48 h, respectively. This suggested that the same dynamic process was occurring. However, it was accelerated by the elevated temperatures. Further support for this was seen in comparing the 50 °C and 75 °C sample after 1.5 h of deposition. A higher coverage of particles is apparent in the AFM image of the 75 °C sample (Figure 2d), which reflected the observation that the film thickness for the 75 °C sample was double that of the 50 °C sample. This also paralleled the doubling of film thickness observed at room temperature for the 48 h sample relative to the 24 h sample.

For the implementation of surMOFs into most potential applications, it is necessary for the films to be continuous across the substrate and have controllable thicknesses. Preliminary investigations found that at lower concentrations of the codeposition solution, less material was anchored to the substrate. It would follow that at higher concentration, one could increase the film thickness. However, the solubility of the reagents within the solution was prohibitive to investigating higher concentration. Additionally, preliminary work found that significant film formation neither occurred when copper acetate was used as the metal ion source, nor when ethanol was used as the solvent. Furthermore, initial experiments showed that the codeposition solution with dimethylformamide as the solvent resulted in a similar dynamic surface process. However, the initial large particles that occurred were smaller relative to those observed using DMSO at the early time points. Future experiments may investigate the effect of altering the ratio of the metal ion and organic component.

Seeded growth

Film morphology could be tailored by codeposition utilizing time and temperature as variables to tune the structure.

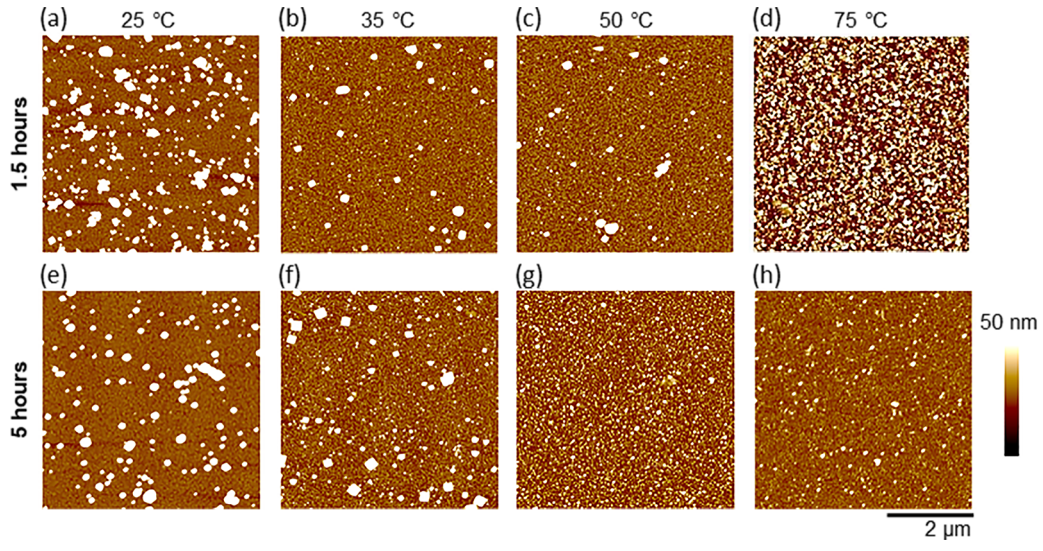

Figure 2: Representative AFM images (5 µm × 5 µm) of HKUST-1 surMOFs fabricated via codeposition at different temperatures (as indicated above each column of images) on SAM-coated Au surfaces. Samples were exposed for different durations; either 1.5 h (a–d) or 5 h (e–h). All images were set to the same *z*-scale (50 nm) for visual comparison.

While an increased film thickness was found at elevated temperatures, the upper bound of film thicknesses for codeposition seems limited (Table 1) and did not result in a continuous film across the substrate. It was hypothesized that the film thickness could be increased by LBL deposition on top of samples with foundational surMOF crystallites formed by codeposition.

To investigate whether the underlying morphology of the codeposited seed layer crystallites could be maintained throughout the LBL deposition process, codeposited samples with unique surface morphologies were identified. The room-temperature study (25 °C) investigated samples exposed to the codeposition solution for different durations and revealed that distinct morphologies could be controlled by tuning exposure times. The 1.5 h and 48 h samples had similar thicknesses (7.6 ± 1.3 nm and 6.22 ± 0.88 nm), but very different morphologies. Qualitatively, the morphology of the 1.5 h sample had lower surface coverage with larger particles relative to the 48 h sample. Quantitative analysis of AFM images showed that the roughness of the 1.5 h sample was four times that of the 48 h sample. While this type of control of surface morphology has potential, the time requirements for the smooth film could be prohibitive. The temperature study confirmed that the same dynamic process resulting in distinct morphologies at room temperature could be accelerated by elevating the temperature. That is, the morphology, roughness, and thickness found after 48 h for the 25 °C sample could be achieved more readily after 5 h at 50 °C. (For comparison, a representative AFM 500 nm × 500 nm image of the sample codeposited for 5 h at 50 °C can be found in Supporting Information File 1.)

To potentially template film morphologies, samples seeded with unique surface morphologies were fabricated by codeposition for 1.5 h at 25 °C and 5 h at 50 °C (Figure 3a,b). These two conditions produced films with similar thicknesses, yet with different morphologies that were shown quantitatively to have had roughnesses of 19.3 ± 5.6 nm and 6.3 ± 1.3 nm at 25 °C and 50 °C, respectively. These films were then taken in parallel through four LBL deposition cycles. The film thickness in both of these cases increased by ca. 7 nm, which was consistent with four cycles of deposition on a MHDA SAM-coated substrate [11]. After this LBL process, surface morphologies were consistent with that of the underlying seed crystallites (Figure 3c,d). These two films fabricated by LBL deposition on top of films seeded by codeposition had similar average film thicknesses (14 nm). However, they had significantly different average film roughnesses with 32.8 ± 14.2 nm and 12.8 ± 5.7 nm observed for the films deposited on the substrate seeded by using codeposition for 1.5 h at 25 °C and for 5 h at 50 °C, respectively.

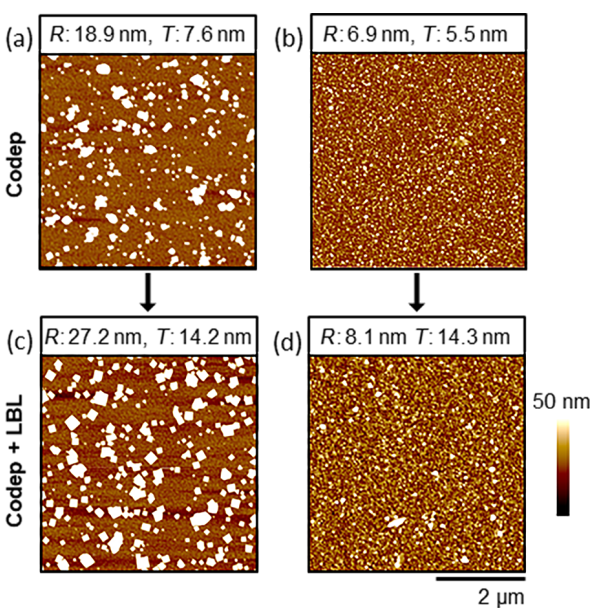

Figure 3: Representative AFM images (5 µm × 5 µm) of HKUST-1 surMOFs fabricated via codeposition (codep) at 25 °C for 1.5 h (a) and 50 °C for 5 h (b) on SAM-coated Au surfaces. Additional layers of HKUST-1 were added to these codeposited samples via layer-by-layer (LBL) deposition. The subsequent surface morphology was imaged (c,d) and the previous surface morphology was maintained. Data regarding the roughness (*R*) for the image shown here and average film thickness (*T*), as measured by ellipsometry, are provided above the images for comparison. All images were set to the same *z*-scale (50 nm).

This research shows that LBL deposition on substrates seeded with crystallites formed by codeposition could result in thicker films and maintain tailored morphologies. This control over film thickness and morphology is important for the integration of MOFs into a range of thin film architectures. In contrast to the successful seeding via codeposited crystals for subsequent LBL deposition, initial attempts to use surMOF films formed by LBL as seed crystallites for codeposition were unsuccessful. In this case, neither increased film thicknesses nor preservation of the initial film morphology was observed.

Associated with the studies herein, dropcasting on substrates seeded by codeposition or LBL deposition was investigated. Dropcasting a solution (containing the inorganic and organic components of the MOF) onto a substrate followed by heating to eliminate the solvent and crystallize the film is a common method for the formation of continuous, albeit thick, MOF films. To form continuous films across a substrate, high solution concentrations are required and these result in thicknesses commonly on the micrometer-scale. Preliminary investigations using seeded surMOF films formed by codeposition or LBL were effective for fabricating conformal, continuous, and thinner films from more dilute dropcast solutions. Future research will further optimize this process by controlling solu-

tion concentration, temperature, and atmospheric conditions to permit the formation of sub-micrometer, conformal films.

Conclusion

Films formed by codeposition were similar to those formed by LBL in that they were composed of nanocrystallites and were not conformal films produced by a van der Merwe growth mechanism. However, the Volmer–Weber growth mechanism (with crystallite nucleation and ripening) that was observed for the LBL deposition was not observed in the same manner for the codeposition. Throughout the codeposition procedure, a dynamic process was observed at the substrate interface. Large particles initially formed on the substrate, followed by the increased prevalence of smaller crystallites alongside the disappearance of the larger particles, and finally the substrate became covered with a high density of small (ca. 10 nm) crystallites. Altering deposition time and temperature was found to control size and density of the particles on the surface, resulting in films with distinctly different morphologies and surface roughnesses. Elevated temperatures were found to expedite the film formation, thus obtaining the full range of surface morphologies within reasonable time frames. Initial morphological properties of the codeposited films were conserved when performing the LBL deposition process on substrates that were seeded under two different codeposition conditions.

Experimental

Materials

Trimesic acid (TMA, 95%), dimethyl sulfoxide (DMSO, Aldrich, spectrophotometric grade), and 16-mercaptohexadecanoic acid (MHDA, 90%) were obtained from Aldrich (St. Louis, MO, USA). The DMSO was purged with nitrogen and passed through columns of molecular sieves. Copper(II) nitrate hemi(pentahydrate) (ACS grade) and copper(II) acetate monohydrate were received from Fisher Scientific (Fair Lawn, NJ, USA). Absolute, anhydrous ethyl alcohol (200 proof, ACS/USP grade) was attained from Pharmco-Aaper (Shelbyville, KY, USA). All chemicals were used as received, unless otherwise noted. Gold substrates were obtained from Platypus Technologies (New Orleans, LA) in the form of silicon wafers with a 5 nm titanium adhesion layer and 100 nm of gold.

Methods

Substrate Preparation: HKUST-1 surMOF films were fabricated by the codeposition of TMA and copper ions onto a gold substrate previously functionalized by a self-assembled monolayer (SAM) that consisted of MHDA. The gold substrate was first fully immersed in approximately 10 mL of a 1 mM MHDA ethanol solution for 1 h, which formed the foundational anchor for the framework. Once removed from solution, the sample was rinsed thoroughly with ethanol and dried with nitrogen gas.

Codeposition SurMOF formation: The codeposition solution was prepared, consisting of 0.53 M copper nitrate and 0.27 M TMA in DMSO. This concentration was half of the typical solution from which MOF powders were crystallized [10,22]. The codeposition solution was sonicated and stirred for 5 min, after which approximately 10 mL were used to submerge the substrate. Following submersion, a hotplate was used to achieve and maintain temperatures above 25 °C for the duration of the deposition process. The sample was then removed from solution, rinsed with ethanol, dried with nitrogen, and stored in a dry box.

Layer-by-Layer SurMOF formation: The LBL deposition of surMOF on a gold substrate functionalized by a SAM was fabricated according to the literature by alternating, solution-phase deposition [11]. This process was automated by a Midas III automated slide stainer. For all experiments herein, solutions were held at room temperature.

Characterization

All samples were characterized by atomic force microscopy (Figures 1–3) and ellipsometry (Table 1). In addition, characterization by infrared spectroscopy was conducted to confirm composition, and representative data is presented in Supporting Information File 1 (Figure S2) [13,14].

Atomic force microscopy: Multiple images (512 × 512 pixels) were obtained for each sample at 5 μm × 5 μm and 500 nm × 500 nm and used a Dimension Icon atomic force microscope (Bruker, Santa Barbara, CA, USA), which was operated in peak force tapping mode. Etched silicon tips, SCANASYST-AIR (Bruker, Santa Barbara, CA, USA), with a spring constant range of 0.2–0.8 N/m and a resonant frequency range of 45–95 kHz were used. Scan parameters were as follows: 1 Hz scan rate, 12 μm *z*-range, 250 mV amplitude set point, and 100 mV drive amplitude. AFM data presented herein are representative of the compilations of data specific to each sample set.

Image analysis: Image analysis was routinely carried out using the Nanoscope Analysis software (Bruker, Santa Barbara, CA, USA). This program was used to appropriately flatten and scale the image. The geometric average surface roughness, *R*q, was calculated for each image. The reported roughness values and standard deviations herein (Table 1) reflect the average *R*q from a minimum of three images taken per sample at 5 μm × 5 μm.

Ellipsometry: To investigate film growth, film thickness was characterized by using a variable-angle discrete wavelength ellipsometer (PHE-101 VADE, Angstrom Advanced, Braintree, MA). Note that the film thickness determined by ellipsometry is an average of the thickness of particulates within the samples

region of the 1 mm laser spot size. The use of proximal probes in addition to optical methods to characterize these types of films has been highlighted previously in the literature [11]. Data were acquired for each sample and collected from a minimum of five areas at a wavelength of 632.8 nm and fixed angle of 70°. The PHE-101 analysis software used the following refractive index values to calculate film thickness for the gold substrate: $n_s = 0.148$ and $k_s = 3.594$ and for the organic thin film: $n_f = 1.5$ and $k_f = 0$. The average film thickness and standard deviations are reported in Table 1.

Supporting Information

Supporting Information features a representative image data set (500 nm × 500 nm) for the samples codeposited for 5 h at 50 °C and for 5 h at 75 °C, as well as representative IR spectra for samples produced by codeposition and seeded growth.

Supporting Information File 1

Additional experimental data.
[http://www.beilstein-journals.org/bjnano/content/supplementary/2190-4286-8-230-S1.pdf]

Acknowledgements

This research was supported by the National Science Foundation (Chem RUI Grant #1508244, Chem REU Grant #1263097, and Chem MRI Grant #1126462) and the American Chemical Society (PRF-UNI5 Grant #54106). Additional funding was provided by the Towsley Foundation and Hope College. We thank Prof. Jennifer Hampton for technical assistance.

References

1. Eslava, S.; Zhang, L.; Esconjauregui, S.; Yang, J.; Vanstreels, K.; Baklanov, M. R.; Saiz, E. *Chem. Mater.* **2013,** *25,* 27–33. doi:10.1021/cm302610z
2. Shekhah, O.; Liu, J.; Fischer, R. A.; Woll, C. *Chem. Soc. Rev.* **2011,** *40,* 1081–1106. doi:10.1039/c0cs00147c
3. Liu, J.; Redel, E.; Walheim, S.; Wang, Z.; Oberst, V.; Liu, J.; Heissler, S.; Welle, A.; Moosmann, M.; Scherer, T.; Bruns, M.; Gliemann, H.; Wöll, C. *Chem. Mater.* **2015,** *27,* 1991–1996. doi:10.1021/cm503908g
4. Bétard, A.; Fischer, R. A. *Chem. Rev.* **2012,** *112,* 1055–1083. doi:10.1021/cr200167v
5. Zacher, D.; Schmid, R.; Wöll, C.; Fischer, R. A. *Angew. Chem., Int. Ed.* **2011,** *50,* 176–199. doi:10.1002/anie.201002451
6. Falcaro, P.; Ricco, R.; Doherty, C. M.; Liang, K.; Hill, A. J.; Styles, M. J. *Chem. Soc. Rev.* **2014,** *43,* 5513–5560. doi:10.1039/C4CS00089G
7. Talin, A. A.; Centrone, A.; Ford, A. C.; Foster, M. E.; Stavila, V.; Haney, P.; Kinney, R. A.; Szalai, V.; El Gabaly, F.; Yoon, H. P.; Léonard, F.; Allendorf, M. D. *Science* **2014,** *343,* 66–69. doi:10.1126/science.1246738
8. Lu, G.; Farha, O. K.; Zhang, W.; Huo, F.; Hupp, J. T. *Adv. Mater.* **2012,** *24,* 3970–3974. doi:10.1002/adma.201202116
9. Falcaro, P.; Buso, D.; Hill, A. J.; Doherty, C. M. *Adv. Mater.* **2012,** *24,* 3153–3168. doi:10.1002/adma.201200485
10. Chui, S. S.-Y.; Lo, S. M.-F.; Charmant, J. P. H.; Orpen, A. G.; Williams, I. D. *Science* **1999,** *283,* 1148–1150. doi:10.1126/science.283.5405.1148
11. Ohnsorg, M.; Beaudoin, C. K.; Anderson, M. E. *Langmuir* **2015,** *31,* 6114–6121. doi:10.1021/acs.langmuir.5b01333
12. Summerfield, A.; Cebula, I.; Schröder, M.; Beton, P. H. *J. Phys. Chem. C* **2015,** *119,* 23544–23551. doi:10.1021/acs.jpcc.5b07133
13. Shekhah, O.; Wang, H.; Zacher, D.; Fischer, R. A.; Wöll, C. *Angew. Chem., Int. Ed.* **2009,** *48,* 5038–5041. doi:10.1002/anie.200900378
14. Shekhah, O.; Wang, H.; Kowarik, S.; Schreiber, F.; Paulus, M.; Tolan, M.; Sternemann, C.; Evers, F.; Zacher, D.; Fischer, R. A.; Wöll, C. *J. Am. Chem. Soc.* **2007,** *129,* 15118–15119. doi:10.1021/ja076210u
15. Zhuang, J.-L.; Kind, M.; Grytz, C.; Farr, F.; Diefenbach, M.; Tussupbayev, S.; Holthausen, M. C.; Terfort, A. *J. Am. Chem. Soc.* **2015,** *137,* 8237–8243. doi:10.1021/jacs.5b03948
16. Biemmi, E.; Scherb, C.; Bein, T. *J. Am. Chem. Soc.* **2007,** *129,* 8054–8055. doi:10.1021/ja0701208
17. Liu, J.; Shekhah, O.; Stammer, X.; Arslan, H. K.; Liu, B.; Schüpbach, B.; Terfort, A.; Wöll, C. *Materials* **2012,** *5,* 1581–1592. doi:10.3390/ma5091581
18. Hermes, S.; Schröder, F.; Chelmowski, R.; Wöll, C.; Fischer, R. A. *J. Am. Chem. Soc.* **2005,** *127,* 13744–13745. doi:10.1021/ja053523l
19. Zacher, D.; Baunemann, A.; Hermes, S.; Fischer, R. A. *J. Mater. Chem.* **2007,** *17,* 2785–2792. doi:10.1039/b703098c
20. Gassensmith, J. J.; Erne, P. M.; Paxton, W. F.; Valente, C.; Stoddart, J. F. *Langmuir* **2011,** *27,* 1341–1345. doi:10.1021/la103958z
21. Ladnorg, T.; Welle, A.; Heißler, S.; Wöll, C.; Gliemann, H. *Beilstein J. Nanotechnol.* **2013,** *4,* 638–648. doi:10.3762/bjnano.4.71
22. Ameloot, R.; Gobechiya, E.; Uji-i, H.; Martens, J. A.; Hofkens, J.; Alaerts, L.; Sels, B. F.; De Vos, D. E. *Adv. Mater.* **2010,** *22,* 2685–2688. doi:10.1002/adma.200903867
23. Carbonell, C.; Imaz, I.; Maspoch, D. *J. Am. Chem. Soc.* **2011,** *133,* 2144–2147. doi:10.1021/ja2002428
24. Falcaro, P.; Hill, A. J.; Nairn, K. M.; Jasieniak, J.; Mardel, J. I.; Bastow, T. J.; Mayo, S. C.; Gimona, M.; Gomez, D.; Whitfield, H. J.; Riccò, R.; Patelli, A.; Marmiroli, B.; Amenitsch, H.; Colson, T.; Villanova, L.; Buso, D. *Nat. Commun.* **2011,** *2,* 237. doi:10.1038/ncomms1234
25. Witters, D.; Vergauwe, N.; Ameloot, R.; Vermeir, S.; De Vos, D.; Puers, R.; Sels, B.; Lammertyn, J. *Adv. Mater.* **2012,** *24,* 1316–1320. doi:10.1002/adma.201104922
26. Zhuang, J.-L.; Ar, D.; Yu, X.-J.; Liu, J.-X.; Terfort, A. *Adv. Mater.* **2013,** *25,* 4631–4635. doi:10.1002/adma.201301626
27. Doherty, C. M.; Grenci, G.; Riccò, R.; Mardel, J. I.; Reboul, J.; Furukawa, S.; Kitagawa, S.; Hill, A. J.; Falcaro, P. *Adv. Mater.* **2013,** *25,* 4701–4705. doi:10.1002/adma.201301383
28. Dimitrakakis, C.; Marmiroli, B.; Amenitsch, H.; Malfatti, L.; Innocenzi, P.; Grenci, G.; Vaccari, L.; Hill, A. J.; Ladewig, B. P.; Hill, M. R.; Falcaro, P. *Chem. Commun.* **2012,** *48,* 7483–7485. doi:10.1039/c2cc33292b
29. Holden, M. A.; Cubillas, P.; Attfield, M. P.; Gebbie, J. T.; Anderson, M. A. *J. Am. Chem. Soc.* **2012,** *134,* 13066–13073. doi:10.1021/ja303814p

30. Shoaee, M.; Anderson, M. W.; Attfield, M. P. *Angew. Chem., Int. Ed.* **2008,** *47,* 8525–8528. doi:10.1002/anie.200803460
31. Szelagowska-Kunstman, K.; Cyganik, P.; Goryl, M.; Zacher, D.; Puterova, Z.; Fischer, R. A.; Szymonski, M. *J. Am. Chem. Soc.* **2008,** *130,* 14446–14447. doi:10.1021/ja8069743
32. Cubillas, P.; Anderson, M. A.; Attfield, M. P. *Cryst. Growth Des.* **2013,** *13,* 4526–4532. doi:10.1021/cg401001f

License and Terms

BEILSTEIN JOURNAL OF NANOTECHNOLOGY

Expanding the molecular-ruler process through vapor deposition of hexadecanethiol

Alexandra M. Patron[1], Timothy S. Hooker[2], Daniel F. Santavicca[2], Corey P. Causey[*1,§] and Thomas J. Mullen[*1,¶]

Letter

Open Access

Address:
[1]Department of Chemistry, University of North Florida, Jacksonville, FL 32224, USA and [2]Department of Physics, University of North Florida, Jacksonville, FL 32224, USA

Email:
Corey P. Causey[*] - corey.causey@unf.edu;
Thomas J. Mullen[*] - tj.mullen@unf.edu

* Corresponding author
§ Phone: +1 904 620 2098; Fax: +1 904 620 3535
¶ Phone: +1 904 620 1377; Fax: +1 904 620 3535

Keywords:
hybrid nanolithography; metal-ligated multilayer; molecular ruler; self-assembled monolayers; vapor-phase deposition

Beilstein J. Nanotechnol. **2017,** *8,* 2339–2344.
doi:10.3762/bjnano.8.233

Received: 30 June 2017
Accepted: 09 October 2017
Published: 07 November 2017

This article is part of the Thematic Series "Nanoscale patterning and characterization".

Guest Editor: S. A. Claridge

Abstract

The development of methods to produce nanoscale features with tailored chemical functionalities is fundamental for applications such as nanoelectronics and sensor fabrication. The molecular-ruler process shows great utility for this purpose as it combines top-down lithography for the creation of complex architectures over large areas in conjunction with molecular self-assembly, which enables precise control over the physical and chemical properties of small local features. The molecular-ruler process, which most commonly uses mercaptoalkanoic acids and metal ions to generate metal-ligated multilayers, can be employed to produce registered nanogaps between metal features. Expansion of this methodology to include molecules with other chemical functionalities could greatly expand the overall versatility, and thus the utility, of this process. Herein, we explore the use of alkanethiol molecules as the terminating layer of metal-ligated multilayers. During this study, it was discovered that the solution deposition of alkanethiol molecules resulted in low overall surface coverage with features that varied in height. Because features with varied heights are not conducive to the production of uniform nanogaps via the molecular-ruler process, the vapor-phase deposition of alkanethiol molecules was explored. Unlike the solution-phase deposition, alkanethiol islands produced by vapor-phase deposition exhibited markedly higher surface coverages of uniform heights. To illustrate the applicability of this method, metal-ligated multilayers, both with and without an alkanethiol capping layer, were utilized to create nanogaps between Au features using the molecular-ruler process.

Findings

In a time when many technological advances are driven by the miniaturization of fabrication methods, much effort has been placed on the development of novel methods to produce nanoscale features with chemical functionalities that go beyond traditional semiconductors [1-3]. Recent advances in the field allow for the fabrication of molecular-scale features into surfaces that template the assembly and growth of metals, polymers, biomolecules, and cellular structures [3-11]. In addition, these surface assemblies have been utilized as molecular-scale resists for lithography [12,13]. One promising strategy for such fabrication utilizes top-down lithography to create complex architectures over large areas in conjunction with molecular self-assembly, which enables precise control over the physical and chemical properties of the small features [1,2]. The molecular-ruler process is a notable example of this hybrid approach as it couples conventional patterning methods with molecular self-assembly [14].

The molecular-ruler process can be employed to form nanogaps between registered metal surface features that have been generated using conventional lithographic techniques such as photolithography or electron-beam lithography (Figure 1) [14-24]. In short, a metal structure that has been patterned on a non-metal substrate (e.g., Si) using conventional lithography is subsequently covered by a metal-ligated multilayer through the iterative deposition of bifunctional organic molecules and metal ions. Note that the use of a thiol as one of the two functionalities ensures that deposition and growth of the multilayer only occurs on the surface of the metal, not the exposed substrate. By using molecules of discrete length, the thickness of the multilayer can be precisely controlled through the number of deposition steps. Once the desired thickness has been achieved, a second metal deposition is used to cover the entire sample of the substrate, including the exposed substrate and the surface of the multilayer. Following this second metal deposition, a chemical lift-off removes the labile multilayer, thus exposing the initial metal feature and the portion of the substrate that was masked by the multilayer, yielding a nanogap between the two metal surfaces. The size of this gap is defined by the thickness of the multilayer. Utilization of the molecular-ruler process in this way provides a general and widely applicable method to fabricate registered, nanometer-scale features for potential applications including nanoelectronics, molecular-scale junctions, and electrochemical sensors [17,18,20,21,25,26].

Although mercaptoalkanoic acid molecules, such as 16-mercaptohexadecanoic acid (MHDA), are the most widely studied molecules used in the molecular-ruler process, this method is inherently versatile through the use of molecules with alternate functionalities [27-31]. Towards this end, we set out to explore the use of an alkanethiol, specifically 1-hexadecanethiol (C16), as the terminating layer of a metal-ligated multilayer. This molecule was selected as it is commonly used to produce well-ordered self-assembled monolayers, has a relatively well understood terminal functionality (e.g., a methyl group), and enables direct comparison of thickness to MHDA molecules. Figures 2A and 2B show representative 2 µm × 2 µm and 500 nm × 500 nm atomic force microscopy (AFM) images of a Cu-ligated MHDA-C16 bilayer formed from the solution deposition of MHDA for 18 h, $Cu(ClO_4)_2{\cdot}6H_2O$ for 5 min, and C16 for 1 h. Figure 2C displays a representative cursor profile across several islands as indicated by the red line in Figure 2B. Although C16 is very similar in structure to MHDA, the solution

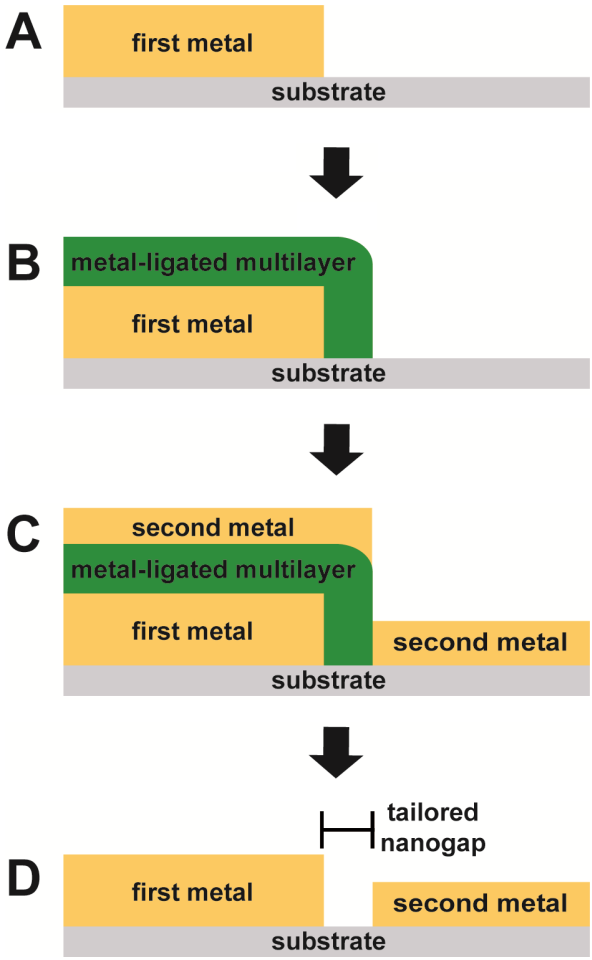

Figure 1: Key steps for the molecular-ruler process. (A) A metal is patterned on a substrate via conventional lithography. (B) A molecular-ruler, consisting of alternating layers of thiol molecules and metal ions, is created only on the first metal structure. (C) A second metal is deposited. (D) Upon removal of the molecular-ruler and the second metal on top of the multilayer via a chemical lift-off, a tailored nanogap is generated with a width that corresponds to the thickness of the multilayer.

deposition of C16 results in structures that exhibit islands of various apparent heights, ranging from 3.4 to 24.8 nm, with relatively low surface coverages (38.2 ± 3.3%). This is in contrast to Cu-ligated MHDA bilayers, which exhibit islands of uniform height (ca. 2.2 nm) and have surface coverages of about 50% [27-29,32]. The C16 islands of the Cu-ligated MHDA-C16 bilayers are observed across the Au{111} substrate and are attributed to C16 molecules bound to a MHDA monolayer via cupric ions. The morphology of these islands is consistent with previous AFM topographic images of solution-deposited Cu-ligated MHDA-C16 bilayers [27]. This surface morphology results in a RMS roughness of 3.2 ± 0.5 nm, which is considerably larger than previously reported RMS roughnesses for MHDA monolayers (ca. 0.1 nm) and MHDA bilayers (1.0 nm) [32]. Similar morphology and slightly higher coverages of the C16 islands are observed when C16 is deposited from solution at 80 °C (Figure S1, Supporting Information File 1). Given the roughness and variations in the surface morphology of the Cu-ligated MHDA-C16 bilayers, it seems that the solution deposition of C16 is not suitable for use in the molecular-ruler process, and specifically for producing nanogaps with reproducible uniformity.

To overcome this limitation, the vapor deposition of C16 is explored. Interestingly, when C16 is deposited from the vapor phase onto MHDA monolayers to produce Cu-ligated MHDA-C16 bilayers, protruding islands with uniform thickness are observed across the Au{111} substrate (Figure 3). Figure 3A and Figure 3B show representative 2 µm × 2 µm and 500 nm × 500 nm AFM images of a Cu-ligated MHDA-C16 bilayer formed from the solution deposition of MHDA for 18 h and $Cu(ClO_4)_2·6H_2O$ for 5 min followed by vapor deposition of C16 for 1 h at 80 °C. Figure 3C displays a representative cursor profile across several islands as indicated by the red line in Figure 3B. The apparent height of these protruding islands (3.6 ± 0.2 nm) is consistent with the least-protruding C16 islands of the Cu-ligated MHDA-C16 bilayers formed via solution deposition. Protruding islands of greater thicknesses are not observed. The surface morphology of the Cu-ligated MHDA-C16 bilayer formed via vapor deposition results in a RMS roughness of 1.3 ± 0.1 nm, which is smaller than a Cu-ligated MHDA-C16 bilayer formed via solution deposition. Further, the surface coverage of these C16 islands (69.9 ± 1.8%) is considerably higher than the C16 surface coverage for the MHDA-C16 bilayer formed via solution deposition. Given the increase in surface coverage coupled with the marked decrease in roughness, this method is far more amendable to our goal of nanogap formation. It should be noted that thickness of the C16 islands is roughly twice as thick as predicted, which has been observed in other studies [27,33,34]. Although the explanation of this height discrepancy it not completely clear, it is conceivable that

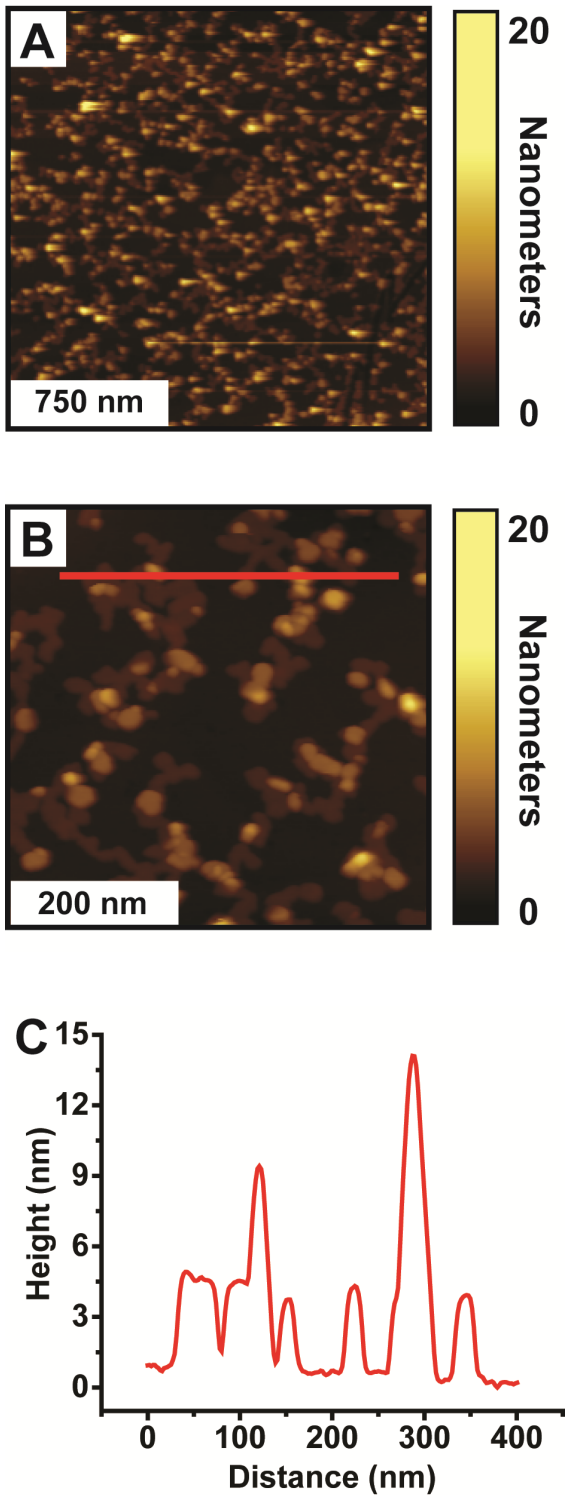

Figure 2: Cu-ligated MHDA-C16 bilayer formed from solution-phase deposition of C16. Representative (A) 2 µm × 2 µm and (B) 500 nm × 500 nm AFM images of a Cu-ligated MHDA-C16 bilayer formed from the solution deposition of MHDA for 18 h, $Cu(ClO_4)_2·6H_2O$ for 5 min, and C16 for 1 h. (C) Corresponding cursor profile across the C16 islands.

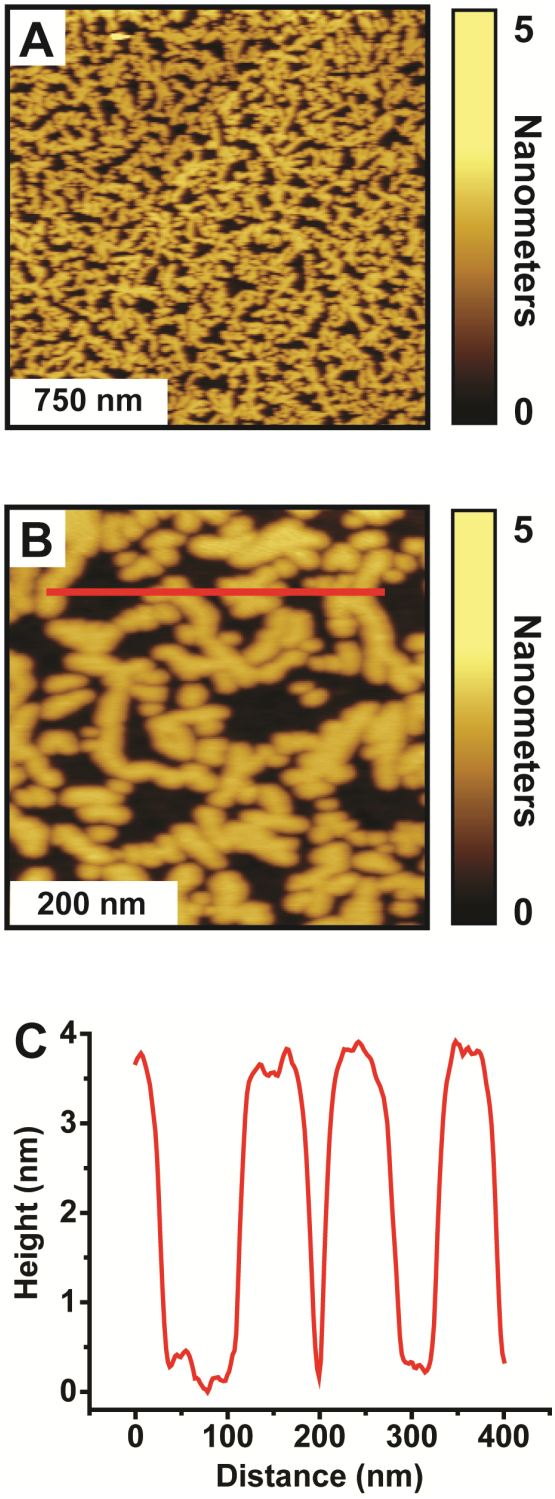

Figure 3: Cu-ligated MHDA-C16 bilayer formed from vapor-phase deposition of C16. Representative (A) 2 μm × 2 μm and (B) 500 nm × 500 nm AFM images of a of a Cu-ligated MHDA-C16 bilayer formed from the solution deposition of MHDA for 18 h and $Cu(ClO_4)_2{\cdot}6H_2O$ for 5 min and the vapor deposition of C16 for 1 h at 80 °C. (C) Corresponding cursor profile across the C16 islands.

the doubling in height results from disulfides that are intercalated into the hydrocarbon tails of the Cu-ligated C16 molecules.

To illustrate the applicability of the vapor-phase deposition of C16 in the molecular ruler process, Cu-ligated MHDA multilayers with and without a C16 capping layer are utilized to create nanogaps via the molecular-ruler process. Figure 4A shows a scanning electron microscope (SEM) image of the resulting nanogaps from nine iterations of the solution deposition of MHDA and $Cu(ClO_4)_2{\cdot}6H_2O$ followed by the solution deposition of MHDA for 1 h. The higher-intensity region corresponds to the first Au deposition (100 nm thick) before multilayer growth, and the lower-intensity region corresponds to the second Au deposition (30 nm thick) after multilayer growth. The lowest-intensity region between the two Au regions corresponds to the nanogap where the Si substrate is exposed. This nanogap measures 26.0 ± 4.3 nm and is consistent with the

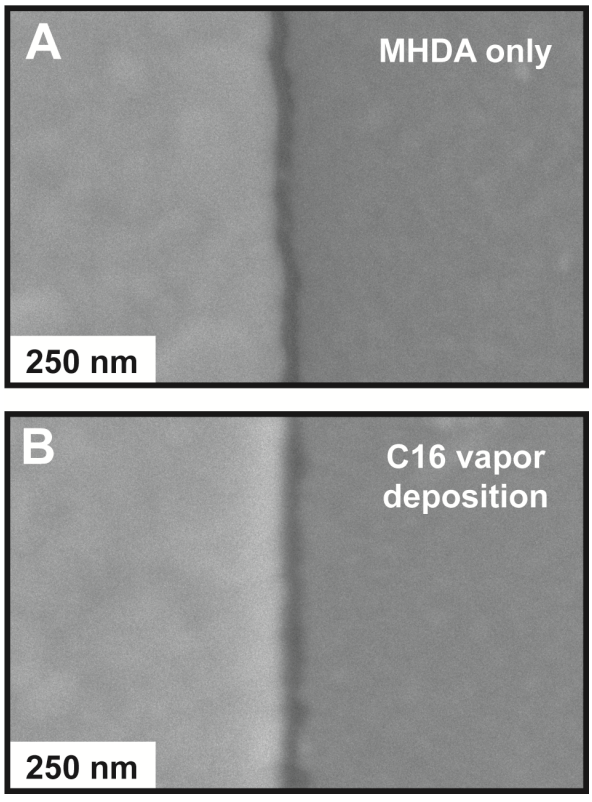

Figure 4: Nanogaps from MHDA only and MHDA with vapor-phase deposition of C16. (A) A representative SEM image of a nanogap fabricated from nine iterations of the solution deposition of MHDA and $Cu(ClO_4)_2{\cdot}6H_2O$ followed by the solution deposition of MHDA. (B) A representative SEM image of a nanogap from ten iterations of the solution deposition of MHDA and $Cu(ClO_4)_2{\cdot}6H_2O$ followed by the vapor deposition of C16. In both SEM images, the initial Au structure (100 nm thick) is on the left, and the second layer of Au (30 nm thick) is on the right.

thickness of the Cu-ligated MHDA decalayer measured via spectroscopic ellipsometry (24.8 ± 0.1 nm) and the thickness of Cu-ligated MHDA decalayers from previous studies [28].

Figure 4B shows an SEM image of the resulting nanogaps from ten iterations of the solution deposition of MHDA and $Cu(ClO_4)_2 \cdot 6H_2O$ followed by the vapor deposition of C16 at 80 °C for 1 h. Similar higher and lower intensity regions are observed and correspond to the first and second Au deposition steps. The nanogap between the two Au regions measures 31.0 ± 9.4 nm, which is both larger and exhibits greater variability than the nanogap without the C16 capping layer. The width is consistent with the thickness of a Cu-ligated MHDA decalayer with the C16 capping (31.0 ± 1.0 nm) measured via spectroscopic ellipsometry.

The standard deviations of the nanogap widths, thus the quality of the nanogaps, result from the morphologies of the Cu-ligated multilayers of MHDA only and MHDA with vapor-phase deposition of C16 (Figure S2, Supporting Information File 1). The surface morphology of the 10-layer Cu-ligated MHDA multilayer with a C16 capping layer appears rougher with protruding islands with larger cross sections when compared to the 10-layer Cu-ligated MHDA multilayer without a C16 capping layer. Although the nanogaps produced from the Cu-ligated MHDA multilayer with a C16 capping layer have somewhat larger standard deviation, these nanogaps illustrate that alternate chemical functionalities can be utilized in the molecular-ruler process.

In conclusion, Cu-ligated MHDA-C16 bilayers formed from the solution and vapor deposition of C16 have been characterized with AFM revealing varied surface morphologies. The solution deposition of C16 results in structures that exhibit protruding islands of varying heights with relatively low surface coverages. These results agree with previous AFM topographic images of solution deposited Cu-ligated MHDA-C16 bilayers [27]. The vapor deposition of C16 produces protruding islands with uniform apparent heights and relatively high surface coverages. Given the increase in surface coverage coupled with the marked decrease in roughness for C16 islands formed from the vapor-phase deposition, Cu-ligated MHDA multilayers, without and with a vapor-phase deposited C16 capping layer, were utilized to create nanogaps between Au features using the molecular-ruler process. Although the quality of the nanogaps formed using the vapor-phase deposited C16 capping layer is diminished (i.e., the standard deviation is larger) when compared to MHDA multilayers, this is a minor tradeoff considering this approach enables the utilization of molecules with alternate functionalities beyond carboxylic acid into the molecular-ruler process. Efforts to explore the underling mechanism for the increased thickness of the C16 islands and to apply this strategy to other bifunctional thiol molecules are ongoing.

Supporting Information

Supporting Information features additional AFM data and experimental details.

Supporting Information File 1

Additional experimental data.
[http://www.beilstein-journals.org/bjnano/content/supplementary/2190-4286-8-233-S1.pdf]

Acknowledgements

This work was supported by the National Science Foundation (CMMI-1536528) and a UNF Academic Affairs Faculty Development Scholarship Grant. We thank Mr. Jackson Neuman, Mr. Joel Serrano, Mr. Cameron Kilgore, Mr. Michael VanMiddlesworth, Prof. Josh Melko, and Prof. Tao Ye for helpful and insightful discussions and the UNF Materials Science and Engineering Research Facility (MSERF) for the use of equipment.

References

1. Mullen, T. J.; Srinivasan, C.; Shuster, M. J.; Horn, M. W.; Andrews, A. M.; Weiss, P. S. *J. Nanopart. Res.* **2008,** *10,* 1231–1240. doi:10.1007/s11051-008-9395-y
2. Saavedra, H. M.; Mullen, T. J.; Zhang, P.; Dewey, D. C.; Claridge, S. A.; Weiss, P. S. *Rep. Prog. Phys.* **2010,** *73,* 036501. doi:10.1088/0034-4885/73/3/036501
3. Smith, R. K.; Lewis, P. A.; Weiss, P. S. *Prog. Surf. Sci.* **2004,** *75,* 1–68. doi:10.1016/j.progsurf.2003.12.001
4. Whitesides, G. M.; Ostuni, E.; Takayama, S.; Jiang, X. Y.; Ingber, D. E. *Annu. Rev. Biomed. Eng.* **2001,** *3,* 335–373. doi:10.1146/annurev.bioeng.3.1.335
5. Kasemo, B. *Surf. Sci.* **2002,** *500,* 656–677. doi:10.1016/S0039-6028(01)01809-X
6. Mantooth, B. A.; Weiss, P. S. *Proc. IEEE* **2003,** *91,* 1785–1802. doi:10.1109/JPROC.2003.818320
7. Tirrell, M.; Kokkoli, E.; Biesalski, M. *Surf. Sci.* **2002,** *500,* 61–83. doi:10.1016/S0039-6028(01)01548-5
8. Pathem, B. K.; Claridge, S. A.; Zheng, Y. B.; Weiss, P. S. *Annu. Rev. Phys. Chem.* **2013,** *64,* 605–630. doi:10.1146/annurev-physchem-040412-110045
9. Alivisatos, A. P.; Andrews, A. M.; Boyden, E. S.; Chun, M.; Church, G. M.; Deisseroth, K.; Donoghue, J. P.; Fraser, S. E.; Lippincott-Schwartz, J.; Looger, L. L.; Masmanidis, S.; McEuen, P. L.; Nurmikko, A. V.; Park, H.; Peterka, D. S.; Reid, C.; Roukes, M. L.; Scherer, A.; Schnitzer, M.; Sejnowski, T. J.; Shepard, K. L.; Tsao, D.; Turrigiano, G.; Weiss, P. S.; Xu, C.; Yuste, R.; Zhuang, X. W. *ACS Nano* **2013,** *7,* 1850–1866. doi:10.1021/nn4012847
10. Gates, B. D.; Xu, Q. B.; Stewart, M.; Ryan, D.; Willson, C. G.; Whitesides, G. M. *Chem. Rev.* **2005,** *105,* 1171–1196. doi:10.1021/cr030076o

11. Weiss, P. S. *Acc. Chem. Res.* **2008,** *41,* 1772–1781. doi:10.1021/ar8001443
12. Johnson, S.; Evans, D.; Davies, A. G.; Linfield, E. H.; Wälti, C. *Nanotechnology* **2009,** *20,* 155304. doi:10.1088/0957-4484/20/15/155304
13. Xia, Y. N.; Rogers, J. A.; Paul, K. E.; Whitesides, G. M. *Chem. Rev.* **1999,** *99,* 1823–1848. doi:10.1021/cr980002q
14. Hatzor, A.; Weiss, P. S. *Science* **2001,** *291,* 1019–1020. doi:10.1126/science.1057553
15. Anderson, M. E.; Smith, R. K.; Donhauser, Z. J.; Hatzor, A.; Lewis, P. A.; Tan, L. P.; Tanaka, H.; Horn, M. W.; Weiss, P. S. *J. Vac. Sci. Technol., B* **2002,** *20,* 2739–2744. doi:10.1116/1.1515301
16. Anderson, M. E.; Srinivasan, C.; Hohman, J. N.; Carter, E. M.; Horn, M. W.; Weiss, P. S. *Adv. Mater.* **2006,** *18,* 3258–3260. doi:10.1002/adma.200601258
17. Anderson, M. E.; Srinivasan, C.; Jayaraman, R.; Weiss, P. S.; Horn, M. W. *Microelectron. Eng.* **2005,** *78–79,* 248–252. doi:10.1016/j.mee.2005.01.003
18. Anderson, M. E.; Tan, L. P.; Tanaka, H.; Mihok, M.; Lee, H.; Horn, M. W.; Weiss, P. S. *J. Vac. Sci. Technol., B* **2003,** *21,* 3116–3119. doi:10.1116/1.1621662
19. Srinivasan, C.; Anderson, M. E.; Carter, E. M.; Hohman, J. N.; Bharadwaja, S. S. N.; Trolier-McKinstry, S.; Weiss, P. S.; Horn, M. W. *J. Vac. Sci. Technol., B* **2006,** *24,* 3200–3204. doi:10.1116/1.2393252
20. Srinivasan, C.; Hohman, J. N.; Anderson, M. E.; Weiss, P. S.; Horn, M. W. *J. Vac. Sci. Technol., B* **2007,** *25,* 1985–1988. doi:10.1116/1.2811712
21. Srinivasan, C.; Hohman, J. N.; Anderson, M. E.; Weiss, P. S.; Horn, M. W. *Appl. Phys. Lett.* **2008,** *93,* 083123. doi:10.1063/1.2963982
22. Tanaka, H.; Anderson, M. E.; Horn, M. W.; Weiss, P. S. *Jpn. J. Appl. Phys., Part 2* **2004,** *43,* L950–L953. doi:10.1143/JJAP.43.L950
23. McCarty, G. S. *Nano Lett.* **2004,** *4,* 1391–1394. doi:10.1021/nl049375z
24. Li, C. B.; Hasegawa, T.; Tanaka, H.; Miyazaki, H.; Odaka, S.; Tsukagoshi, K.; Aono, M. *Nanotechnology* **2010,** *21,* 495304. doi:10.1088/0957-4484/21/49/495304
25. Anderson, M. E.; Mihok, M.; Tanaka, H.; Tan, L. P.; Horn, M. W.; McCarty, G. S.; Weiss, P. S. *Adv. Mater.* **2006,** *18,* 1020–1022. doi:10.1002/adma.200600108
26. McCarty, G. S.; Moody, B.; Zachek, M. K. *J. Electroanal. Chem.* **2010,** *643,* 9–14. doi:10.1016/j.jelechem.2010.03.018
27. Daniel, T. A.; Uppili, S.; McCarty, G.; Allara, D. L. *Langmuir* **2007,** *23,* 638–648. doi:10.1021/la0621719
28. Benson, A. S.; Elinski, M. B.; Ohnsorg, M. L.; Beaudoin, C. K.; Alexander, K. A.; Peaslee, G. F.; DeYoung, P. A.; Anderson, M. E. *Thin Solid Films* **2015,** *590,* 103–110. doi:10.1016/j.tsf.2015.07.048
29. Johnson, S.; Chan, J.; Evans, D.; Davies, A. G.; Wälti, C. *Langmuir* **2011,** *27,* 1033–1037. doi:10.1021/la103733j
30. Evans, S. D.; Ulman, A.; Goppert-Berarducci, K. E.; Gerenser, L. J. *J. Am. Chem. Soc.* **1991,** *113,* 5866–5868. doi:10.1021/ja00015a053
31. Freeman, T. L.; Evans, S. D.; Ulman, A. *Thin Solid Films* **1994,** *244,* 784–788. doi:10.1016/0040-6090(94)90571-1
32. Drexler, C. I.; Moore, K. B., III; Causey, C. P.; Mullen, T. J. *Langmuir* **2014,** *30,* 7447–7455. doi:10.1021/la501645w
33. Kim, Y. T.; McCarley, R. L.; Bard, A. J. *Langmuir* **1993,** *9,* 1941–1944. doi:10.1021/la00032a001
34. Woodward, J. T.; Walker, M. L.; Meuse, C. W.; Vanderah, D. J.; Poirier, G. E.; Plant, A. L. *Langmuir* **2000,** *16,* 5347–5353. doi:10.1021/la991672+

License and Terms

BEILSTEIN JOURNAL OF NANOTECHNOLOGY

Increasing the stability of DNA nanostructure templates by atomic layer deposition of Al_2O_3 and its application in imprinting lithography

Hyojeong Kim, Kristin Arbutina, Anqin Xu and Haitao Liu*

Full Research Paper

Open Access

Address:
Department of Chemistry, University of Pittsburgh, 219 Parkman Avenue, Pittsburgh, Pennsylvania 15260, United States of America

Email:
Haitao Liu* - hliu@pitt.edu

* Corresponding author

Keywords:
aluminium oxide (Al_2O_3); atomic layer deposition; DNA nanostructure; nanofabrication; nanoimprint lithography; pattern transfer; polymer stamp; replica molding

Beilstein J. Nanotechnol. **2017,** *8,* 2363–2375.
doi:10.3762/bjnano.8.236

Received: 13 June 2017
Accepted: 02 October 2017
Published: 09 November 2017

This article is part of the Thematic Series "Nanoscale patterning and characterization".

Guest Editor: S. A. Claridge

Abstract

We present a method to increase the stability of DNA nanostructure templates through conformal coating with a nanometer-thin protective inorganic oxide layer created using atomic layer deposition (ALD). DNA nanotubes and origami triangles were coated with ca. 2 nm to ca. 20 nm of Al_2O_3. Nanoscale features of the DNA nanostructures were preserved after the ALD coating and the patterns are resistive to UV/O_3 oxidation. The ALD-coated DNA templates were used for a direct pattern transfer to poly(L-lactic acid) films.

Introduction

In 1982, Seeman et al. first introduced the idea of utilizing DNA to build a mechanically robust nanostructure [1]. Since then, the field of structural DNA nanotechnology has evolved remarkably from immobile Holliday junctions to complex shapes fabricated from single-stranded tiles [2,3]. Through rational design, the self-assembly of DNA can be brought into almost any shape with nanometer-scale precision and accuracy. Examples of such structures are one-dimensional (1D) [4-7], two-dimensional (2D) [8-11] and three-dimensional (3D) [12-15] nanostructures with diverse and complex features. Therefore, self-assembled DNA nanostructures are considered to be an ideal template for nanofabrication because it is easy to control their structural complexity and diversity at the nanoscale.

Many approaches have been developed to use DNA nanostructures as templates to pattern a wide range of materials, such as proteins [16-19], carbon nanotubes [20-23] and metal nanoparticles through the direct assembly of these materials onto the DNA nanostructures [16,18,24-29]. The metallized DNA nano-

structures have been used to pattern graphene [30]. DNA nanostructures have also been used as masks. The patterns of 1D DNA nanotubes and 2D DNA arrays were replicated to metal films by metal evaporation onto the DNA nanostructures and subsequent lift-off of the metal films [31]. Aligned DNA molecular bundles became shadow masks for angled metal vapor deposition and the exposed substrate through shadow gaps was etched to generate trenches with linewidths of sub-10 nm resolution [32]. By differentiating the adsorption of water between DNA nanostructures and a SiO_2 substrate, the rates of HF vapor-phase etching of the SiO_2 substrate [33] and of chemical vapor deposition of SiO_2 and TiO_2 on the DNA nanostructures and the substrate [34] were modulated to replicate the patterns of the DNA nanostructures into those of the inorganic oxides. In both cases, the patterns of the nanostructures were transferred in both positive tone and negative tone at room temperature. Similarly, DNA nanostructures were also used in the anhydrous HF vapor etching of a SiO_2 substrate, producing positive imprints of the DNA nanostructures with sub-10 nm resolution [35]. DNA nanostructures were also converted into carbon nanostructures with shape conservation by atomic layer deposition of Al_2O_3 onto the nanostructures followed by thermal annealing [36]. In addition to the 2D pattern transfer processes, gold nanoparticles with specified 3D shapes were synthesized by growing seed particles in the internal cavities of 3D DNA nanostructures [37,38].

Compared to the above developments, there are only a limited number of studies of the use of DNA nanostructures as master templates for soft lithography. Soft lithography relies on elastomeric stamps or molds bearing fine features of relief on their surfaces to transfer patterns [39]. The spatial resolution and diverse features of the relief structures on the stamps intrinsically limit the application of soft lithography. Thus, the preparation of master templates, where the stamps are derived, has become an important research area. State-of-the-art technologies for fabrication of the master templates are deep ultraviolet lithography (DUL) and electron-beam (e-beam) lithography. However, both of these lithography techniques are not suitable to provide sub-10 nm resolution. DUL with ArF lasers (λ = 193 nm) and water immersion lenses is not able to provide a structure with spacing less than 40 nm because of its diffraction-limited resolution [40]. Although e-beam lithography is capable of reaching resolutions below 10 nm [41], it is difficult to produce the master templates in larger numbers because of its high cost [42-44]. In 2015, the aligned patterns of natural salmon milt DNA bundles were first transferred to negative replicas on unsaturated polyester resins, which were further used to pattern positive replicas on water-swollen polyacrylamide gels [45]. However, the shape of the DNA bundles is limited to 1D patterns, and their dimensions are relatively large compared to the resolution of the state-of-the-art lithographic techniques. The average height and width of the DNA bundles were 90.53 ± 3.08 nm and 878.84 ± 22.79 nm, respectively.

Taking one step further in this direction, we have recently used DNA nanostructures as master templates for a direct pattern transfer to polymers with high diversity, complexity, and fidelity [46]. A wide range of DNA nanostructures, including DNA nanotubes, 1D λ-DNA, 2D DNA brick crystals with 3D features, hexagonal DNA 2D arrays, and DNA origami triangles, were tested for the pattern replication process to poly(methyl methacrylate) (PMMA), poly(L-lactic acid) (PLLA), and photo-cross-linked acryloxy perfluoropolyether (a-PFPE). The resulting negative imprints of the DNA nanostructures on the PMMA and PLLA polymer stamps further served as molds to transfer the patterns to positive imprints on a-PFPE films. In our method, the separation of the polymer film from the DNA nanostructure master template relies on using water to lower the adhesion between the film and the template. The key advantage of our method is that any polymer with hydrophobicity and/or low surface energy can be patterned with the DNA nanostructure master template. Furthermore, because the method uses spin-coating instead of hot-pressing, it is compatible with polymers having a wide range of glass transition temperatures (T_g).

With our method, polymer stamps can be made with nanoscale features of dimensions ranging from several tens of nanometers to micrometers by logically designing and synthesizing DNA nanostructures. Our approach has one substantial technical problem, however, which is that the DNA nanostructure master templates cannot be used in a repetitive manner. The DNA nanostructures were partially damaged during the release of the PMMA and PLLA hydrophobic stamps from the hydrophilic master template. It still remains a challenge to develop an approach to increase the stability of the DNA nanostructure master templates.

In this paper, we establish a method to increase the chemical and/or mechanical stability of DNA nanostructure master templates by a nanometer-thin conformal coating of a protective inorganic oxide film grown by atomic layer deposition (ALD). We test the stability of DNA nanotube master templates with an Al_2O_3 layer against repeated pattern transfer, long-term storage and exposure to UV/O_3. The effect of the thickness of the Al_2O_3 layer on the qualities of pattern transfer and shape conservation is also explored.

Result and Discussion

A DNA nanostructure master template with a protective Al_2O_3 film and a corresponding PLLA stamp were adapted from our

previously published method [46] and the fabrication process is shown in Figure 1. DNA nanostructures were deposited onto a silicon wafer that was cleaned by piranha solution (Figure 1a). The entire surface of the DNA nanostructure master template was coated with a layer of Al_2O_3 by ALD (Figure 1b). After the ALD process, PLLA solution in dichloromethane (3 wt %) was spin-coated onto the template to prepare a PLLA film (Figure 1c). Around the edges of the silicon wafer, the PLLA film was scraped off with a blade and the silicon wafer underneath the PLLA film was revealed (Figure 1d). A polydimethylsiloxane (PDMS) film was placed on top of the PLLA film serving as a flexible backing to assist in the separation of the polymer film from the template (Figure 1e). Droplets of water were added to the exposed edges of the template, separating the hydrophobic PLLA film from the hydrophilic master template by penetration into the interface between them. After one minute, the PLLA/PDMS film was peeled off and the negative replica of the positive pattern of the DNA nanostructure master template formed on the surface of the film that was in contact with the DNA (Figure 1f).

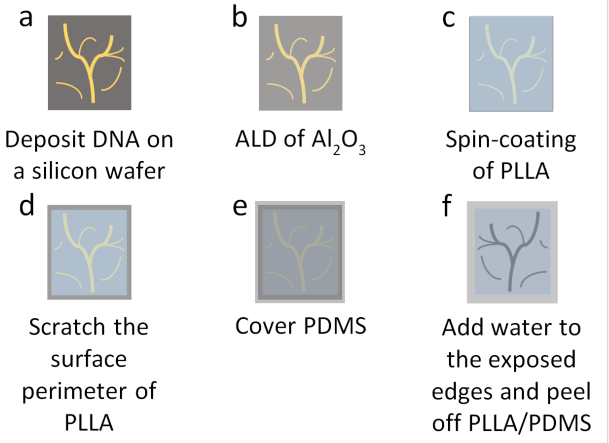

Figure 1: Fabrication process of a polymer stamp using a DNA nanostructure master template with a protective Al_2O_3 film. (a) DNA nanostructures are deposited on a silicon wafer. (b) The silicon wafer is coated with Al_2O_3 by atomic layer deposition. (c) A polymer film (e.g., PLLA) is spin-coated onto the silicon wafer. (d) The edges of the polymer film is scraped off with a blade. (e) A PDMS film is adhered to the polymer film as a backing support. (f) Droplets of water are added to the exposed edges of the silicon wafer and the PLLA/PDMS film is peeled off.

We first evaluate the fabrication process using a self-assembled DNA nanotube template. These DNA nanotubes are 30–70 nm in width and up to 60 μm in length [4]. The nanotubes are collapsed after deposition onto a silicon wafer, showing an average height (n = 10) of 3.4 ± 0.1 nm by atomic force microscopy (AFM). The surface topography of the DNA nanotube master template before (Figure 2a) and after (Figure 2b) deposition of a ca. 2 nm thick Al_2O_3 layer and the corresponding PLLA film (Figure 2c) were characterized by AFM. On the DNA nanotube master template, single DNA nanotubes are observed along with some bundles. After the PLLA stamp was peeled off, the negative replicas of the DNA nanotubes were observed on the polymer stamp, demonstrating a faithful replication process. To quantify the degree of conservation of the surface topography, height/depth and full width at half maximum (FWHM) were measured in four different locations in the AFM images and compared at the same locations throughout the fabrication process (Figure 2f,g). Taking location 1 as an example, the height of the DNA nanotube before (3.73 nm) and after (3.39 nm) the ALD of the Al_2O_3 film was in good agreement with the average depth of the trench (3.32 nm, measured three times at location 1 over a 15 day period) on the PLLA stamp. The FWHM of the nanotube (46.99 nm) slightly decreased after the ALD (41.14 nm) but was significantly larger than the average FWHM of the trench (23.50 nm) on the polymer stamp. The decrease of the FWHM after the ALD is suspected to be due to the dehydration of the nanotube during the ALD process and/or the differences in the probe–sample interactions of the individual AFM tips, which can give different measurements of the same sample. We attribute the decrease in the FWHM from the DNA nanotube master template to the PLLA stamp to the AFM probe convolution effect. These results confirm a faithful pattern transfer from the DNA nanotube master template to the PLLA stamp through the ALD of the Al_2O_3 layer on the template with high fidelity. Moreover, the patterned PLLA stamp was found to be stable at room temperature. We stored the stamp in a plastic petri dish and imaged it again after 1 week (Figure 2d) and 2 weeks (Figure 2e) at the same location. Both the depth and FWHM of the trenches along with cross-sectional analysis on the PLLA stamp at the four locations remained consistent, demonstrating the long-term stability of the PLLA stamp.

As mentioned earlier, the most critical challenge of using the DNA master template without a protective film is the damage of DNA during the separation of the polymer film from the template [46]. We attribute such damage to the water we used to assist the separation. The DNA nanostructures were still damaged even if we replaced the water with the buffer solution that was used to synthesize and store the DNA nanostructures (Figure S1, Supporting Information File 1). To evaluate the effectiveness of the protective Al_2O_3 film on the DNA master template, we imaged the DNA nanostructures in the same location after deposited on a silicon wafer, after 20 cycles of ALD of Al_2O_3, and after 1st, 2nd, 3rd, 4th and 5th replication to PLLA stamps (Figure 3a–g and Figure S2a–f, Supporting Information File 1). As the AFM images indicate, the surface morphology of the DNA template was still well maintained after the 1st pattern transfer (Figure 3c and Figure S2b, Supporting Infor-

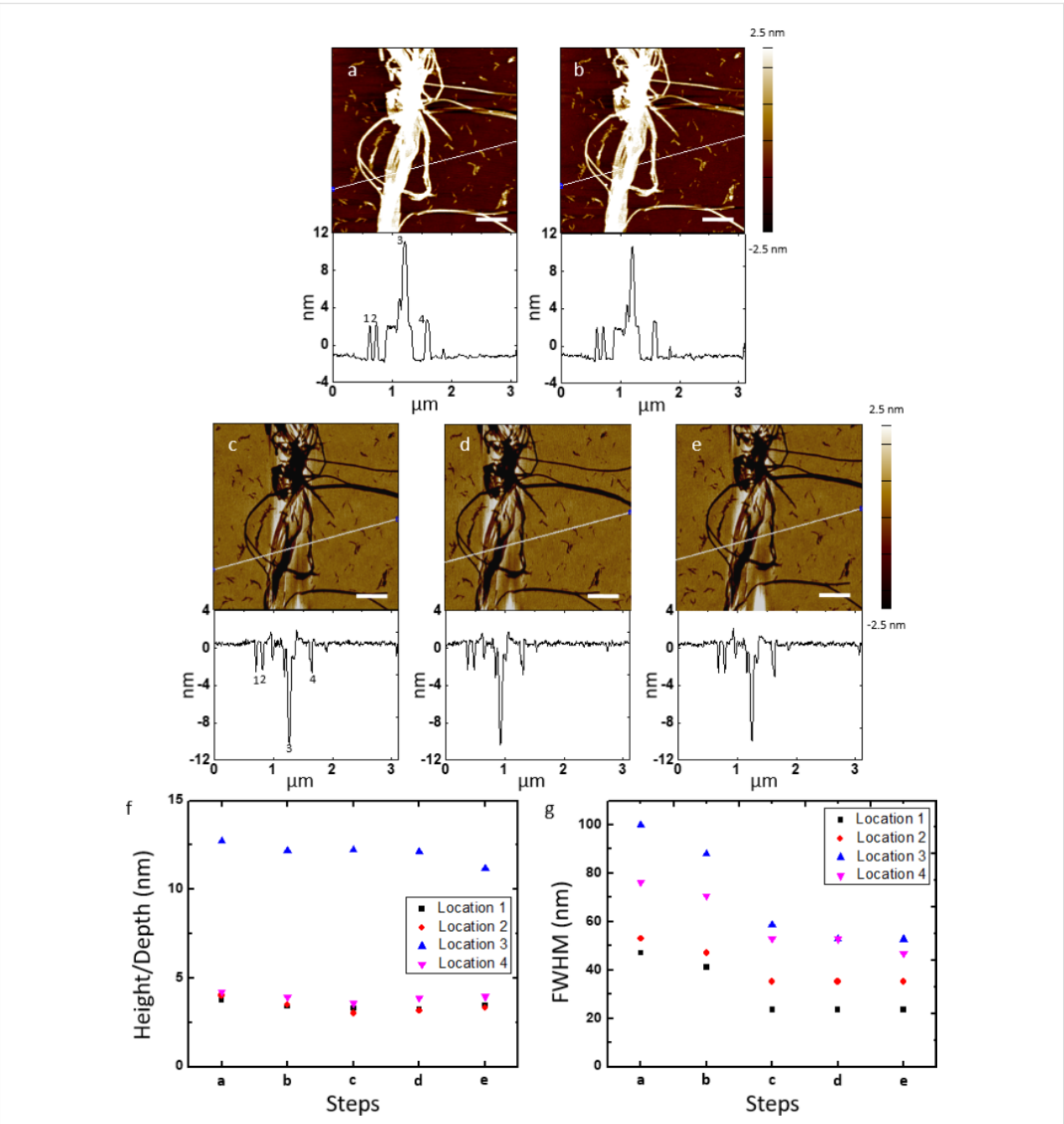

Figure 2: Comparison of features on a DNA nanotube master template with a ca. 2 nm thick Al_2O_3 film and a PLLA stamp, and stability of features on a PLLA stamp of the same area. AFM height images and corresponding cross-sectional analysis of DNA nanotubes after (a) deposited on a silicon wafer and (b) 20 cycles of ALD of Al_2O_3 (ca. 2 nm of Al_2O_3 film), and the negative replicas on a PLLA stamp imaged (c) 1, (d) 8, and (e) 15 days after pattern transfer of the same area. White lines on the AFM images indicate where the cross-sections were determined. (f) Height/depth and (g) FWHM of the DNA nanotubes and their replica trenches in four different locations of the AFM images from (a) to (e). Locations 1, 2, 3, and 4 correspond to 1, 2, 3, and 4 in the cross-sections of the AFM images (a) and (c). Scale bars represent 500 nm. Note: The AFM images from (c) to (e) are mirror-flipped to match the orientations of the AFM images (a) and (b).

mation File 1), showing that the stability of the nanostructures was increased by the ca. 2 nm thick Al_2O_3 film. However, as the replication process was repeated another four more times, the overall height of the DNA nanostructures decreased although their shape was unchanged. To highlight the change in the height of the DNA nanostructures, we plot the height distribution of the AFM images in Figure 3i and Figure S3 (Supporting Information File 1). The height difference between the absolute maximum peak (which represents the background silicon wafer) and the next relative maximum peak (which

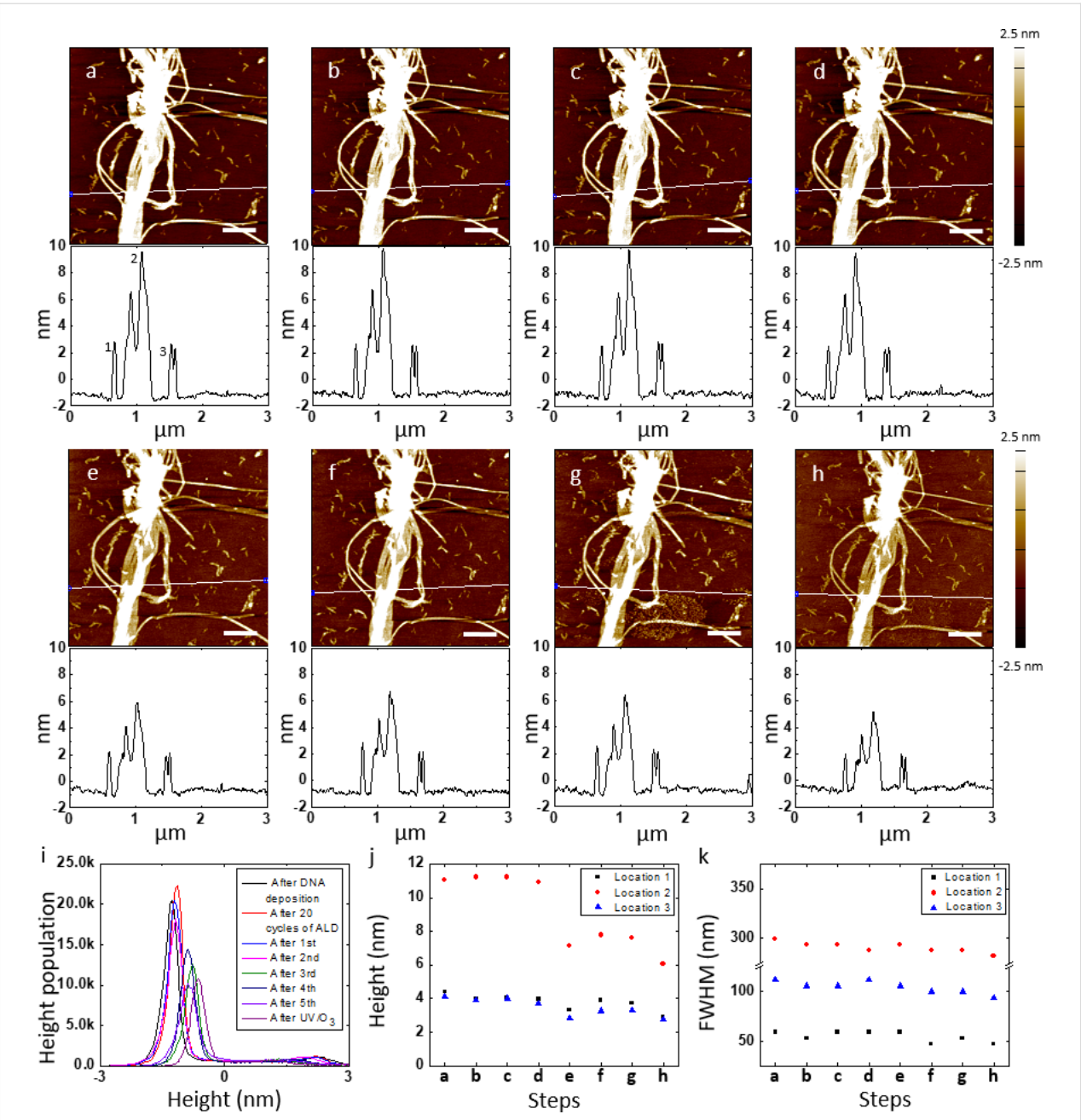

Figure 3: Stability of a DNA nanotube master template with a ca. 2 nm thick Al_2O_3 film for multiple pattern transfers to PLLA stamps. AFM height images and corresponding cross-sectional analysis of DNA nanotubes in the same location after (a) deposited on a silicon wafer, (b) 20 cycles of ALD of Al_2O_3, (c) 1st, (d) 2nd, (e) 3rd, (f) 4th, and (g) 5th pattern transfer to PLLA stamps, and (h) UV/O_3 treatment for 1 h and washing with DI water. White lines on the AFM images indicate where the cross-sections were determined. (i) Histograms of the AFM height images from (a) to (h). (j) Height and (k) FWHM of the DNA nanotubes in three different locations of the AFM images from (a) to (h). Locations 1, 2, and 3 correspond to 1, 2, and 3 in the cross-section of the AFM image (a). Scale bars represent 500 nm. Note: The DNA master template was contaminated before the 5th spin coating of PLLA in dichloromethane solution. The AFM images (a) and (b) are also shown in Figure 2. The enlarged version of the histograms in (i) is available in Figure S3 (Supporting Information File 1).

represents the height of the DNA nanotubes) significantly decreased during the 3rd replication process. The height and FWHM with cross-sectional analysis of the DNA template at the three same locations further support the change in the height of the template (Figure 3j,k). The FWHM at all three locations was comparable during the 3rd replication process. The height of the DNA nanotube bundle decreased from 10.90 nm to 7.12 nm, while the height of the single DNA nanotubes decreased from 3.97 nm and 3.70 nm to 3.32 nm and 2.85 nm, respectively. These results indicate that the higher feature (de-

crease of ca. 35% of its initial height) on the template is less mechanically stable than the lower one (decrease of ca. 15% of its initial height). Along this direction, holes were also formed after the 2nd and 5th pattern transfer to the PLLA stamps, highlighted by the yellow arrows (Figure S2c,f, Supporting Information File 1). The AFM height and phase images with cross-sectional analysis of the hole after the 5th pattern transfer show that the depth of the hole matched well to the thickness of the Al_2O_3 layer and the bundle of the DNA nanotubes originally presented in the hole was removed, possibly by the water used during the separation of the stamp (Figure S2h,i, Supporting Information File 1). Overall, the protective 2 nm Al_2O_3 layer marginally increases the stability of the DNA nanostructures.

Being able to clean the master template is also important for its repeated use. During the five times of the pattern transfer to the PLLA stamps, the surface of the DNA master template was contaminated with polymer residues (see Figure 3g, lower middle area). To verify whether the polymer residues on the DNA master template can be removed with UV/O_3 treatment, the template after the 5th replication process was subjected to UV/O_3 cleaning for an hour, washed with deionized (DI) water, and dried with N_2 gas (Figure 3h and Figure S2g, Supporting Information File 1). The AFM images before and after the treatment show that the morphology of the DNA template was not altered while the polymer residues were removed. The height difference between the absolute maximum peak and the next relative maximum peak in the histogram of the AFM image, however, significantly decreased from 2.28 nm to 1.69 nm (Figure 3i and S3). The height of the DNA nanotubes at three different locations decreased from 3.72 nm, 7.58 nm, and 3.29 nm to 2.87 nm, 6.07 nm, and 2.78 nm, respectively (Figure 3j). The FWHM at these locations also decreased from 52.88 nm, 287.94 nm, and 99.89 nm to 46.98 nm, 281.87 nm, and 93.96 nm, respectively (Figure 3k). These results suggest that although the UV/O_3 treatment is able to eliminate the organic residues on the surface of the master template, the DNA nanostructures beneath the 2 nm of Al_2O_3 coating are likely damaged by the oxidation by O_3.

The long-term stability of the ALD-coated template was also studied. We kept the template in a plastic petri dish that was stored in a common lab bench drawer for 40 days. AFM images with corresponding cross-sectional analysis were scanned in the same location of the template at the beginning and the end of this period (Figure S4a,b, Supporting Information File 1). Not surprisingly, the 40 days of aging in air did not alter the surface topography of the DNA nanostructure master template. While the height of the DNA nanotubes at four different locations remained consistent (Figure S4c, Supporting Information File 1), the FWHM at these locations slightly decreased (Figure S4d, Supporting Information File 1). We speculate that the decrease in the FWHM results from the differences between the AFM probe convolution effects of the individual tips because the decreases are similar to the resolution limit of the AFM image (i.e., one or two pixels in the AFM images). At room temperature, solid-state DNA undergoes degradation and/or aggregation within 30 days when it is exposed to atmospheric water and oxygen [47,48]. Compared to DNA, which is a soft material, Al_2O_3 is much more stable and robust. Through the conformational coating of Al_2O_3, the shelf life of the DNA nanotubes is assumed to be increased while maintaining their morphology longer than the nanotubes without a protective film. Overall, the 20 cycles of ALD of Al_2O_3 allow the DNA nanostructure master template to possess enough chemical stability for long-term storage.

The ca. 2 nm thick Al_2O_3 layer increased the mechanical stability of the DNA nanotube master template only to a limited extent. To verify whether the mechanical stability of the template can be strengthened with the increased thickness of the Al_2O_3 layer while preserving its nanoscale morphology, a ca. 5 nm thick Al_2O_3 layer was deposited onto the template, and the reusability and morphology conservation were evaluated. The DNA nanostructures in the same location were scanned with AFM after deposition on a silicon wafer, 50 cycles of ALD of Al_2O_3, 1st and 5th replication to PLLA stamps, and exposed to UV/O_3 treatment, washed with DI water, and dried with N_2 gas (Figure 4a–e and Figure S5a–c, Supporting Information File 1). Throughout each stage of the fabrication process, we analyzed the height difference between the absolute maximum peak and the next relative maximum peak in the histogram and height and FWHM at four different locations; all these data showed little change throughout the fabrication process (Figure 4f–h and Figure S6, Supporting Information File 1). The ca. 5 nm thick Al_2O_3 film is impermeable to O_3 and protects the underlying DNA nanostructures against the UV/O_3 oxidation. Also, no holes due to the breakage of the protective Al_2O_3 film were found, demonstrating that the both chemical and mechanical stabilities of the DNA nanostructure master template improve with a thicker Al_2O_3 layer. The direct comparison of the height differences between the maximum peaks of the histograms of the 20 and 50 cycles of ALD of Al_2O_3 through the multiple pattern transfer clearly shows the increased stability of the ca. 5 nm thick Al_2O_3 film compared to the ca. 2 nm thick film (Figure 5). We note that the polymer residue was not observed on the surface of the DNA nanotube master template with the ca. 5 nm thick Al_2O_3 film even after the 5th replication. The surface roughness of Al_2O_3 film grown using ALD slowly increases as the number of cycles goes up [49]. Therefore, it does not cause the reduced polymer adsorption on the 5 nm thick Al_2O_3 film. Further study is needed to

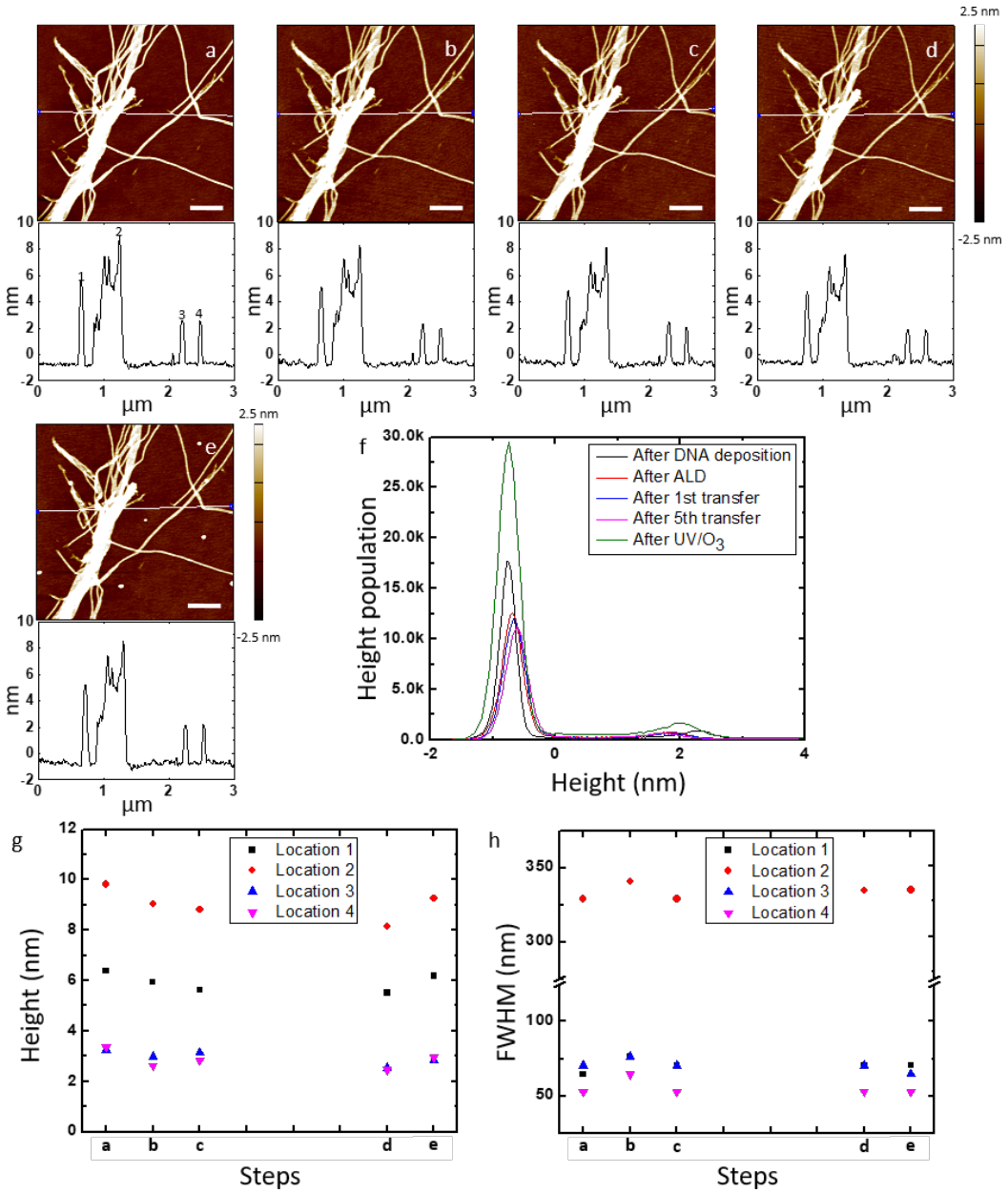

Figure 4: Stability of a DNA nanotube master template with a ca. 5 nm thick Al_2O_3 film for multiple pattern transfers to PLLA stamps. AFM height images and corresponding cross-sectional analysis of DNA nanotubes in the same location after (a) deposited on a silicon wafer, (b) 50 cycles of ALD of Al_2O_3, (c) 1st and (d) 5th pattern transfer to PLLA stamps, and (e) UV/O_3 treatment for 1 h and washing with DI water. White lines on the AFM images indicate where the cross-sections were determined. (f) Histograms of the AFM height images from (a) to (e). (g) Height and (h) FWHM of the DNA nanotubes in four different locations of the AFM images from (a) to (e). Locations 1, 2, 3, and 4 correspond to 1, 2, 3, and 4 in the cross-section of the AFM image (a). Scale bars represent 500 nm. Note: The enlarged version of the histograms in (f) is available in Figure S6 (Supporting Information File 1).

elucidate the difference between the 2 nm and 5 nm of Al_2O_3 films.

The DNA nanotubes tested above are simple one-dimensional linear structures. To evaluate the effectiveness of a protective conformational coating on complex patterns, DNA origami triangle nanostructures were employed as the master templates for the pattern transfer to the PLLA stamp. The DNA origami triangle is a single layer of DNA double strands and has a theoretical height of 2 nm (Figure S7, Supporting Information File 1) [8]. The triangle consists of three trapezoidal domains formed by folding an M13mp18 scaffold strand with short synthetic staple strands. Among the three trapezoidal domains, one has a dangling loop. These domains are further connected to each

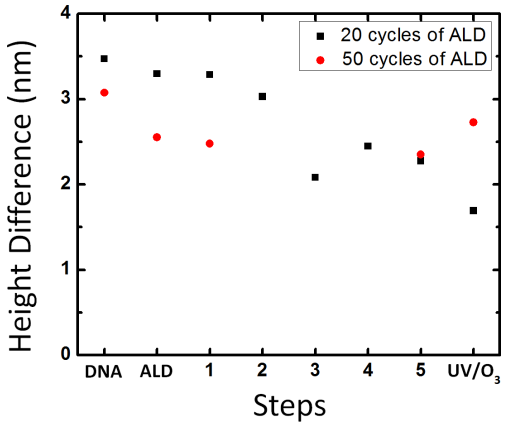

Figure 5: Comparison of the height differences between the maximum peaks of the histograms in Figure 3i and 4f.

other by bridging the edges of the domains with the staple strands. There are three holes at each of the vertex and one large triangular hole in the center of the DNA origami triangle. AFM images show that the three holes at the vertex, the central triangular hole, and the dangling loop were clearly visible before and after ALD, and after replication process with both ca. 2 nm and ca. 5 nm thick Al_2O_3 layers (Figure 6a,b,d). Through these steps, the three holes at the vertex were frequently seen as a linear gap and the depth of the holes or the linear gap was much smaller than the height of the nanostructures due to the limited resolution of the AFM images. The vertex with the holes or the linear gap was highlighted by the blue dots (Figure S8d and Figure S9d, Supporting Information File 1). The dangling loop was also highlighted by the yellow arrows (Figure S8a,d and Figure S9a,d, Supporting Information File 1). The loop might not be seen in some DNA origami triangles if the loops were folded above or beneath the DNA structures. According to the

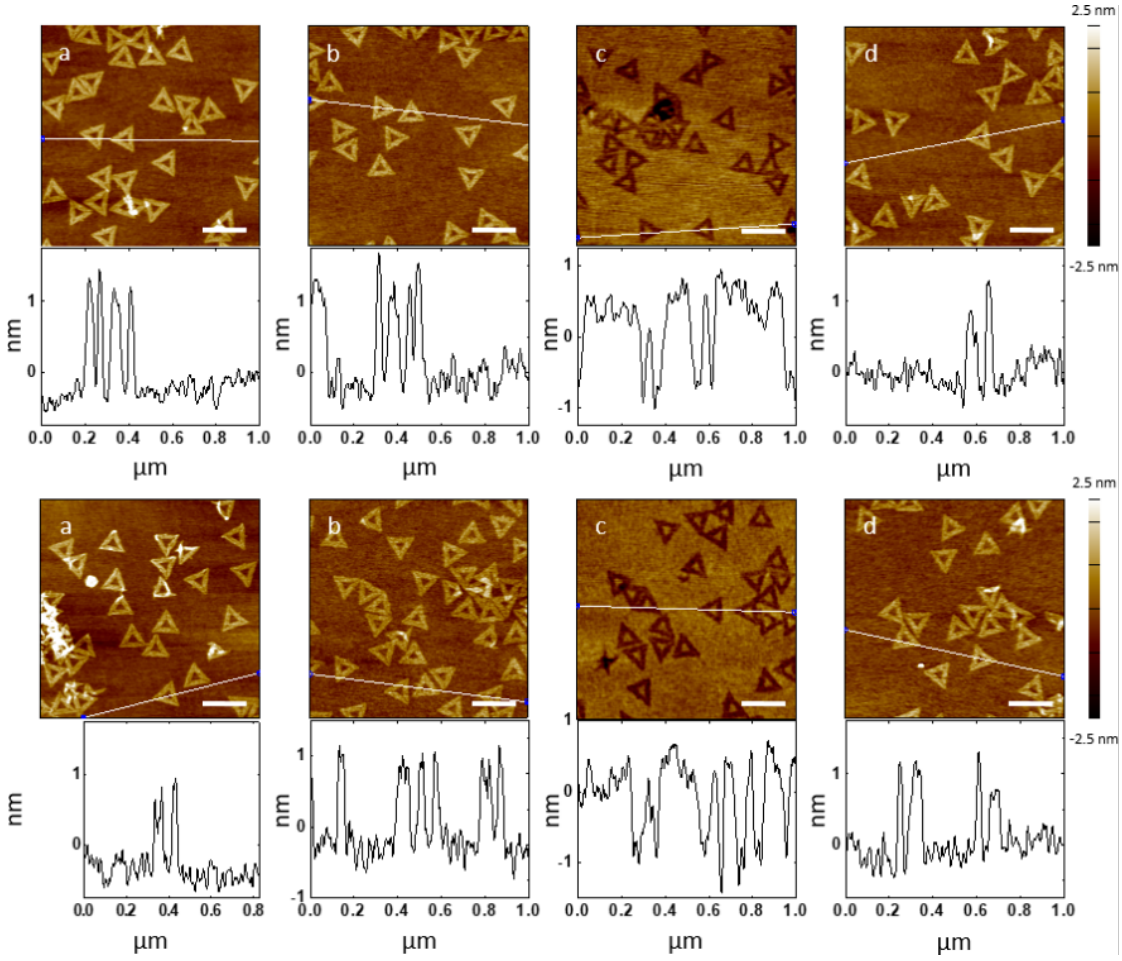

Figure 6: Comparison of features on DNA origami triangle master templates with a ca. 2 nm or a ca. 5 nm thick Al_2O_3 layer and PLLA stamps. AFM height images and corresponding cross-sectional analysis of origami triangles after (a) deposited on silicon wafers, (b) 20 cycles (top) or 50 cycles (bottom) of ALD of Al_2O_3, and (d) pattern transfer to PLLA stamps, and (c) their negative replicas on the PLLA stamps. White lines on the AFM images indicate where the cross-sections were determined. Scale bars represent 200 nm.

cross-sectional analysis of the AFM images, the average height, FWHM, inner length and outer length of the DNA origami triangles remained comparable throughout the replication process including the ALD (Figure 7). All these results prove that the protective Al_2O_3 film successfully preserves the surface morphology of the complex DNA origami triangle nanostructures.

After the replication process, triangular trenches resembling the shape of the DNA origami triangles were formed on the PLLA films (Figure 6c). Compared to the dimensions of the DNA triangles with the protective layers on the templates, the average depth of the trenches remained consistent with the average height of the triangles (Figure 7a). Due to the AFM probe convolution, however, the average outer length (the edge length of the trench measured outside of the triangle) and FWHM of the triangular trenches decreased and the average inner length of the trenches increased (Figure 7b–d). Both the patterns corresponding to the dangling loop and the three holes at the vertex were transferred to the PLLA stamps, but they were difficult to find in the trenches compared to the original features on the templates (Figure S8b,c,e and Figure S9b,c,e, Supporting Information File 1). The parts of the trench responsible for the three holes at the vertex and the dangling loop were also highlighted by the blue dots and the yellow arrows, respectively (Figure S8c,e and Figure S9c,e, Supporting Information File 1). On the PLLA stamps, the holes or the linear gap between the trapezoidal domains of the DNA origami triangles are replicated as a small bump at the vertex of the triangular trenches. The height of the bump, however, never reaches the height of the DNA origami triangles and the bump was frequently not observed in some trenches, as the bump on the PLLA stamp peeled off from the DNA origami triangle master template without the protective film. We attribute these observations to the mechanical instability of the bumps during the scanning with AFM and/or the intrinsic limitation of the resolution of the pattern transfer [46]. In the latter case, the large PLLA molecule may not be able to completely fill the nanometer-sized holes in the DNA origami triangles during the spin-coating process. A decrease in the feature size of the DNA nanostructure appears to result in height decrease and/or lost features in the polymer stamp. Overall, the PLLA film is capable of replicating the overall features of the complex DNA origami triangles with high fidelity and the local features below ca. 5 nm only to some extent even

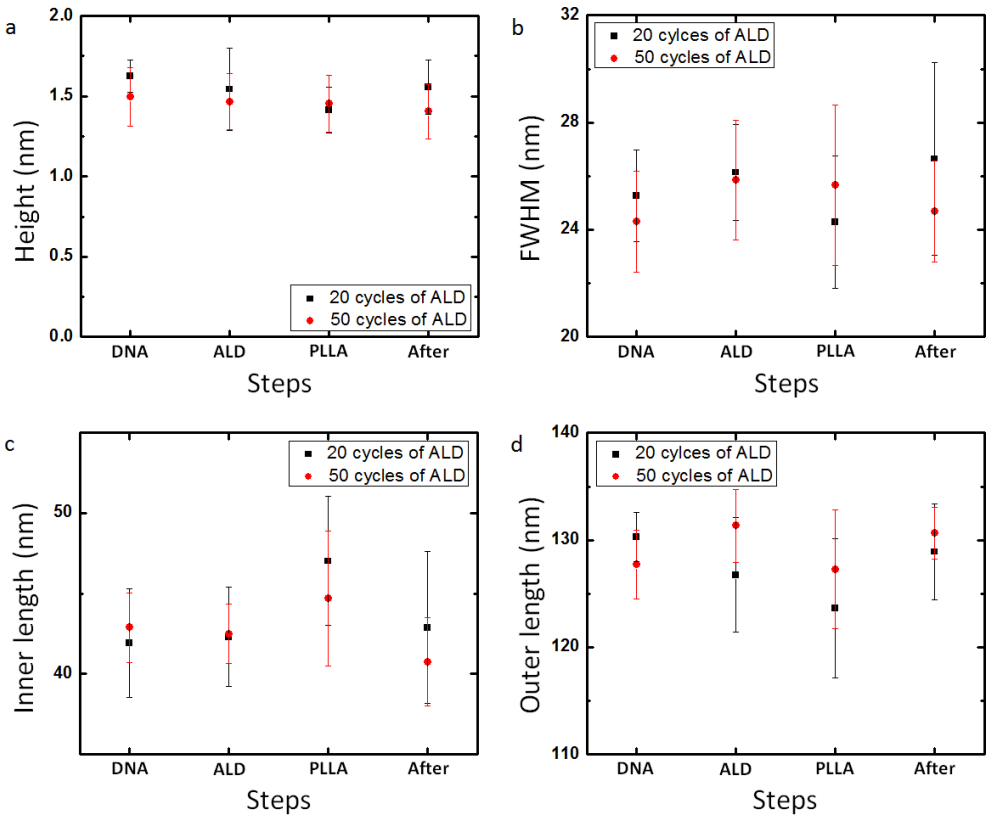

Figure 7: Average (a) height, (b) FWHM, (c) inner length, and (d) outer length (n = 10) of features on DNA origami triangle master templates with a ca. 2 nm or ca. 5 nm of Al_2O_3 layer and PLLA stamps at each step of fabrication process, after (DNA) DNA origami triangles were deposited on a silicon wafers, (ALD) ALD of Al_2O_3, and (After) pattern transfer to PLLA stamps, and (PLLA) their negative replicas on the PLLA stamps.

with the presence of the protective ca. 2 nm or ca. 5 nm thick Al_2O_3 layers.

Finally, we investigated how the surface morphology of the DNA nanostructures was influenced as the thickness of the protective Al_2O_3 film was further increased. We coated both the DNA nanotube (Figure S10a,b, Supporting Information File 1) and the DNA origami triangle (Figure S10c,d, Supporting Information File 1) master templates with ca. 20 nm thick Al_2O_3 layers and compared their AFM images before (Figure S10a,c, Supporting Information File 1) and after (Figure S10b,d, Supporting Information File 1) 200 cycles of ALD. With the ca. 20 nm thick Al_2O_3 film, the DNA nanotubes were still visible and the FWHM stayed consistent (Figure S10b,f, Supporting Information File 1). The height of the DNA nanotubes, however, considerably decreased from 3.83 nm, 9.36 nm, 3.85 nm, and 3.94 nm to 1.54 nm, 2.81 nm, 1.66 nm, and 1.71 nm, respectively (Figure S10e, Supporting Information File 1). In case of the DNA origami triangles, the DNA nanostructures with the average height of 1.68 nm (n = 10) were barely seen and the height profile along the individual DNA triangles also showed the significant increase of roughness (Figure S10d, Supporting Information File 1). These results indicate that there is a limit to the thickness of the protective Al_2O_3 film deposited by ALD to maintain the nanoscale feature of the DNA nanostructure on the template.

Conclusion

We have reported a method to increase the stability of DNA nanostructure master templates through the conformal growth of an inorganic oxide film by ALD and demonstrated its usefulness in soft lithography patterning of polymer films. DNA nanotubes and origami triangles with Al_2O_3 films of ca. 2 nm, ca. 5 nm or ca. 20 nm thickness have been tested as the master templates to imprint their nanoscale features to PLLA films. As the thickness of the Al_2O_3 coating grows, the mechanical and/or chemical stability increases while some of the nanoscale features of the DNA nanostructures are lost. Based on our results, the conformational coating of the ca. 5 nm thick Al_2O_3 layer to the DNA nanostructures provides a good compromise between increasing the stability and maintaining the nanoscale feature of the master template for repeated use in soft lithography. In addition, the ca. 5 nm thick Al_2O_3 layer offered good protection to the underlying DNA nanostructures from exposure to UV/O_3. Although our study focused on the ALD of Al_2O_3, other metals, metal oxides, or inorganic oxides can also be used as long as they can be conformally coated at a temperature below 250 °C. Above 250 °C, the degradation of DNA nanostructures deposited onto silicon wafers starts to occur although the decomposition residue may still maintain their nanoscale features [50,51]. The conformal protective film significantly improves the chemical and mechanical stabilities of DNA nanostructures, allowing them to be used in environments that are incompatible with pristine DNA nanostructures.

Experimental

Materials

Silicon wafers [Si(110), with native oxide] and M13mp18 scaffold strands for DNA origami triangles were purchased from University Wafers (South Boston, MA, USA) and Bayou Biolabs (Metairie, LA, USA), respectively. Staple strands for the DNA origami triangles and strands for DNA nanotubes were synthesized by Integrated DNA Technologies (Coralville, IA, USA). 2-Amino-2-(hydroxymethyl)-1,3-propanediol (Tris), ethylenediaminetetraacetic acid (EDTA), magnesium acetate tetrahydrate, sulfuric acid, hydrogen peroxide solution (30% H_2O_2), and poly(L-lactide) were purchased from Sigma-Aldrich (St. Louis, MO, USA). Acetic acid (glacial), dichloromethane, and ethanol were purchased from Fisher Scientific (Fair Lawn, NJ, USA), Acros Organics (Fair Lawn, NJ, USA), and Decon Laboratories, Inc. (King of Prussia, PA, USA), respectively. PDMS backing stamp was fabricated with Sylgard 184 silicone elastomer kit (Dow Corning, Midland, MI, USA). All materials were used as received. High-purity water (18.3 MΩ) was used throughout the entire experiment by using a Barnstead MicroPure Standard water purification system (Thermo Scientific, Waltham, MA, USA).

Preparation of a silicon wafer

A silicon wafer with a native oxide layer was cleaned by hot piranha solution [7:3 (v/v) concentrated H_2SO_4/30% H_2O_2]. After H_2O_2 was slowly added to concentrated H_2SO_4 in a glass petri dish containing the silicon wafer, a glass cover was placed and a heating plate was set to 40 °C. After 20 min, the heating plate was turned off and the piranha solution was allowed to cool down for an additional 10 min. The wafer was thoroughly washed with deionized water and dried with N_2 gas. Warning: Piranha solution is a strong oxidizing reagent and reacts violently with organic materials. All work should be handled in a fume hood with extra caution. Proper protective equipment is required.

Preparation and deposition of DNA nanotubes on a silicon wafer

The synthesis and assembly of DNA nanotubes followed a previously published procedure [4]. Single strands of DNA nanotubes were diluted to a final concentration of 1 μM in 10 × TAE/Mg^{2+} buffer (125 mM Mg^{2+}). The DNA single strand solution was slowly cooled from 95 to 23 °C over 2 days and stored at 4 °C overnight. Annealed DNA nanotubes were assembled on a clean silicon wafer by incubating the DNA nanotube solution on the wafer for a minimum of 15 min in a

humid chamber to minimize the evaporation of the buffer solution. The sample was dried with N_2 gas, immersed in ethanol/water [9:1 (v/v)] solution for 10 s to remove ionic salt residue from the buffer solution, and re-dried with N_2 gas. After the deposition, the DNA nanotube master template was processed with ALD of Al_2O_3 within 24 h.

Preparation and deposition of DNA origami triangles on a silicon wafer

DNA origami triangles were synthesized and assembled following a formerly reported method [8]. M13mp18 scaffold strands (8.6 μL, 1.6 nM) were thoroughly mixed with a desired set of synthetic 232 short staple strands (15 μL, 16 nM), deionized water (77 μL), and TAE/Mg^{2+} buffer solution (181 μL). The buffer solution was prepared by dissolving Trizma base (40 mM), EDTA (2 mM), acetic acid (2mM), and magnesium acetate tetrahydrate (150 mM) in deionized water and further diluting the solution to make the final concentration of magnesium ions 12.5 mM. The DNA solution was cooled from 95 to 20 °C at a rate of 1 °C/min. After the annealing, excess staple strands were removed by purifying 140 μL of the DNA origami triangle solution using 500–600 μL of the TAE/Mg^{2+} buffer in a Microcon YM-100 100 kDa MW centrifuge filter (Millipore, Billerica, MA, USA) on a single-speed benchtop Galaxy Ministar microcentrifuge (VWR, Radnor, PA, USA) until the final volume of the DNA origami triangle solution was the same as before the purification. The rinsing process was repeated two more times.

DNA origami triangles were assembled on a clean silicon wafer by incubating the purified DNA solution on the wafer for a minimum of 15 min in a humid chamber to minimize the evaporation of the buffer solution. The sample was dried with N_2 gas, immersed in ethanol/water [9:1 (v/v)] solution for 3 s to remove ionic salt residue from the buffer solution, and re-dried with N_2 gas. After the deposition, the DNA origami triangle master template was processed with ALD of Al_2O_3 within 24 h.

Atomic layer deposition (ALD) of Al_2O_3 as a protective inorganic film on a DNA master template

ALD of Al_2O_3 on a DNA/SiO_2 substrate followed a previously published method [36]. ALD was conducted using a Fiji ALD system by Norman Gottron in Nanofabrication Facility at Carnegie Mellon University (Ultratech/CNT, Waltham, MA, USA). Chamber and substrate heaters were set to 200 °C. Total Ar gas flow was at 260 sccm and 200 mTorr. Trimethylaluminum (TMA) and H_2O were used as precursors and one ALD cycle consisted of a 0.06 s long TMA pulse, a 10 s long interval, a 0.06 s long H_2O pulse and a 10 s long interval. Deposition was looped 20 times, 50 times, and 200 times for the 2 nm, 5 nm, and 20 nm preset deposition thickness of the oxide films, respectively.

Preparation of a PDMS backing film

PDMS precursor was mixed with curing agent at a 9:1 (v/v) ratio. The prepolymer mixture was vigorously stirred by hand at least for 5 min and degassed in a vacuum desiccator. The mixture was poured over a piranha cleaned silicon wafer. The wafer with the mixture was placed in the vacuum desiccator for further degassing. The PDMS prepolymer on the silicon wafer was cured for 1 hour at 60 °C. The thickness of the resulting PDMS layer was 1–2 mm.

Fabrication of a PLLA stamp using a DNA nanostructure master template with a protective Al_2O_3 film

PLLA stamps were fabricated following our previously demonstrated procedure [33]. PLLA in dichloromethane solution (3 wt %) was spin-coated four times onto a DNA nanostructure master template with an Al_2O_3 film at 4000 rpm for 30 s. Around the border of PLLA film surface, the surface perimeter of the PLLA film with the widths of ca. 1 mm were scraped off to expose the underlying template. A PDMS stamp with a thickness of ca. 1–2 mm was placed on top of the PLLA film as a backing stamp. Droplets of water were added to the exposed edges of the template. If the water droplets filled out the interface between the PLLA film and the PDMS backing stamp, they were removed using a paper wiper to increase the adhesion between the polymer film and the backing stamp. After a minute, the PLLA/PDMS film was peeled off and the surface of the PLLA film was gently dried with N_2.

UV/Ozone treatment

A DNA nanotube master template with an Al_2O_3 film was placed in a PSD Pro 4 Digital UV Ozone Cleaner (Novascan Technologies, Inc., Ames, IA, USA). Before UV irradiation, the chamber was flushed with O_2 for 3 min, and the sample was subjected to UV/O_3 treatment for 60 min at room temperature.

Characterization methods

Ellipsometry: The experimental thickness of an Al_2O_3 film was measured by an Alpha-Spectroscopic Ellipsometer with Complete Ease Software using Cauchy model (JA Woollam Co., Lincoln, NE, USA). Duration time was “Standard” and the measurement angle was 70°. For each sample, the average thickness of the Al_2O_3 layer was obtained by measuring the thickness with MSE values below 5 at five different locations.

Atomic Force Microscopy: The surface morphologies of a DNA nanostructure master template and a PLLA stamp at each step of fabrication process were imaged using tapping-mode on

an MFP-3D atomic force microscope with RTESPA-300, NSC15/Al BS, or SSS-FMR-SPL AFM probes in air at room temperature (Oxford Instruments Asylum Research, Inc., Santa Barbara, CA, USA). The RTESPA-300 (300 kHz, 40 N/m) and NSC15/AL BS (325 kHz, 40 N/m) AFM probes were purchased from Bruker (Camarillo, CA, USA) and MikroMasch (Lady's Island, SC, USA), respectively, and used to scan the DNA nanotube master templates and the corresponding PLLA stamps. The SSS-FMR-SPL AFM probe (75 kHz, 2.8 N/m) was purchased from NanoAndMore USA (Watsonville, CA, USA) and was used to scan the DNA origami triangle master templates and the corresponding PLLA stamps.

Supporting Information

Supporting Information File 1

Additional experimental data.
[http://www.beilstein-journals.org/bjnano/content/supplementary/2190-4286-8-236-S1.pdf]

Acknowledgements

H. L. acknowledges partial support from the NSF (CHE-1507629) and University of Pittsburgh CRDF fund.

References

1. Seeman, N. C. *J. Theor. Biol.* **1982,** *99,* 237–247. doi:10.1016/0022-5193(82)90002-9
2. Seeman, N. C. *Annu. Rev. Biochem.* **2010,** *79,* 65–87. doi:10.1146/annurev-biochem-060308-102244
3. Zhang, F.; Nangreave, J.; Liu, Y.; Yan, H. *J. Am. Chem. Soc.* **2014,** *136,* 11198–11211. doi:10.1021/ja505101a
4. Liu, H.; Chen, Y.; He, Y.; Ribbe, A. E.; Mao, C. *Angew. Chem., Int. Ed.* **2006,** *45,* 1942–1945. doi:10.1002/anie.200504022
5. Rothemund, P. W. K.; Ekani-Nkodo, A.; Papadakis, N.; Kumar, A.; Fygenson, D. K.; Winfree, E. *J. Am. Chem. Soc.* **2004,** *126,* 16344–16352. doi:10.1021/ja044319l
6. Tian, C.; Zhang, C.; Li, X.; Hao, C.; Ye, S.; Mao, C. *Langmuir* **2014,** *30,* 5859–5862. doi:10.1021/la402326b
7. Yin, P.; Hariadi, R. F.; Sahu, S.; Choi, H. M. T.; Park, S. H.; LaBean, T. H.; Reif, J. H. *Science* **2008,** *321,* 824–826. doi:10.1126/science.1157312
8. Rothemund, P. W. K. *Nature* **2006,** *440,* 297–302. doi:10.1038/nature04586
9. He, Y.; Chen, Y.; Liu, H.; Ribbe, A. E.; Mao, C. *J. Am. Chem. Soc.* **2005,** *127,* 12202–12203. doi:10.1021/ja0541938
10. Wei, B.; Dai, M.; Yin, P. *Nature* **2012,** *485,* 623–626. doi:10.1038/nature11075
11. Zhang, F.; Jiang, S.; Wu, S.; Li, Y.; Mao, C.; Liu, Y.; Yan, H. *Nat. Nanotechnol.* **2015,** *10,* 779–784. doi:10.1038/nnano.2015.162
12. Andersen, E. S.; Dong, M.; Nielsen, M. M.; Jahn, K.; Subramani, R.; Mamdouh, W.; Golas, M. M.; Sander, B.; Stark, H.; Oliveira, C. L. P.; Pedersen, J. S.; Birkedal, V.; Besenbacher, F.; Gothelf, K. V.; Kjems, J. *Nature* **2009,** *459,* 73–76. doi:10.1038/nature07971
13. Chandrasekaran, A. R.; Levchenko, O. *Chem. Mater.* **2016,** *28,* 5569–5581. doi:10.1021/acs.chemmater.6b02546
14. Han, D.; Pal, S.; Nangreave, J.; Deng, Z.; Liu, Y.; Yan, H. *Science* **2011,** *332,* 342–346. doi:10.1126/science.1202998
15. Ke, Y.; Ong, L. L.; Shih, W. M.; Yin, P. *Science* **2012,** *338,* 1177–1183. doi:10.1126/science.1227268
16. Becerril, H. A.; Ludtke, P.; Willardson, B. M.; Woolley, A. T. *Langmuir* **2006,** *22,* 10140–10144. doi:10.1021/la061740+
17. Shimada, J.; Maruyama, T.; Kitaoka, M.; Yoshinaga, H.; Nakano, K.; Kamiya, N.; Goto, M. *Chem. Commun.* **2012,** *48,* 6226–6228. doi:10.1039/C2CC30618B
18. Yan, H.; Park, S. H.; Finkelstein, G.; Reif, J. H.; LaBean, T. H. *Science* **2003,** *301,* 1882–1884. doi:10.1126/science.1089389
19. Rahman, M.; Neff, D.; Norton, M. L. *Chem. Commun.* **2014,** *50,* 3413–3416. doi:10.1039/C3CC49637F
20. Chen, Y.; Liu, H.; Ye, T.; Kim, J.; Mao, C. *J. Am. Chem. Soc.* **2007,** *129,* 8696–8697. doi:10.1021/ja072838t
21. Keren, K.; Berman, R. S.; Buchstab, E.; Sivan, U.; Braun, E. *Science* **2003,** *302,* 1380–1382. doi:10.1126/science.1091022
22. Li, S.; He, P.; Dong, J.; Guo, Z.; Dai, L. *J. Am. Chem. Soc.* **2005,** *127,* 14–15. doi:10.1021/ja0446045
23. Mangalum, A.; Rahman, M.; Norton, M. L. *J. Am. Chem. Soc.* **2013,** *135,* 2451–2454. doi:10.1021/ja312191a
24. Braun, E.; Eichen, Y.; Sivan, U.; Ben-Yoseph, G. *Nature* **1998,** *391,* 775–778. doi:10.1038/35826
25. Liu, J.; Geng, Y.; Pound, E.; Gyawali, S.; Ashton, J. R.; Hickey, J.; Woolley, A. T.; Harb, J. N. *ACS Nano* **2011,** *5,* 2240–2247. doi:10.1021/nn1035075
26. Uprety, B.; Gates, E. P.; Geng, Y.; Woolley, A. T.; Harb, J. N. *Langmuir* **2014,** *30,* 1134–1141. doi:10.1021/la403617r
27. Pilo-Pais, M.; Goldberg, S.; Samano, E.; LaBean, T. H.; Finkelstein, G. *Nano Lett.* **2011,** *11,* 3489–3492. doi:10.1021/nl202066c
28. Pearson, A. C.; Liu, J.; Pound, E.; Uprety, B.; Woolley, A. T.; Davis, R. C.; Harb, J. N. *J. Phys. Chem. B* **2012,** *116,* 10551–10560. doi:10.1021/jp302316p
29. Uprety, B.; Westover, T.; Stoddard, M.; Brinkerhoff, K.; Jensen, J.; Davis, R. C.; Woolley, A. T.; Harb, J. N. *Langmuir* **2017,** *33,* 726–735. doi:10.1021/acs.langmuir.6b04097
30. Jin, Z.; Sun, W.; Ke, Y.; Shih, C.-J.; Paulus, G. L. C.; Hua Wang, Q.; Mu, B.; Yin, P.; Strano, M. S. *Nat. Commun.* **2013,** *4,* 1663. doi:10.1038/ncomms2690
31. Deng, Z.; Mao, C. *Angew. Chem., Int. Ed.* **2004,** *43,* 4068–4070. doi:10.1002/anie.200460257
32. Becerril, H. A.; Woolley, A. T. *Small* **2007,** *3,* 1534–1538. doi:10.1002/smll.200700240
33. Surwade, S. P.; Zhao, S.; Liu, H. *J. Am. Chem. Soc.* **2011,** *133,* 11868–11871. doi:10.1021/ja2038886
34. Surwade, S. P.; Zhou, F.; Wei, B.; Sun, W.; Powell, A.; O'Donnell, C.; Yin, P.; Liu, H. *J. Am. Chem. Soc.* **2013,** *135,* 6778–6781. doi:10.1021/ja401785h
35. Diagne, C. T.; Brun, C.; Gasparutto, D.; Baillin, X.; Tiron, R. *ACS Nano* **2016,** *10,* 6458–6463. doi:10.1021/acsnano.6b00413
36. Zhou, F.; Sun, W.; Ricardo, K. B.; Wang, D.; Shen, J.; Yin, P.; Liu, H. *ACS Nano* **2016,** *10,* 3069–3077. doi:10.1021/acsnano.5b05159
37. Helmi, S.; Ziegler, C.; Kauert, D. J.; Seidel, R. *Nano Lett.* **2014,** *14,* 6693–6698. doi:10.1021/nl503441v
38. Sun, W.; Boulais, E.; Hakobyan, Y.; Wang, W. L.; Guan, A.; Bathe, M.; Yin, P. *Science* **2014,** *346,* 1258361. doi:10.1126/science.1258361

39. Lipomi, D. J.; Martinez, R. V.; Cademartiri, L.; Whitesides, G. M. Soft Lithographic Approaches to Nanofabrication. In *Polymer Science: A Comprehensive Reference;* Matyjaszewski, K.; Möller, M., Eds.; Elsevier Science: Amsterdam, Netherlands, 2012; pp 211–231. doi:10.1016/B978-0-444-53349-4.00180-1
40. Totzeck, M.; Ulrich, W.; Göhnermeier, A.; Kaiser, W. *Nat. Photonics* **2007,** *1,* 629–631. doi:10.1038/nphoton.2007.218
41. Manfrinato, V. R.; Zhang, L.; Su, D.; Duan, H.; Hobbs, R. G.; Stach, E. A.; Berggren, K. K. *Nano Lett.* **2013,** *13,* 1555–1558. doi:10.1021/nl304715p
42. Lin, B. J. *Proc. SPIE* **2012,** *8323,* 832302. doi:10.1117/12.919747
43. Wieland, M. J.; de Boer, G.; ten Berge, G. F.; van Kervinck, M.; Jager, R.; Peijster, J. J. M.; Slot, E.; Steenbrink, S. W. H. K.; Teepen, T. F.; Kampherbeek, B. J. *Proc. SPIE* **2010,** *7637,* 76370F. doi:10.1109/JPROC.2007.911853
44. Pease, R. F.; Chou, S. Y. *Proc. IEEE* **2008,** *96,* 248–270. doi:10.1109/JPROC.2007.911853
45. Qu, J.; Hou, X.; Fan, W.; Xi, G.; Diao, H.; Liu, X. *Sci. Rep.* **2015,** *5,* 17872. doi:10.1038/srep17872
46. Tian, C.; Kim, H.; Sun, W.; Kim, Y.; Yin, P.; Liu, H. *ACS Nano* **2017,** *11,* 227–238. doi:10.1021/acsnano.6b04777
47. Bonnet, J.; Colotte, M.; Coudy, D.; Couallier, V.; Portier, J.; Morin, B.; Tuffet, S. *Nucleic Acids Res.* **2010,** *38,* 1531–1546. doi:10.1093/nar/gkp1060
48. Colotte, M.; Coudy, D.; Tuffet, S.; Bonnet, J. *Biopreserv. Biobanking* **2011,** *9,* 47–50. doi:10.1089/bio.2010.0028
49. Elam, J. W.; Sechrist, Z. A.; George, S. M. *Thin Solid Films* **2002,** *414,* 43–55. doi:10.1016/S0040-6090(02)00427-3
50. Kim, H.; Surwade, S. P.; Powell, A.; O'Donnell, C.; Liu, H. *Chem. Mater.* **2014,** *26,* 5265–5273. doi:10.1021/cm5019663
51. Pillers, M. A.; Lieberman, M. *J. Vac. Sci. Technol., B* **2014,** *32,* 040602. doi:10.1116/1.4879417

License and Terms

BEILSTEIN JOURNAL OF NANOTECHNOLOGY

Refractive index sensing and surface-enhanced Raman spectroscopy using silver–gold layered bimetallic plasmonic crystals

Somi Kang[1], Sean E. Lehman[2], Matthew V. Schulmerich[3], An-Phong Le[2], Tae-woo Lee[4], Stephen K. Gray[4], Rohit Bhargava[3] and Ralph G. Nuzzo[*1,2]

Full Research Paper

Open Access

Address:
[1]Department of Materials Science and Engineering, University of Illinois at Urbana-Champaign, Urbana, Illinois 61801, USA, [2]Department of Chemistry, University of Illinois at Urbana-Champaign, Urbana, Illinois 61801, USA, [3]Beckman Institute for Advanced Science and Technology, University of Illinois at Urbana-Champaign, Urbana, Illinois 61801, USA, and [4]Chemistry Division and Center for Nanoscale Materials, Argonne National Laboratory, 9700 Cass Ave., Lemont, Illinois 60439, USA

Email:
Ralph G. Nuzzo[*] - r-nuzzo@illinois.edu

* Corresponding author

Keywords:
finite-difference time-domain; nanoimprint soft lithography; plasmonics; surface plasmon resonance

Beilstein J. Nanotechnol. **2017,** *8,* 2492–2503.
doi:10.3762/bjnano.8.249

Received: 07 July 2017
Accepted: 26 October 2017
Published: 24 November 2017

This article is part of the Thematic Series "Nanoscale patterning and characterization".

Guest Editor: S. A. Claridge

Abstract

Herein we describe the fabrication and characterization of Ag and Au bimetallic plasmonic crystals as a system that exhibits improved capabilities for quantitative, bulk refractive index (RI) sensing and surface-enhanced Raman spectroscopy (SERS) as compared to monometallic plasmonic crystals of similar form. The sensing optics, which are bimetallic plasmonic crystals consisting of sequential nanoscale layers of Ag coated by Au, are chemically stable and useful for quantitative, multispectral, refractive index and spectroscopic chemical sensing. Compared to previously reported homometallic devices, the results presented herein illustrate improvements in performance that stem from the distinctive plasmonic features and strong localized electric fields produced by the Ag and Au layers, which are optimized in terms of metal thickness and geometric features. Finite-difference time-domain (FDTD) simulations theoretically verify the nature of the multimode plasmonic resonances generated by the devices and allow for a better understanding of the enhancements in multispectral refractive index and SERS-based sensing. Taken together, these results demonstrate a robust and potentially useful new platform for chemical/spectroscopic sensing.

Introduction

Studies of surface plasmons have attracted significant attention due to the diverse range of applications and processes in which they can be exploited. These applications include, but are not limited to: laser emission, light trapping, optical modulation, and label-free means of chemical or biological sensing [1-6]. Surface plasmons are collective oscillations of conduction electrons near metal surfaces that are excited by electromagnetic radiation incident at a metal/dielectric interface. This results in an evanescent decaying electric field that extends from the metal surface for ≈100–200 nm (surface plasmon polaritons), or it can also manifest as a localized surface plasmon resonance at the surface of a metal nanostructure (localized surface plasmons). The attributes of these excitations are highly sensitive to local refractive index changes, which in turn allow for their exploitation in chemical and biological sensing [7-9]. In this way, surface plasmonic resonance (SPR) sensors are promising as an analytical technique for real-time, fully label-free detection of molecules, both quantitatively and qualitatively, as well as for monitoring surface interactions [5,10,11]. Surface-enhanced Raman spectroscopy, better known as SERS, is another important analytical application that utilizes enhanced electromagnetic fields generated by surface plasmons [12,13]. Raman scattering signals can be dramatically amplified on a plasmonic substrate, reportedly by as much as 10 to 11 orders of magnitude, reaching levels of sensitivity suitable for single molecule detection [14,15].

In general, photons cannot directly elicit plasmonic excitations on metal films in air due to conservation requirements [16,17]. To compensate for the mismatch in momentum between an incident photon and a plasmonic resonance, most studies to date have focused on metallic nanostructures such as nanoparticles, line gratings, and nanoscale holes or voids to effect couplings and further obtain stronger electromagnetic fields and higher spatial resolution from localized surface plasmon resonance (LSPR) [18-27]. Many fabrication methods have been described that provide structures capable of generating these plasmonic features [28-33]. Our work in this area has exploited soft nanoimprint lithography, a technique that permits reproducible replication of precisely defined nanometer-sized features over a large area (greater than 1×1 cm^2), as a way to fabricate quantitative imaging-mode and multispectral plasmonic optics [23,24,34-36]. This fabrication method yields highly uniform arrays of nanoholes in a dielectric substrate that upon metallization provide a plasmonic platform for SPR sensing and SERS [22-26,37,38].

Noble metals such as Au and Ag are the most commonly used plasmonic materials because they generate strong plasmonic resonances at visible and near-infrared frequencies [39]. Metallic Ag generates a stronger evanescent field and a narrower plasmon resonance than Au, which in principle is advantageous for both optical sensing and SERS [40-42]. It is Au, however, that is more widely utilized for analytical applications due to its long-term environmental stability, ease of surface modification, and biocompatibility [43]. The present study explores means for realizing synergy in utilizing the complementary attributes of each material. Here we examine a bilayer/multi-metallic Ag/Au plasmonic crystal (PC) motif that is characterized by higher analytical sensitivity and more strongly enhanced electric fields than our previously reported monometallic PC systems. Manipulating the composition of the thin metal films, their spatial distribution, and the design rules of the PC optical elements (in terms of the lattice parameter and the size of the features of the nanoholes) is found to be an effective approach to optimizing the response in multispectral and SERS-based sensing. To illustrate the properties of these devices, the optical response from exemplary PCs was acquired by 0^{th}-order transmission measurements. Finite-difference time-domain (FDTD) calculations were performed to assist in characterizing how each system behaved in order to understand and obtain an optimized device form factor. The data illustrate that Ag/Au bimetallic PCs possess potential for implementation in chemical sensing.

Experimental

Materials

The reagents were used as received without further purification unless otherwise specified. Spin-on-glass (SOG) 315F was purchased from Filmtronics and was filtered twice sequentially using 0.22 μm (Millipore) and 0.02 μm (Whatman Anotop 10) syringe filters immediately before use in order to remove nanoparticles in the SOG sol formed by hydrolysis [26]. Polydimethylsiloxane (soft PDMS; Sylgard 184, Dow corning) was prepared in a 10:1 ratio of PDMS base with curing agent. Hard PDMS components, poly(25–30% methylhydrosiloxane)-(dimethylsiloxane) (HMS-301), poly(7–8% vinylmethylsiloxane)-(dimethylsiloxane), (VDT-731), platinum divinyltetramethyldisiloxane (SIP6831.1) and (1,3,5,7-tetravinyl-1,3,5,7-tetramethylcyclotetrasiloxane) (7900), were purchased from Gelest. Polyethylene glycol (PEG, M_W = 10,000 g/mol) and benzenethiol (BT) (99.99 %) were purchased from Aldrich. 100% ethyl alcohol (Decon) was used to solvate benzenethiol. Ultrapure water (18.2 MΩ·cm) was generated using a Millipore Milli-Q Academic A-10 system and used to prepare the PEG buffer (0–5.6 wt %) solutions.

Plasmonic crystal fabrication via soft nanoimprint lithography

The PCs were fabricated using soft nanoimprint lithography as previously reported [22-26,37,38]. In brief, a composite hard-

PDMS/soft-PDMS mixture was cast on a patterned photoresist master with arrays of nanohole relief structures in order to fabricate the PCs. A glass slide was fully covered with liquid SOG, and spin cast (≈950 rpm for 6 s) to produce a thin, uniform layer of liquid SOG on the glass slide surface. The PDMS stamp was then pressed into the SOG-coated glass slide and fastened in place to achieve conformal contact between the PDMS stamp and SOG film. Before baking, the sample was left at room temperature for 7 min to facilitate evaporation of volatile organic components of the SOG material. The sample was soft baked at 110 °C for 5 min, followed by the careful removal the PDMS stamp. The embossed SOG film was then further cured at 200 °C for 5 min followed by baking at 160 °C overnight. Finally, the fully cured SOG film was annealed at 450 °C under nitrogen for 1 h. The replicated SOG nanostructures consist of well-defined square arrays of nanoholes, patterned using sixteen different design rules that offer a broad variation of response to optical frequencies. A ≈5 nm titanium dioxide adhesion layer was deposited using atomic layer deposition (Cambridge nanotech) on the embossed SOG nanostructure followed by deposition of a ≈50 nm metallic film (Au, Ag or both) via one of the various methods. Sputter deposition in a 5 mTorr argon atmosphere (AJA International) was utilized for substrates prepared for bulk refractive index (bulk RI) sensing experiments and electron beam (e-beam) evaporation (Temescal) was used for samples made for SERS measurement. The schematic illustration of both SOG PC structures is given in Figure 1a and the scanning electron microscopy (SEM) images of nanohole arrays of different metal distributions are shown in Figure 1b (sputter deposition) and Figure 1c (e-beam evaporation). The island-like metallic film structures of the quasi-3D structures (shown in inset of Figure 1c) were found to be susceptible over time to the penetration of liquid solution into the interfaces formed between the metal films and the SOG substrate. To prevent the degradation in performance that this engendered, a conformal ≈6 nm thick Al_2O_3 passivation film was deposited on top of the metal by atomic layer deposition (Cambridge Nanotech).

Bulk refractive index sensing via transmission-mode spectroscopy

Transmission spectra in air and bulk RI dependent PC data were measured using a Varian 5G UV–vis–NIR spectrophotometer with normal incident light and no temperature control. Bulk RI measurements were carried out using methods that have been previously reported [22,24,26,37,44,45]. In this protocol, a PDMS flow cell was mounted on top of the PC and PEG buffer solutions of increasing concentration (pure water, 1.4, 2.8, 4.8, and 5.6 wt %) were injected into the PDMS flow cell with a syringe pump (Harvard Apparatus) at a flow rate of 0.1 mL/min. To change the solution, a new PEG solution was injected at a flow rate of 1.0 mL/min at the beginning stage for two minutes to completely flush the previous solution from the PDMS cell. This was followed by injection at a normal flow rate of 0.1 mL/min. Transmission spectra over a wavelength range of 355–1000 nm were collected throughout the process in order to monitor changes in multiple plasmonic responses to changes in the surrounding dielectric environment. The refractive index of the PEG solutions was measured using an Abbe refractometer, corrected to 25 °C.

Integrated multispectral response calculation

In quantitative work, we consider both the position and intensity changes that occur in the plasmonic features present in the transmission spectrum over the entire range of collected wavelengths. The absolute difference values were calculated using the differences between transmission spectra collected in each PEG solution and a spectrum recorded in pure water. These values were integrated to account for wavelength dependence of both negative and positive changes in spectroscopic intensity using Equation 1, a value having units of Δ%T·nm.

$$\text{Integrated Response} = \int_{\text{wavelength}} |\Delta(\%T(\lambda)|\mathrm{d}\lambda. \qquad (1)$$

Surface-enhanced Raman spectroscopy (SERS) measurements

A self-assembled monolayer of benzenethiol on top of the quasi-3D PCs was prepared by immersing them in a 15 mM benzenethiol ethanolic solution for 12 h, rinsing thoroughly with ethanol, and then drying with a stream of nitrogen gas. SERS measurements were made using a SENTERRA dispersive Raman microscope (Bruker Optics) with an excitation laser wavelength of 785 nm, an excitation power of ≈5 mW, focal length of 45 mm and acquisition time of 30 s. Raman spectra were collected over a Raman shift range of 500–1800 cm^{-1}.

Finite-difference time-domain simulation of plasmonic nanostructures

A set of 3D FDTD simulations were used to model the normal incidence transmission spectra in air and water and the electromagnetic field distribution for full-3D PCs. The unit cell geometry was defined as an infinite square array of nanostructured holes on a metal film that are parallel to the *x*–*y* plane with a semi-infinite SOG material under the nanoholes and air above them. The unit cell spacing was 2 nm in all three dimensions with a total unit cell size of $N_x \times N_y \times N_z = 292 \times 292 \times 1200$ grid points. The total simulation time for each unit cell was 100 fs. Perfectly matched uniaxial layers were applied on both sides of the z-grid to avoid artificial reflection errors from the domain boundaries. Appropriate periodic boundary conditions were used to define the square array. The frequency-

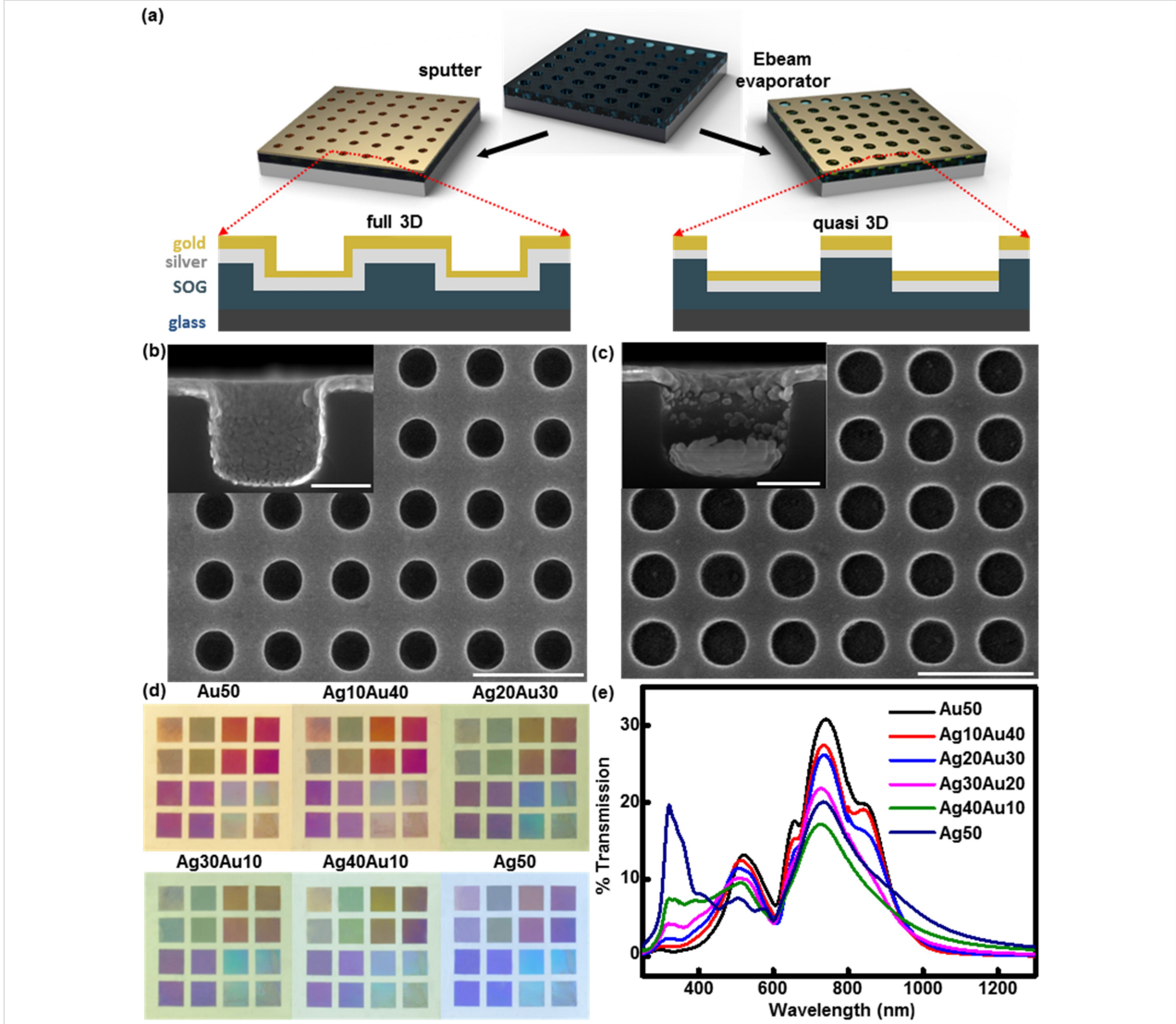

Figure 1: (a) 3D and 2D schematic illustration of the full-3D and quasi-3D plasmonic crystals (PCs). To fabricate the metal films, sputtering was used for the full-3D PC and e-beam evaporating was used for the quasi-3D PC. SEM images of a (b) full-3D and (c) quasi-3D PC with diameters and periodicities of ≈380 and 580 nm. The scale bar corresponds to 5 μm. Inset: cross-sectional SEM image of an individual nanohole. The scale bar corresponds to 100 nm. (d) Optical images of embossed PCs with different metal layer compositions: ≈50 nm Au (Au50), ≈10 nm Ag/≈40 nm Au (Ag10Au40), ≈20 nm Ag/≈30 nm Au (Ag20Au30), ≈30 nm Ag/≈20 nm Au (Ag30Au20), ≈40 nm Ag/≈10 nm Au (Ag40Au10), ≈50 nm Ag (Ag50). The hole depth is ≈340 nm and the hole spacing varies from ≈500 nm to ≈1740 nm. (e) Normal incident transmission spectra of five full-3D PCs with different metal composition.

dependent Au[22] and Ag[46] permittivities are described by the Drude–Lorentzian model over a wavelength range of 355–1500 nm. The dielectric constants for SOG and air were taken to be 1.43 and 1.00, respectively.

Results and Discussion

Structure and properties of bimetallic plasmonic crystals

Periodic nanostructures in metal films have been widely studied as a system to better understand the underlying physics of plasmon resonances as well as to develop high-performance platforms for a variety of SPR applications [21,46,47]. Compared to other work on nanoparticles or 2D arrays, the 3D plasmonic constructs described here have notable differences in terms of both the underlying physics as well as the analytical approaches they support. A specific contrast compared to freely diffusing nanoparticles in solution, sensing on plasmonic crystals provides specific advantages, being well-suited for use as chemoresponsive/multispectral imaging optics as well as not being subject to temporal instabilities that arise from interparticle interactions mediated via operando sensitive attributes of surface charge. This intrinsically makes plasmonic crystals more attractive for sensing applications as the need to modify the surface chemistry/charge figures heavily in design of capac-

ities to support the recognition of specific solution-phase analytes. Additionally, local electromagnetic hotspots and fano resonances generated at the surface are much more accessible by design in photonic crystal systems due to the intrinsically controllable geometry of the array openings. In contrast, the interaction of nanoparticles can be used to modulate the effective electromagnetic field generated at hotspots but these ultimately depend on solution conditions in ways that can be hard to control and vary both within and between assays. The optimal morphology for a given application will necessarily depend on the specific parameters required including response time, harshness of solution conditions, and overall spectroscopic detection figures-of-merit required. The work described herein demonstrates how a systematically varied metallic composition can be used to tailor the bulk RI and spectroscopic sensing capabilities of PC optics. The work establishes figures-of-merit for these tailored systems and might serve to benefit analysis in biological as well as other, more general, analytical contexts. This work further establishes protocols that afford effective materials approaches to stabilize Au/Ag metal multilayer PC optics against environments that would otherwise degrade their performance in use.

Efforts in this field have been directed particularly toward the unique optical properties of periodic nanostructures because of their capacities for extraordinary optical transmission, visual wavelength responsiveness, and high optical sensitivity to changes in the local environment [48-50]. In this study, we used square arrays of nanoholes molded into the surface of an inorganic SOG film using soft nanoimprint lithography. The SOG-supported PC structure affords a chemically and thermally stable sub-wavelength optical device, especially when a protective metal oxide overlayer is included, for SPR sensing and for SERS measurements, as has been discussed in previously published work [26].

The SPRs produced using nanostructured metal films can be easily tuned by adjusting the geometric shape, thickness, and composition of the metal film, as well as the surrounding dielectric environment. Sputter coating and e-beam evaporation are both widely used tools for fabricating metal thin films, yet the distribution of the deposited metal film resulting from each of the two methods are quite different due to the distinctive deposition characteristics. The step coverage of e-beam evaporation, in particular, is poor since it only offers an essentially unidirectional collision of source material atoms with the substrate, with most of the metal being deposited on the surface and bottom of the nanoholes. Sputtering, in contrast, is a less-directed deposition process that conformally coats the entire substrate. We have termed the metal nanostructures fabricated by e-beam deposition as quasi-3D structures because the metal disk at the bottom of the nanohole is physically separated from the metal film on the top of the SOG substrate, while the PCs with more continuous/conformal metal layers formed by sputter deposition are termed full-3D PCs [37]. Figure 1a schematically illustrates the metal film distribution differences resulting from the fabrication using these two methods. The geometric differences in the metal films of the quasi-3D and the full-3D PCs were characterized using cross-sectional SEM imaging (inset of Figure 1b,c). The top view SEM images of PCs in Figure 1b,c demonstrate that PCs consist of uniform square arrays of nanoholes with a periodicity of ≈580 nm. Despite the fact that the diameter of the embossed SOG nanostructures of both PCs are identical (≈380 nm), the final diameter of nanoholes in the full-3D PC (Figure 1b) appears slightly smaller than those of the quasi-3D PC (Figure 1c). This effect was attributed to differences in sidewall metal deposition resulting from the specific technique used.

In addition to changing the geometry of the nanohole arrays and the metal by altering the metal film deposition method, modification of the metal film composition provides an additional means through which the optical response of the PC can be systematically controlled. In this study, we used bimetallic layers to engineer the plasmonic response of the device over a wider wavelength range, here exploiting the unique plasmonic modes of Ag in the visible range to supplement and enhance those provided by Au. This distinctive PC design further serves to compensate for the chemical instability of Ag by coating it with thin films of Au. To explore the variation in function resulting from the double layer film structure, we used five different ratios of Ag and Au while maintaining a constant overall metal film thickness on the SOG nanohole arrays. The ratios used were: 50 nm Au (Au50), 10 nm Ag/40 nm Au (Ag10Au40), 20 nm Ag/30 nm Au (Ag20Au30), 30 nm Ag/20 nm Au (Ag30Au20), and 40 nm Ag/10 nm Au (Ag40Au10). Figure 1d presents optical images of an entire series of PCs with varying compositions of Ag and Au. The sixteen squares (4×4 mm^2) given on each plasmonic substrate exhibit distinctive colors due to light scattering from the nanohole arrays according to the different design rules, with periodicities ranging from 0.49 to 1.75 μm and corresponding hole diameters ranging from 0.17 to 1.12 μm. The color changes seen, from the typical color of bulk Au to that of Ag, follow an intuitive trend as the ratio of Ag in the metal film increases. Metrological data developed using SEM demonstrated a high fidelity of the replicated structure to its imprint master, as illustrated in the nearly identical geometry (≈340 nm hole depth, ≈380 nm hole diameter, and ≈580 nm hole spacing) of an exemplary pair of PCs shown in Figure 1b (full-3D) and Figure 1c (quasi-3D). The former structures have a particularly useful response in the visible wavelength region of the optical spectrum. This is illus-

trated by the data presented in Figure 1e, which shows the 0^{th}-order transmission spectra for six full-3D PCs recorded in air for varying ratios of Au and Ag. The variations in the transmission spectra can be attributed to the changes in the film composition (Ag and Au thickness). The small discontinuity seen near 800 nm is an instrumental artifact, which results from a change of detectors during the scan. In Figure 1e, the largest transmission peak, spanning the near-infrared (NIR) range, is blue-shifted and its intensity decreases as the proportion of Ag in the metal film increases. Across the near UV–vis regions, enhanced transmission magnitudes and more spectroscopic features are observed as the mass-coverage of the Ag increases. The intensity of the characteristic peak for the Au surface plasmon resonance (at ≈500 nm) is reduced as the proportion of Ag increases, while the peak intensity (at ≈350 nm) corresponding to the bulk plasmon mode of Ag is enhanced. These qualitative trends are more quantitatively described by the results of theoretical modeling.

Finite-difference time-domain modeling

FDTD calculations provide theoretical understanding of how the electromagnetic field interacts with the PC [51-53]. The transmission spectra of the periodic nanohole arrays in each of the PCs have multiple optical responses, such as localized surface plasmon resonances (LSPRs), Bloch wave surface plasmon polaritons (BW-SPPs), Wood's anomalies (WAs), or a combination of these features [28,48,54-60]. Contributions from the transmission of light also originate from the coupling of light directly transmitted through the metal film, as well as from the background metal absorption (at ≈500 nm for Au and ≈350 nm for Ag). The peaks in the transmission spectra, which correspond to BW-SPPs and WAs, are correlated with the periodic structure of the nanoholes arrays, whereas LSPRs can be created by specific sub-wavelength-sized features of the metallic structures.

The appropriate optical constants for each material and the geometrical model of the periodic nanohole array are crucial for FDTD modeling because all of the plasmonic modes are highly sensitive to the structural details and dielectric properties of the environment. The design rules for an optimized PC were used in the calculations (see below), and based on experimentally measured data, they were defined as a square array of nanoholes in a layer of SOG with a diameter of 380 nm, depth of 340 nm, and a center-to-center spacing of 580 nm. The dimensions of the metal film above the SOG nanohole arrays were as follows: top metal layer of ≈50 nm thickness, bottom metal layer of ≈20 nm thickness, and sidewall metal layer thickness of ≈15 nm (details are given in Supporting Information File 1, Figure S1). The different thickness values account for the shadowing effect which limits the degree of conformal coverage realized in the sputter coating metallization step. In the calculation, we used a Drude plus two-pole Lorentzian model to obtain the dielectric constant of the metal as a function of wavelength [48,61]. Figure 2 presents the experimentally measured and calculated normal incidence transmission spectra and electric field distributions around the nanoholes for full-3D PCs with Au50 (Figure 2a), Ag50 (Figure 2b), and Ag30Au20 (Figure 2c) mass-coverage metal films. The Al_2O_3 passivation layer was not included in the calculations as it was found to impart only very small modifications to the experimentally determined transmission spectra.

The calculations and experimental data shown are for PCs in air, and assignments for specific features seen in the data are revealed by the calculations. The largest peak (labeled C in the spectra) is the result of strong LSPR excitations that are confined in the nanohole. Fano-like resonances, appearing as peak minima or maxima, are correlated with either BW-SPPs or WAs [22,60]. The wavelengths of the expected BW-SPPs can be predicted using Equation S1 in Supporting Information File 1 and solutions for this equation are listed in Supporting Information File 1, Table S1. From this theoretical analysis, we can verify that the peak minima labeled A in the transmission spectra originate from BW-SPPs. At these wavelengths, the field intensity distributions seen near the interface of the top metal layer and air stand in good agreement with the characteristic field distribution expected for BW-SPPs. Even so, many of the optical features observed in the transmission spectra are likely the result of complex interactions of light diffraction and concurrent plasmonic modes. The electric field distributions calculated for the wavelength at position B in each of the spectra are examples of features involving such coupling of multiple plasmonic modes. The intensity concentrated in the nanohole and near the sidewalls, for example, likely corresponds to LSPRs. Moreover, electric fields located at the metal–air interface are largely due to BW-SPPs and/or WAs.

The FDTD results (Figure 2) are consistent with the experimental results in terms of the dependence of the 0^{th}-order transmission spectra as a function of changes in the metal overlayer composition (presented in Figure 1e). The data show, for example, that the peak intensities are reduced and the intensity of the transmission maxima (position C) are blue-shifted with increasing Ag content. The calculations further demonstrate several BW-SPP features that characterize transmission for the Ag PCs at wavelengths around 400 nm – a complexity in the blue wavelength region expected for Ag in contrast to Au. The optical features appearing between 400–600 nm for the Ag PCs suggest a possibility for a highly sensitive response for such PCs at near-UV and visible wavelengths [62,63].

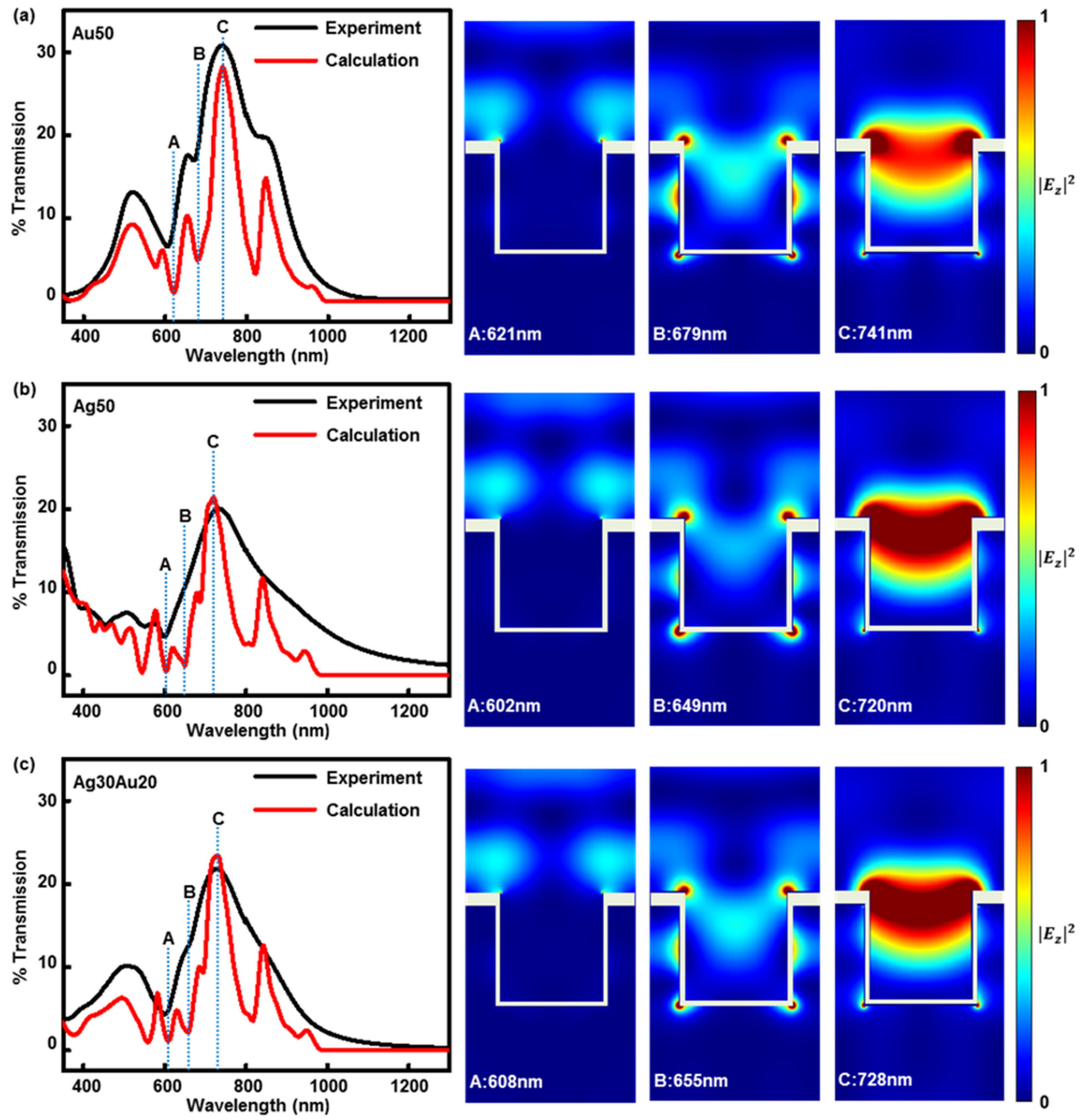

Figure 2: Experimental transmission spectra (black), electrodynamic modeling transmission spectra (red), and 2D calculated electric field plots corresponding to wavelengths for peaks labeled as A, B, and C in the transmission plot of (a) Au50, (b) Ag50 and (c) Au20Ag30 full-3D PCs (≈380 nm hole diameter, ≈340 nm relief depth, ≈580 nm hole spacing, ≈50 nm top metal layer, ≈20 nm metal sidewall, and ≈15 nm bottom metal layer).

Bulk refractive index sensitivity of bimetallic plasmonic crystals

A single resonance peak analysis methodology does not provide a suitable means to determine the RI sensitivity of an imaging sensor. For this reason, we employed a multispectral protocol to quantify figures-of-merit (FOM) for sensitivity, as described in earlier reports on chemical sensing using PCs as an optical element for imaging and spectroscopic detection [22,24,26,37]. Here we used a flow cell design, the same as that previously reported, to expose the PC to PEG solutions of varying concentrations to determine a FOM for its multispectral RI sensitivity. Because sensitivity to bulk RI changes has been previously shown to be better for the full-3D PC structure as compared with the quasi-3D counterpart, the transmittance spectra for the former over a range of 355–1000 nm were collected as a function of time while PEG solutions of different concentration (from 1.4 to 5.6 wt %) were passed through the flow cell [37]. Integrated multispectral RI responses of five full-3D PCs with different mass-coverage metal films were measured to investigate and validate the best design for the PC for bulk RI sensing.

To determine an optimal nanohole array design for RI sensing in the visible wavelength range before considering the effects of mass fraction in metal thin film on plasmon resonances, we per-

formed bulk RI sensing measurements (Supporting Information File 1, Figure S2a) and FDTD calculations (Supporting Information File 1, Figure S2b) using four design rules of nanoholes chosen from sixteen squares on a PC: 580 nm (p580), 780 nm (p780), 1100 nm (p1100), and 1600 nm (p1600). From the results of bulk solution-phase RI sensing (shown in Supporting Information File 1, Figure S2a), the most sensitive geometry for RI changes measured over a wavelength range of 300–800 nm was found to be a nanohole array with ≈580 nm periodicity and ≈380 nm hole diameter. The FDTD calculation for this structure (presented in Supporting Information File 1, Figure S2b) confirms the physical origin of the bulk RI sensing results in which the p580 Au50 full-3D plasmonic substrates generated the strongest plasmonic features at frequencies in the visible range (wavelengths spanning 600–800 nm). From the transmittance measurements made in air (shown in Figure 1e), we can further infer that the shifts of peak maxima that occur as a result of changes made in the metal overlayer composition are small if nanohole geometries are identical. We therefore selected the p580 nanohole array as a suitable exemplar for the bulk RI sensitivity evaluation of bimetallic PCs carried out in this study.

Figure 3a shows the integrated responses of five full-3D PCs selected for a design rule giving optimal RI responses with different metal compositions, here plotted as a function of time. The small baseline shift seen in the data over the course of the measurement is due to a small, uncompensated change in temperature. Figure 3b demonstrates the linear integrated response changes for the Au50 and Ag10Au40 full-3D PC as a consequence of changes made in the bulk refractive index (ΔRI) of the contacting PEG solutions.

The Ag10Au40 full-3D PC exhibits the largest RI sensitivity among the five PCs studied (the FOM values measured for these PCs are listed in Table 1). From 355–1000 nm, the RI sensitivity for the Ag10Au40 bimetallic PC (45,000 Δ%T·nm/RIU) is nearly ≈1.41 times that of the Au thin film PC (32,000 Δ%T·nm/RIU). Higher mass-fractions of Ag in the bilayer stack progressively weaken the plasmonic response, as seen in the lower values of the FOM.

Transmission spectra measured in water provide an important qualitative insight into the differences in the bulk RI sensitivity of the PCs. We note that sharp, intense optical features are more significantly weighted in the multispectral RI response calculation (Equation 1) as compared to broad, weak transmission features. Supporting Information File 1, Figure S3a shows the transmission spectra of PCs measured in water that illustrate these effects. Of particular note are the transmission intensity minima (appearing as sharp features near 600 nm and 800 nm) and peak transmission maxima (a generally more complex feature appearing above 800 nm). One sees here that the full-3D Ag10Au40 PCs, the best system for bulk RI sensing, has the narrowest peak minima and the highest transmission feature (seen here at ≈900 nm) as the qualitative associations described

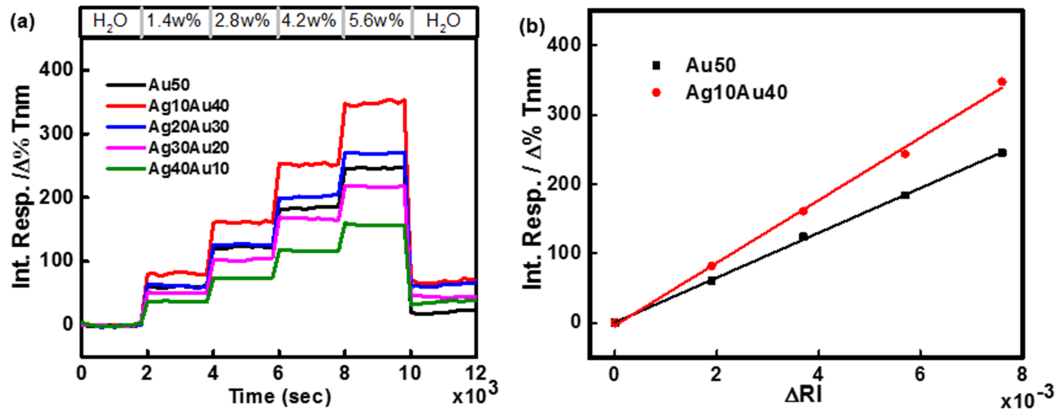

Figure 3: (a) Integrated multispectral response of five full-3D PCs with different metal composition to injections of increasing concentration of aqueous PEG solutions (from 1.4 to 5.6 wt %). Transmittance changes as a function of time were collected over a wavelength range of 355–1000 nm. (b) Linear change in the average integrated response with refractive index change on Au50 and Ag10Au40 full-3D PCs.

Table 1: Figure-of-merit (FOM, Δ%T·nm/RIU) for PCs with different ratios of Ag and Au.

Wavelength (nm)	Au50	Ag10Au40	Ag20Au30	Ag30Au20	Ag40Au10
355–1000	32,000	45,000	36,000	29,000	21,000

above predict. The FDTD results calculated for PCs immersed in water do not agree perfectly with the transmission spectra acquired experimentally because the mounted PDMS flow cell is not considered in the calculation. To allow solution flow and direct contact with liquids during measurements, a closed sampling cell is required and, in such cases, presents a glass–solution interface through which the incident radiation passes. Due to its complexity, the presence of this glass layer was not accounted for within the FDTD simulation; it is this omission to which the observed deviations are ascribed.

They do, however, still affirm the intuitive correlations noted above. Considering the calculated transmission spectra in water for the five PCs (shown in Supporting Information File 1, Figure S3b), as predicted, the Ag10Au40 full-3D PC presents both the narrowest peak minima and highest intensity in the calculated transmission response. Overall, due to the structure of the fabricated device, there will be an intrinsic sensitivity to certain variable physical parameters, such as the exact specifications of the flow cell geometry and/or the overall optical path length due to the mounting of the device in the radiation path. Ultimately, this will lead to slight variations in analytical sensitivity, requiring rigorous experimental design to provide integrated plasmonic devices with suitable analytical sensitivities for detection with high reproducibility.

SERS enhancement of bimetallic plasmonic crystals

Nanohole arrayed PCs are also promising as an easily replicable substrate for SERS. We have shown in an earlier report that plasmonic crystals formed on a molded SOG substrate provided excellent performance for Raman spectroscopy measurements [26]. In this study, we demonstrate that even greater Raman signal enhancements are achievable by using a bimetallic PC compared to those offered by more conventional monometallic systems. The total double metal layer thickness (50 nm) and the SOG nanohole array design rules (580 nm periodicity and 380 nm diameter) used for the SERS measurement are the same as those adopted in the RI measurements described above. Optimized thicknesses of the Ag and Au metal films on the embossed SOG PC were tested using the quasi-3D PC device motif, which was found to be a more suitable design for SERS measurement in earlier work [25]. The data presented in Supporting Information File 1, Figure S4 experimentally confirmed that a larger SERS enhancement does in fact result for the quasi-3D PC compared to the full-3D design for the bimetallic case as well. Table 2 shows the Raman intensities measured for each quasi-3D PC as a function of the different Au and Ag thickness ratios. As the data reveal, the best SERS enhancement is provided by the Ag40Au10 quasi-3D PC, with a Raman intensity that was ≈2.3 times higher than that of a comparable Au-coated PCs (shown in Figure 4).

The major Raman active vibrational modes of benzenethiol are located at 1073 cm^{-1} and 1574 cm^{-1} (which correspond to Raman shift peaks relative to the 785 nm laser excitation at 857 nm and 896 nm, respectively) [64]. Past work has noted that an approximate requirement for SERS enhancement by a PC is an enhanced electric field following at an optical frequency halfway between the laser excitation wavelength (λ_{ex} = 785 nm) and the scattered wavelength of the Raman active mode of interest [25,64,65]. This, then, corresponds to the case for the noted modes of benzenethiol where the PC provides maximal transmittance at wavelengths of 821 nm and 840 nm (the halfway point between λ_{ex} and λ_{Raman}). The experimental transmission spectra of Au50 and Ag40Au10 quasi-3D PCs measured in air shown in Figure 4b qualitatively confirm this correlation between the magnitude of the SERS enhancement and the underlying optical properties of the plasmonic substrate.

FDTD simulations theoretically confirm the underlying mechanism and optimized PC structures for SERS enhancement. Calculated top field intensity distributions at 5 nm away from the surface of PCs (shown in Figure 4c) exhibit that the Ag40Au10 quasi-3D PC generates a stronger enhanced field compared with Au50 quasi-3D PC, which is in good accord with the correlation between the strength of the plasmonic resonance and the SERS intensity. SERS enhancement theory suggests that the intensity of the Raman scattered radiation is proportional to the square of the electric field [12]. FDTD-computed electromagnetic SERS enhancement factors ($|E|^4$) for PCs with different Au layer thicknesses at wavelengths of 821 nm and 840 nm show similar trends as compared to the experimental results in that the SERS intensity increases as the thickness of the Ag layer increases (presented in Supporting Information File 1, Figure S5). The quantitative discrepancies between the measured SERS intensities and calculated enhancement factors

Table 2: Raman intensity (counts) at 1073 cm^{-1} and 1573 cm^{-1} for five different full-3D PCs with 580 nm periodicity.

	Au50	Ag10Au40	Ag20Au30	Ag30Au20	Ag40Au10
1073 cm^{-1}	3133	3395	4461	4845	7095
1573 cm^{-1}	5499	5048	6437	7359	12830

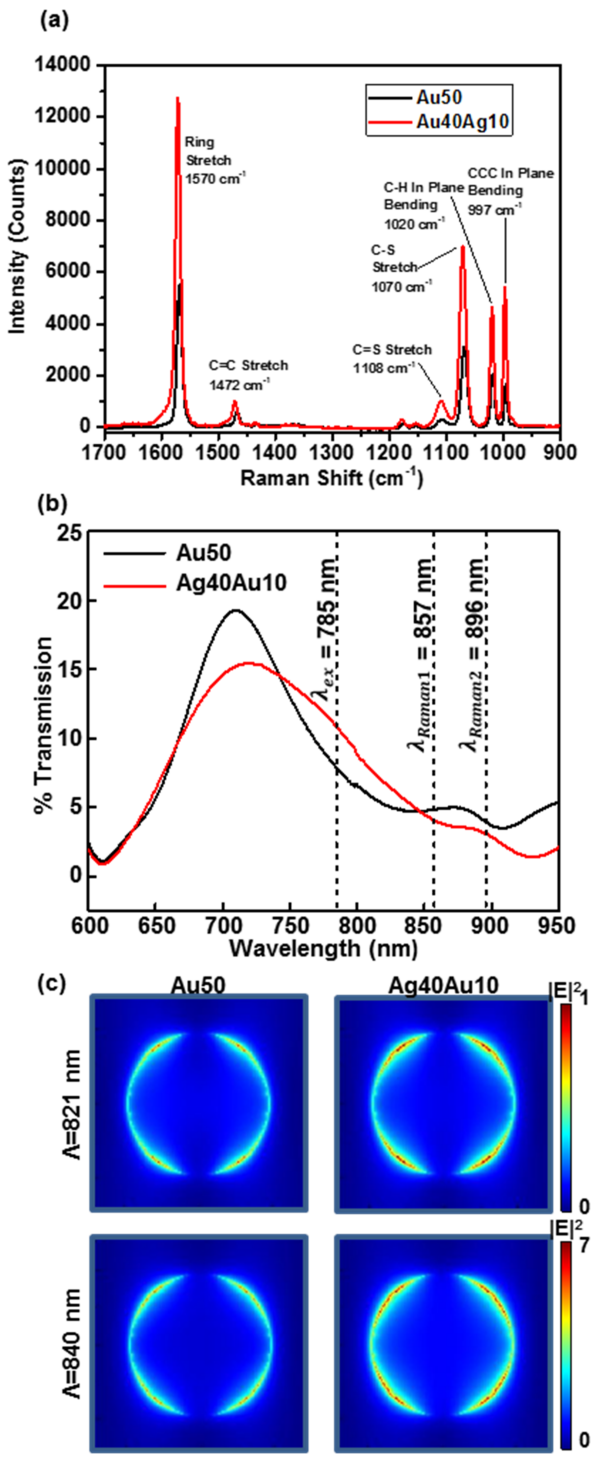

Figure 4: (a) SERS spectra of benzenethiol adsorbed onto Au50 and Ag40Au10 quasi-3D PCs measured with laser power of ≈5 mW. (b) Experimental transmission spectra in air for Au50 and Ag40Au10 quasi-3D PCs used to collect the Raman spectra in (a). The locations of the laser excitation and Raman peaks are marked as λ_{ex}, λ_{Raman1} and λ_{Raman2}, respectively. (c) FDTD-computed top (*x*–*y*) intensity distribution at 5 nm away from the surface of Au50 and Ag40Au10 quasi-3D PCs at λ = 821 nm and 840 nm.

as a function of the Au layer thickness likely originate as a consequence of the inexact model used for quasi-3D PCs (illustrated in Figure 1a). The latter does not take into account that there are some metal particles on the sidewall near the bottom disk and top layer (shown in inset of Figure 1c), which are structures that can contribute to the spectroscopic response of the PC optic.

These correlations are not fully predictive of optimal performance in SERS for a broader range of PC design rules. The larger data, for example, specifically show that the p580 PC is not the best design rule for SERS measurements and that the optical properties needed to obtain an optimized performance are more complex and likely application-specific. We have found that by using benzenethiol as an exemplary reporter molecule, for instance, signals of a p780 quasi-3D Ag40Au10 PC are higher than those of the p580 quasi-3D Ag40Au10 PC, demonstrating an approximately ≈1.3–1.8-fold enhancement (Supporting Information File 1, Figure S6a). The general correlation of the SERS intensity enhancement with specific features of the transmission intensity apparently still retain a useful qualitative character when one notes that the experimental results show higher transmission values at 820 nm and 841 nm for the p780 PC as compared with the p580 PC case (shown in Supporting Information File 1, Figure S6b). We believe further work, concomitant with theoretical insights, will be required to better understand associations between the optical properties and performance, as was observed here in this work.

Conclusion

The influence of the mass coverage of Ag and Au thin films as well as the geometrical parameters of the nanohole arrays of bimetallic (bilayer) plasmonic crystals were characterized through multispectral bulk RI sensing and SERS measurements combined with insights from theoretical modeling. This work demonstrates the feasibility of Ag/Au bimetallic PCs for analytical applications, further establishing that bimetallic systems markedly surpass the quantitative performance of monometallic systems reported previously. With FDTD calculations, the nature of the different optical and plasmonic features that provide these performance attributes was confirmed. An optimized system was developed through careful engineering of the system and analysis of the transmission spectra both experimentally and computationally. The methods described here hold additional value in that they provide guidance for further optimization of a design framework for plasmonic devices to suit specific features of analytical applications. More directly, though, the multilayered bimetallic PC is found to offer great flexibility in terms of ease of fabrication and features of performance, thereby establishing it as an interesting platform for highly sensitive forms of plasmonic-based chemical sensing.

Supporting Information

Supporting Information File 1

Additional theoretical and experimental information. Details: Theoretical analysis of Bloch wave surface plasmon polaritons and Wood's anomalies of PCs; Schematic illustration of a nanohole; Experimental and FDTD calculated transmission spectra in water of the full-3D PCs; Integrated multispectral response and computational normal incident transmission spectra of full-3D PCs with different nanohole array periodicity; SERS spectra of benzenethiol and experimental transmission spectra in air for Ag40Au10 quasi-3D PC with 580 nm and 780 nm periodicity; SERS spectra of benzenethiol adsorbed onto full-3D and quasi-3D PCs. [http://www.beilstein-journals.org/bjnano/content/supplementary/2190-4286-8-249-S1.pdf]

Acknowledgements

This work was supported by the U.S. Department of Energy under prime Award No. DE-SC0001293 via subcontract 67N-1087758 from California Institute of Technology as part of the DOE Energy Frontier Research Center on Light-Material Interactions in Energy Conversion and was performed using resources at the Frederick Seitz Materials Research Laboratory Central Facilities at the University of Illinois, including the Center for Microanalysis of Materials; the Micro/Nanofabrication Facility; and the Laser and Spectroscopy Facility. We also acknowledge the use of the Turing cluster, maintained and operated by the Computational Science and Engineering Program at the University of Illinois. The bulk of the work presented here in modified form was originally from the doctoral dissertation of the first author, Dr. Somi Kang [66].

References

1. Oulton, R. F.; Sorger, V. J.; Zentgraf, T.; Ma, R.-M.; Gladden, C.; Dai, L.; Bartal, G.; Zhang, X. *Nature* **2009,** *461,* 629–632. doi:10.1038/nature08364
2. Pillai, S.; Catchpole, K. R.; Trupke, T.; Green, M. A. *J. Appl. Phys.* **2007,** *101,* 093105. doi:10.1063/1.2734885
3. Corcoran, C. J.; Kang, S.; Li, L.; Guo, X.; Chanda, D.; Nuzzo, R. G. *ACS Appl. Mater. Interfaces* **2013,** *5,* 4239–4246. doi:10.1021/am400408g
4. Pacifici, D.; Lezec, H. J.; Atwater, H. A. *Nat. Photonics* **2007,** *1,* 402–406. doi:10.1038/nphoton.2007.95
5. Homola, J.; Yee, S. S.; Gauglitz, G. *Sens. Actuators, B* **1999,** *54,* 3–15. doi:10.1016/S0925-4005(98)00321-9
6. Anker, J. N.; Hall, W. P.; Lyandres, O.; Shah, N. C.; Zhao, J.; Van Duyne, R. P. *Nat. Mater.* **2008,** *7,* 442–453. doi:10.1038/nmat2162
7. Knoll, W. *Annu. Rev. Phys. Chem.* **1998,** *49,* 569–638. doi:10.1146/annurev.physchem.49.1.569
8. Barnes, W. L.; Dereux, A.; Ebbesen, T. W. *Nature* **2003,** *424,* 824–830. doi:10.1038/nature01937
9. Maier, S. A. *Plasmonics: Fundamentals and Applications;* Springer: New York, NY, U.S.A., 2007.
10. Zhao, J.; Zhang, X.; Yonzon, C. R.; Haes, A. J.; Van Duyne, R. P. *Nanomedicine* **2006,** *1,* 219–228. doi:10.2217/17435889.1.2.219
11. Brockman, J. M.; Nelson, B. P.; Corn, R. M. *Annu. Rev. Phys. Chem.* **2000,** *51,* 41–63. doi:10.1146/annurev.physchem.51.1.41
12. Campion, A.; Kambhampati, P. *Chem. Soc. Rev.* **1998,** *27,* 241–250. doi:10.1039/a827241z
13. Willets, K. A.; Van Duyne, R. P. *Annu. Rev. Phys. Chem.* **2007,** *58,* 267–297. doi:10.1146/annurev.physchem.58.032806.104607
14. Camden, J. P.; Dieringer, J. A.; Zhao, J.; Van Duyne, R. P. *Acc. Chem. Res.* **2008,** *41,* 1653–1661. doi:10.1021/ar800041s
15. Nie, S.; Emory, S. R. *Science* **1997,** *275,* 1102–1106. doi:10.1126/science.275.5303.1102
16. Sambles, J. R.; Bradbery, G. W.; Yang, F. Z. *Contemp. Phys.* **1991,** *32,* 173–183. doi:10.1080/00107519108211048
17. Lezec, H. J.; Degiron, A.; Devaux, E.; Linke, R. A.; Martin-Moreno, L.; Garcia-Vidal, F. J.; Ebbesen, T. W. *Science* **2002,** *297,* 820–822. doi:10.1126/science.1071895
18. Murphy, C. J.; San, T. K.; Gole, A. M.; Orendorff, C. J.; Gao, J. X.; Gou, L.; Hunyadi, S. E.; Li, T. *J. Phys. Chem. B* **2005,** *109,* 13857–13870. doi:10.1021/jp0516846
19. Kuwata, H.; Tamaru, H.; Esumi, K.; Miyano, K. *Appl. Phys. Lett.* **2003,** *83,* 4625–4627. doi:10.1063/1.1630351
20. Tan, W.-C.; Preist, T. W.; Sambles, J. R.; Wanstall, N. P. *Phys. Rev. B* **1999,** *59,* 12661–12666. doi:10.1103/PhysRevB.59.12661
21. Ebbesen, T. W.; Lezec, H. J.; Ghaemi, H. F.; Thio, T.; Wolff, P. A. *Nature* **1998,** *391,* 667–669. doi:10.1038/35570
22. Stewart, M. E.; Mack, N. H.; Malyarchuk, V.; Soares, J. A. N. T.; Lee, T.-W.; Gray, S. K.; Nuzzo, R. G.; Rogers, J. A. *Proc. Natl. Acad. Sci. U. S. A.* **2006,** *103,* 17143–17148. doi:10.1073/pnas.0606216103
23. Stewart, M. E.; Yao, J.; Maria, J.; Gray, S. K.; Rogers, J. A.; Nuzzo, R. G. *Anal. Chem.* **2009,** *81,* 5980–5989. doi:10.1021/ac900819j
24. Yao, J.; Stewart, M. E.; Maria, J.; Lee, T.-W.; Gray, S. K.; Rogers, J. A.; Nuzzo, R. G. *Angew. Chem., Int. Ed.* **2008,** *47,* 5013–5017. doi:10.1002/anie.200800501
25. Baca, A. J.; Truong, T. T.; Cambrea, L. R.; Montgomery, J. M.; Gray, S. K.; Abdula, D.; Banks, T. R.; Yao, J.; Nuzzo, R. G.; Rogers, J. A. *Appl. Phys. Lett.* **2009,** *94,* 243109. doi:10.1063/1.3155198
26. Yao, J.; Le, A.-P.; Schulmerich, M. V.; Maria, J.; Lee, T.-W.; Gray, S. K.; Bhargava, R.; Rogers, J. A.; Nuzzo, R. G. *ACS Nano* **2011,** *5,* 5763–5774. doi:10.1021/nn201464t
27. Cole, R. M.; Baumberg, J. J.; Garcia de Abajo, F. J.; Mahajan, S.; Abdelsalam, M.; Bartlett, P. N. *Nano Lett.* **2007,** *7,* 2094–2100. doi:10.1021/nl0710506
28. Prikulis, J.; Hanarp, P.; Olofsson, L.; Sutherland, D.; Käll, M. *Nano Lett.* **2004,** *4,* 1003–1007. doi:10.1021/nl0497171
29. Haynes, C. L.; Van Duyne, R. P. *J. Phys. Chem. B* **2001,** *105,* 5599–5611. doi:10.1021/jp010657m
30. Malinsky, M. D.; Kelly, K. L.; Schatz, G. C.; Van Duyne, R. P. *J. Phys. Chem. B* **2001,** *105,* 2343–2350. doi:10.1021/jp002906x
31. Aizpurua, J.; Hanarp, P.; Sutherland, D. S.; Käll, M.; Bryant, G. W.; García de Abajo, F. J. *Phys. Rev. Lett.* **2003,** *90,* 057401. doi:10.1103/PhysRevLett.90.057401

32. Rindzevicius, T.; Alaverdyan, Y.; Dahlin, A.; Höök, F.; Sutherland, D. S.; Käll, M. *Nano Lett.* **2005,** *5,* 2335–2339. doi:10.1021/nl0516355
33. Hanarp, P.; Käll, M.; Sutherland, D. S. *J. Phys. Chem. B* **2003,** *107,* 5768–5772. doi:10.1021/jp027562k
34. Gates, B. D.; Xu, Q.; Stewart, M.; Ryan, D.; Willson, C. G.; Whitesides, G. M. *Chem. Rev.* **2005,** *105,* 1171–1196. doi:10.1021/cr030076o
35. Ganesan, R.; Dinachali, S. S.; Lim, S. H.; Saifullah, M. S. M.; Chong, W. T.; Lim, A. H. H.; Yong, J. J.; Thian, E. S.; He, C.; Low, H. Y. *Nanotechnology* **2012,** *23,* 315304. doi:10.1088/0957-4484/23/31/315304
36. Le, A.-P.; Kang, S.; Thompson, L. B.; Rubakhin, S. S.; Sweedler, J. V.; Rogers, J. A.; Nuzzo, R. G. *J. Phys. Chem. B* **2013,** *117,* 13069–13081. doi:10.1021/jp402731f
37. Yao, J.; Le, A.-P.; Gray, S. K.; Moore, J. S.; Rogers, J. A.; Nuzzo, R. G. *Adv. Mater.* **2010,** *22,* 1102–1110. doi:10.1002/adma.200904097
38. Truong, T. T.; Maria, J.; Yao, J.; Stewart, M. E.; Lee, T.-W.; Gray, S. K.; Nuzzo, R. G.; Rogers, J. A. *Nanotechnology* **2009,** *20,* 434011. doi:10.1088/0957-4484/20/43/434011
39. Johnson, P. B.; Christy, R. W. *Phys. Rev. B* **1972,** *6,* 4370–4379. doi:10.1103/PhysRevB.6.4370
40. Zynio, S. A.; Samoylov, A. V.; Surovtseva, E. R.; Mirsky, V. M.; Shirshov, Y. M. *Sensors* **2002,** *2,* 62–70. doi:10.3390/s20200062
41. Freeman, R. G.; Hommer, M. B.; Grabar, K. C.; Jackson, M. A.; Natan, M. J. *J. Phys. Chem.* **1996,** *100,* 718–724. doi:10.1021/jp951379s
42. Liu, C. H.; Hong, M. H.; Cheung, H. W.; Zhang, F.; Huang, Z. Q.; Tan, L. S.; Hor, T. S. A. *Opt. Express* **2008,** *16,* 10701–10709. doi:10.1364/OE.16.010701
43. Wang, Y.; Chen, H.; Dong, S.; Wang, E. *J. Chem. Phys.* **2006,** *125,* 044710. doi:10.1063/1.2216694
44. Maria, J.; Truong, T. T.; Yao, J.; Lee, T.-W.; Nuzzo, R. G.; Leyffer, S.; Gray, S. K.; Rogers, J. A. *J. Phys. Chem. C* **2009,** *113,* 10493–10499. doi:10.1021/jp9024552
45. Stewart, M. E.; Anderton, C. R.; Thompson, L. B.; Maria, J.; Gray, S. K.; Rogers, J. A.; Nuzzo, R. G. *Chem. Rev.* **2008,** *108,* 494–521. doi:10.1021/cr068126n
46. Ghaemi, H. F.; Thio, T.; Grupp, D. E.; Ebbesen, T. W.; Lezec, H. J. *Phys. Rev. B* **1998,** *58,* 6779–6782. doi:10.1103/PhysRevB.58.6779
47. Porto, J. A.; García-Vidal, F. J.; Pendry, J. B. *Phys. Rev. Lett.* **1999,** *83,* 2845–2848. doi:10.1103/PhysRevLett.83.2845
48. Lezec, H. J.; Thio, T. *Opt. Express* **2004,** *12,* 3629–3651. doi:10.1364/OPEX.12.003629
49. Reilly, T. H., III; Chang, S.-H.; Corbman, J. D.; Schatz, G. C.; Rowlen, K. L. *J. Phys. Chem. C* **2007,** *111,* 1689–1694. doi:10.1021/jp066802j
50. Gao, H.; McMahon, J. M.; Lee, M. H.; Henzie, J.; Gray, S. K.; Schatz, G. C.; Odom, T. W. *Opt. Express* **2009,** *17,* 2334–2340. doi:10.1364/OE.17.002334
51. Hagness, S. C.; Taflove, A. *Computational Electrodynamics: The Finite-Difference Time-Domain Method,* 3rd ed.; Artech House: Boston, MA, U.S.A., 2005.
52. Maier, S. A.; Friedman, M. D.; Barclay, P. E.; Painter, O. *Appl. Phys. Lett.* **2005,** *86,* 071103. doi:10.1063/1.1862340
53. Artar, A.; Yanik, A. A.; Altug, H. *Appl. Phys. Lett.* **2009,** *95,* 051105. doi:10.1063/1.3202391
54. Wannemacher, R. *Opt. Commun.* **2001,** *195,* 107–118. doi:10.1016/S0030-4018(01)01333-5
55. Degiron, A.; Lezec, H. J.; Yamamoto, N.; Ebbesen, T. W. *Opt. Commun.* **2004,** *239,* 61–66. doi:10.1016/j.optcom.2004.05.058
56. Salomon, L.; Grillot, F.; Zayats, A. V.; de Fornel, F. *Phys. Rev. Lett.* **2001,** *86,* 1110–1113. doi:10.1103/PhysRevLett.86.1110
57. Darmanyan, S. A.; Zayats, A. V. *Phys. Rev. B* **2003,** *67,* 035424. doi:10.1103/PhysRevB.67.035424
58. Treacy, M. M. J. *Appl. Phys. Lett.* **1999,** *75,* 606–608. doi:10.1063/1.124455
59. Sarrazin, M.; Vigneron, J.-P.; Vigoureux, J.-M. *Phys. Rev. B* **2003,** *67,* 085415. doi:10.1103/PhysRevB.67.085415
60. Chang, S.-H.; Gray, S. K.; Schatz, G. C. *Opt. Express* **2005,** *13,* 3150–3165. doi:10.1364/OPEX.13.003150
61. Lee, T.-W.; Gray, S. K. *Opt. Express* **2005,** *13,* 9652–9659. doi:10.1364/OPEX.13.009652
62. Chen, H.; Kou, X.; Yang, Z.; Ni, W.; Wang, J. *Langmuir* **2008,** *24,* 5233–5237. doi:10.1021/la800305j
63. Sagle, L. B.; Ruvuna, L. K.; Ruemmele, J. A.; Van Duyne, R. P. *Nanomedicine* **2011,** *6,* 1447–1462. doi:10.2217/nnm.11.117
64. Chanda, D.; Shigeta, K.; Truong, T.; Lui, E.; Mihi, A.; Schulmerich, M.; Braun, P. V.; Bhargava, R.; Rogers, J. A. *Nat. Commun.* **2011,** *2,* 479. doi:10.1038/ncomms1487
65. Haynes, C. L.; Van Duyne, R. P. *J. Phys. Chem. B* **2003,** *107,* 7426–7433. doi:10.1021/jp027749b
66. Kang, S. Fabrication, Design, and Analytical Applications of Nanostructured Plasmonic Crystals. Ph.D. Thesis, University of Illinois at Urbana-Champaign, 2014.

License and Terms

BEILSTEIN JOURNAL OF NANOTECHNOLOGY

Patterning of supported gold monolayers via chemical lift-off lithography

Liane S. Slaughter[1,2,§], Kevin M. Cheung[1,2], Sami Kaappa[3], Huan H. Cao[1,2], Qing Yang[1,2], Thomas D. Young[1,2], Andrew C. Serino[1,4], Sami Malola[3], Jana M. Olson[5], Stephan Link[5,6], Hannu Häkkinen[*3,7], Anne M. Andrews[*1,2,8] and Paul S. Weiss[*1,2,4]

Full Research Paper

Open Access

Address:
[1]California NanoSystems Institute, University of California, Los Angeles, Los Angeles, CA 90095, USA, [2]Department of Chemistry and Biochemistry, University of California, Los Angeles, Los Angeles, CA 90095, USA, [3]Department of Physics, Nanoscience Center, University of Jyväskylä, FI-40014 Jyväskylä, Finland, [4]Department of Materials Science and Engineering, University of California, Los Angeles, Los Angeles, CA 90095, USA, [5]Department of Chemistry, Rice University, Houston, Texas, 77005, USA, [6]Department of Electrical and Computer Engineering, Rice University, Houston, Texas, 77005, USA, [7]Department of Chemistry, Nanoscience Center, University of Jyväskylä, FI-40014 Jyväskylä, Finland and [8]Department of Psychiatry and Biobehavioral Sciences, Semel Institute for Neuroscience and Human Behavior, and Hatos Center for Neuropharmacology, University of California, Los Angeles, Los Angeles, CA 90095, USA

Email:
Hannu Häkkinen[*] - hannu.j.hakkinen@jyu.fi; Anne M. Andrews[*] - aandrews@mednet.ucla.edu; Paul S. Weiss[*] - psw@cnsi.ucla.edu

* Corresponding author
§ Current address: Division of Life Science and Institute for Advanced Study, The Hong Kong University of Science and Technology

Keywords:
chemical patterning; hybrid material; monolayer; soft lithography; two-dimensional material

Beilstein J. Nanotechnol. **2017,** *8,* 2648–2661.
doi:10.3762/bjnano.8.265

Received: 20 September 2017
Accepted: 24 November 2017
Published: 08 December 2017

This article is part of the Thematic Series "Nanoscale patterning and characterization".

Guest Editor: S. A. Claridge

Abstract

The supported monolayer of Au that accompanies alkanethiolate molecules removed by polymer stamps during chemical lift-off lithography is a scarcely studied hybrid material. We show that these Au–alkanethiolate layers on poly(dimethylsiloxane) (PDMS) are transparent, functional, hybrid interfaces that can be patterned over nanometer, micrometer, and millimeter length scales. Unlike other ultrathin Au films and nanoparticles, lifted-off Au–alkanethiolate thin films lack a measurable optical signature. We therefore devised fabrication, characterization, and simulation strategies by which to interrogate the nanoscale structure, chemical functionality, stoichiometry, and spectral signature of the supported Au–thiolate layers. The patterning of these layers laterally encodes their functionality, as demonstrated by a fluorescence-based approach that relies on dye-labeled complementary DNA hybridization. Supported thin Au films can be patterned via features on PDMS stamps (controlled contact), using patterned Au substrates prior to

lift-off (e.g., selective wet etching), or by patterning alkanethiols on Au substrates to be reactive in selected regions but not others (controlled reactivity). In all cases, the regions containing Au–alkanethiolate layers have a sub-nanometer apparent height, which was found to be consistent with molecular dynamics simulations that predicted the removal of no more than 1.5 Au atoms per thiol, thus presenting a monolayer-like structure.

Introduction

Chemical lift-off lithography (CLL) is a subtractive technique for patterning self-assembled alkanethiol molecules on Au surfaces via rupture of Au–Au bonds at the Au–monolayer interface [1,2]. In CLL, hydroxyl-terminated molecules (or other species with reactive termini) in preformed self-assembled monolayers (SAMs) are lifted off Au surfaces through contact with O_2-plasma-activated poly(dimethylsiloxane) (PDMS) stamps. Compared with microcontact or transfer printing methods [3-6], CLL produces crisp, stable patterns with sub-20 nm resolution and patterned areas of more than square millimeters [1,7]. We have used CLL on gold to control the placement and nanoscale environment around surface-immobilized biomolecules and to simplify patterning steps in device fabrication [1,2,7-13].

Two-dimensional (2D) materials have proven to be extremely rich in terms of new and potentially useful properties [14-18]. Here, we have investigated Au–alkanethiolate layers on PDMS that were produced during CLL specifically for their 2D material properties. The existence of Au on the PDMS stamp following lift-off was initially discovered using X-ray photoelectron spectroscopy (XPS) to investigate post-CLL PDMS stamps [1]. These Au layers had been predicted in a gedanken-experiment by George Whitesides, in which he described the strength of the Au–S bond as stronger than the (weakened) bond between the top layer of alkanethiolate-bound Au atoms and the underlying Au substrate. The layers removed during CLL have not yet been well characterized.

In CLL, the height difference between the remaining SAM and the contact region (where molecules were removed) was the thicknesses of the SAM plus ≈4 Å [1]. This height difference is consistent with one or at most two layers of Au being removed by CLL. Although not fully elucidated, we refer to the lifted-off species as a (supported) Au–alkanethiolate monolayer (vide infra).

Chemical lift-off lithography differs from other subtractive or deterministic transfer printing techniques [6,19-23] in that the stamp "inks" used during the transfer have a different composition than the inks originally deposited onto the substrates. While other types of thin Au films and Au nanoparticles are identified through their measurable geometry- or size-dependent optical and electronic properties (e.g., localized surface plasmons) [24-26], we show that CLL lifted-off monolayers lack significant optical signals that make them distinguishable from the PDMS supporting matrix. Using contrast methodologies, we determine that the chemistry of the supported Au monolayers remains consistent with that of bulk Au.

We used experimental and computational strategies to characterize the hybrid Au–alkanethiolate 2D material formed at PDMS surfaces via lift-off lithography. Chemical lift-off lithography was used to pattern featureless (flat) PDMS substrates with Au–alkanethiolate monolayers, which enabled direct characterization of the nanometer-scale heights of the supported Au monolayers through scanning probe microscopy, as well as the exploration of spatially encoded functionality using fluorescence microscopy. Otherwise, when topographically patterned PDMS stamps are used to pattern Au monolayers, the traits of the latter are overwhelmed by the PDMS features that are hundreds of nanometers thick. These features are indiscernible on flat PDMS without the application of patterned reference regions, i.e., regions that contain only PDMS adjacent to areas containing monolayers of Au–alkanethiolate complexes.

To gain insight into lift-off lithography removal mechanisms and outcomes of the lift-off process at the atomic scale, we simulated lift-off using molecular dynamics and density functional theory. We determined the energetics of this complex system during lift-off. The simulations were used to predict the stoichiometry and structure of the lifted-off Au–alkanethiolate monolayers. The calculated stoichiometry estimated the limits for the structure of the Au–alkanethiolate monolayers, guiding our interpretation of the existence of Au monolayers.

Results and Discussion

Au-on-Si master substrates were patterned by a first round of CLL. Here, topographically patterned PDMS stamps were used to lift-off hydroxyl-terminated self-assembled alkanethiols (Figure S1, Supporting Information File 1) [1,9]. Following this CLL step, Au in the lifted-off (exposed) regions was removed by wet etching to form Au features in the noncontact regions. Next, hydroxyl-terminated alkanethiols were self-assembled on the patterned Au masters (Figure 1, left). Topographically flat, activated PDMS was brought into contact with the patterned Au masters to carry out a second round of CLL that resulted in

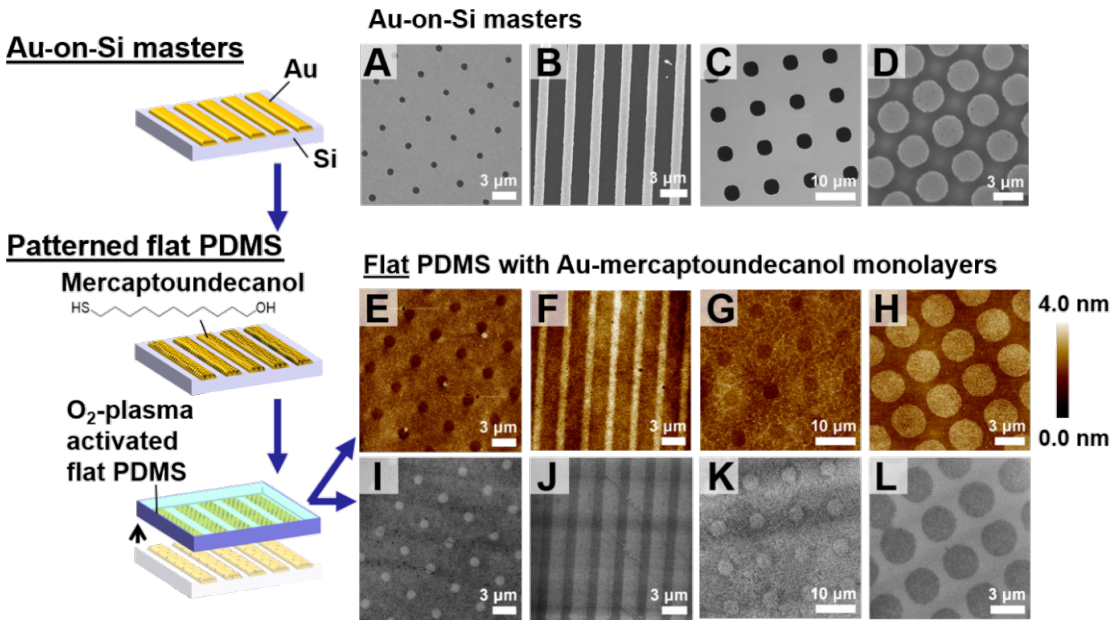

Figure 1: (Left) Scheme for patterning flat poly(dimethylsiloxane) (PDMS) substrates with Au–mercaptoundecanol monolayers. The Au features (100 nm height) on the Au-on-Si masters were functionalized with mercaptoundecanol and contacted with topographically flat PDMS stamps. (A–D) Scanning electron micrographs of Au-on-Si masters with (A) 1 µm diameter holes, (B) 1 µm lines, (C) 5 µm diameter holes, and (D) 3 µm diameter raised circles. The Au regions appear bright in these images. (E–H) Height maps of Au–mercaptoundecanol monolayers on PDMS produced from the Au masters in panels A–D, respectively. Images were acquired by peak-force atomic force microscopy. (I–L) Variable-pressure scanning electron micrographs of the same Au–alkanethiolate patterns on PDMS visualized in panels E–H. Images in panels I–L are contrast-enhanced to visualize the features more clearly. The original images are shown in Figure S2 (Supporting Information File 1).

otherwise featureless PDMS that was patterned only with the Au–alkanethiolate monolayers.

We imaged patterns of Au–alkanethiolate monolayers on PDMS substrates using nanoscale characterization tools. The topographies were measured using peak-force atomic force microscopy (PF-AFM), an intermittent-contact mode suitable for interrogating soft samples [27]. The AFM topography map in Figure 1E shows a pattern of recessed circular holes, which are each approximately 1 µm in diameter with a center-to-center separation of 4 µm. These features directly reproduced the lateral dimensions and periodicity of the Au features on the corresponding Au-on-Si master imaged by SEM in Figure 1A. The remaining images in Figure 1F–H demonstrate the same characteristics; the protruding regions in each AFM height map of post-lift-off PDMS corresponded directly to the raised Au features on the related Au-on-Si masters. Thus, the PDMS substrate was patterned by the addition of the Au–mercaptoundecanol monolayers from the patterned Au regions on the Au-on-Si masters, and not by imprinting, as nanoimprinting would result in inverse height topographies from those observed in Figure 1E–H. Notably, after reannealing and further self-assembly of new alkanethiol monolayers, the Au-on-Si masters could be reused a number of times to pattern multiple PDMS samples (Figure S3, Supporting Information File 1).

Patterned lifted-off monolayers were also imaged using variable-pressure scanning electron microscopy (VP-SEM), as shown in Figure 1I–L. Compared with AFM, SEM can be used to image patterns more efficiently as it provides chemical sensitivity and faster image acquisition over larger areas (up to square millimeters) [5,28-30]. The VP-SEM modality accommodates nonconducting samples by injecting water vapor into the sample chamber to offset destructive charging of the sample. In all cases, the dimensions and feature arrangement on patterned PDMS samples were consistent with those observed by AFM. In the VP-SEM images, functionalized regions consistently appeared less intense than the surrounding regions. We previously observed a similar contrast inversion while imaging self-assembled alkanethiols on Au surfaces [5]. In earlier studies, changing the operating voltage (i.e., the voltage of the primary electron beam) during SEM image acquisition was shown to reverse the contrast for images taken from the same sample. For PDMS, which is not conducting, the accelerating voltage, sample height, and vapor pressure were adjusted so that patterns could be discerned. The level of contrast in VP-SEM also depends on the nature of the alkanethiol molecules and SAM disorder (e.g., the orientation and conformation of the molecules in the SAM) [5]. The Au–mercaptoundecanol monolayers on PDMS are disordered as only 60–70% of alkanethiol molecules are removed during CLL [1,10,31]. The resulting

incomplete coverage may also influence the observed contrast. These Au–alkanethiolate monolayers on PDMS are composed of Au atoms bound to the PDMS by organic alkanethiol molecules. Thus, the observed contrast of Au, as seen in the SEM images of the Au-on-Si masters (Figure 1A–D), is not necessarily comparable to that of the SEM images of Au–alkanethiolate monolayers (Figure 1I–L).

We were unable to image patterned lifted-off monolayers on PDMS using optical extinction spectroscopy (Figure S4, Supporting Information File 1). We attempted to quantify the optical extinction of lifted-off Au monolayers on PDMS using a strategy previously employed to measure extinction from assemblies of Au nanoparticles or nanometer-thin Au films [32]. As shown in Figure S4C (Supporting Information File 1), the optical extinction was indistinguishable from the instrument noise in the visible wavelength region. Furthermore, there were no discernable differences in transmission between regions containing the Au monolayers and unmodified PDMS. Therefore, the Au–alkanethiolate hybrid material is transparent at visible wavelengths to within our measurement capabilities.

Although the Au monolayers were not optically detectable, we labeled them with thiolated DNA using a strategy to detect even minor amounts of species via their chemical properties [33-35]. In doing so, we demonstrated the chemical functionality of the Au–alkanethiolate monolayers (Figure 2). Complementary DNA was hybridized to thiolated single-stranded DNA self-assembled on lifted-off Au-containing regions on PDMS samples. Complementary sequences were fluorescently labeled, enabling indirect visualization of patterned Au monolayers. Only regions containing Au–alkanethiolates appeared bright in fluorescence microscopy images (Figure 2).

Using this straightforward functionalization and visualization method, we investigated patterns of lifted-off Au monolayers on PDMS as substrates for DNA recognition. Upon hybridization of dye-labeled complementary strands, fluorescent patterns were readily observed (Figure 2A,C,D). No measurable fluorescence was detected when DNA-functionalized substrates were exposed to dye-labeled non-complementary DNA (Figure 2B). Thus, the fluorescence patterns observed in Figure 2 derive from specific hybridization between thiolated DNA strands and their complementary sequences. Also, no patterns were observed in control experiments investigating nonspecific adsorption of complementary strands to patterned substrates in the absence of self-assembled thiolated DNA, hybridization with noncomplementary self-assembled DNA, or self-assembly and hybridization of DNA on unpatterned PDMS (Figure S5, Supporting Information File 1).

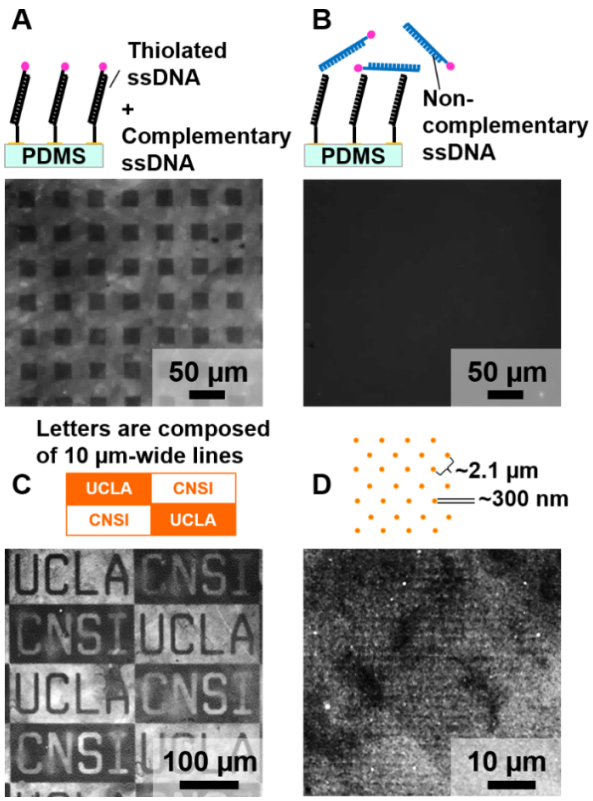

Figure 2: Fluorescence visualization of patterned lifted-off Au–alkanethiolate monolayers via DNA self-assembly and hybridization. (A) (Top) Scheme for complementary DNA hybridization experiments. (Bottom) Fluorescence microscopy image of a Au–alkanethiolate monolayer pattern on flat poly(dimethylsiloxane) (PDMS) after incubation with thiolated single-stranded DNA. Bright (lifted-off) regions between squares are indicative of hybridization of AlexaFluor® 488-labeled complementary DNA. Square regions are dark due to the absence of Au, and therefore, also the absence of self-assembled DNA necessary for hybridization. (B) (Top) Scheme for noncomplementary control experiments. (Bottom) Similar substrate and DNA self-assembly as in panel A with the exception that scrambled, noncomplementary, fluorescently labeled DNA was used for hybridization. (C) Flat PDMS was patterned with Au–alkanethiolate monolayers in the "CNSI" lettered and "UCLA" relief regions. The patterns were then visualized using the same DNA self-assembly and hybridization procedure as in panel A. (D) A different region of the same PDMS sample shown in panel C but patterned with 300 nm dots having a nearest-neighbor center-to-center separation of 2.1 μm.

Using CLL and fluorescence imaging, we produced images over square-millimeter areas with a lateral feature size spanning several orders of magnitude on the same substrates (Figure 2C,D). We have yet to determine the limits of the feature size and area that can be patterned by CLL, where features as small as 5 nm have been removed from the original monolayer [2]. In addition to the production of a wide range of feature sizes, another important advantage is that the supported Au monolayer on PDMS samples were stable for at least six months (Figure S6, Supporting Information File 1). These results suggest that while the optical properties of the lifted-off monolayers are different from those of bulk Au (i.e., the former

are optically transparent), lifted-off Au monolayers are chemically similar to bulk Au since they are amenable to self-assembly of thiols, and thus, to forming Au–S bonds. The chemical ability to modify the supported Au monolayers resulting from CLL implies opportunities for large-scale, transparent, sensor technologies, which could be straightforwardly fabricated under ambient conditions.

Having established characterization modalities to evaluate Au–alkanethiolate monolayers on PDMS, we developed an additional strategy for patterning PDMS with Au–alkanethiolate monolayers that takes advantage of the chemical selectivity associated with CLL. We previously determined that methyl-terminated SAMs do not react with activated PDMS and are therefore inert to lift-off. Terminal functional groups that are "CLL compatible" include hydroxyl, amino, carboxylate, and phosphonate moieties, such that these groups react with oxidized PDMS and are lifted off [1,10,11].

Performing CLL with flat PDMS stamps and patterned SAMs having regions of reactive and unreactive molecules on Au was anticipated to yield patterns on PDMS. The scheme in Figure 3A illustrates this concept. First, CLL was performed using stamps with wells of 7.5 µm diameter and mercaptoundecanol SAMs on the Au surfaces, leaving behind SAMs in the circular regions. Octadecanethiol (C18) molecules were then inserted into the contact regions, resulting in patterned monolayers on Au substrates. Octadecanethiol was selected for the study because we hypothesized its chain length would give sufficient contrast in post-CLL AFM imaging and that it would not displace the remaining mercaptoundecanol monolayer in the circular regions (or prevent it from undergoing CLL with a flat stamp) [36,37]. Two-component SAMs on Au having patterned regions distinguished by different terminal groups were then used for a second CLL step involving flat PDMS.

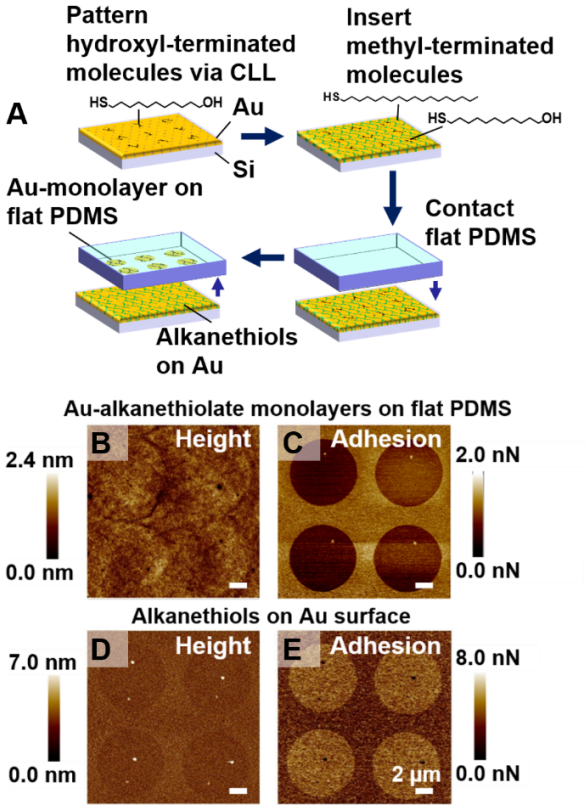

Figure 3: Chemically selective lift-off onto a flat poly(dimethylsiloxane) (PDMS) sample. (A) First, chemical lift-off lithography (CLL) was performed with a stamp having recessed circular features and a preformed self-assembled monolayer of mercaptoundecanol. Methyl-terminated alkanethiol molecules were then inserted into the contact regions, resulting in a self-assembled monolayer with patterned terminal functionalities. Performing a second round of CLL using this substrate and flat PDMS sample resulted in lift-off of the Au–alkanethiolate monolayer from regions containing hydroxyl-terminated molecules. (B) Height and (C) adhesion maps of the Au–alkanethiolate features on PDMS. These maps were simultaneously acquired using peak-force atomic force microscopy. (D) Height and (E) adhesion maps of the remaining alkanethiols on Au after CLL. The topography and adhesion maps in panels B and C show inverted contrast from those in panels D and E, respectively.

Height maps of post-CLL flat PDMS and the corresponding Au surface shown in Figure 3B and Figure 3D, respectively, had the expected inverted contrast. The regions with Au–mercaptoundecanol monolayers were observed as protruding circles on the flat PDMS, while regions on the Au-on-Si substrate, from which Au complexes were removed, appeared as recessed circles, demonstrating that lift-off occurred in a chemically selective manner.

The X-ray photoelectron spectroscopy (XPS) spectra of patterned PDMS illustrated the presence of Au in the regions predominantly containing mercaptoundecanol (noncontact regions associated with the first CLL step), but also in the contact regions dominated by inserted octadecanethiol. Residual mercaptoundecanol in the contact regions is due to the incomplete removal of molecules during the first CLL step. This partial removal has been used to advantage in fabricating tethered DNA for high-efficiency hybridization [10] and for investigating spin selectivity in electron transport through DNA [12]. Comparing the XPS peak areas suggested that the amount of Au in the lift-off regions is approximately double the surface concentration of Au in the noncontact regions. We note that the contrast in the topographic AFM map of the Au–alkanethiolate monolayers produced via two-component SAMs (Figure 3B) appears lower than that of the monolayers produced via Au-on-Si masters (Figure 1E–H). We attribute the low topographic contrast in the height maps in Figure 3 to the presence of Au–alkanethiolate compounds in all regions of the patterned PDMS.

In addition to topographic height measurements, we used PF-AFM to determine the adhesion force (i.e., the force needed to pull an AFM tip off a surface) to investigate chemical contrast on patterned PDMS [38]. The patterns of circles seen in the AFM adhesion maps in Figure 3C,E are consistent with differential molecular compositions in the lifted-off vs non-lifted-off regions and the chemically selective removal of molecules terminating in hydroxyl groups and not methyl groups during the second lift-off step, whereby patterned PDMS was produced. Collectively, the data in Figure 3 demonstrate a CLL-centered strategy for regional control of chemical composition on flat PDMS supporting materials.

To evaluate the Au–alkanethiol–PDMS hybrid material further, we quantified the apparent heights of the regions containing the lifted-off Au monolayers using AFM topography maps of patterned PDMS (Figure 1E,F,H). To recognize and to differentiate between regions containing Au–mercaptoundecanol monolayers and PDMS-only background regions, we employed a recently developed image analysis algorithm based on Chan–Vese segmentation [39-41]. This algorithm is an enhanced version of a region-based segmentation method that can be used to detect artifacts and differentiates pattern features from topographically uneven backgrounds, which thresholding strategies cannot straightforwardly accomplish [40]. Furthermore, this algorithm minimizes user bias inherent in delineating regions of interest and maximizes the number of image data points considered. Details and demonstrations of our implementation are provided in the Experimental section and in Figures S8–S10 (Supporting Information File 1).

The Au–mercaptoundecanol monolayers (Figure 4A–C) were associated with heights ranging from 0.63 ± 0.01 nm to 0.93 ± 0.01 nm determined from the Chan–Vese analysis (Figure 4D–I). These apparent heights are smaller than the height of a SAM of mercaptoundecanol on a Au surface, which is 1.3–1.4 nm with a 30° tilt angle relative to the surface normal [42-44]. Considering an interlayer spacing of Au{111} of 2.35 Å [45], the complete lift-off of alkanethiol SAMs from Au surfaces would yield Au–alkanthiol layers approximately

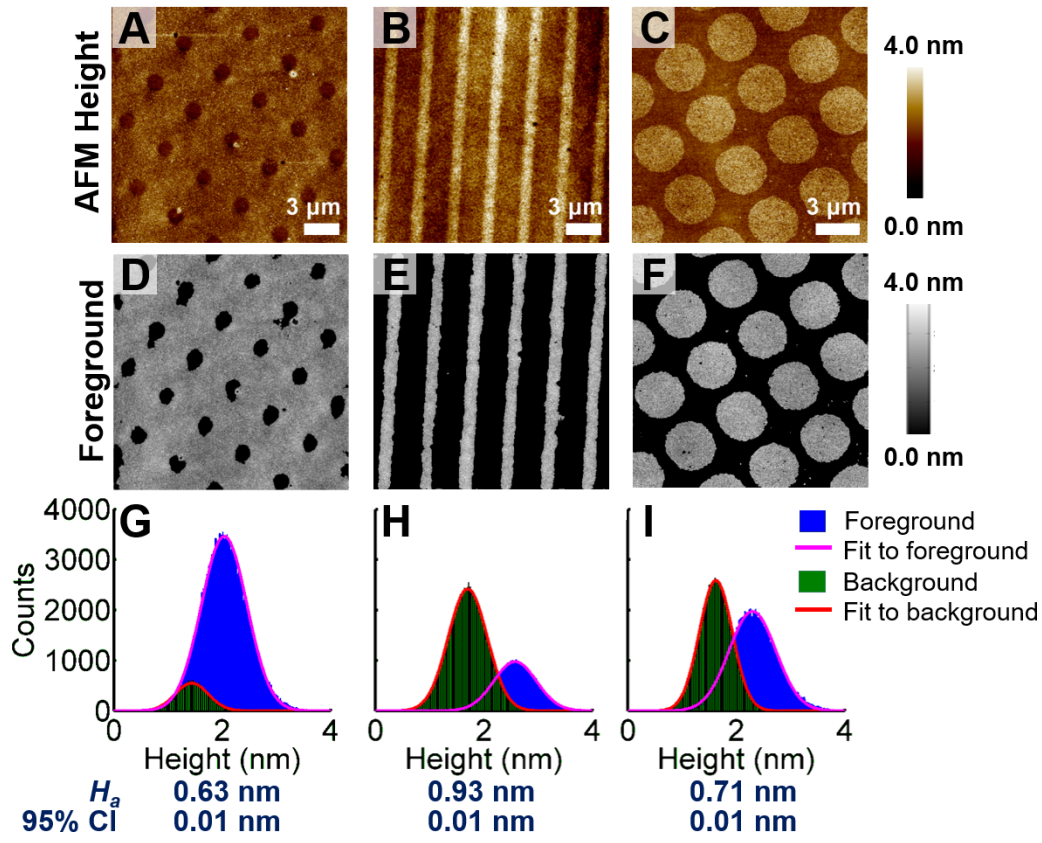

Figure 4: (A–C) Height maps of three different patterns of Au–mercaptoundecanol monolayers on poly(dimethylsiloxane) (PDMS) acquired using peak-force atomic force microscopy. (D–F) Regions classified as "foreground" are determined using the image segmentation algorithm and contain Au–mercaptoundecanol monolayers corresponding to the images shown in panels A–C. (G–I) Histograms of the heights represented by the intensities of foreground and background classifications of pixels. Each histogram was fit to a Gaussian distribution and was consistent with a normal distribution. The calculated apparent height, H_a, determined from each image was the difference in the mean of the foreground and background pixel intensities. The values for H_a and 95% confidence intervals (95% CI) are shown below each graph.

1.6 nm in height, assuming that the molecules retain their original orientation and each thiol removes one Au atom.

Nonetheless, we know that the Au–alkanethiolate monolayers on PDMS resulting from typical CLL experiments are indicative of incomplete lift-off [1,10,31]. Moreover, the dimensions of the Au–alkanethiol complexes that compose the lifted-off monolayer on PDMS are smaller than the spatial resolution of ambient AFM [46]. As such, an average can be calculated for the apparent height by multiplying the typical 60–70% yield of CLL with the full Au–alkanethiolate monolayer height calculated above. Doing so yields an apparent height range of 0.96–1.12 nm, which is still greater than the measured heights (Figure 4). The Au–alkanethiolate complexes on PDMS are expected to adopt a variety of orientations relative to the surface, similar to the variety of orientations of self-assembled alkanethiols at incomplete coverage on Au surfaces [47,48], further reducing our estimate of the apparent height. In all, our measured estimate of the topographic height of a Au–alkanethiol monolayer on PDMS is consistent with all previous CLL characterization attempts and with the predicted one or two atoms lifted-off per alkanethiolate molecule (vide infra).

The assumptions made above regarding the structure of Au–alkanethiolate monolayers on PDMS are in agreement with estimates of the stoichiometry of the Au–alkanethiolate monolayer calculated through molecular dynamics simulations. Atomic rearrangement during the CLL process was modeled using density functional theory and the grid-based projector-augmented wave (GPAW) method [49]. The simulations revealed that a densely packed SAM of chemisorbed butanethiolates was pulled from a Au{111} surface. The details of the initial Au–thiolate surface structure and the pulling speed were varied (see Experimental section). Figure 5 shows the initial structures and later snapshots from two representative simulations. Figure 5A shows the initial structure having RS–Au–SR units (where "R" refers to the butyl chain) on top of a Au{111} surface with defects, while Figure 5B indicates a close-packed layer of butanethiolates on an ideal fcc Au{111} surface.

During lift-off, some Au surface atoms remain attached to the lifting sulfur atoms, breaking the Au surface symmetry and causing reconstruction of the remaining Au surface layer. As lifting continues, some Au atoms move between the sulfur atoms, forming RS–Au–SR structures that are still able to bond to additional Au atoms. Before complete separation, a chain consisting of two or three Au atoms between each thiol and the Au surface is formed and finally ruptures, usually after the first or second Au atom has attached to each sulfur atom. As a consequence of lift-off, a limited number of Au atoms remain bonded to the lifted thiolate layer, forming a Au–thiol complex with a stoichiometry of up to 1.5 Au atoms per thiol. This stoichiometry corresponds to the removal of 50% of the outermost Au{111} layer bearing a densely packed alkanethiol SAM.

We further computationally analyzed the XPS core-level shifts (CLSs) for each Au atom in the lifted-off complexes (Figure S11, Supporting Information File 1). These calculated spectra

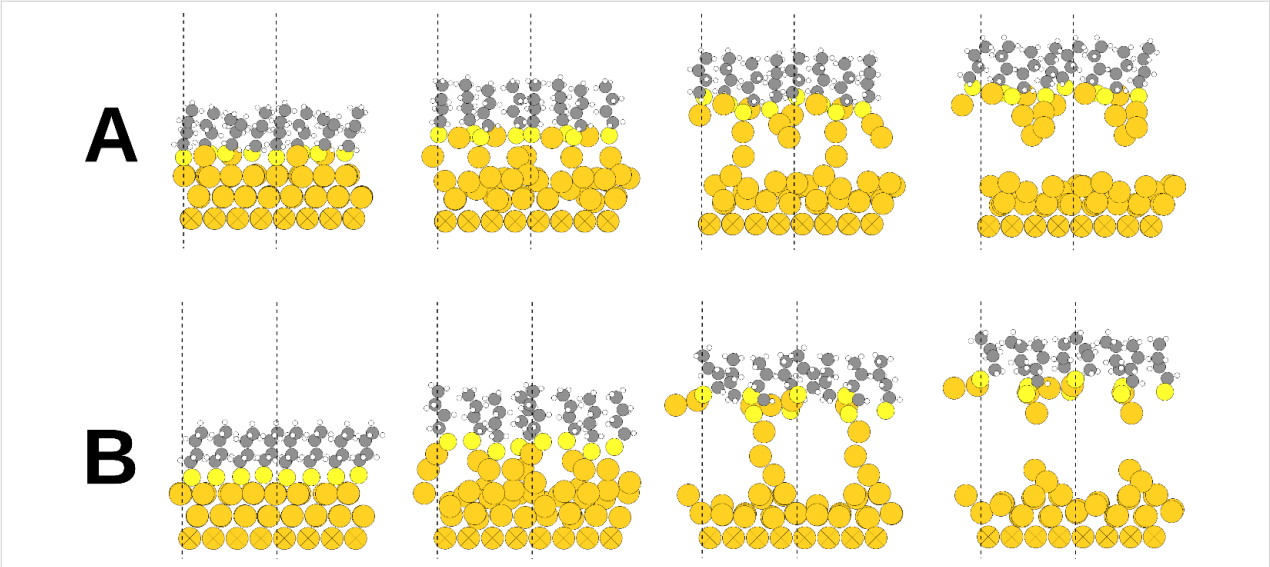

Figure 5: Two configurations calculated by molecular dynamics simulations of lift-off of a butanethiolate SAM on Au{111}. (A) Initially, densely packed RS–Au–SR (R = butyl) units occur on Au{111} having surface vacancies. The number of vacancies equals the number of RS–Au–SR units. (B) Initially, a dense packing of individual butane thiolates occurs at the face-centered cubic sites of a defect-free Au{111} surface. The dashed vertical lines define the borders of each computational unit cell, i.e., in the figure there are two unit cells side by side in each configuration. Atom colors: hydrogen (white); carbon (gray); sulfur (yellow); Au (orange).

are signatures of the predicted structures resulting from CLL of SAMs packed on Au with and without defects. When comparing the spectra and the structures, we found that the shifts are spread ≈1.5 eV around the bulk reference value, and similar chemical environments of the Au atoms resulted in similar core-level shift energies. These simulations indicate that the CLSs of a Au atom in a Au–alkanethiolate monolayer are sensitive to its local environment in the system and that spectral features would reflect the arrangement of self-assembled molecules on the gold surface at initial and/or intermediate stages of CLL. Our current observations are consistent with the predicted stoichiometries, and these simulations form the basis of work to interrogate the structure and stoichiometry of the lifted-off Au monolayer further.

The potential to lift-off Au via PDMS contact is consistent with the discovery that Au–thiolate complexes are the mobile species in SAM diffusion [2,50]. The electronegative sulfur atoms (thiol head groups) withdraw charge from Au atoms, causing measurable changes in the physical properties of Au, including the increased binding energy of Au 4f electrons measured by XPS [51], decreased Au–Au rupture forces in molecular break-junction experiments [52-54], and shorter Au–S bonds compared with Au–Au bonds measured by electron diffraction [55,56]. At molecular resolution, scanning probe measurements have revealed the rearrangement of Au surface atoms [57-59], diffusion and alignment of adatom–adsorbate complexes [50,60], and phase separation of SAMs composed of molecules with different backbones or terminal functionalities [61-63]. Phase separation is driven by stronger intermolecular interactions between one type of SAM molecule vs another in mixed SAMs. The rearrangement and displacement of molecules in mixed monolayers can also be manipulated by choosing other head groups, such as selenols, in place of thiols [64,65].

Theorists have investigated the influence of collective interactions among alkanethiol backbones on the removal of clusters of SAM molecules from Au surfaces [66,67]. For example, less nanomechanical force is required to pull a monolayer of heptanethiolates and Au atoms from a Au substrate than a monolayer of propanethiolates. In addition to previously demonstrated lift-off "compatible" and "incompatible" terminal groups [10,11], the head groups and backbones of the SAM molecules themselves are potential parameters for customizing the composition and chemical state of the lifted-off Au monolayers.

Conclusion

We have devised a suite of fabrication, imaging, and computation strategies to address the structure, functionality, and stoichiometry of Au monolayers lifted-off during chemical lift-off lithography and we have demonstrated a new 2D Au hybrid material with unique properties. Using CLL, we produced a functional hybrid material of Au–alkanethiolate monolayers on topographically flat PDMS that spatially encodes chemical functionality at the surface of PDMS, while preserving the transparency and flexibility of the PDMS. The lateral dimensions and periodicity of the lifted-off monolayers were preserved from the Au-on-Si masters when patterning the lifted-off monolayers on PDMS, as determined by AFM and SEM imaging. These patterns of Au monolayers were recognizable in fluorescence microscopy when functionalized with thiolated DNA that was hybridized with dye-labeled complementary DNA.

The analysis of the relative heights from AFM images revealed that less than a complete monolayer of Au–alkanethiolates remains on the PDMS material, which is consistent with previous findings and indicates that CLL removes ≈70% of molecules from contact regions. In agreement with indirect evidence that a monolayer of Au is removed during CLL, molecular dynamics simulations converged on a stoichiometry of ≤1.5 Au atoms per thiol. These simulations also demonstrate that the lifted-off Au atoms are in an environment distinct from that at the surface of the bulk Au and are predicted to be distinguishable in photoelectron spectra.

This body of evidence demonstrates that CLL, an already straightforward method for patterning square centimeter areas of alkanethiol monolayers of Au-on-Si substrates, can also be used to pattern PDMS with Au and to impart encoded chemical functionality without affecting the flexibility or transparency of PDMS. Incorporating chemical functionality onto PDMS will be useful for integrating sensing functions into microfluidic devices [68-80]. Compared with many techniques used to impart sub-micrometer features onto PDMS [74-76], CLL is parallel, high-throughput, and is performed under ambient conditions.

Further studies will test the impact of the composition of the supporting molecules on the properties of the lifted-off Au monolayer. The structural and electronic properties of the Au monolayer can be tailored by varying the properties of the supporting molecules [2]. For example, limiting the degrees of freedom of the supporting monolayer by replacing mercaptoundecanol with unsaturated alkanethiols or rigid cage molecules may result in a monolayer that better maintains a planar two-dimensional geometry [2]. Additionally, carboranethiols, which are known to form pristine and nearly defect-free SAMs [61,81,82], or molecules with additional interactions among the backbones, such as 3-mercapto-*N*-nonylpropionamide, which forms hydrogen-bonding networks [83,84], are hypothesized to

increase the yield of lifted-off molecules during CLL and to produce more intact, supported monolayers [2]. Replacing thiol moieties with groups that bind more strongly to Au [4,64,65], such as selenolates, will also be investigated. Thus, a rich variety of tunable variables, including stamp geometry, chemical backbone, and anchor groups remain to be explored for CLL.

Ultimately, the resolution of CLL will be defined by the ability to control the separation between individual lifted-off Au–alkanethiolate regions on PDMS (or other supports). It may be possible to dilute the "liftable" alkanethiols on gold [8] to reach the ultimate limit of lifting off single molecules. However, the fidelity of the features achieved (i.e., the ability to replicate features defined by the alkanethiol monolayers on Au onto the PDMS) will increase with increasing CLL yield. In addition, increasing the CLL yield will improve the fidelity of the patterns of Au–alkanethiols lifted-off on PDMS, and thus, presumably more complete and closely packed supported Au monolayers on PDMS.

The computation, fabrication, and visualization strategies established herein form a basic toolbox for interrogating the influence of these variables on CLL and the structure and functionality of the resulting hybrid materials. Further development of CLL has significant potential for fabricating sensors, biocompatible platforms, and other applications that will benefit from flexible, transparent, bio-inert materials combined with the extensive functionalization chemistries of Au.

Experimental

Fabricating patterned polydimethylsiloxane stamps

Stamps with topographic features were prepared as previously described [85]. The Sylgard® 184 silicone elastomer kits were purchased from Dow Corning (Midland, MI, USA). The elastomer base and curing agent were mixed in a 10:1 ratio by weight, stirred for 3–5 min, and degassed in a vacuum desiccator for at least 1 h to remove air bubbles. Degassed mixtures were poured over silicon molds (purchased from KTek Nanotechnology, LLC, Wilsonville, OR, USA or fabricated by photolithography) situated in Petri dishes. After degassing again, the PDMS stamps were cured in an oven at 60 °C for 12 h. The PDMS stamps were separated from the silicon masters carefully and cut into desired sizes.

Patterning Au-on-silicon masters

Silicon wafers with 100 nm Au and 5 nm titanium adhesion layers (Platypus, Madison, WI, USA) were trimmed with a diamond scribe to ≈1 × 1 cm sample size. The substrates were annealed with a hydrogen flame and incubated in 1.0 mM ethanolic solutions of mercaptoundecanol overnight at room temperature and ambient pressure to form SAMs. The patterned PDMS stamps were treated with oxygen plasma (Harrick, Ithaca, NY, USA) for 40 s and contacted with SAMs. The stamps were removed from Au substrates after 2 h. The substrates were then treated with 20 mM iron(III) nitrate and 30 mM thiourea for 10–15 min to etch the Au selectively from the exposed regions.

Fabricating flat poly(dimethylsiloxane) stamps

The PDMS stamps were templated using featureless silicon wafers. The silicon wafer pieces (Silicon Quest International, San Jose, CA, USA) were degreased by sonicating sequentially for 5 min in ethanol, 3 min in deionized water, and 5 min in ethanol. The silicon wafer pieces were immediately rinsed with ethanol and blown dry with compressed nitrogen gas. They were then exposed to hexamethyldisilazane vapor for 10 min in a closed chamber to facilitate later removal of PDMS. Glass slides (VWR, Radnor, PA, USA) were trimmed to ≈2.5 × 2.5 cm squares and sonicated for 20 min in 1% (w/v) Alconox, rinsed with deionized water, and cleaned two additional times. Clean glass pieces were stored in deionized water until they were rinsed and blown dry immediately before use.

Using a plastic spatula with a tapered tip, 1–2 drops of degassed PDMS (10:2 elastomer/curing agent by weight) were placed on the silicon pieces and degassed for an additional 5–10 min. Flat PDMS films were physically attached to glass slide pieces to minimize damage to their surfaces during handling. Dry glass slide pieces were treated with an oxygen plasma for 40 s. Upon removing the silicon pieces with PDMS from the desiccator, a small drop of PDMS was placed on each glass slide, which was then placed gently on top of the PDMS. The "sandwiches" were cured on a hot plate at 110 °C under a 4.5 kg steel-brick weight. After 10 min, the heat was turned off while the "sandwiches" remained under the weight overnight.

Patterning flat poly(dimethylsiloxane) stamps

The patterned Au-on-Si masters were annealed with a hydrogen flame and then immersed in 1.0 mM mercaptoundecanol overnight to form new SAMs on the patterned Au regions. Prior to performing CLL, the masters were sonicated three times for 1 s in fresh ethanol, rinsed, and blown dry. The PDMS on glass pieces was removed from the silicon templates immediately before use, rinsed with ethanol, blown dry with compressed nitrogen, and O_2-plasma-treated for 40 s to activate surfaces. The Au-on-Si masters were placed face down on the PDMS samples. After initial contact and gently pressing by hand, no additional vertical pressure was applied. The contacted regions were lightly marked on the glass underside with a permanent

marker. After contact for 2–24 h, depending on the experiment, the Au-on-Si masters were carefully removed from the PDMS. The marked regions were scratched lightly into the PDMS before each sample was rinsed on both sides with ethanol and blown dry.

Peak-force atomic force microscopy

A Bruker Dimension Icon scanning probe microscope (Bruker Nano, Santa Barbara, CA, USA) was used to map the topography and mechanical properties of flat PDMS stamps patterned with Au–alkanethiolate monolayers. The AFM images of the PDMS stamps (flat and patterned) were measured using the peak force quantitative nanomechanical property mapping mode. ScanAsyst-Air cantilevers (Bruker, spring constant = 0.4 ± 0.1 N/m) were calibrated with a clean piece of silicon before each measurement. A peak-force set-point between 200 and 400 pN was maintained, except where otherwise indicated. These conditions enabled sufficient contact between tips and samples for imaging, while minimizing the load from the cantilever applied to the PDMS.

Scanning electron microscopy of Au-on-Si masters

Scanning electron microscopy was performed using a JEOL JSM-6700F scanning electron microscope (JEOL, Inc., Tokyo, Japan) with a 750 V DC detector bias and 5 kV accelerating voltage.

Field-emission gun variable pressure electron microscopy of Au on PDMS

The scanning electron micrographs of Au–alkanethiolate monolayers on flat PDMS were imaged with a low-vacuum detector in a Nova NanoSEM 230 microscope (FEI, Czech Republic) operating at an accelerating voltage of 5 kV. The samples were affixed to the SEM stub and grounded by conductive carbon and copper tape. Variable pressure SEM (VP-SEM) was performed under 50 Pa of water vapor in the sample chamber to avoid charging of the insulating PDMS surfaces by the electron beam.

Functional DNA patterns on supported Au monolayers

As-received DNA (Integrated DNA Technologies, Coralville, IA, USA) was diluted in nuclease-free water (QIAGEN, Valencia, CA, USA) to make 100 μM stock solutions. Immediately prior to experiments, the DNA stock solutions were diluted 1:100 with 1× phosphate buffered saline (PBS) ([NaCl] = 138 mM, [KCl] = 2.7 mM, and [$MgCl_2$] = 5 mM) pH 7.4 (Sigma-Aldrich, St. Louis, MO, USA) to make 1 μM solutions. The patterns of Au–alkanethiolate monolayers on flat PDMS substrates were functionalized with thiolated single-stranded DNA solutions by pipetting 50–100 μL of 1 μM DNA solutions onto the substrates to cover the patterned regions and incubating for ≈20 h at room temperature. The substrates were then thoroughly rinsed with deionized water and blown dry with nitrogen gas. For DNA hybridization on Au–alkanethiolate monolayers on flat PDMS, 50–100 μL of 1 μM AlexaFluor® 488-labeled complementary DNA was pipetted onto the substrates, which were then incubated for 1 h at room temperature. During incubation, the substrates were kept in the dark to minimize photobleaching of fluorescent dyes by ambient light. The substrates were rinsed again with deionized water and blown dry with nitrogen gas.

The DNA duplexes on Au–alkanethiolate monolayers were imaged at an emission wavelength of 517 nm (AlexaFluor® 488; excitation at 492 nm) with an inverted fluorescence microscope (Model: Axio Observer.D1) equipped with an AxioCam MRm charged-coupled device camera (Carl Zeiss Micro-Imaging, Inc., Thornwood, NY, USA) and a fluorescence filter with excitation and emission wavelengths at 470 ± 20 nm and 525 ± 25 nm, respectively (38 HE/high efficiency, Carl Zeiss Micro-Imaging, Inc.).

In Figure 2A,B, the patterns were formed on an unsupported slab of PDMS. These patterns were functionalized with thiolated single-stranded DNA (5′-TCT CAA GAA TCG GCA TTA GCT CAA CTG TCA ACT CCT CTT T/3ThioMC3-D/-3′) using the procedure described above. Thiolated DNA strands were hybridized with dye-labeled complementary strands (5′-AAA GAG GAG TTG ACA GTT GAG CTA ATG CCG ATT CTT GAG A/3AlexF488N/-3′). The samples were then imaged with the patterned side facing down in a drop of deionized water on a clean cover slip. The magnification and exposure time was adjusted appropriately for each patterned region. The same preparation and imaging strategy was employed for samples in Figure S5, Supporting Information File 1.

For patterns in Figure 2C,D, the samples were prepared on thin PDMS substrates supported on glass, similar to the sample shown in the photograph in Figure S4, Supporting Information File 1. Thiolated DNA and dye-labeled complementary sequences were 5′-/5-thioMC6-D/ GCA CGA AAC CCA AAC CTG ACC TAA CCA ACG TGC T-3′ and 5′-/5-Alex488N/ AGC ACG TTG GTT AGG TCA GGT TTG GGT TTC GTG C-3′. For control experiments, substrates functionalized with thiolated DNA were incubated with 1 μM AlexaFluor® 488-labeled fully scrambled DNA sequences (5′-/5-Alex488N/ CAT GAA CCA ACC CAA GTC AAC GCA AAC GCA TCA A-3′) to test the specificity of DNA hybridization on patterns of Au–alkanethiolate monolayers. In other experiments, the substrates were incubated with 1× PBS pH 7.4 without thiolated

DNA followed by incubation of 1 μM AlexaFluor® 488-labeled complementary DNA. Each substrate was positioned on the microscope sample holder such that the PDMS side was facing away from the light source and the rear side (glass side) of the substrate was facing toward the light source. The images were collected under dry or aqueous conditions. Deionized water drops were pipetted onto the PDMS side of glass substrates to cover the ultrathin Au patterns for imaging under aqueous conditions.

X-ray photoelectron spectroscopy

The XPS spectra were acquired on an AXIS Ultra DLD instrument (Kratos Analytical Inc., Chestnut Ridge, NY, USA) under ultrahigh vacuum conditions (10^{-9} torr) using a monochromatic Al Kα X-ray source (20 mA, 14 kV) with a 200 μm diameter circular spot size. The pass energy was 80 mV for the survey spectra and 20 mV for high-resolution spectra of the C 1s, S 2p, O 1s, and Au 4f regions. All data points were acquired with a 200 ms dwell time. For adequate signal-to-noise, the number of scans was adjusted for different regions of the spectrum to account for different relative sensitivity factors and low amounts of Au, ranging from 20 scans for C 1s to 100 scans for Au 4f. Because PDMS is an insulator, a charge neutralizer (flood gun) was used to offset charging of the samples that otherwise impedes spectral acquisition. Doing so, however, causes the peak to shift to lower energies as compared to their expected energy obtained without using a flood gun.

Chan–Vese segmentation

In our implementation, AFM topography maps were segmented into foreground regions, which contained lifted-off complexes, and background regions, which contained only PDMS. The algorithm also output a matrix indicating the location of artifacts, which were then excluded from subsequent analysis of both the foreground and background regions (Figure S8B). During post-segmentation analysis, the histograms of the two regions were plotted and then fit to Gaussian distributions. Because the data were normally distributed, the apparent height of the lifted-off layers was calculated through the difference of the mean of the foreground and background pixel intensities.

Calculating the apparent height line-by-line along the fast-scan direction (a conventional way of calculating the average intensity difference in each line) gave similar values for the apparent height as that calculated using all image pixels (Figure S9, Supporting Information File 1). The imaging force set-point chosen for use in these studies provided sufficient force for imaging, while minimizing the deformation of Au–alkanethiolate monolayers. The apparent height was shown to be equally and minimally influenced by the imaging force (Figure S10, Supporting Information File 1).

Molecular dynamics simulations

Molecular dynamics simulations were carried out using density functional theory with the Perdew–Burke–Ernzerhof functional [86] using a gridded-based projector augmented wave code [49,87]. In total, 12 pulling simulations were performed using a grid basis (with a grid spacing of 0.2 Å) and a linear combination of atomic orbitals basis with double-zeta polarized functions. The thermal movement of atoms was simulated using the Langevin thermostat targeting room temperature, implemented in the atomic simulation environment [88]. The thermostat adds both a small, random contribution to the force on the atoms and a small friction factor that slows them down, aiming for an average total kinetic energy of the atoms that corresponds to the target temperature. The time step for molecular dynamics was 2 fs. To maintain the stability of hydrogen atoms on this time scale, the mass was increased to the mass of deuterium.

The unit cell was orthogonal with a size of 8.87 Å in the x-direction and 10.24 Å in the y-direction, in which the unit cell was also set to be periodic. In the z-direction, a 10 Å vacuum was set both above and below the structure. In the unit cell, the Au slab consisted of (3, 4, 3) atoms in the (x, y, z) directions, respectively, fulfilling a {111} surface structure with the surface vector pointing in the z-direction. The lattice constant was 4.18 Å, corresponding to the theoretical lattice constant of Au in the Perdew–Burke–Ernzerhof approximation. Gamma-points were used in each direction. In addition, four 1-butanethiolates were set on the Au surface forming a $(3 \times 2\sqrt{3})$-rectangular-symmetric structure. Individual thiolates were set to the fcc positions of the Au{111} surface. In the case of the RS–Au–SR units, the Au adatoms were set to bridge positions and the sulfur atoms to positions above the surface and next to adatoms. Butyl was chosen for the alkyl tail as long enough to form the (3 Å $\approx 2\sqrt{3}$) rectangular symmetry naturally but short enough to keep computational costs as low as possible [89].

Before removal, the system was heated up to room temperature using the Langevin thermostat with a friction parameter of 0.002 s^{-1}; the heating procedure was run for 2 ps in simulated time. The lowest layer of Au was fixed in its initial position to enable the removal of the thiolates. The pulling moved the terminal carbon atoms with constant velocity outward from the Au surface. Typically, a velocity of 0.5 Å/ps was used. The calculation was continued until thiolate/Au complexes had been completely separated from the surface. The Langevin thermostat was used throughout the calculation to maintain the total energy of the system damping to the energy added due to pulling.

Core-level shifts were calculated for the Au atoms in the modeled structures that were removed from surfaces in the

simulations. The density functional theory with the PBE functional was used again via GPAW to calculate the energies of the structures. The procedure followed the one used by Grönbeck [90]. After relaxing the removed structure to a local energy minimum with residual forces below 0.05 eV/Å on any atom, an electron was removed from the 4f core of a Au atom and the change in the total energy of the system was calculated. To make the results comparable, the energy shift of a bulk Au atom was then subtracted from this energy change.

Supporting Information

Supporting Information File 1

Additional figures.

Details: The supporting information contains additional figures detailing the fabrication of the Au-on-Si masters, unmodified VP-SEM images, reusability, optical, stability, and AFM imaging force studies, fluorescence control experiments, image segmentation details, and computational core-level shift spectra.

[http://www.beilstein-journals.org/bjnano/content/supplementary/2190-4286-8-265-S1.pdf]

Acknowledgments

The work was supported by U.S. Department of Energy Grant #DE-SC-1037004 for fabrication and experimental measurements and the W.M. Keck Foundation Center for Leveraging Sparsity for the development and application of the image analysis tools. A.M.A. thanks the Shirley and Stephan Hatos Foundation for support. S.L. acknowledges support from the Robert A. Welch Foundation (Grant C-1664). The computational work was supported by grants 294217 and 266492 from the Academy of Finland and by the Academy Professorship for H.H. The simulations were run at the CSC – the Finnish IT Center for Science in Espoo, Finland. S.K. thanks Pekka Koskinen for helpful discussions and assistance in preparation of the molecular dynamics simulations. L.S.S. thanks the Merkin Family Foundation for the Merkin Family Foundation Postdoctoral Fellowship. We thank Dr. Adam Stieg and the Nano Pico Characterization facility at UCLA for assistance with AFM, and Dr. Sergey Prikhodko for assistance with VP-SEM. We thank Profs. Andrea Bertozzi, Peter Nordlander, Ya-Hong Xie, Francisco Zaera, and Dominique Zosso, and Drs. Wei-Shun Chang, Ilkeun Lee, Alejandro Manjavacas, Sergey Ryazantsev and Ming Xia for insightful discussions and preliminary measurements and simulations. We thank Profs. Andrea Kasko, Scott Warren, and Shimon Weiss, and Drs. Steven Hawks, Jaemyung Kim, Nako Nakatsuka, Jeffrey Schwartz, Kristina C. Wilson, and Xiaobin Xu, as well as John M. Abendroth for their input and assistance in preparing this manuscript.

ORCID® iDs

Liane S. Slaughter - https://orcid.org/0000-0001-9251-775X
Kevin M. Cheung - https://orcid.org/0000-0003-1586-0364
Sami Kaappa - https://orcid.org/0000-0001-6989-6077
Qing Yang - https://orcid.org/0000-0003-4422-5300
Andrew C. Serino - https://orcid.org/0000-0003-2767-1026
Jana M. Olson - https://orcid.org/0000-0001-9213-4986
Stephan Link - https://orcid.org/0000-0002-4781-930X
Anne M. Andrews - https://orcid.org/0000-0002-1961-4833
Paul S. Weiss - https://orcid.org/0000-0001-5527-6248

References

1. Liao, W.-S.; Cheunkar, S.; Cao, H. H.; Bednar, H. R.; Weiss, P. S.; Andrews, A. M. *Science* **2012,** *337,* 1517–1521. doi:10.1126/science.1221774
2. Andrews, A. M.; Liao, W.-S.; Weiss, P. S. *Acc. Chem. Res.* **2016,** *49,* 1449–1457. doi:10.1021/acs.accounts.6b00034
3. Xia, Y.; Whitesides, G. M. Self-assembled Monolayer Films: Microcontact Printing. *Encyclopedia of Materials: Science and Technology;* Elsevier Science Ltd., 2001; pp 8309–8315. doi:10.1016/B0-08-043152-6/01487-X
4. Smith, R. K.; Lewis, P. A.; Weiss, P. S. *Prog. Surf. Sci.* **2004,** *75,* 1–68. doi:10.1016/j.progsurf.2003.12.001
5. Srinivasan, C.; Mullen, T. J.; Hohman, J. N.; Anderson, M. E.; Dameron, A. A.; Andrews, A. M.; Dickey, E. C.; Horn, M. W.; Weiss, P. S. *ACS Nano* **2007,** *1,* 191–201. doi:10.1021/nn7000799
6. Carlson, A.; Bowen, A. M.; Huang, Y.; Nuzzo, R. G.; Rogers, J. A. *Adv. Mater.* **2012,** *24,* 5284–5318. doi:10.1002/adma.201201386
7. Xu, X.; Yang, Q.; Cheung, K. M.; Zhao, C.; Wattanatorn, N.; Belling, J. N.; Abendroth, J. M.; Slaughter, L. S.; Mirkin, C. A.; Andrews, A. M.; Weiss, P. S. *Nano Lett.* **2017,** *17,* 3302–3311. doi:10.1021/acs.nanolett.7b01236
8. Claridge, S. A.; Liao, W.-S.; Thomas, J. C.; Zhao, Y.; Cao, H. H.; Cheunkar, S.; Serino, A. C.; Andrews, A. M.; Weiss, P. S. *Chem. Soc. Rev.* **2013,** *42,* 2725–2745. doi:10.1039/C2CS35365B
9. Kim, J.; Rim, Y. S.; Chen, H.; Cao, H. H.; Nakatsuka, N.; Hinton, H. L.; Zhao, C.; Andrews, A. M.; Yang, Y.; Weiss, P. S. *ACS Nano* **2015,** *9,* 4572–4582. doi:10.1021/acsnano.5b01211
10. Cao, H. H.; Nakatsuka, N.; Serino, A. C.; Liao, W.-S.; Cheunkar, S.; Yang, H.; Weiss, P. S.; Andrews, A. M. *ACS Nano* **2015,** *9,* 11439–11454. doi:10.1021/acsnano.5b05546
11. Cao, H. H.; Nakatsuka, N.; Liao, W.-S.; Serino, A. C.; Cheunkar, S.; Yang, H.; Weiss, P. S.; Andrews, A. M. *Chem. Mater.* **2017,** *29,* 6829–6839. doi:10.1021/acs.chemmater.7b01970
12. Abendroth, J. M.; Nakatsuka, N.; Ye, M.; Kim, D.; Fullerton, E. E.; Andrews, A. M.; Weiss, P. S. *ACS Nano* **2017,** *11,* 7516–7526. doi:10.1021/acsnano.7b04165
13. Zhao, C.; Xu, X.; Yang, Q.; Man, T.; Jonas, S. J.; Schwartz, J. J.; Andrews, A. M.; Weiss, P. S. *Nano Lett.* **2017,** *17,* 5035–5042. doi:10.1021/acs.nanolett.7b02269
14. Butler, S. Z.; Hollen, S. M.; Cao, L.; Cui, Y.; Gupta, J. A.; Gutiérrez, H. R.; Heinz, T. F.; Hong, S. S.; Huang, J.; Ismach, A. F.; Johnston-Halperin, E.; Kuno, M.; Plashnitsa, V. V.; Robinson, R. D.; Ruoff, R. S.; Salahuddin, S.; Shan, J.; Shi, L.; Spencer, M. G.; Terrones, M.; Windl, W.; Goldberger, J. E. *ACS Nano* **2013,** *7,* 2898–2926. doi:10.1021/nn400280c

15. Bhimanapati, G. R.; Lin, Z.; Meunier, V.; Jung, Y.; Cha, J.; Das, S.; Xiao, D.; Son, Y.; Strano, M. S.; Cooper, V. R.; Liang, L.; Louie, S. G.; Ringe, E.; Zhou, W.; Kim, S. S.; Naik, R. R.; Sumpter, B. G.; Terrones, H.; Xia, F.; Wang, Y.; Zhu, J.; Akinwande, D.; Alem, N.; Schuller, J. A.; Schaak, R. E.; Terrones, M.; Robinson, J. A. *ACS Nano* **2015,** *9,* 11509–11539. doi:10.1021/acsnano.5b05556
16. Zhang, H. *ACS Nano* **2015,** *9,* 9451–9469. doi:10.1021/acsnano.5b05040
17. Tan, C.; Cao, X.; Wu, X.-J.; He, Q.; Yang, J.; Zhang, X.; Chen, J.; Zhao, W.; Han, S.; Nam, G.-H.; Sindoro, M.; Zhang, H. *Chem. Rev.* **2017,** *117,* 6225–6331. doi:10.1021/acs.chemrev.6b00558
18. Jacoby, M. *Chem. Eng. News* **2017,** *95* (22), 36–40.
19. Kung, L. A.; Kam, L.; Hovis, J. S.; Boxer, S. G. *Langmuir* **2000,** *16,* 6773–6776. doi:10.1021/la000653t
20. Meitl, M. A.; Zhu, Z.-T.; Kumar, V.; Lee, K. J.; Feng, X.; Huang, Y. Y.; Adesida, I.; Nuzzo, R. G.; Rogers, J. A. *Nat. Mater.* **2006,** *5,* 33–38. doi:10.1038/nmat1532
21. Hovis, J. S.; Boxer, S. G. *Langmuir* **2001,** *17,* 3400–3405. doi:10.1021/la0017577
22. Wisser, F. M.; Schumm, B.; Mondin, G.; Grothe, J.; Kaskel, S. *J. Mater. Chem. C* **2015,** *3,* 2717–2731. doi:10.1039/C4TC02418D
23. Rogers, J. A. *Science* **2012,** *337,* 1459. doi:10.1126/science.1228493
24. Doron-Mor, I.; Barkay, Z.; Filip-Granit, N.; Vaskevich, A.; Rubinstein, I. *Chem. Mater.* **2004,** *16,* 3476–3483. doi:10.1021/cm049605a
25. Zheng, J.; Zhou, C.; Yu, M.; Liu, J. *Nanoscale* **2012,** *4,* 4073–4083. doi:10.1039/c2nr31192e
26. Slaughter, L.; Chang, W.-S.; Link, S. *J. Phys. Chem. Lett.* **2011,** *2,* 2015–2023. doi:10.1021/jz200702m
27. Dokukin, M. E.; Sokolov, I. *Langmuir* **2012,** *28,* 16060–16071. doi:10.1021/la302706b
28. Lopez, G. P.; Biebuyck, H. A.; Whitesides, G. M. *Langmuir* **1993,** *9,* 1513–1516. doi:10.1021/la00030a015
29. Bittermann, A. G.; Jacobi, S.; Chi, L. F.; Fuchs, H.; Reichelt, R. *Langmuir* **2001,** *17,* 1872–1877. doi:10.1021/la0004956
30. Mack, N. H.; Dong, R.; Nuzzo, R. G. *J. Am. Chem. Soc.* **2006,** *128,* 7871–7881. doi:10.1021/ja060248+
31. Kim, E.; Park, K.; Hwang, S. *Electrochim. Acta* **2017,** *246,* 165–172. doi:10.1016/j.electacta.2017.05.195
32. Slaughter, L. S.; Wang, L.-Y.; Willingham, B. A.; Olson, J. M.; Swanglap, P.; Dominguez-Medina, S.; Link, S. *Nanoscale* **2014,** *6,* 11451–11461. doi:10.1039/C4NR02839B
33. Seaborg, G. T.; Wahl, A. C. *J. Am. Chem. Soc.* **1948,** *70,* 1128–1134. doi:10.1021/ja01183a076
34. Seaborg, G. T. *Acc. Chem. Res.* **1995,** *28,* 257–264. doi:10.1021/ar00054a003
35. Claridge, S. A.; Castleman, A. W., Jr.; Khanna, S. N.; Murray, C. B.; Sen, A.; Weiss, P. S. *ACS Nano* **2009,** *3,* 244–255. doi:10.1021/nn800820e
36. Schwartz, D. K. *Annu. Rev. Phys. Chem.* **2001,** *52,* 107–137. doi:10.1146/annurev.physchem.52.1.107
37. Schreiber, F. *Prog. Surf. Sci.* **2000,** *65,* 151–257. doi:10.1016/S0079-6816(00)00024-1
38. Schönherr, H.; Vancso, G. J. Atomic Force Microscopy in Practice. *Scanning Force Microscopy of Polymers,* 1st ed.; Springer-Verlag: Berlin, Germany, 2010; pp 25–75. doi:10.1007/978-3-642-01231-0_2
39. Chan, T. F.; Vese, L. A. *IEEE Trans. Image Process.* **2001,** *10,* 266. doi:10.1109/83.902291
40. Zosso, D.; An, J.; Stevick, J.; Takaki, N.; Weiss, M.; Slaughter, L. S.; Cao, H. H.; Weiss, P. S.; Bertozzi, A. L. *Inverse Probl. Imaging* **2017,** *11,* 577–600. doi:10.3934/ipi.2017027
41. Zosso, D.; Tran, G.; Osher, S. J. *SIAM J. Imaging Sci.* **2015,** *8,* 787–826. doi:10.1137/140972664
42. Love, J. C.; Estroff, L. A.; Kriebel, J. K.; Nuzzo, R. G.; Whitesides, G. M. *Chem. Rev.* **2005,** *105,* 1103–1170. doi:10.1021/cr0300789
43. Zaccari, I.; Catchpole, B. G.; Laurenson, S. X.; Davies, A. G.; Wälti, C. *Langmuir* **2014,** *30,* 1321–1326. doi:10.1021/la403983b
44. Kim, D.-J.; Koo, K.-K. *Ind. Eng. Chem. Res.* **2004,** *10,* 920–926.
45. Biscarini, F.; Bustamante, C.; Kenkre, V. M. *Phys. Rev. B* **1995,** *51,* 11089–11102. doi:10.1103/PhysRevB.51.11089
46. Wastl, D. S. *Microsc. Res. Tech.* **2017,** *80,* 50–65. doi:10.1002/jemt.22730
47. Shuster, M. J.; Vaish, A.; Gilbert, M. L.; Martinez-Rivera, M.; Nezarati, R. M.; Weiss, P. S.; Andrews, A. M. *J. Phys. Chem. C* **2011,** *115,* 24778–24787. doi:10.1021/jp207396m
48. Schwartz, J. J.; Hohman, J. N.; Morin, E. I.; Weiss, P. S. *ACS Appl. Mater. Interfaces* **2013,** *5,* 10310–10316. doi:10.1021/am403259q
49. Enkovaara, J.; Rostgaard, C.; Mortensen, J. J.; Chen, J.; Dułak, M.; Ferrighi, L.; Gavnholt, J.; Glinsvad, C.; Haikola, V.; Hansen, H. A.; Kristoffersen, H. H.; Kuisma, M.; Larsen, A. H.; Lehtovaara, L.; Ljungberg, M.; Lopez-Acevedo, O.; Moses, P. G.; Ojanen, J.; Olsen, T.; Petzold, V.; Romero, N. A.; Stausholm-Møller, J.; Strange, M.; Tritsaris, G. A.; Vanin, M.; Walter, M.; Hammer, B.; Häkkinen, H.; Madsen, G. K. H.; Nieminen, R. M.; Nørskov, J. K.; Puska, M.; Rantala, T. T.; Schiøtz, J.; Thygesen, K. S.; Jacobsen, K. W. *J. Phys.: Condens. Matter* **2010,** *22,* 253202. doi:10.1088/0953-8984/22/25/253202
50. Stranick, S. J.; Parikh, A. N.; Allara, D. L.; Weiss, P. S. *J. Phys. Chem.* **1994,** *98,* 11136–11142. doi:10.1021/j100094a024
51. Chaudhuri, A.; Lerotholi, T. J.; Jackson, D. C.; Woodruff, D. P.; Dhanak, V. *Phys. Rev. Lett.* **2009,** *102,* 126101. doi:10.1103/PhysRevLett.102.126101
52. Xue, Y.; Li, X.; Li, H.; Zhang, W. *Nat. Commun.* **2014,** *5,* 4348. doi:10.1038/ncomms5348
53. Huang, Z.; Chen, F.; Bennett, P. A.; Tao, N. *J. Am. Chem. Soc.* **2007,** *129,* 13225–13231. doi:10.1021/ja074456t
54. Frei, M.; Aradhya, S. V.; Hybertsen, M. S.; Venkataraman, L. *J. Am. Chem. Soc.* **2012,** *134,* 4003–4006. doi:10.1021/ja211590d
55. Azubel, M.; Koivisto, J.; Malola, S.; Bushnell, D.; Hura, G. L.; Koh, A. L.; Tsunoyama, H.; Tsukuda, T.; Pettersson, M.; Häkkinen, H.; Kornberg, R. D. *Science* **2014,** *345,* 909–912. doi:10.1126/science.1251959
56. Jadzinsky, P. D.; Calero, G.; Ackerson, C. J.; Bushnell, D. A.; Kornberg, R. D. *Science* **2007,** *318,* 430–433. doi:10.1126/science.1148624
57. Maksymovych, P.; Sorescu, D. C.; Yates, J. T., Jr. *Phys. Rev. Lett.* **2006,** *97,* 146103. doi:10.1103/PhysRevLett.97.146103
58. Wang, Y.; Chi, Q.; Hush, N. S.; Reimers, J. R.; Zhang, J.; Ulstrup, J. *J. Phys. Chem. C* **2009,** *113,* 19601–19608. doi:10.1021/jp906216k
59. Vericat, C.; Vela, M. E.; Salvarezza, R. C. *Phys. Chem. Chem. Phys.* **2005,** *7,* 3258–3268. doi:10.1039/b505903h
60. Alaee, R.; Menzel, C.; Huebner, U.; Pshenay-Severin, E.; Bin Hasan, S.; Pertsch, T.; Rockstuhl, C.; Lederer, F. *Nano Lett.* **2013,** *13,* 3482–3486. doi:10.1021/nl4007694
61. Hohman, J. N.; Zhang, P.; Morin, E. I.; Han, P.; Kim, M.; Kurland, A. R.; McClanahan, P. D.; Balema, V. P.; Weiss, P. S. *ACS Nano* **2009,** *3,* 527–536. doi:10.1021/nn800673d
62. Stranick, S. J.; Parikh, A. N.; Tao, Y.-T.; Allara, D. L.; Weiss, P. S. *J. Phys. Chem.* **1994,** *98,* 7636–7646. doi:10.1021/j100082a040

63. Smith, R. K.; Reed, S. M.; Lewis, P. A.; Monnell, J. D.; Clegg, R. S.; Kelly, K. F.; Bumm, L. A.; Hutchison, J. E.; Weiss, P. S. *J. Phys. Chem. B* **2001,** *105,* 1119–1122. doi:10.1021/jp0035129
64. Hohman, J. N.; Thomas, J. C.; Zhao, Y.; Auluck, H.; Kim, M.; Vijselaar, W.; Kommeren, S.; Terfort, A.; Weiss, P. S. *J. Am. Chem. Soc.* **2014,** *136,* 8110–8121. doi:10.1021/ja503432f
65. Monnell, J. D.; Stapleton, J. J.; Jackiw, J. J.; Dunbar, T.; Reinerth, W. A.; Dirk, S. M.; Tour, J. M.; Allara, D. L.; Weiss, P. S. *J. Phys. Chem. B* **2004,** *108,* 9834–9841. doi:10.1021/jp037728x
66. Ribas-Arino, J.; Marx, D. *Chem. Rev.* **2012,** *112,* 5412–5487. doi:10.1021/cr200399q
67. Seema, P.; Behler, J.; Marx, D. *Phys. Rev. Lett.* **2015,** *115,* 036102. doi:10.1103/PhysRevLett.115.036102
68. Chai, J.; Wong, L. S.; Giam, L.; Mirkin, C. A. *Proc. Natl. Acad. Sci. U. S. A.* **2011,** *108,* 19521–19525. doi:10.1073/pnas.1116099108
69. Cerf, A.; Cipriany, B. R.; Benítez, J. J.; Craighead, H. G. *Anal. Chem.* **2011,** *83,* 8073–8077. doi:10.1021/ac202506j
70. Levy-Sakin, M.; Grunwald, A.; Kim, S.; Gassman, N. R.; Gottfried, A.; Antelman, J.; Kim, Y.; Ho, S. O.; Samuel, R.; Michalet, X.; Lin, R. R.; Dertinger, T.; Kim, A. S.; Chung, S.; Colyer, R. A.; Weinhold, E.; Weiss, S.; Ebenstein, Y. *ACS Nano* **2013,** *8,* 14–26. doi:10.1021/nn4050694
71. Kartalov, E. P.; Quake, S. R. *Nucleic Acids Res.* **2004,** *32,* 2873–2879. doi:10.1093/nar/gkh613
72. Sun, Y.; Perch-Nielsen, I.; Dufva, M.; Sabourin, D.; Bang, D. D.; Høgberg, J.; Wolff, A. *Anal. Bioanal. Chem.* **2012,** *402,* 741–748. doi:10.1007/s00216-011-5459-4
73. Trappmann, B.; Gautrot, J. E.; Connelly, J. T.; Strange, D. G. T.; Li, Y.; Oyen, M. L.; Cohen Stuart, M. A.; Boehm, H.; Li, B.; Vogel, V.; Spatz, J. P.; Watt, F. M.; Huck, W. T. S. *Nat. Mater.* **2012,** *11,* 642–649. doi:10.1038/nmat3339
74. Bai, H.-J.; Shao, M.-L.; Gou, H.-L.; Xu, J.-J.; Chen, H.-Y. *Langmuir* **2009,** *25,* 10402–10407. doi:10.1021/la900944c
75. Tseng, P.; Di Carlo, D. *Adv. Mater.* **2014,** *26,* 1242–1247. doi:10.1002/adma.201304607
76. Tseng, P.; Pushkarsky, I.; Di Carlo, D. *PLoS One* **2014,** *9,* e106091. doi:10.1371/journal.pone.0106091
77. Heyries, K. A.; Marquette, C. A.; Blum, L. J. *Langmuir* **2007,** *23,* 4523–4527. doi:10.1021/la070018o
78. Chen, C. S.; Mrksich, M.; Huang, S.; Whitesides, G. M.; Ingber, D. E. *Science* **1997,** *276,* 1425–1428. doi:10.1126/science.276.5317.1425
79. Chen, Y.; Kung, S.-C.; Taggart, D. K.; Halpern, A. R.; Penner, R. M.; Corn, R. M. *Anal. Chem.* **2010,** *82,* 3365–3370. doi:10.1021/ac100362u
80. Hou, X.; Zhang, Y. S.; Trujillo-de Santiago, G.; Alvarez, M. M.; Ribas, J.; Jonas, S. J.; Weiss, P. S.; Andrews, A. M.; Aizenberg, J.; Khademhosseini, A. *Nat. Rev. Mater.* **2017,** *2,* 17016. doi:10.1038/natrevmats.2017.16
81. Thomas, J. C.; Boldog, I.; Auluck, H. S.; Bereciartua, P. J.; Dušek, M.; Macháček, J.; Bastl, Z.; Weiss, P. S.; Baše, T. *Chem. Mater.* **2015,** *27,* 5425–5435. doi:10.1021/acs.chemmater.5b02263
82. Thomas, J. C.; Schwartz, J. J.; Hohman, J. N.; Claridge, S. A.; Auluck, H. S.; Serino, A. C.; Spokoyny, A. M.; Tran, G.; Kelly, K. F.; Mirkin, C. A.; Gilles, J.; Osher, S. J.; Weiss, P. S. *ACS Nano* **2015,** *9,* 4734–4742. doi:10.1021/acsnano.5b01329
83. Kim, M.; Hohman, J. N.; Serino, A. C.; Weiss, P. S. *J. Phys. Chem. C* **2010,** *114,* 19744–19751. doi:10.1021/jp106211y
84. Thomas, J. C.; Goronzy, D. P.; Dragomiretskiy, K.; Zosso, D.; Gilles, J.; Osher, S. J.; Bertozzi, A. L.; Weiss, P. S. *ACS Nano* **2016,** *10,* 5446–5451. doi:10.1021/acsnano.6b01717
85. Qin, D.; Xia, Y.; Whitesides, G. M. *Nat. Protoc.* **2010,** *5,* 491–502. doi:10.1038/nprot.2009.234
86. Perdew, J. P.; Burke, K.; Ernzerhof, M. *Phys. Rev. Lett.* **1996,** *77,* 3865–3868. doi:10.1103/PhysRevLett.77.3865
87. Mortensen, J. J.; Hansen, L. B.; Jacobsen, K. W. *Phys. Rev. B* **2005,** *71,* 035109. doi:10.1103/PhysRevB.71.035109
88. Bahn, S. R.; Jacobsen, K. W. *Comput. Sci. Eng.* **2002,** *4,* 56–66. doi:10.1109/5992.998641
89. Guo, Q.; Li, F. *Phys. Chem. Chem. Phys.* **2014,** *16,* 19074–19090. doi:10.1039/C4CP00596A
90. Grönbeck, H. *Nanoscale* **2012,** *4,* 4178–4182. doi:10.1039/c2nr30903c

License and Terms

BEILSTEIN JOURNAL OF NANOTECHNOLOGY

Wafer-scale bioactive substrate patterning by chemical lift-off lithography

Chong-You Chen, Chang-Ming Wang, Hsiang-Hua Li, Hong-Hseng Chan and Wei-Ssu Liao*

Full Research Paper

Open Access

Address:
Department of Chemistry, National Taiwan University, Taipei 10617, Taiwan

Email:
Wei-Ssu Liao* - wsliaochem@ntu.edu.tw

* Corresponding author

Keywords:
bioactive substrate; chemical lift-off lithography; patterning; self-assembled monolayer

Beilstein J. Nanotechnol. **2018,** *9,* 311–320.
doi:10.3762/bjnano.9.31

Received: 04 November 2017
Accepted: 17 January 2018
Published: 26 January 2018

This article is part of the Thematic Series "Nanoscale patterning and characterization".

Guest Editor: S. A. Claridge

Abstract

The creation of bioactive substrates requires an appropriate interface molecular environment control and adequate biological species recognition with minimum nonspecific attachment. Herein, a straightforward approach utilizing chemical lift-off lithography to create a diluted self-assembled monolayer matrix for anchoring diverse biological probes is introduced. The strategy encompasses convenient operation, well-tunable pattern feature and size, large-area fabrication, high resolution and fidelity control, and the ability to functionalize versatile bioarrays. With the interface-contact-induced reaction, a preformed alkanethiol self-assembled monolayer on a Au surface is ruptured and a unique defect-rich diluted matrix is created. This post lift-off region is found to be suitable for insertion of a variety of biological probes, which allows for the creation of different types of bioactive substrates. Depending on the modifications to the experimental conditions, the processes of direct probe insertion, molecular structure change-required recognition, and bulky biological species binding are all accomplished with minimum nonspecific adhesion. Furthermore, multiplexed arrays via the integration of microfluidics are also achieved, which enables diverse applications of as-prepared substrates. By embracing the properties of well-tunable pattern feature dimension and geometry, great local molecular environment control, and wafer-scale fabrication characteristics, this chemical lift-off process has advanced conventional bioactive substrate fabrication into a more convenient route.

Introduction

Patterning on the micro- to nanoscale plays a key role in modern scientific and engineering research fields. Particularly, the creation of bioactive surfaces with well-defined geometries has drawn lots of attention due to its versatile applications in chemistry, biology, biophysics, and bioengineering [1-4]. In order to achieve the feature size and procedure convenience

requirements that satisfy the specific needs for different applications, the adaptation of appropriate micro/nanofabrication approaches is necessary. The fact that optical lithography allows for large-area fabrication provides an accessible route to bioactive substrate manufacturing but is limited by light diffraction when very fine control is required. On the other hand, scanning beam-based lithographic techniques allow for highly controllable fine feature dimensions but are restricted by a much slower production speed for large-area patterns. Combinational and complimentary approaches are therefore widely adopted in the fabrication of bioactive substrates, which also provide the advantages of convenient process, economical operation, large-scale reproduction, and high resolution control.

Conventional strategies to fabricate bioactive substrates rely on the creation of different local molecular environments that are suitable for subsequent biological species attachment. For example, the supported lipid bilayer system has been widely used for many biophysical studies due to its mimetic property toward cell membranes [5,6]. These platforms often use a flat glass surface to support the formation of lipid bilayers via vesicle fusion. With the combination of microfluidic devices and lithographic techniques, the creation of multiplexed arrays has been achieved and delivers applications such as protein–ligand binding study and biological species sensing [7-9]. The other widely adopted system, the self-assembled monolayer (SAM), provides ease of operation and high stability under ambient conditions [10,11]. These approaches utilize the self-arrangement of silane or thiol molecules on silica or Au surfaces, which has been proven as a convenient route for the fabrication of functional surfaces toward versatile targets [12-16]. In addition to direct surface modification, the versatility of anchoring molecule tail groups provides further functionality choices which benefit the fabrication of variable recognition arrays [17-20]. It should be noted that the establishment of a proper surface environment for biological species recognition requires appropriate molecular moiety selection not only for better ligand–target interaction, but also lower non-specific binding of objects. A highly controllable molecular manipulation over large area surfaces is consequently highly sought after in bioactive substrate fabrication.

The recently developed chemical lift-off lithography (CLL) technique is a straightforward approach to create distinct regions carrying dissimilar surface properties for a variety of applications [21]. With conformal contact-induced reactions, the top layer Au–Au bond breakage on an alkanethiol SAM covered Au substrate leads to the exposure of fresh Au toward the exterior environment. These vacancies can therefore be fulfilled with different molecules, e.g., ligands, and the substrate is active for biological responses. Comparing to conventional lithographic stamping processes which use mobile inks, this approach solves the problems of molecular lateral diffusion and gas transport obstacles. The fabricated feature resolution can therefore be accomplished down to the sub-30 nm scale with high pattern fidelity [22-24]. Furthermore, the great stability of the created pattern, which could be attributed to the atomic scale step-edge from the lift-off process, allows for long-term usage of the generated platform [25,26]. It is important to note that the lift-off process creates a local molecular environment that is very unique and highly suitable for the insertion of bioactive probes [26,27]. Due to the incompleteness of the contact-induced reaction, the post lift-off region represents an unusual behavior compared to other SAM systems. Here, the lift-off process creates a diluted molecular matrix environment which is expected to be due to partial Au thiolate removal in SAMs. With the appropriate adjustment of the experimental conditions, this "diluted artificial defect-rich" matrix provides an abundance of opportunities to create different bioactive substrates via a straightforward one-step SAM defect control. Compared to conventional biological platform generation, this matrix provides the advantages of wide probe compatibility, minimized nonspecific biospecies adhesion, versatile platform creation, precisely controlled biomolecule positioning, and straightforward operation. To investigate the capability of the lift-off process to fabricate various bioactive substrates, probes with different molecular behavior and multiplexed array construction are tested. The unique surface environments created are also applied to execute patterns with diverse geometries, a wide range of feature dimensions, and structure repeatability, which are important in practical bioactive substrate assembly. To further expand this approach toward biologically important probe-anchored multiplexed patterns, a novel integration of microfluidics with CLL operation is also introduced. In addition, this strategy enables straightforward creation of wafer-scale bioactive substrates via one-step surface defect-rich matrix generation, which greatly advances the creation of a biofunctional platform manufacturing for practical uses.

Experimental

Materials. 11-Mercaptoundecanol (MCU), 1-undecanethiol (UT), tri(ethylene glycol) undecanethiol (TEG), hexaammineruthenium(III) {$[Ru(NH_3)_6]^{3+}$} chloride and 4-(2-hydroxyethyl)piperazine-1-ethanesulfonic acid (HEPES) were purchased from Sigma-Aldrich (St. Louis, MO, USA). Biotin-terminated hexa(ethylene glycol)undecanethiol was purchased from Nanoscience Instruments Inc. (Phoenix, AZ, USA). Streptavidin was purchased from Invitrogen Inc. (Carlsbad, CA, USA). FITC-labelled antistreptavidin antibody was purchased from Abcam Inc. (Cambridge, MA, USA). Tris(hydroxy-methyl)aminomethane (TRIS) and tris(2-carboxy-

ethyl)phosphine (TCEP) were obtained from Acros Organics (Geel, Belgium). Bovine serum albumin (BSA), and 10× phosphate buffered saline (PBS) containing 1.37 M NaCl, 0.027 M KCl, 0.10 M Na_2HPO_4, and 0.018 M KH_2PO_4 were purchased from Bioman Scientific Co., Ltd (Taipei, Taiwan). Deionized water (>18 MΩ·cm) was obtained from the ELGA PURELAB classic system (Taipei, Taiwan).

Oligonucleotide sequences. Oligonucleotides purified by HPLC were purchased from PURIGO Biotechnology Co., Ltd. (Taipei, Taiwan). The oligonucleotide sequences are listed in the following:

1. Hg^{2+}-specific probe (30 bp): 5' HS-$(CH_2)_6$-ACT CAT GAT TCT TTC TTC CCC TTG TTT GTT-FAM-3' (FAM: carboxyfluorescein)
2. adenosine-specific probe (35 bp): 5' HS-$(CH_2)_6$-ACT CAT GAA CCT GGG GGA GTA TTG CGG AGG AAG GT-FAM-3'
3. cocaine-specific probe (46 bp): 5' HS-$(CH_2)_6$-ACT CAT GAG GGA GAC AAG GAA AAT CCT TCA ATG AAG TGG GTC TCC C-FAM-3'
4. target DNA-specific probe (42 bp): 5' HS-$(CH_2)_6$-GCG ACT GGG ATT AAA TAA AAT AGT AAG AAT GTA TAG CCC AGT-FAM-3'
5. target DNA (33 bp): 5'-GCT ATA CAT TCT TAC TAT TTT ATT TAA TCC CAG-3'

Before tethering the thiolated probes onto CLL-treated substrates, 5 μL of the 10 μM probe solution was first mixed with 5 μL of 20 μM reducing agent (TCEP) in 25 mM TRIS buffer (150 mM NaCl, pH 8.2) for 30 min. The probe solution was then diluted to a final concentration of 0.5 μM in 25 mM TRIS buffer (150 mM NaCl, pH 8.2), and kept in the dark before use.

Bioactive substrate preparation by the CLL process. Silicon substrates (Mustec Corp., Hsinchu, Taiwan) with 100 nm thick Au and 5 nm chromium adhesive layers were prepared by thermal evaporation. The Au substrates were immersed in 0.5 mM MCU or TEG ethanolic solution for >6 h to form self-assembled monolayers. After SAM formation, the substrates were washed with ethanol to remove excess thiol molecules, and blown dry with nitrogen gas. Polydimethylsiloxane (PDMS) stamps with various patterns were fabricated by standard photolithography-created masters. A 10:1 mass ratio of SYLGARD 184 silicone elastomer base and curing agent (Dow Corning, Midland, MI, USA) was thoroughly mixed, degassed under vacuum, cast onto master molds, and cured on an aluminum-top hot plate at 100 °C overnight. The PDMS stamps were separated from the master molds, sequentially rinsed with acetone and isopropanol, and then blown dry with nitrogen gas. The prepared stamps were activated by 40 s of oxygen plasma exposure at a power of 18 W with 0.5 mbar oxygen flow. Thereafter, the stamps were conformally sealed onto the SAM-modified substrates to initiate a contact-induced reaction for typically 60 min. After separating the contact-sealed stamps from the Au substrates, 0.5 μM thiolate probe solutions were quickly dropped onto the surfaces to anchor the biological probes into the post-chemical lift-off regions. After typically 1 h of incubation, the substrates were gently rinsed by deionized water, immersed in buffer solution, and stored at 4 °C in the dark.

Fluorescence image recording. An epifluorescence microscope (Axio Imager, M2, Carl Zeiss Microscopy, Jena, Germany) equipped with an X-Cite® 120 LED (Lumen Dynamics Group Inc., Mississauga, Canada) lamp and a fluorescence filter set with excitation and emission wavelengths of 480 ± 15 nm and 535 ± 20 nm, respectively, was used. The relative fluorescence intensity was processed with the rectangle function in ZEN 2012 (blue edition) Service Pack 2 software (Carl Zeiss Microscopy, Jena, Germany).

Atomic force microscopy characterization. The bioactive substrate fabrication process was step-wisely characterized by the tapping mode atomic force microscopy (AFM, Dimension Fastscan, Bruker Nano Surfaces, Hsinchu, Taiwan). Topographic AFM images were collected using a silicon cantilever with a spring constant of 48 N/m and a resonance frequency of 190 kHz (Nanosensors, Neuchatel, Switzerland). The substrates were gently rinsed by deionized water and carefully blown dry with nitrogen gas before characterization.

Cyclic voltammetry (CV) measurements. Electrochemical experiments were performed on the CH Instruments 627A electrochemical analyzer in a three-electrode system consisting of the prepared substrate (with an exposed area of 0.28 cm^2), an Ag/AgCl (3 M KCl) reference electrode, and a Pt wire counter electrode. CV measurements were carried out with 1 mM $[Ru(NH_3)_6]^{3+}$ in 25 mM TRIS buffer (pH 7.4) at a scan rate of 100 mV/s.

Target capture. For binding partner recognition, the substrates were rinsed with 25 mM TRIS buffer (150 mM NaCl, pH 7.4) in advance. Target DNA solutions in 25 mM TRIS buffer (150 mM NaCl, pH 7.4) was thereafter dropped onto the target DNA-specific probe-modified substrates for a 5 min incubation period. For sandwich-like array signal reporting, biotinylated thiol-patterned substrates were first exposed to 10 mg/mL BSA for 5 min to reduce nonspecific protein adsorption. The patterned surfaces were then treated with 50 μg/mL streptavidin solution for 20 min followed by 20 min of 10 μg/mL

FITC-labelled antistreptavidin antibody incubation. These substrates were all rinsed with deionized water between single steps.

Multiplexed biological probe-anchored platform. After 40 s of oxygen plasma treatment, a flat PDMS stamp was conformally sealed onto a MCU SAM modified Au substrate for 60 min. After the stamp removal, the Au substrate was conformally sealed to another plasma-treated stamp rendering 20 µm microchannels. Three different thiolated probe solutions (5 µM in 25 mM TRIS buffer, 150 mM NaCl, 1 µM TCEP, pH 8.2) were introduced into separated channels for 60 min biomolecule insertion. The microchannel stamp was then quickly separated from the Au substrate in a deionized water bath. Finally, the Au surface was gently rinsed with deionized water and 25 mM TRIS buffer (pH 7.4) before further use.

Results and Discussion

The use of CLL for the fabrication of bioactive substrates depends on several governing factors to create a proper surface environment for biomolecule recognition. Hydrophilic group-terminated alkanethiol molecules provide a strong interaction toward an oxygen-plasma-treated PDMS surface, which is the best option for generating SAM ruptures by substrate top layer Au–Au bond breakage [11,28-32]. Another important task in the CLL operation is the choice of an appropriate molecular matrix, where the influence of molecular-level steric effects dominates the insertion of biological probes or the corresponding partner recognition [27]. An eleven carbon-chain-based 11-mercaptoundecanol (MCU) molecule is therefore selected in this study due to its great self-assembly behavior on Au and the suitable hydroxy-tail group toward the activated PDMS surface for the contact reaction [18,19,24,27]. A schematic illustration of the standard CLL operation is demonstrated in Figure 1, including PDMS activation, contact-induced reaction, lift-off steps, and biomolecule anchoring. It should be noted that the conformal contact reaction requires no external pressure, and the lift-off operation is performed under ambient conditions. As shown in the AFM images of Figure 1, the SAM-modified Au surface reveals a depressed square pattern after CLL operation when a PDMS stamp with a protruding square pattern is used. This depression region represents a freshly exposed Au area, which provides a position for subsequent biological probe insertion. For visualization, thiolated molecules of longer molecular length are used and give an inversed protruding topographic image, depicting successful probe insertion.

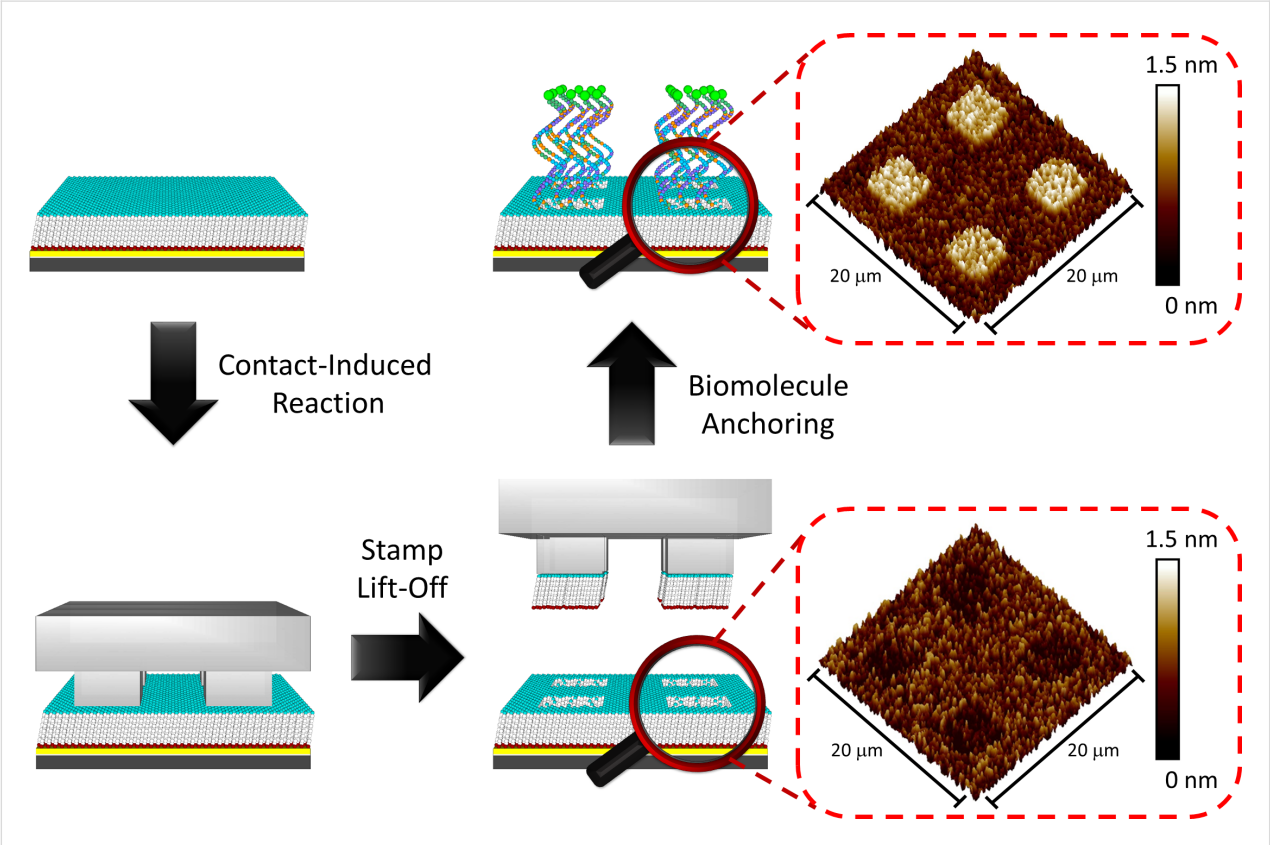

Figure 1: Schematic illustration and corresponding topographic AFM images of biological-probe-patterned surface fabrication using the chemical lift-off lithography (CLL) process.

The biological species filled inside the freshly created Au regions in this approach should maintain their activity toward targets for perspective practical applications. For investigation convenience, a fluorescence signal read-out based approach is applied and depicted via microscopic images. Three different categories of biological probes and their binding partner recognition capability are studied, including direct signal reporter-labelled probe insertion, binding partner recognition triggered probe structure change, and sandwich-like signal reporting with inserted probes, as shown in Figure 2. A thiolated six carbon chain based nucleotide probe with a carboxyfluorescein (FAM) moiety labelled tail is selected in the most straightforward probe direct insertion approach for demonstration (Figure 2A). The anchoring of this probe on the surface presents a high fluorescence image contrast, which indicates sufficient space and proper molecule orientation on the platform. This observation is attributed to the incomplete contact-induced reaction resulting in alkanethiol molecule residuals in the post lift-off region, allowing for inserted molecule self-orienting and reduced nonspecific probe–substrate adhesion. In Figure 2B, the second type of bioactive substrate fabrication approach relies on a labelled probe attachment with subsequent binding partner recognition induced signal output. A FAM-labelled thiolated hairpin-structured nucleotide probe is first inserted into the post lift-off region, and its complimentary nucleotide partner is thereafter introduced. Before the binding partner introduction, the fluorescence signal is quenched by the close distance of the dye to Au, where the subsequently observed high-contrast fluorescence image indicates sufficient surface space required in the binding partner recognition step. This result confirms that the diluted molecular matrix supported by the post lift-off region provides steric hindrance-free environ-

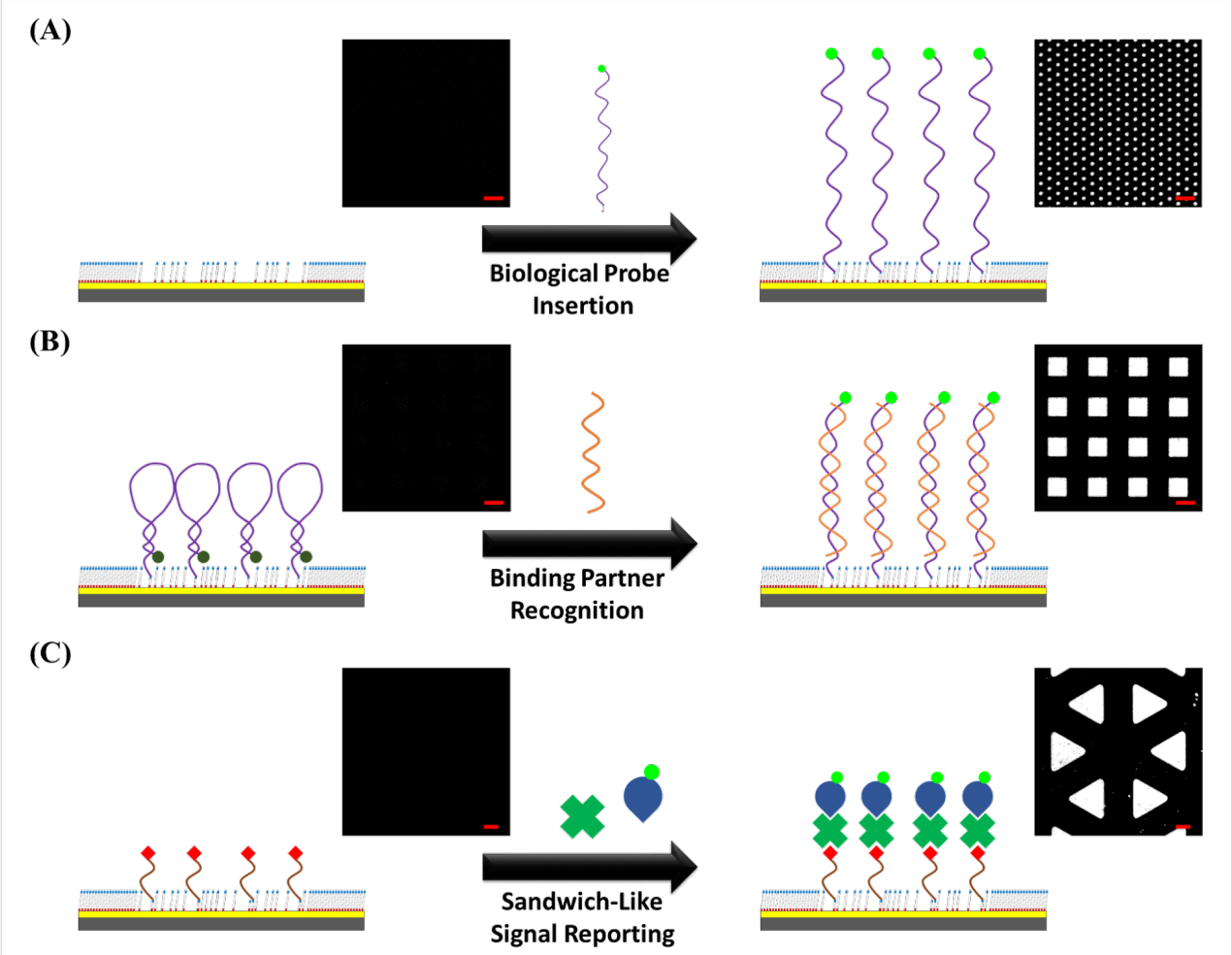

Figure 2: Different types of bioactive surfaces fabricated by the chemical lift-off lithograpy (CLL) process with corresponding fluorescence images. (A) Direct signal reporter-labelled probe insertion: the CLL-treated substrate before (left) and after (right) FAM-labelled Hg^{2+}-specific probe insertion. (B) Binding partner recognition triggered probe structure change inducing signal readout: the CLL-treated substrate anchoring with the FAM-labelled hairpin-structured DNA probe before (left) and after (right) target DNA introduction. (C) Sandwich-like signal reporting with the inserted probe: the CLL-treated substrate anchoring with the biotinylated thiol before (left) and after (right) the conjugation with streptavidin and FITC-labelled antistreptavidin antibody. The scale bars are 20 µm.

ment, which benefits in the recognition of other molecules onto the substrate. The third type of fabricated bioactive substrate lies on the anchoring of an active ligand, which can recognize a corresponding protein partner in the solution (Figure 2C). In order to minimize the protein nonspecific adsorption, an oligo(ethylene glycol) moiety containing TEG molecule is selected as the matrix material, which can also be lifted off by activated PDMS stamps in the CLL operation [21]. After the ligand–protein binding process, a sandwich-like assay is employed via the sequential attachment of primary and reporter-labelled secondary antibodies. This bulky assay design requires the spatial surrounding to give efficient recognition comparing to the previous two substrate types. It is clear that the fluorescence pattern created via this approach also presents very high contrast, indicating that a proper environment was provided by the post lift-off region even with bulky biological species. From the great capability of three bioactive substrate types toward diverse molecules and recognition processes under appropriate experimental condition adjustments, the great potential of CLL-treated surfaces for a variety of applications is ratified.

It should be noted that molecular matrix composition plays a key role in biological species selective recognition [14,15,33,34]. A different probe density requirement is therefore expected when diverse biocapturing environments are employed. Taking advantage of the straightforward CLL operation and convenience of alkanethiol SAM formation, the interface-contact-induced reaction can be applied to satisfy appropriate probe quantity control. As depicted in Figure 3, different percentages of hydroxy-group-terminated MCU and methyl-terminated UT molecules are utilized to form SAMs on Au. The substrates are thereafter treated by the CLL process and incubated with FAM-labelled nucleotide probes under the same conditions. It is clear to see that the probe-anchored area fluorescence intensity decreases along with the MCU percentage, which can be attributed to two presumable factors. First, the lack of a contact-induced reaction toward the activated PDMS surface of methyl-terminated alkanethiol diminishes the amount of lift-able Au thiolates in the matrix, resulting in reduced SAM defect creation in the CLL process. A consistent observation of decreased $[Ru(NH_3)_6]^{3+}$ CV response along with larger redox peak separation ΔE_p (from 0.08 V to 0.15 V) under reduced MCU percentage also indicates less defects in the SAM environment (Figure S1, Supporting Information File 1). Second, the increase of hydrophobicity due to the presence of methyl-terminated alkanethiol leads to unfavorable hydrophilic biological probe insertion. The observed fluorescence signals are therefore reduced with the increase of UT molecule ratio in the matrix. It is important to note that although single-stranded DNA probes may adsorb nonspecifically on methyl-terminated SAMs [35], their contribution to fluorescence image contrast is deducted due to the close dye-to-Au distance induced nonradiative energy transfer. Given the controllable matrix composition and the ease of CLL operation, the surface probe quantity is well-tunable to satisfy the various needs of different biological platforms.

The CLL-created unique molecular environment can also be extended to fabricate multiplexed bioactive arrays. As illustrated in Figure 4, a spatially addressed biological-probe-anchored substrate is fabricated via the combination of a microfluidic device and a CLL-treated surface. The diluted MCU alkanethiol matrix is first generated by applying activated featureless PDMS to interact with the whole SAM-modified Au surface followed by a subsequent lift-off step. This post lift-off surface

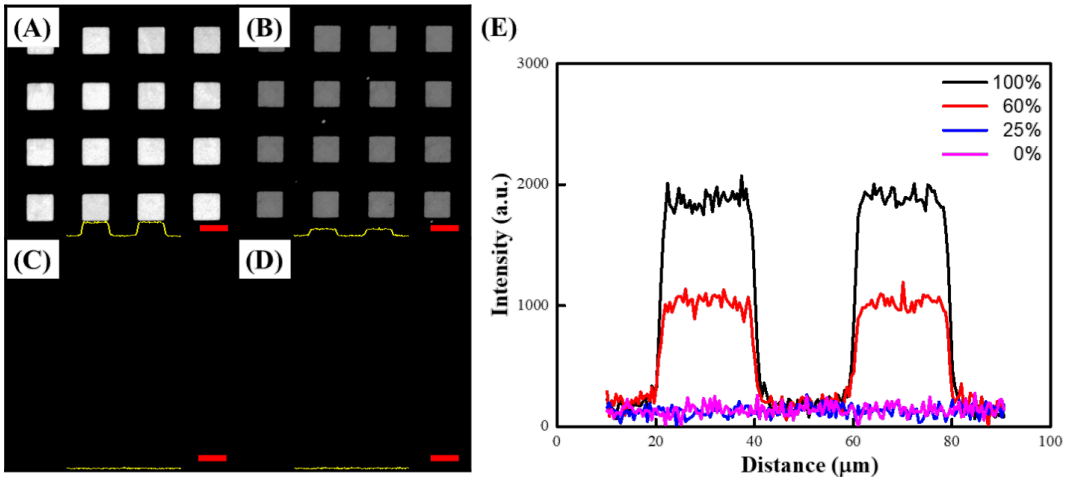

Figure 3: Fluorescence images (A–D) and intensity profiles (E) of FAM-labelled DNA-patterned surfaces fabricated by CLL for (A) 100% MCU SAM (0% UT), (B) 60% MCU SAM (40% UT), (C) 25% MCU SAM (75% UT), and (D) 0% MCU SAM (100% UT). The scale bars are 20 μm.

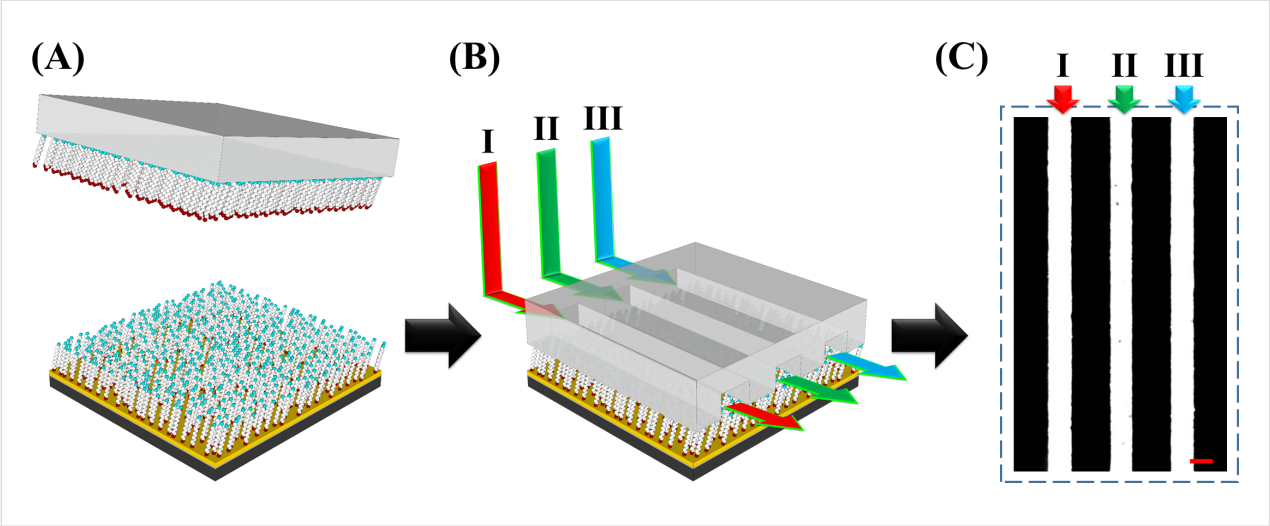

Figure 4: Schematic illustration of multiplexed bioactive surface fabrication by the combination of chemical lift-off lithography (CLL) and microfluidics: (A) CLL treatment with an activated featureless PDMS stamp. (B) Probe insertion by the combination of a microfluidic device. (C) The fluorescence image represents a multiplexed surface spatially anchored with different probes including (I) Hg^{2+}-specific, (II) adenosine-specific, and (III) cocaine-specific probes. The scale bar is 20 µm.

is thereafter conformally sealed with a PDMS microfluidic device, rendering three 20 µm channels with 30 µm spacing in between. Three individual solutions containing different types of thiolated bioactive probes (targeting Hg^{2+}, adenosine, and cocaine) are accordingly injected into these channels for a 60 min of probe insertion duration. Finally, the PDMS device is separated from the Au surface and a multiplexed bioactive-probe-anchored substrate is created. For demonstration, this spatially addressed bioactive substrate is tested with the signal reporter labelled probe direct insertion approach. It is found that three different molecules all insert into the desired position during fluidic incubation and give a multiplexed image with high fluorescence signal, as shown in Figure 4C. Channel I, II, and III are Hg^{2+}, adenosine, and cocaine-specific probe anchored positions, respectively. To demonstrate the anchored probe's selectivity toward its corresponding target, this multiplexed substrate was tested with a 1 mM adenosine solution. The obvious disappearance in the fluorescence signal in column II (Figure S2, Supporting Information File 1) points to the high platform selectivity toward its corresponding targets. The results indicate that CLL-fabricated substrates not only render high versatility for biological probes, but also entail great potential toward analytical technique integration. It is also important to note that biologically interesting closed-packed different chemical patterns on the same substrate could also be achieved via this approach. For example, the lift-able and reactive amine-terminated alkanethiol SAM-modified substrate can be integrated with a microfluidic device and functionalized with different moieties through various injected solutions. The device can thereafter be separated and the exposed post lift-off regions can be back-filled with a different chemical functionality. These multiplexed and closed-packed chemical patterns can therefore be utilized for an abundance of biological recognition applications [14,20,24].

Because the bioactive surface feature size and geometry may affect the substrate's capability toward practical application and the functionality of the anchored probes, the CLL-based fabrication process was tested to create surfaces with a variety of molecule arrangements in different dimensions. As shown in Figure 5, different PDMS stamps rendering diverse geometries, either with protruding (Figure 5A,C,E,G, and H) or depressed (Figure 5B,D, and F) features, were applied on the SAM-modified Au surface to create molecular matrix patterns. With the adoption of a simply operated signal reporter labelled probe insertion strategy, high-contrast fluorescence images with versatile geometries are obtained and no obvious signal output fluctuation is observed with the different sizes. It should be noted that bioactive substrates created by the CLL process can also be made very uniform over a large area. As demonstrated in Figure 6, fluorescence images obtained from distinct sampling spots on a 4 inch silicon wafer substrate represent the same results with minimized signal fluctuation. The high repeatability and scale up capability of fabricated biologically active patterns confirms the technique's potential toward practical applications.

Conclusion

The chemical lift-off process enables fabrication of diverse bioactive substrates in a straightforward manner. The approach generates abundant alkanethiol SAM defects via interface-contact-induced reactions between the activated PDMS stamp and

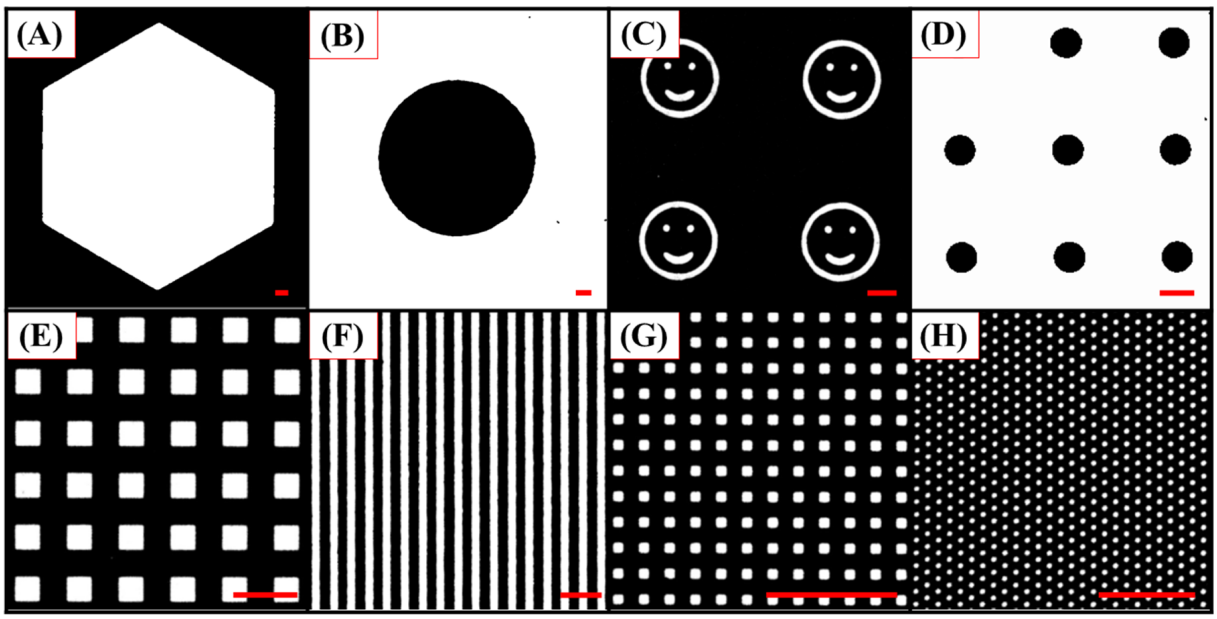

Figure 5: Fluorescence microscopy images (A–H) of FAM-labelled DNA patterned surfaces with various features and sizes created by CLL. The scale bars are 50 μm.

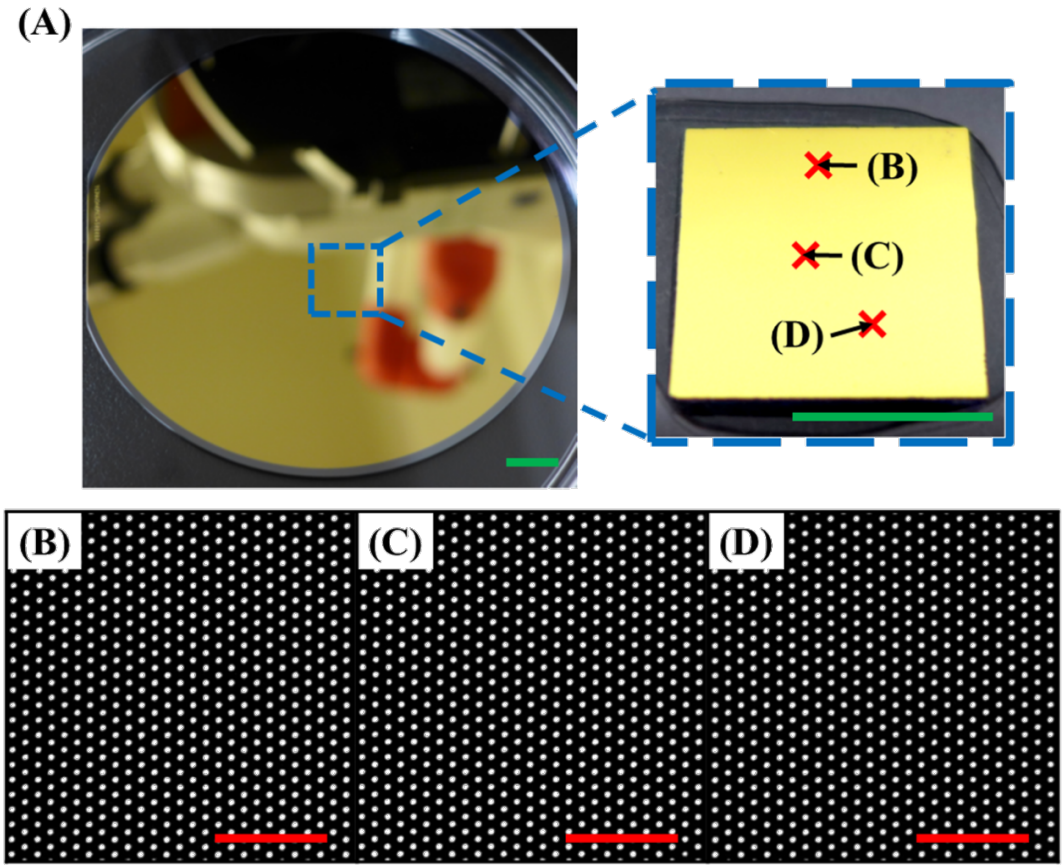

Figure 6: A representative photo (A) and fluorescence images (B–D) of the large-area bioactive surface fabricated by CLL. (A) Photo images showing a wafer-scale patterning achieved by CLL. (B–D) Fluorescence images obtained from different sampling spots indicated in (A) on the same surface. The green and red scale bars are 1.0 cm and 20 μm, respectively.

hydroxy-group-terminated SAM molecules. The separation of these two surfaces leads to the creation of molecular level matrix defects, which enables the subsequent bioactive probe anchoring. This CLL-based substrate is capable of conjugating a variety of biological species, such as nucleotide-tethered probes, orientation changeable molecules, and bulky proteins or antibodies. It is found that these surface-tethered probes maintain their biological activity and the fabricated pattern sizes and geometries are well-tunable. In addition, the creation of multiplexed arrays can also be accomplished by the integration of the CLL process with a microfluidic device, indicating the great potential of this strategy toward practical bioapplications. The observed bioactive substrate properties are attributed to the unique diluted SAM environment created by the CLL-process-induced Au-thiolate rupture happening at the interface. Due to the randomly distributed thiol molecule residual generated during the process, a diluted matrix rendering copious SAM defects is expected. This environment is therefore able to support the tethering of biological probes with controllable density, and offers sufficient space for biorecognition under the adjustment of experimental conditions. We believe that this CLL-treated surface can be used in conjunction with various biomolecules and a convenient approach to fabricate large-scale bioactive substrates with well-defined patterns is anticipated.

Supporting Information

Supporting Information File 1

Additional information.
[https://www.beilstein-journals.org/bjnano/content/supplementary/2190-4286-9-31-S1.pdf]

Acknowledgements

This work was supported by the Taiwan Ministry of Science and Technology (MOST 106-2113-M-002-015-MY2 and MOST 106-2622-M-002-002-CC2). The authors would like to thank Prof. Chun-Hsien Chen at National Taiwan University, Profs. Paul S. Weiss and Anne M. Andrews, and Dr. Huan H. Cao at University of California, Los Angeles for instrument support and helpful discussions.

References

1. Demers, L. M.; Park, S.-J.; Taton, T. A.; Li, Z.; Mirkin, C. A. *Angew. Chem., Int. Ed.* **2001,** *40,* 3071–3073. doi:10.1002/1521-3773(20010817)40:16<3071::AID-ANIE3071>3.0.CO;2-S
2. Keren, K.; Krueger, M.; Gilad, R.; Ben-Yoseph, G.; Sivan, U.; Braun, E. *Science* **2002,** *297,* 72–75. doi:10.1126/science.1071247
3. Chung, S.-W.; Ginger, D. S.; Morales, M. W.; Zhang, Z.; Chandrasekhar, V.; Ratner, M. A.; Mirkin, C. A. *Small* **2005,** *1,* 64–69. doi:10.1002/smll.200400005
4. Schena, M.; Shalon, D.; Davis, R. W.; Brown, P. O. *Science* **1995,** *270,* 467–470. doi:10.1126/science.270.5235.467
5. Liu, C.; Huang, D.; Yang, T.; Cremer, P. S. *Anal. Chem.* **2015,** *87,* 7163–7170. doi:10.1021/acs.analchem.5b00999
6. Cong, X.; Poyton, M. F.; Baxter, A. J.; Pullanchery, S.; Cremer, P. S. *J. Am. Chem. Soc.* **2015,** *137,* 7785–7792. doi:10.1021/jacs.5b03313
7. Shi, J.; Yang, T.; Kataoka, S.; Zhang, Y.; Diaz, A. J.; Cremer, P. S. *J. Am. Chem. Soc.* **2007,** *129,* 5954–5961. doi:10.1021/ja069375w
8. Shi, J.; Yang, T.; Cremer, P. S. *Anal. Chem.* **2008,** *80,* 6078–6084. doi:10.1021/ac800912f
9. Shi, J.; Chen, J.; Cremer, P. S. *J. Am. Chem. Soc.* **2008,** *130,* 2718–2719. doi:10.1021/ja077730s
10. Gooding, J. J.; Mearns, F.; Yang, W.; Liu, J. *Electroanalysis* **2003,** *15,* 81–96. doi:10.1002/elan.200390017
11. Claridge, S. A.; Liao, W.-S.; Thomas, J. C.; Zhao, Y.; Cao, H. H.; Cheunkar, S.; Serino, A. C.; Andrews, A. M.; Weiss, P. S. *Chem. Soc. Rev.* **2013,** *42,* 2725–2745. doi:10.1039/C2CS35365B
12. Xu, C.; Taylor, P.; Ersoz, M.; Fletcher, P. D. I.; Paunov, V. N. *J. Mater. Chem.* **2003,** *13,* 3044–3048. doi:10.1039/b307788h
13. Lange, S. A.; Benes, V.; Kern, D. P.; Hörber, J. K. H.; Bernard, A. *Anal. Chem.* **2004,** *76,* 1641–1647. doi:10.1021/ac035127w
14. Shuster, M. J.; Vaish, A.; Cao, H. H.; Guttentag, A. I.; McManigle, J. E.; Gibb, A. L.; Martinez, M. M.; Nezarati, R. M.; Hinds, J. M.; Liao, W.-S.; Weiss, P. S.; Andrews, A. M. *Chem. Commun.* **2011,** *47,* 10641–10643. doi:10.1039/c1cc13002a
15. Mullen, T. J.; Srinivasan, C.; Hohman, J. N.; Gillmor, S. D.; Shuster, M. J.; Horn, M. W.; Andrews, A. M.; Weiss, P. S. *Appl. Phys. Lett.* **2007,** *90,* 063114. doi:10.1063/1.2457525
16. Römhildt, L.; Pahlke, C.; Zörgiebel, F.; Braun, H.-G.; Opitz, J.; Baraban, L.; Cuniberti, G. *ACS Appl. Mater. Interfaces* **2013,** *5,* 12029–12035. doi:10.1021/am4038245
17. Lalander, C. H.; Zheng, Y.; Dhuey, S.; Cabrini, S.; Bach, U. *ACS Nano* **2010,** *4,* 6153–6161. doi:10.1021/nn101431k
18. Palla, K. S.; Hurlburt, T. J.; Buyanin, A. M.; Somorjai, G. A.; Francis, M. B. *J. Am. Chem. Soc.* **2016,** *139,* 1967–1974. doi:10.1021/jacs.6b11716
19. Vaish, A.; Shuster, M. J.; Cheunkar, S.; Singh, Y. S.; Weiss, P. S.; Andrews, A. M. *ACS Chem. Neurosci.* **2010,** *1,* 495–504. doi:10.1021/cn1000205
20. Liao, W.-S.; Cao, H. H.; Cheunkar, S.; Shuster, M. J.; Altieri, S. C.; Weiss, P. S.; Andrews, A. M. *J. Phys. Chem. C* **2013,** *117,* 22362–22368. doi:10.1021/jp402921y
21. Liao, W.-S.; Cheunkar, S.; Cao, H. H.; Bednar, H. R.; Weiss, P. S.; Andrews, A. M. *Science* **2012,** *337,* 1517–1521. doi:10.1126/science.1221774
22. Zhao, C.; Xu, X.; Yang, Q.; Man, T.; Jonas, S. J.; Schwartz, J. J.; Andrews, A. M.; Weiss, P. S. *Nano Lett.* **2017,** *17,* 5035–5042. doi:10.1021/acs.nanolett.7b02269
23. Xu, X.; Yang, Q.; Cheung, K. M.; Zhao, C.; Wattanatorn, N.; Belling, J. N.; Abendroth, J. M.; Slaughter, L. S.; Mirkin, C. A.; Andrews, A. M.; Weiss, P. S. *Nano Lett.* **2017,** *17,* 3302–3311. doi:10.1021/acs.nanolett.7b01236
24. Cao, H. H.; Nakatsuka, N.; Liao, W.-S.; Serino, A. C.; Cheunkar, S.; Yang, H.; Weiss, P. S.; Andrews, A. M. *Chem. Mater.* **2017,** *29,* 6829–6839. doi:10.1021/acs.chemmater.7b01970
25. Andrews, A. M.; Liao, W.-S.; Weiss, P. S. *Acc. Chem. Res.* **2016,** *49,* 1449–1457. doi:10.1021/acs.accounts.6b00034

26. Chen, C.-Y.; Wang, C.-M.; Chen, P.-S.; Liao, W.-S. *Nanoscale* **2018**. doi:10.1039/C7NR07381J
27. Cao, H. H.; Nakatsuka, N.; Serino, A. C.; Liao, W.-S.; Cheunkar, S.; Yang, H.; Weiss, P. S.; Andrews, A. M. *ACS Nano* **2015,** *9,* 11439–11454. doi:10.1021/acsnano.5b05546
28. Yu, M.; Bovet, N.; Satterley, C. J.; Bengió, S.; Lovelock, K. R. J.; Milligan, P. K.; Jones, R. G.; Woodruff, D. P.; Dhanak, V. *Phys. Rev. Lett.* **2006,** *97,* 166102. doi:10.1103/PhysRevLett.97.166102
29. Moore, A. M.; Mantooth, B. A.; Donhauser, Z. J.; Yao, Y.; Tour, J. M.; Weiss, P. S. *J. Am. Chem. Soc.* **2007,** *129,* 10352–10353. doi:10.1021/ja0745153
30. Woodruff, D. P. *Phys. Chem. Chem. Phys.* **2008,** *10,* 7211–7221. doi:10.1039/b813948b
31. Maksymovych, P.; Voznyy, O.; Dougherty, D. B.; Sorescu, D. C.; Yates, J. T., Jr. *Prog. Surf. Sci.* **2010,** *85,* 206–240. doi:10.1016/j.progsurf.2010.05.001
32. Häkkinen, H. *Nat. Chem.* **2012,** *4,* 443–455. doi:10.1038/nchem.1352
33. Vaish, A.; Shuster, M. J.; Cheunkar, S.; Weiss, P. S.; Andrews, A. M. *Small* **2011,** *7,* 1471–1479. doi:10.1002/smll.201100094
34. Macedo, L. J. A.; Miller, E. N.; Opdahl, A. *Anal. Chem.* **2017,** *89,* 1757–1763. doi:10.1021/acs.analchem.6b04048
35. Kaufmann, R.; Averbukh, I.; Naaman, R.; Daube, S. S. *Langmuir* **2008,** *24,* 927–931. doi:10.1021/la702799v

License and Terms

BEILSTEIN JOURNAL OF NANOTECHNOLOGY

Perfusion double-channel micropipette probes for oxygen flux mapping with single-cell resolution

Yang Gao[1], Bin Li[1], Riju Singhal[2], Adam Fontecchio[1], Ben Pelleg[1], Zulfiya Orynbayeva[*3], Yury Gogotsi[*2] and Gary Friedman[*1]

Full Research Paper

Open Access

Address:
[1]Department of Electrical and Computer Engineering, Drexel University, 3141 Chestnut Street, Philadelphia, PA 19104, USA, [2]Department of Material Science and Engineering, Drexel University, 3141 Chestnut Street, Philadelphia, PA 19104, USA and [3]Department of Surgery, Drexel University, 245 N. 15th Street, Philadelphia, PA 19102, USA

Email:
Zulfiya Orynbayeva[*] - zo25@drexel.edu; Yury Gogotsi[*] - yg36@drexel.edu; Gary Friedman[*] - gary@ece.drexel.edu

* Corresponding author

Keywords:
double-barrel pipette; hydrodynamic confinement; perfusion; oxygen flux; single-cell metabolic analysis

Beilstein J. Nanotechnol. **2018,** *9,* 850–860.
doi:10.3762/bjnano.9.79

Received: 20 October 2017
Accepted: 21 February 2018
Published: 09 March 2018

This article is part of the Thematic Series "Nanoscale patterning and characterization".

Guest Editor: S. A. Claridge

Abstract

Measuring cellular respiration with single-cell spatial resolution is a significant challenge, even with modern tools and techniques. Here, a double-channel micropipette is proposed and investigated as a probe to achieve this goal by sampling fluid near the point of interest. A finite element model (FEM) of this perfusion probe is validated by comparing simulation results with experimental results of hydrodynamically confined fluorescent molecule diffusion. The FEM is then used to investigate the dependence of the oxygen concentration variation and the measurement signal on system parameters, including the pipette's shape, perfusion velocity, position of the oxygen sensors within the pipette, and proximity of the pipette to the substrate. The work demonstrates that the use of perfusion double-barrel micropipette probes enables the detection of oxygen consumption signals with micrometer spatial resolution, while amplifying the signal, as compared to sensors without the perfusion system. In certain flow velocity ranges (depending on pipette geometry and configuration), the perfusion flow increases oxygen concentration gradients formed due to cellular oxygen consumption. An optimal perfusion velocity for respiratory measurements on single cells can be determined for different system parameters (e.g., proximity of the pipette to the substrate). The optimum perfusion velocities calculated in this paper range from 1.9 to 12.5 μm/s. Finally, the FEM model is used to show that the spatial resolution of the probe may be varied by adjusting the pipette tip diameter, which may allow oxygen consumption mapping of cells within tissue, as well as individual cells at subcellular resolution.

Introduction

Transport, production and consumption of gasses, ions, and organic molecules are fluxes that sustain life. Relatively few tools are available to control and map these fluxes at the microscopic scale commensurate with the size of individual cells. While there has been progress in obtaining snapshots of genomic and transcriptomic information from single cells [1-3],

the lack of microscopic tools that measure and control fluxes limits studies of metabolic variability of cells within cell populations. Measurements of single-cell metabolic rates are important, as it has been shown that even genetically identical cells can behave differently [4]. The use of molecular or nanoparticle fluorescent reporters is a well-developed technique for imaging of concentrations of various molecular and ionic species in cells and tissues [5,6], but non-uniformities in the natural distribution of fluorescent reporters limits their applications in assessing fluxes due to individual cells. Furthermore, concerns often exist regarding potential toxicity of exogenous fluorescent agents [7]. An alternative approach is to map concentration gradients using scanning probes that may employ some means of sensing such as electrochemical or optical [8-15]. These types of probes can attain subcellular scale resolution when their tip size is smaller than the size of a cell [10,11]. However, the sensitivity of most sensors is typically proportional to their effective area, so sensors with relatively higher spatial resolution have lower sensitivity [14-16], or require a drastically increased measurement time. Here we propose and investigate a scanning flux measurement system for individual cells that offers high sensitivity and high spatial resolution. The main concept of the developed scanning probe is the confinement of the flux being measured by use of flow perfusion through double-channel micropipettes.

We specifically focus on the measurement of oxygen consumption by individual cells as a case study, although various other types of functional analyses are possible [12,17]. Since the time of the 1931 Nobel Prize winning work of Otto Warburg [18], respirometry has been widely employed to characterize metabolism and mitochondrial functions of cell cultures, tissues and larger organisms [19-23]. Commercially available respirometry tools that are capable of carrying out measurements on about 10^5–10^6 cells typically rely on sealing cells within oxygen tight chambers while measuring reduction of oxygen concentration over time as various sequences of mitochondrial modulators and substrates are added to the cell suspension [24,25].

Recent work using oxygen sensing, based on quenching of luminescence due to oxygen, has demonstrated the capability to carry out respirometry on single cells in sealed microchambers [26-28]. However, the primary difficulty with sealed chamber approaches is maintaining control over the cellular environment during an experimental time scale longer than tens of minutes. Maintaining a relatively constant carbon dioxide concentration, oxygen concentration, pH and nutrient supply requires using relatively large amounts of extracellular fluid per cell (typically few millions of cells per 1 mL [29]), reducing the sensitivity to oxygen concentration variations. Electrochemical scanning probes have been used to measure oxygen concentration variations near cells due to their respiration [30] and can be made with tips smaller than 100 nm in diameter [9,31,32]. However, no clear relationship between oxygen consumption and oxygen concentration near the cells has been obtained [30,33]. Another alternative that has been considered for measuring respiration of embryos and oocytes is to employ a system where linear oxygen gradients are measured by moving a sensor along a small tube with the embryo (a group of cells) at one end [34]. This technique demonstrated the ability to measure respiration rates of around 0.7 fmol/s, which is 100–1000 times faster than typical oxygen consumption rates of small individual cells.

The general idea behind the proposed use of a double-channel pipette for oxygen consumption measurement by individual cells in a cell culture is illustrated in Figure 1a. The SEM images of two theta pipettes (whose cross-sections looks like the Greek letter θ, where the top and bottom opening are associated with different channels) with tip diameters (dw) of 8 μm and 300 nm are shown in Figure 1b,c. Although the theta pipette is one type of double-channel pipette, there are other types, such as those with concentric channels [35] that can be manufactured and used. The key function of the pipette is to confine the oxygen flux between its two ends, reducing the lateral spread of the oxygen molecules being detected, while permitting the use of sensors with larger effective areas positioned further away from source of flux. The focus of this paper is on investigating the effects of various system parameters such as the half-angle of a theta pipette, position of the oxygen sensors within the pipette, perfusion flow rate and distance of the pipette tip from the substrate on oxygen flux sensitivity. The effects of varying the aforementioned parameters will be studied below using a finite element model (FEM) of the double-barrel pipette with perfusion. To validate this model, we first compare hydrodynamic confinement obtained from the model with experiments using a fluorescent dye. Later in the paper, we also show that FEM results agree qualitatively with a simplified analytical model.

Results and Discussion

Hydrodynamic confinement

Consider flow within a long channel: a molecule cannot diffuse outside the channel due to the presence of hard channel walls. However, if the channel walls are missing along some length segment of the flow, the molecule may diffuse outside the channel, unless the flow velocity is high enough that the molecule moves through this section before it has a chance to diffuse through the gap. Therefore, in the section where the channel walls are missing, like the section at the tip of the double-barrel pipette, the molecule could remain hydrodynamically confined to the flow. The time that it takes a molecule to

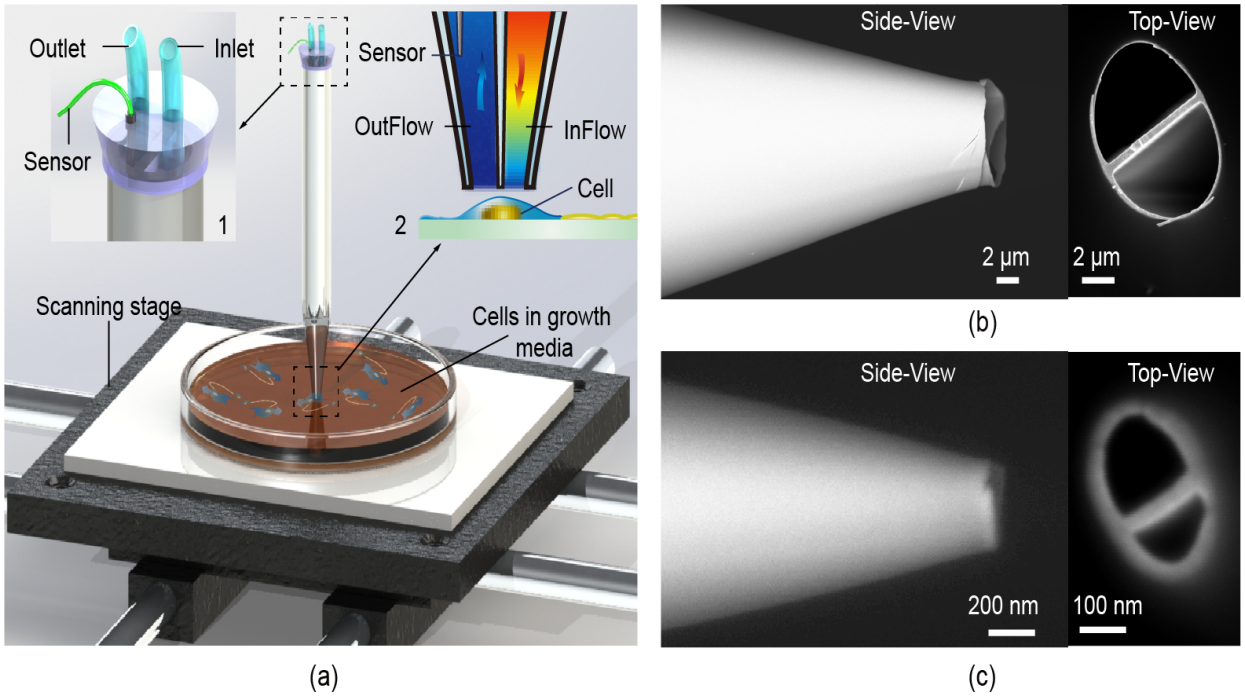

Figure 1: a) Illustration of the double-barrel perfusion-based single-cell respirometry probe. The cell culture or tissue dish is shown on top of an *x*–*y*–*z* positioning set-up. The inset (1) shows tubing for the inlet and outlet channels in both channels as well as a sensor in the outlet channel. The inset (2) illustrates the differences in oxygen concentration upstream and downstream from the cell within the theta pipette. The different colors represent different oxygen concentrations that are obtained from a finite element simulation of convection–diffusion equations. Inset (2) also illustrates that an oxygen sensor positioned downstream from the cell can be used to determine the cell's oxygen consumption rate when the sensor's measurement refers to the oxygen concentration at the top of the theta pipette. b) SEM images of a micrometer-scale theta pipette, side-view and top-view. The tip width (approximately representing the tip diameter (dw) parameter used in the simulation model) measured from the outer wall in the side-view image is 8 µm. c) SEM images of a nanometer-scale theta pipette, side-view and top-view. The tip width measured from the outer wall in the side-view image is 300 nm.

diffuse across the section of length b along the flow is b^2/D, where D is the diffusion coefficient, and the time it takes the flow to cross the same distance is roughly b/v, where v is the flow velocity. Taking the ratio of these times, we obtain the Peclet number $Pe = bv/D$, which indicates the relative importance of convective transport (flow) over the diffusion. When the Peclet number is large, the diffusion time is larger than convective transport time and the likelihood that a molecule remains confined in the flow is high. This simple idea of hydrodynamic confinement has been discussed in the microfluidics literature [28,36] and in some biological applications [33,37,38], some of which employed a concentric double-channel pipette [38].

Here, we report experimental observation of hydrodynamic confinement at the tip of the theta pipette and compare it with a finite element method (FEM) model that implements both Navier–Stokes equations to model the fluid flow and convection–diffusion equations to model molecular diffusion (see Experimental section for a detailed discussion). In the experiment, the fluid is being withdrawn at a fixed rate of 5 µL/min through one channel, while pressures from 2 to 16 hPa are applied to the injection channel. Experimentally observed diffusion of the fluorescent dye for different injection pressures is shown in Figure 2a. Two qualitative trends can be noted. One is the increasing size of the fluorescent plume with the increase in the pressure applied to the injection channel. It is clear from the images that at low pressure (≈2–3 hPa), the plume is smaller than the pipette tip, while at higher pressure (15–17 hPa), the plume is larger than the pipette tip. The other trend is the change in the tilt of the diffusion plume with increasing pressure applied to the injection channel. At lower injection pressures, the plume shape is dominated by the existing flow field near the tip, which develops due to the strong suction exerted by the extraction channel to support the applied flow rate and appears tilted away from the extraction channel. At higher injection pressures, the injection channel is able to contribute more fluid to the extraction channel. Thus, the suction exerted by the extraction channel is reduced and the resulting flow field near the tip (and the plume shape) starts to evolve and tilt more towards the extraction channel. Therefore, the average dye concentration in the extraction channel also increases as the injec-

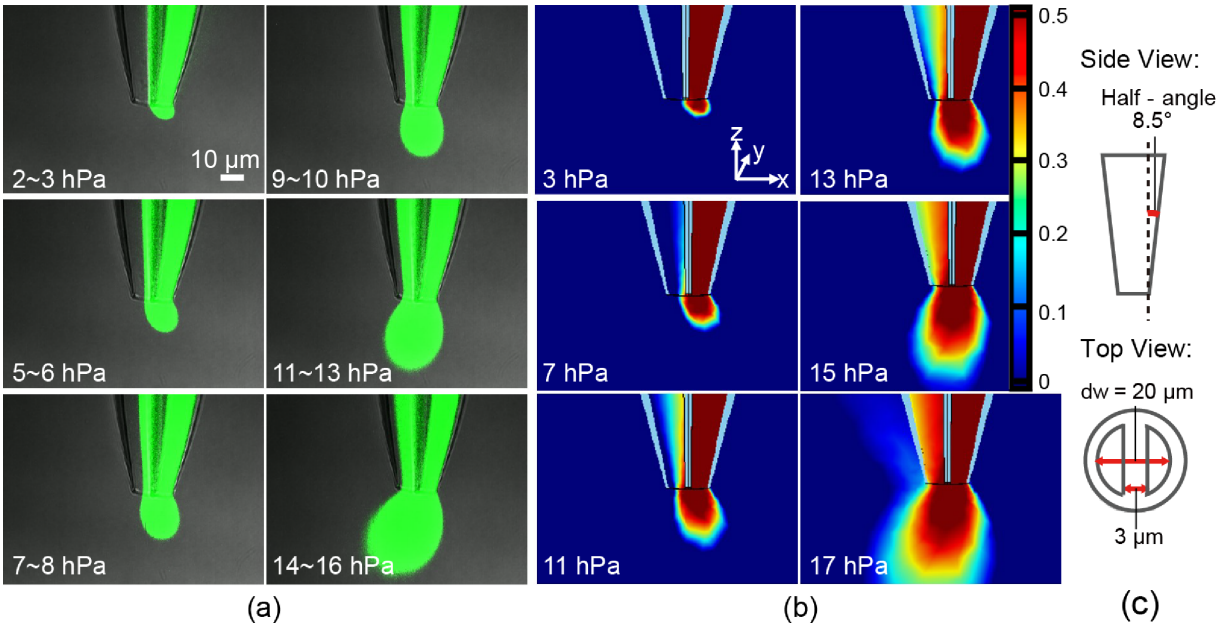

Figure 2: Comparison between experimental and simulated perfusion flow patterns. a) Microscope images of flow patterns. The injecting flow is a saturated solution (0.08 wt %) of fluorescein. Images 1–6 show patterns at increasing injection pressure, while the extraction flow rate is held constant (5 µL/min). The left channel is the extraction channel, and the right channel is the pressurized injection channel, $P_{in} = P_{applied\_total\_pressure} - 1$ atm, 1 hPa = 100 Pa. b) Simulated perfusion flow patterns. The geometrical parameters to define the pipette were obtained by measurements from optical microscope images in Figure 2a (septum thickness, side wall half-angle, etc.) and similar pressure/suction settings were used as in the experiment. c) Geometrical sketches of Figure 2a and Figure 2b, side view (top) and cross-section (bottom) view.

tion pressure is increased. Figure 2b shows the results of the FEM where the pipette diameter at the tip and other geometrical parameters of the pipette were similar to the experimental parameters. The flow rate in the extraction channel in the simulations was set equal to the experimental flow rate, and the pressure through the injection channel (in the simulation) was adjusted until the diffusion plume size and shape matched what was experimentally observed. It can be seen that there is close agreement between injection pressures in the FEM model and the experimental observations for any given size and shape of the plume, suggesting that the model is valid over this range of conditions.

Oxygen confinement due to pipette and effect of increased pipette diameter

One influence of the pipette is the confinement of oxygen diffusion within it. Oxygen can diffuse freely along the pipette axis (*z*-axis as in Figure 3a), but remains confined by the pipette walls. To demonstrate the effect of this confined diffusion, consider a small oxygen sensor positioned at a small distance from the cell. The geometry parameters used in the model are demonstrated in Figure 3a. As demonstrated by FEM simulations results shown in Figure 3b (curve 1 vs 2), the oxygen concentration difference signal (the difference between the concentration of a saturated oxygen solution in water at room temperature and the oxygen concentration at the specific point under investigation) obtained by the sensor positioned at the tip of the pipette has around 1.5 times greater signal than the same size sensor placed at the same distance away from the cell, but without the pipette. This is because of the proximity of the pipette to the cell results in an oxygen concentration gradient within the pipette due to oxygen consumption by the cell. The oxygen gradient within the pipette is larger than the gradient of oxygen in the surrounding fluid because oxygen is constrained within the pipette to diffuse effectively only along the pipette length. This results in oxygen diffusing slower within the pipette than in the surrounding fluid. Thus, the mere presence of the pipette over the cell increases the oxygen concentration difference that can be sensed.

Figure 3b also shows that moving the same sensor within the pipette much further from the cell, while maintaining the same distance of the pipette tip from the cell, reduces the signal, as might be expected. Most of this reduction can be attributed to the expansion of the pipette diameter away from the cell due to a non-zero pipette half-angle. This conclusion can be confirmed by considering a theta pipette with a zero half-angle (theta tube, curve 3 in Figure 3b). As demonstrated in Figure 3b, the signal obtained by a sensor placed 150 µm away from the tip of the theta tube is nearly the same as the signal ob-

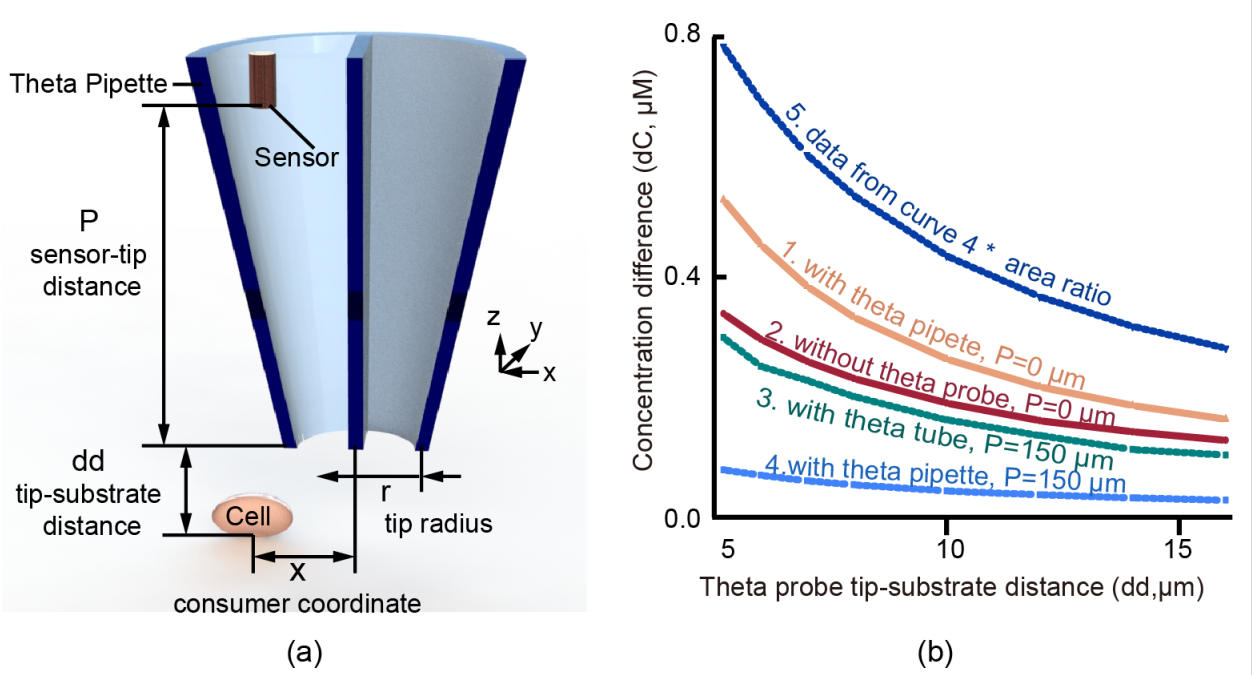

Figure 3: a) Demonstration of the simulation geometry parameters. Details of the parameters used in the model are specified in the Experimental section. b) Dependence of signal (oxygen concentration difference) strength on the proximity of the theta pipette tip to the substrate, for two sensor locations, and two pipette half-angles (with the cell noted as the consumer beneath the pipette, and without flow between barrels). Curve 1 is plotted from a sensor located at the tip of a typical theta pipette which has a half-angle of 8.5° and a tip diameter of 20 µm; Curve 2 is from a sensor at the same location, but without a theta pipette surrounding it; Curve 3 is from a sensor located inside a theta tube (0° half-angle, and tip diameter of 20 µm) and 150 µm above the tip; Curve 4 is a plot from the sensor located inside a typical theta pipette and 150 µm above its tip; Curve 5 is curve 4 multiplied by the area ratio of this location and the tip.

tained by placing the sensor close to the cell without the tube (curve 2 in Figure 3b).

So far, we have considered sensors that remain the same in size regardless of their position along the axis of the theta pipette. However, considering that the diameter of the pipette increases away from the tip (for non-zero half-angles), sensors that are larger in size can be facilitated. If we scale the sensor area with the increasing pipette diameter, the signal can be improved significantly depending on the nature of the sensor. For example, the electrical current used as the signal in electrochemical sensors is proportional to the effective sensor area. If we take the sensor sensitivity to be proportional to the area, we can significantly increase the overall sensitivity of the probe as we move the sensor further away from the pipette tip, which is also indicated in Figure 3b (curve 5 vs 1). Therefore, this analysis suggests an opportunity to improve sensitivity without sacrificing resolution. One may wonder why the signal strength is increased when the concentration decreases in a pipette whose cross-sectional area increases along its *z*-axis (as in Figure 3a). Diffusion along a non-zero half-angle pipette, whose diameter increases along its axis proportional to the axial distance, can be modeled as diffusion in a solid angle of a sphere. Such a model would yield a concentration that decreases linearly with the axial distance. At the same time, the sensor area would increase as the square of the axial distance, resulting in a linear gain of sensitivity with distance for a sensor whose sensitivity is proportional to its area.

Effects of perfusion on oxygen consumption signaling

One may expect that losing less molecules to the diffusion away from the sensor should increase the probe sensitivity. As shown in Figure 4, this effect is indeed confirmed by the FEM calculations when considering a sensor placed 150 µm downstream within the theta pipette. One would expect significant amplification of the signal (oxygen concentration difference) due to perfusion to occur when diffusion dominates over the convection and the Peclet number is significantly smaller than 1, say 0.1. In such operating regime, all oxygen molecules are not fully retained within the flow, and increases in the flow velocity help to retain oxygen molecules. At larger flow velocities, most oxygen molecules are already confined to the flow and further velocity increases do not amplify the signal. This logic can provide a rough estimate of the perfusion velocity range beyond which no signal is gained. As an example, we consider a pipette that is located at dd = 10 µm from the substrate. Taking the oxygen diffusion coefficient of 2000 $\mu m^2/s$ and assuming that

amplification occurs mostly below the Peclet number of 0.1, one finds that no significant signal gain should occur beyond the velocity $v_{max} \approx Pe{\cdot}D/dd = (0.1 \times 2000)/10 = 20$ µm/s. This is in quantitative agreement with the velocity of maximal signal calculated by the FEM and shown in Figure 4.

As the velocity increases further, the flux of oxygen in the pipette due to flow should start dominating the flux due to oxygen consumption, reducing the oxygen concentration difference along the z-axis of the extraction channel. The reduction of oxygen concentration difference between different positions along the flow at higher flow velocities can be demonstrated by a simplified analytical model (see Supporting Information File 1) and is given by Equation 1:

$$S = C_0 - C_r(x) \approx \frac{Rb}{v}\left(\exp\left(\frac{v}{D}d\right) - \exp\left(\frac{v}{D}x\right)\right) \propto \frac{Rb}{v} \quad (1)$$

where R is the oxygen consumption rate per unit length of the flow, b is the length of the oxygen consumption region in the flow, $d >> b$ is the distance from the tip of the pipette to the place in the flow where a constant oxygen concentration, C_o, exists due to contact with the environment, x is the position of the sensor downstream from the consumption region and $C_r(x)$ is the oxygen concentration measured by the sensor.

As shown in Figure 4, calculated based on a normal human prostate cell oxygen consumption rate (10^{-17} mol/s), an oxygen concentration difference of 0.27 µM could be measured by the sensor at P = 150 µm under optimized flow conditions. This concentration difference is close to commercial oxygen optical probe resolution with a similar sensing area (from data sheet of fiber optic oxygen sensor from Pyroscience, with a tip size of 35 µm in diameter and a resolution of 0.78 µM at 20% oxygen). In a real case scenario, we can assume the oxygen consumption rate of a tumor cell is 10 times higher than that of a normal cell [39], which yields a resolution of 2.7 µM with the designed sensor.

Spatial resolution

One important role of the theta pipette probe is to increase sensitivity by placing sensor further up the pipette and using the perfusion flow, while preserving spatial resolution to permit measurements from individual cells in cell culture. Figure 5 illustrates that high resolution is achievable. In fact, it shows that the resolution is on the order of the pipette diameter and, since diameters smaller than micrometers are readily achiev-

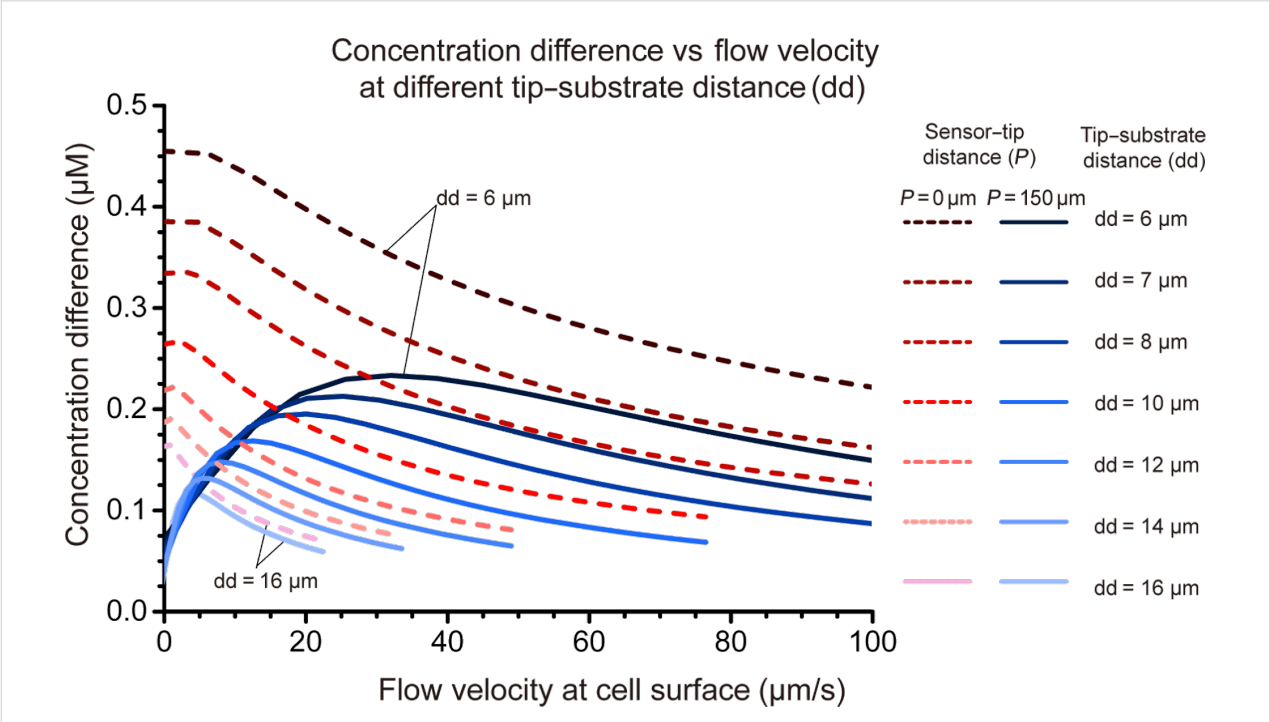

Figure 4: Dependence of signal (oxygen concentration difference) strength on perfusion flow velocity for different tip–substrate distances (dd), and for sensors at different locations (0 µm and 150 µm above the tip) inside a typical theta pipette (tip diameter dw = 20 µm, half-angle = 8.5°). Other parameter settings are the same as those used for Figure 3. The group of red dotted curves are measured from the sensors at the tip of the theta pipette. The group of blue solid curves are measurements from sensors inside the theta pipette, 150 µm above the tip. For both color groups, from dark color to light color, the distance from the theta pipette tip to substrate increases.

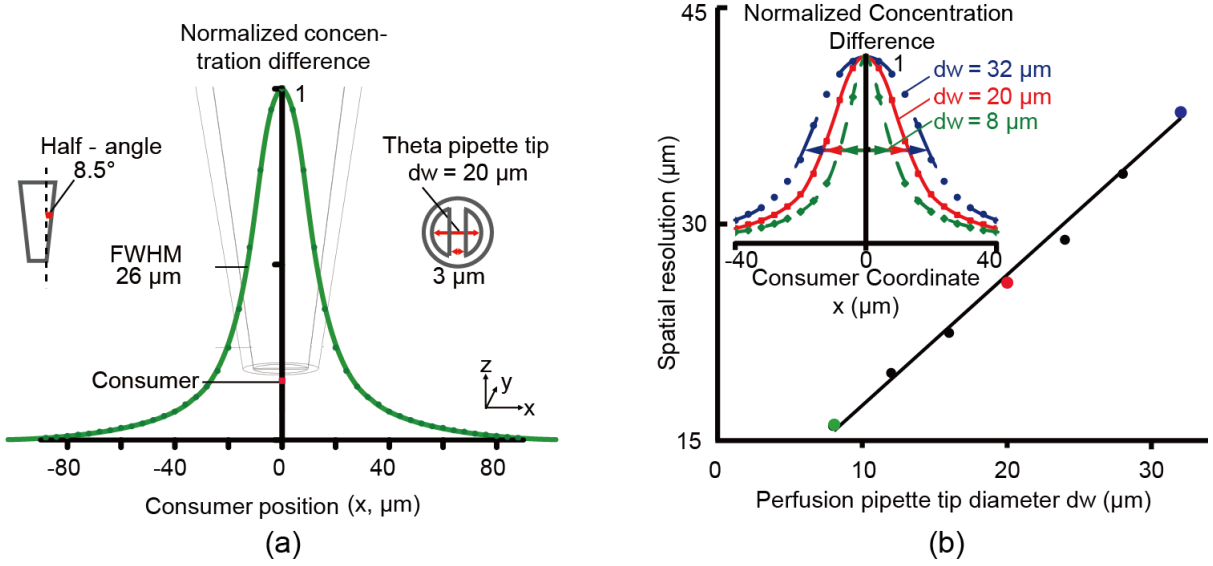

Figure 5: Spatial resolution of the scanning theta pipette probe. a) Illustration of the spatial resolution of a perfusion respirometry probe with tip diameter (dw) of 20 µm. The probe is located at the center of the *x*-axis and the specific tip geometry (as in insets) is the same as in the previous simulations. The oxygen concentration difference is the desired signal and is measured by the sensor inside the probe, 150 µm above the tip. A tiny, cubic consumer element of volume 2 × 2 × 2 μm^3 is located on the substrate. The distance from substrate to theta pipette tip is set at 6 µm. The pressure applied at the input channel is (1 atm + 2 Pa), and at the output is (1 atm − 2 Pa). With these pressure values, the impact of perfusion on improving the signal is most significant. The green curve is a plot of the measured signals as the center position of the consumer moves from left (x = −90 µm) to right (x = 90 µm) along the *x*-axis. The full width at half maximum (FWHM) of this curve is 26 µm, and can be defined as the spatial resolution. b) The probe spatial resolution vs tip diameter. The pressure at the inlet and outlet of the theta pipette is set to achieve best improvement of signal at 150 µm above the tip for each tip diameter, respectively. The theta pipette tip diameter increases from 8 to 32 µm with a step size of 4 µm, while the half-angle of the pipette is fixed (8.5°). Inset: the oxygen concentration difference plot at tip sizes of 8, 20 and 32 µm.

able [40-42], spatial resolution on the order of micrometers is possible.

Conclusion

This paper studies a perfusion double-barrel micropipette, in particular, a theta pipette, as a microfluidic system that is potentially important for investigating metabolic variations among individual cells associated with changes in biological functions and disease development. The use of FEM to study the behavior of this microfluidic system not only verifies the experimental results, demonstrating the feasibility of the proposed approach, but also allows theoretical insights into pipette performance/sensitivity to be obtained that would otherwise require extensive studies, if done experimentally. In particular, the effects of the theta micropipette operational parameters on the system oxygen sensing capacity were considered first. It was found that the mere presence of the pipette over the cell increases the oxygen concentration difference that can be sensed. Also, the use of the theta pipette increases the overall sensitivity of the probe as the sensor is moved away from the pipette tip, due to oxygen confinement. In addition, the larger diameter of the pipette channel far from the tip allows the use of sensors with larger surface area. When the sensor is placed far from the tip end, introducing an appropriate perfusion flow to the system not only maintains a constant cell microenvironment, but also further confines the free diffusion, amplifying the signal (oxygen concentration difference) at the sensor location and preventing back diffusion. Finally, in this paper we focused on theta pipettes with micrometer-scale tips (Figure 1b), which would cover an average cell area to maximize the signal intensity. However, pipettes with sub-micrometer tips (Figure 1c) could be produced to obtain spatial resolution at subcellular levels. It is also worth mentioning that the developed probe is certainly not limited to oxygen measurement. By using different sensors, including electrochemical or optical ones, other types of analyses can be carried out over the surface of living tissue. One can also envision applications of the proposed approach in analytical chemistry or forensic study for spatially resolved microanalysis.

Experimental

Description of experimental set-up for experimental hydrodynamic confinement

In this paper, a 1.5 mm outer diameter double-barrel glass that has a theta-style cross-section (Sutter Instrument Co.) was pulled using a laser glass puller (Sutter Instrument Co., P-2000) to form theta micropipettes as shown in Figure 1b,c. Depending on the pulling parameters, the pipette tip diameter can be varied

from tens of micrometers down to hundreds of nanometers. The injection channel of the theta micropipette was loaded with a saturated fluorescein (Acros Organics, Fisher Scientific; excitation/emission wavelengths 498/518 nm) aqueous solution (0.08 wt %). The extraction channel was loaded with pure water. Two plastic tubes were then inserted into the two unmodified channels at the other end of the theta capillary and sealed with epoxy (Bob Smith Ind., quick-cure 5 min epoxy). The injection channel was then connected to a source of positive pressure, while the extraction channel was connected to a source of negative pressure. In this work, the positive pressure was supplied by a pressure pump (Eppendorf, FemtoJet), and a syringe pump (New Era Pump Systems, Inc., Dual-NE-1000) was used to supply suction. To study the effects of perfusion flow on molecular diffusion around the tip of the theta pipette, the pipette tip was immersed at a 5° angle to the substrate into a large drop of water (0.3 mL) placed on a microscope slide, while fluorescent molecules where perfused through the pipette tip as illustrated in Figure 6. An inverted fluorescent microscope (Olympus FluoView FV1000 Confocal Laser Scanning Microscope; sampling speed: 2.0 µs/pixel) with a lens (LUMPLFL, 100X W NA: 1.00) placed near the bottom of the microscope slide focused on the tip end area was employed to observe the size and intensity of the fluorescent plume. A constant withdraw speed of 5 µL/min provided by the syringe pump was maintained at the probe's extraction channel. Multiple experiments were performed at different injection channel pressures, varying from 100 hPa to 116 hPa with of 2–3 hPa increments, and then decreased back to 100 hPa with the same step size. The fluorescent dye plumes in the water droplet were observed and recorded.

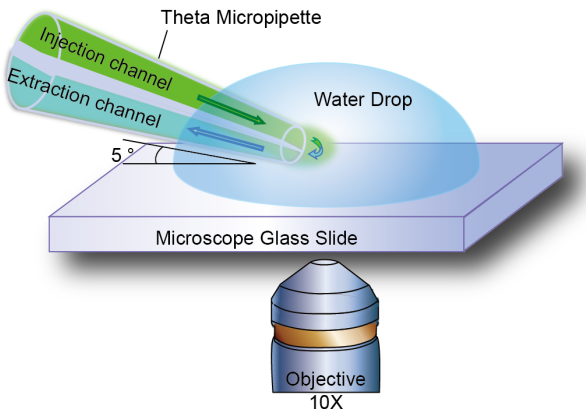

Figure 6: Illustration of the experimental setup for investigating the effect of perfusion flow on the diffusion of fluorescent dye. The blue hemisphere is the water drop (0.3 mL) formed over a microscope glass slide. The theta pipette tip is inserted into the water drop. The injection channel is preloaded with a saturated fluorescein aqueous solution (0.08 wt %). The green color represents the fluorescein dye (fluorescein), with the green intensity proportional to the dye concentration. The small green area volume within the water drop represents roughly the diffusion boundary of the florescent dye. The arrows show the fluid flow direction. A constant withdraw rate of 5 µL/min is applied by a syringe pump to the pipette's extraction channel. The injection pressure was increased from 100 hPa to 116 hPa with an increment of 2–3 hPa and then decreased back to 100 hPa with the same step size. The fluorescent dye plumes in the water droplet were observed at each pressure for 15 s before changing the injection pressure. The total recording length was 7 minutes. During this time, the water droplet size did not change significantly due to evaporation.

Finite element model

A 3D model was built in COMSOL Multiphysics (v4.4) to evaluate the perfusion probe's performance (see Supporting Information File 2). Two different stationary models were developed and coupled in this model, one for the Navier–Stokes equations (Equation 2 and Equation 3) for flow parameters inside the computational region [43,44]:

$$\rho(\vec{v}\cdot\nabla)\vec{v} = \nabla\cdot\left[-p\vec{I} + \mu\left(\nabla\vec{v} + (\nabla\vec{v})^T\right)\right] + \vec{F} \quad (2)$$

$$\rho\nabla\cdot\vec{v} = 0 \quad (3)$$

where ρ is the density, $\vec{v}$ is the calculated flow velocity field, p is the pressure, $\vec{I}$ is the unit vector, µ is the dynamic viscosity, and $\vec{F}$ is the volume force field. Another study solved the convection diffusion equations (Equation 4 and Equation 5) for concentration distribution [45,46]:

$$\nabla\cdot(-D\nabla c) + \nabla\cdot(\vec{v}c) = R \quad (4)$$

$$\vec{N} = -D\nabla c + \vec{v}c \quad (5)$$

Where D is the diffusion coefficient, c is the species mass concentration, $\vec{v}$ is the flow velocity field calculated from the previous study, R is the reaction rate, and $\vec{N}$ is the flux, respectively.

For hydrodynamic confinement verification, a 400 µm long quartz theta pipette was built at the top center in a water-filled rectangular computational region of (500 × 400 × 400 µm^3). The theta pipette had a tip diameter of 20 µm, and its outer wall was formed by a truncated cone with half-angle of 8.5°. Its separation was formed by a rectangle frustum, used in the simulation to achieve a similar pipette tip geometry as for the experimental images. All the walls of this geometry were defined as no-slip walls. A negative pressure and a positive pressure was defined respectively on the top boundaries of the two channels to form the injection and extraction flow in the laminar flow module. The calculated flow field was then used as the flow parameters in the convection and diffusion study. Under our ex-

perimental conditions, diffusion was found to have practically no effect on the flow. To set up the flow conditions, a constant pressure of −120 hPa was provided at one channel of this pipette to apply suction. At the other channel, a positive pressure was applied from 100 to 117 hPa at several step increments. The upper boundary of the model is set to open boundary. These flow parameters were set to match experimental conditions. For convection and diffusion studies, the initial species concentration of the whole computational area was set to zero and the inflow concentration was set to 2407 μM (fluorescein saturated aqueous solution). The diffusion coefficient was set to 0.425×10^{-5} cm^2/s (fluorescein diffusion coefficient in water at room temperature [47]). No cells or consumers were included in this hydrodynamic confinement discussion.

Then similar model parameters were used to evaluate the probe for cell oxygen consumption sensing with modifications to introducing the cell and the substrate to the model (Figures 3–5). To be specific, the rectangular computational region was reduced to ($410 \times 300 \times 300$ μm^3) and the substrate was placed at the bottom of the calculation area. For Figure 3, the tip diameter of the pipette was set to 12 μm to have a high spatial resolution necessary for single-cell studies. An ellipsoid with 5 μm, 5 μm, and 2.5 μm related to the *a*-, *b*- and *c*-axes, respectively, was attached to the substrate to represent a cell. This ellipsoid was defined as an oxygen reactor with reaction rate of 0.04 mol/m^3s, which resulted in a total oxygen consumption rate of 10^{-17} mol/s. The boundaries of the reactor were set to be slip so that the flow velocity does not artificially set to zero. Simulations were run for tip–substrate distances varying from 5.2 μm to 16 μm. A negative pressure and an equal value positive pressure were defined respectively on the top boundaries of the two channels to form the injection and extraction flow. The upper boundary of the model was set as open boundary. For convection and diffusion studies, the injection boundary concentration was set to 250 μM (saturated oxygen concentration in water at room temperature [48]). A symmetric boundary condition of 250 μM was set to the extraction boundary, as well as the upper boundary of the computational region. The diffusion coefficient of oxygen was set to 2×10^{-5} cm^2/s (oxygen in water at room temperature [49]). The oxygen concentration difference was recorded inside the extraction channel of the theta pipette at $P = 0$, or 150 μm above the tip for Figure 3, and $P = 150$ μm for Figure 4 and Figure 5. A tetrahedral mesh with maximum mesh size of 14.4 μm, minimum mesh size of 0.615 μm, maximum element growth rate of 1.35, curvature factor of 0.3, and resolution of narrow regions of 0.85 was used to divide the system for FEM calculation. We verified that the meshes and the computational region size used here were appropriate for solving by comparing to a finer mesh setting or larger computational region. The calculated concentration differences between these two cases is less than 5%, and compared to a wider computational region setting of $410 \times 320 \times 320$ μm^3, the calculated concentration differences between these two cases is less than 1%. Directed solvers were selected in all studies to have the most accurate result with relative tolerance set to 10^{-6}.

Supporting Information

Supporting Information File 1

1D analytical model of the system.
[https://www.beilstein-journals.org/bjnano/content/supplementary/2190-4286-9-79-S1.pdf]

Supporting Information File 2

Open theta cell.
[https://www.beilstein-journals.org/bjnano/content/supplementary/2190-4286-9-79-S2.pdf]

Acknowledgements

This work is partially based on the doctoral dissertation of Dr. Yang Gao. The support of Cornelius Beukenkamp's endowment is highly appreciated. The authors would like to acknowledge the use of the Core Facilities in the College of Engineering at Drexel University, and Mr. Edward Basgall for training and assistance with acquiring SEM images. The authors thank Dr. Alyssa Bellingham for her help with experiments.

ORCID® iDs

Zulfiya Orynbayeva - https://orcid.org/0000-0002-7401-2165
Yury Gogotsi - https://orcid.org/0000-0001-9423-4032

References

1. Van Loo, P.; Voet, T. *Curr. Opin. Genet. Dev.* **2014,** *24,* 82–91. doi:10.1016/j.gde.2013.12.004
2. Wei, W.; Shin, Y. S.; Ma, C.; Wang, J.; Elitas, M.; Fan, R.; Heath, J. R. *Genome Med.* **2013,** *5,* 75. doi:10.1186/gm479
3. Morris, J.; Singh, J. M.; Eberwine, J. H. *J. Visualized Exp.* **2011,** e2634. doi:10.3791/2634
4. van Heerden, J. H.; Wortel, M. T.; Bruggeman, F. J.; Heijnen, J. J.; Bollen, Y. J. M.; Planqué, R.; Hulshof, J.; O'Toole, T. G.; Wahl, S. A.; Teusink, B. *Science* **2014,** *343,* 1245114. doi:10.1126/science.1245114
5. Spencer, J. A.; Ferraro, F.; Roussakis, E.; Klein, A.; Wu, J.; Runnels, J. M.; Zaher, W.; Mortensen, L. J.; Alt, C.; Turcotte, R.; Yusuf, R.; Côté, D.; Vinogradov, S. A.; Scadden, D. T.; Lin, C. P. *Nature* **2014,** *508,* 269–273. doi:10.1038/nature13034
6. Sakadžić, S.; Roussakis, E.; Yaseen, M. A.; Mandeville, E. T.; Srinivasan, V. J.; Arai, K.; Ruvinskaya, S.; Devor, A.; Lo, E. H.; Vinogradov, S. A.; Boas, D. A. *Nat. Methods* **2010,** *7,* 755–759. doi:10.1038/nmeth.1490
7. Papkovsky, D. B.; Dmitriev, R. I. *Chem. Soc. Rev.* **2013,** *42,* 8700–8732. doi:10.1039/c3cs60131e

8. Nebel, M.; Grützke, S.; Diab, N.; Schulte, A.; Schuhmann, W. *Angew. Chem., Int. Ed.* **2013,** *52,* 6335–6338. doi:10.1002/anie.201301098
9. Hu, K.; Gao, Y.; Wang, Y.; Yu, Y.; Zhao, X.; Rotenberg, S.; Gökmeşe, E.; Mirkin, M. V.; Friedman, G.; Gogotsi, Y. *J. Solid State Electrochem.* **2013,** *17,* 2971–2977. doi:10.1007/s10008-013-2173-5
10. Gao, Y.; Longenbach, T.; Vitol, E. A.; Orynbayeva, Z.; Friedman, G.; Gogotsi, Y. *Nanomedicine* **2013,** *9,* 153–168. doi:10.2217/nnm.13.196
11. Vitol, E. A.; Orynbayeva, Z.; Friedman, G.; Gogotsi, Y. *J. Raman Spectrosc.* **2012,** *43,* 817–827. doi:10.1002/jrs.3100
12. Singhal, R.; Orynbayeva, Z.; Kalyana Sundaram, R. V.; Niu, J. J.; Bhattacharyya, S.; Vitol, E. A.; Schrlau, M. G.; Papazoglou, E. S.; Friedman, G.; Gogotsi, Y. *Nat. Nanotechnol.* **2011,** *6,* 57–64. doi:10.1038/nnano.2010.241
13. Momotenko, D.; Cortes-Salazar, F.; Lesch, A.; Wittstock, G.; Girault, H. H. *Anal. Chem.* **2011,** *83,* 5275–5282. doi:10.1021/ac2006729
14. Takahashi, Y.; Shiku, H.; Murata, T.; Yasukawa, T.; Matsue, T. *Anal. Chem.* **2009,** *81,* 9674–9681. doi:10.1021/ac901796r
15. Tan, W.; Shi, Z.-Y.; Smith, S.; Birnbaum, D.; Kopelman, R. *Science* **1992,** *258,* 778–781. doi:10.1126/science.1439785
16. Wang, J.; Myung, N. V.; Yun, M.; Monbouquette, H. G. *J. Electroanal. Chem.* **2005,** *575,* 139–146. doi:10.1016/j.jelechem.2004.08.023
17. Vitol, E. A.; Orynbayeva, Z.; Bouchard, M. J.; Azizkhan-Clifford, J.; Friedman, G.; Gogotsi, Y. *ACS Nano* **2009,** *3,* 3529–3536. doi:10.1021/nn9010768
18. Warburg, O.; Wind, F.; Negelein, E. *J. Gen. Physiol.* **1927,** *8,* 519–530. doi:10.1085/jgp.8.6.519
19. Sena, L. A.; Chandel, N. S. *Mol. Cell* **2012,** *48,* 158–167. doi:10.1016/j.molcel.2012.09.025
20. Tejera, A.; Herrero, J.; de los Santos, M. J.; Garrido, N.; Ramsing, N.; Meseguer, M. *Fertil. Steril.* **2011,** *96,* 618–623. doi:10.1016/j.fertnstert.2011.06.059
21. Brand, M. D.; Nicholls, D. G. *Biochem. J.* **2011,** *435,* 297–312. doi:10.1042/BJ20110162
22. Semenza, G. L. *Wiley Interdiscip. Rev.: Syst. Biol. Med.* **2010,** *2,* 336–361. doi:10.1002/wsbm.69
23. Gnaiger, E. Oxygen Conformance of Cellular Respiration. In *Hypoxia. Advances in Experimental Medicine and Biology;* Roach, R. C.; Wagner, P. D.; Hackett, P. H., Eds.; Springer: Boston, MA, 2003; Vol. 543, pp 39–55. doi:10.1007/978-1-4419-8997-0_4
24. Pike Winer, L. S.; Wu, M. *PLoS One* **2014,** *9,* e109916. doi:10.1371/journal.pone.0109916
25. Pesta, D.; Gnaiger, E. High-Resolution Respirometry: OXPHOS Protocols for Human Cells and Permeabilized Fibers from Small Biopsies of Human Muscle. *Mitochondrial Bioenergetics;* Methods in Molecular Biology, Vol. 810; 2012; pp 25–58. doi:10.1007/978-1-61779-382-0_3
26. Kelbauskas, L.; Ashili, S. P.; Houkal, J.; Smith, D.; Mohammadreza, A.; Lee, K. B.; Forrester, J.; Kumar, A. V.; Youngbull, C. A.; Tian, Y.; Holl, M. R.; Johnson, R. H.; Meldrum, D. R.; Anis, Y. H.; Paulson, T. G. *J. Biomed. Opt.* **2012,** *17,* 037008. doi:10.1117/1.JBO.17.3.037008
27. Molter, T. W.; McQuaide, S. C.; Suchorolski, M. T.; Strovas, T. J.; Burgess, L. W.; Meldrum, D. R.; Lidstrom, M. E. *Sens. Actuators, B* **2009,** *135,* 678–686. doi:10.1016/j.snb.2008.10.036
28. O'Connell, M. A.; Snowden, M. E.; McKelvey, K.; Gayet, F.; Shirley, I.; Haddleton, D. M.; Unwin, P. R. *Langmuir* **2014,** *30,* 10011–10018. doi:10.1021/la5020412
29. Kuznetsov, A. V.; Veksler, V.; Gellerich, F. N.; Saks, V.; Margreiter, R.; Kunz, W. S. *Nat. Protoc.* **2008,** *3,* 965–976. doi:10.1038/nprot.2008.61
30. Bergner, S.; Vatsyayan, P.; Matysik, F.-M. *Anal. Chim. Acta* **2013,** *775,* 1–13. doi:10.1016/j.aca.2012.12.042
31. Yu, Y.; Gao, Y.; Hu, K.; Blanchard, P.-Y.; Noël, J.-M.; Nareshkumar, T.; Phani, K. L.; Friedman, G.; Gogotsi, Y.; Mirkin, M. V. *ChemElectroChem* **2015,** *2,* 58–63. doi:10.1002/celc.201402312
32. Sun, P.; Laforge, F. O.; Abeyweera, T. P.; Rotenberg, S. A.; Carpino, J.; Mirkin, M. V. *Proc. Natl. Acad. Sci. U. S. A.* **2008,** *105,* 443–448. doi:10.1073/pnas.0711075105
33. Ainla, A.; Jeffries, G. D. M.; Brune, R.; Orwar, O.; Jesorka, A. *Lab Chip* **2012,** *12,* 1255–1261. doi:10.1039/c2lc20906c
34. Lopes, A. S.; Greve, T.; Callesen, H. *Theriogenology* **2007,** *67,* 21–31. doi:10.1016/j.theriogenology.2006.09.026
35. Roberts, W. M.; Almers, W. *Pfluegers Arch.* **1984,** *402,* 190–196. doi:10.1007/bf00583334
36. McKelvey, K.; Nadappuram, B. P.; Actis, P.; Takahashi, Y.; Korchev, Y. E.; Matsue, T.; Robinson, C.; Unwin, P. R. *Anal. Chem.* **2013,** *85,* 7519–7526. doi:10.1021/ac401476z
37. Juncker, D.; Schmid, H.; Delamarche, E. *Nat. Mater.* **2005,** *4,* 622–628. doi:10.1038/nmat1435
38. Feinerman, O.; Moses, E. *J. Neurosci. Methods* **2003,** *127,* 75–84. doi:10.1016/S0165-0270(03)00099-2
39. Panov, A.; Orynbayeva, Z. *PLoS One* **2013,** *8,* e72078. doi:10.1371/journal.pone.0072078
40. Singhal, R.; Bhattacharyya, S.; Orynbayeva, Z.; Vitol, E.; Friedman, G.; Gogotsi, Y. *Nanotechnology* **2010,** *21,* 015304. doi:10.1088/0957-4484/21/1/015304
41. Schrlau, M. G.; Falls, E. M.; Ziober, B. L.; Bau, H. H. *Nanotechnology* **2008,** *19,* 015101. doi:10.1088/0957-4484/19/01/015101
42. Schrlau, M. G.; Brailoiu, E.; Patel, S.; Gogotsi, Y.; Dun, N. J.; Bau, H. H. *Nanotechnology* **2008,** *19,* 325102. doi:10.1088/0957-4484/19/32/325102
43. Bird, R. B.; Stewart, W. E.; Lightfoot, E. N. *Transport Phenomena,* 2nd ed.; John Wiley & Sons, Inc., 2006; pp 75–104.
44. Bird, R. B.; Stewart, W. E.; Lightfoot, E. N. *Transport Phenomena,* 2nd ed.; John Wiley & Sons, Inc., 2006; pp 11–37.
45. Bird, R. B.; Stewart, W. E.; Lightfoot, E. N. *Transport Phenomena,* 2nd ed.; John Wiley & Sons, Inc., 2006; pp 513–539.
46. Bird, R. B.; Stewart, W. E.; Lightfoot, E. N. *Transport Phenomena,* 2nd ed.; John Wiley & Sons, Inc., 2006; pp 582–606.
47. Culbertson, C. T.; Jacobson, S. C.; Ramsey, J. M. *Talanta* **2002,** *56,* 365–373. doi:10.1016/S0039-9140(01)00602-6
48. Truesdale, G. A.; Downing, A. L. *Nature* **1954,** *173,* 1236. doi:10.1038/1731236a0
49. Ferrell, R. T.; Himmelblau, D. M. *J. Chem. Eng. Data* **1967,** *12,* 111–115. doi:10.1021/je60032a036